Doctoral theses at NTNU, 2021:203

Tobias Martin

A new CFD-based framework for modelling the interaction of open ocean aquaculture structures and complex free surface hydrodynamics

Doctoral thesis

NTNU
Norwegian University of Science and Technology
Thesis for the Degree of Philosophiae Doctor
Faculty of Engineering
Department of Civil and Environmental Engineering

NTNU
Norwegian University of Science and Technology

Tobias Martin

A new CFD-based framework for modelling the interaction of open ocean aquaculture structures and complex free surface hydrodynamics

Thesis for the Degree of Philosophiae Doctor

Trondheim, June 2021

Norwegian University of Science and Technology
Faculty of Engineering
Department of Civil and Environmental Engineering

NTNU
Norwegian University of
Science and Technology

NTNU
Norwegian University of Science and Technology

Thesis for the Degree of Philosophiae Doctor

Faculty of Engineering
Department of Civil and Environmental Engineering

ISBN 978-82-326-6630-0 (printed ver.)
ISBN 978-82-326-6197-8 (electronic ver.)
ISSN 1503-8181 (printed ver.)
ISSN 2703-8084 (online ver.)

Doctoral theses at NTNU, 2021:203

Printed by NTNU Grafisk senter

Abstract

The work presented in this PhD thesis provides the first numerical framework for the detailed simulation of open ocean aquaculture structures in the sea environment. It enables the simulation of the fluid-structure interaction of rigid floating structures and nets with a viscous fluid including a free surface. As part of the thesis, new approaches for modelling mooring dynamics, dynamics of nets and the rigid body dynamics of floating structures as well as their interaction with the fluid are developed by the author. All models are integrated into the viscous two-phase Computational fluid dynamics (CFD) solver REEF3D. This is in contrast to existing numerical approaches which either neglect important non-linearities or the interaction between the structures and the fluid.

The Reynolds-averaged Navier-Stokes equations including a free surface are solved as the basis of the two-phase numerical wave tank REEF3D. Here, a k-ω turbulence model including an additional source term for the free surface treatment is applied. The equations are solved on a staggered rectilinear grid using finite differences. The convection terms are discretised using fifth-order accurate weighted essentially non-oscillatory (WENO) schemes. An incremental pressure-correction algorithm is added by the author for handling the pressure-velocity coupling. The free surface is represented implicitly by the zero level set of a smooth signed distance function. This function is propagated in time and space by solving the linear advection equation. Waves are generated at the inlet using the relaxation method, and a numerical beach prevents excessive reflections at the end of the tank. Full parallelisation is enabled using a ghost-point approach and the message passing interface (MPI) protocol.

An improved version of a continuous direct forcing immersed boundary method is derived in this thesis for modelling rigid floating objects in the three-dimensional numerical wave tank. It is based on a new implicit representation of the body on a stationary grid using a level set function. The motion of the rigid body is described using Euler parameters and Hamiltonian mechanics. The dynamic boundary conditions are enforced by coupling the conservation laws of fluid and rigid body dynamics at the interface between fluid and structure. This effectively avoids computationally expensive reconstruction processes as used in existing approaches and enables the application to large three-dimensional structures.

In addition, a new quasi-static mooring model is presented. Here, each mooring cable is divided into finite truss elements, and the static force equilibria are solved at

each knot in each time step. Thus, the steady-state solution for the shape of an elastic cable and the tension force distribution under consideration of hydrodynamic loads is found. A successive approximation is applied to the resulting system of equations which leads to a significant reduction of the matrix size in comparison to the usage of Newton-Raphson methods. Here, the unknown internal and external forces are separated, and the system is corrected iteratively using the intermediate results for the unit vectors until convergence is reached. The resulting model presents a novel compromise between dynamic and analytical solutions for mooring lines because it combines the flexibility of a generically formulated numerical approach with similar efficiency and simplicity as an analytical solution.

The structural dynamics of large tensile and flexible structures undergoing large motions and deformations, such as nets, are solved with a novel approach based on the lumped mass method. The discrete structure is represented by several elastic bars and knots connecting up to four bars. Non-linear material laws are incorporated which is in contrast to previous models for this type of structures. An implicit system of equations is derived from the fundamental relations of dynamics, kinematics and material laws. It is solved using an improved Newton's method. Hence, a robust model is derived which can be easily coupled to any fluid dynamics solver without restricting the general time step criterion.

In contrast to common tensile structures such as membranes, the considered nets are characterised by high porosities and consist of a large number of individual twines. The length scale of the flow around each twine is significantly smaller than the length scale of the flow around the whole floating structure. This prevents the resolution of the net on the same numerical grid as the fluid domain, and an alternative representation of the fluid-structure interaction between net and fluid has to be introduced. Within this thesis, the author presents a new Lagrangian approach to account for this coupling. The model is based on solving the momentum equations for the fluid on the Eulerian grid and including a source term to account for the disturbances due to the presence of the net. These disturbances represent the momentum transfer between fluid and net and are calculated from the acting forces on the structure. The forces are approximated using a screen force model on Lagrangian points discretising the surface of the net. A suitable interpolation kernel is applied to distribute the forcing term on the fluid domain. In comparison to approaches based on porous media representations, the new model is based on a physical derivation and is suitable for arbitrary geometries and large motions.

Multiple validation cases are presented for the different modules in the course of establishing the framework. It includes the simulation of current flows and wave propagation through fixed and flexible nets as well as the analysis of moored-floating objects in waves with and without nets attached. Finally, a semi-submersible and a mobile-floating open ocean aquaculture structure are investigated to highlight the possibilities of the numerical approach for future applications in this field.

Acknowledgements

I would like to start by acknowledging that the problem at the center of this thesis is not only restricted to technical practicalities and advances. The question of sustainable aquaculture is multidimensional, and to begin with, ethical implications concerning the killing of multiple million fish have to be addressed. It has been shown that fish, like mammals, have physical sensations. This ultimately leads to the desire to avoid unpleasant experiences like pain. This capacity for suffering is not only necessary but also sufficient in order to say that fish have interests. At an absolute minimum, the interest in not suffering. Philosophers like Peter Singer argue that this interest has to be taken into account when evaluating the morality of their killing for human consumption.

Another question is concerned with the sustainability of aquaculture facilities in the light of the UN goal of being more self-sufficient. Raising animals on grain is wasteful as each kilogram of fish requires more than one kilogram of forage. At the same time, a typical salmon farm churns through more than three kilogram of wild fish for every kilogram of salmon that it produces, and the rain forest is devastated for the production of forage. A more sustainable way of feeding the growing population could thus be to eliminate the fish as a wasteful link between plants and humans.

Finally, the emerging challenges resulting from increased cage volumes and fish populations have to be discussed. Not just in the light of technical challenges, as considered in this thesis, but also because of the current developments in land-based factory farming. The consequences arising from cultured breeds, over-populated cages and automatisation are devastating for the number and quality of jobs involved, the environment and the animals. Therefore, future solutions might aim at balancing economical interests, enviromental boundaries and human wellbeing equally.

With that being said, I would like to thank my supervisor Hans Bihs for providing me with the opportunity to pursue this PhD. You had a lot of confidence in my abilities in advance, and I hope that I could at least partly fulfil the expectations. I am also thankful to Arun Kamath for the pleasant conversations about politics and bikes and the introduction to the tasteful world of Indian food. Further, I like to thank Weizhi Wang for being an open-hearted and curious colleague who always have a minute or two. My thanks also go to my former colleagues Csaba Pakozdi for the inspiring technical discussions, Nadeem Ahmad for his support in the office and Ankit Aggarwal for his

calm mind. In addition, I would like to express my gratitude to all my colleagues in the Department and particularly in the basement for the pleasant working atmosphere.

Further, my thanks go to my parents and brothers for enabling me a privileged education and childhood as well as teaching me important matters of life. Finally, I want to express my gratitude to Nora. Your support is essential for me to stay calm and grounded. None of my achievements in life would mean the same without you. Thanks for being on my side whatever direction I am heading.

Contents

List of publications

List of international journal and conference articles appended in this thesis:

Paper 1 Martin, T., Kamath, A. and Bihs, H. (2021). Accurate modelling of the interaction of constrained floating structures and complex free surfaces using a new quasi-static mooring model. *Int. J. Numer. Meth. Fluids, Vol. 93(2), pp. 504–526, doi: 10.1002/fld.4894.*

Paper 2 Martin, T., Kamath, A. and Bihs, H. (2020). A Lagrangian approach for the coupled simulation of fixed net structures in a Eulerian fluid model. *Journal of Fluids and Structures, Vol. 94, doi: 10.1016/j.jfluidstructs.2020.102962.*

Paper 3 Martin, T. and Bihs, H. (2021). A non-linear implicit approach for modelling the dynamics of porous tensile structures interacting with fluids. *Journal of Fluids and Structures, Vol. 100, doi: 10.1016/j.jfluidstructs.2020.103168.*

Paper 4 Martin, T., Tsarau, A. and Bihs, H. (2021). A numerical framework for modelling the dynamics of open ocean aquaculture structures in viscous fluids. *Applied Ocean Research, Vol. 106, doi: 10.1016/j.apor.2020.102410.*

Paper 5 Martin, T. and Bihs, H. (2021). A CFD approach for modelling the fluid-structure interaction of offshore aquaculture cages and waves. *ASME 40th International Conference on Ocean, Offshore and Artic Engineering, OMAE2021, Accepted.*

Declaration of authorship

In the four international journal articles and the conference article appended to this thesis, the thesis author was the main contributor and responsible for developing the algorithms, validations, simulation setups, analyses and paper writing. The co-authors contributed with supervising and critically reviewing the corresponding parts of the work.

Additional international journal papers authored or co-authored by the candidate but not included in the thesis:

1. Martin, T. and Bihs, H. (2021). A numerical solution for modelling mooring dynamics, including bending and shearing effects, using a geometrically exact beam model. *Journal of Marine Science and Engineering, Vol. 9(5), doi:10.3390/jmse9050486.*

2. Martin, T., Wang, G. and Bihs, H. (2020). Numerical Modelling of the Interaction of Moving Fish Nets and Fluid. *Journal of Offshore Mechanics and Arctic Engineering, doi:10.1115/1.4051088.*

3. Martin, T., Kamath, A. and Bihs, H. (2020). Modeling and Simulation of Moored-Floating Structures Using the Tension Element Method. *Journal of Offshore Mechanics and Arctic Engineering, Vol. 142(1), doi: 10.1115/1.4044289.*

4. Wang, G., Martin, T., Huang, L. and Bihs, H. (2020). An improved screen force model based on CFD simulations of the hydrodynamic loads on knotless net panels. *Submitted to Applied Ocean Research.*

5. Wang, G., Martin, T., Huang, L. and Bihs, H. (2020). Modelling the flow around and wake behind net panels using Improved Delayed Detached Eddy Simulations. *Submitted to Ocean Engineering.*

6. Wang, W., Martin, T., Kamath, A. and Bihs, H. (2020). An Improved Depth-Averaged Non-Hydrostatic Shallow Water Model with Quadratic Pressure Approximation. *Int. J. Numer. Meth. Fluids, doi: 10.1002/fld.4807.*

7. Wang, W., Kamath, A., Martin, T., Pakozdi, C. and Bihs, H. (2020). A Comparison of Different Wave Modelling Techniques in An Open-Source Hydrodynamic Framework. *J. Mar. Sci. Eng, Vol. 8(7), doi: 10.3390/jmse8070526.*

8. Gärtner, J., Kronenburg, A. and Martin, T. (2020). Efficient WENO library in OpenFOAM. *SoftwareX, Vol. 12, doi:10.1016/j.softx.2020.100611.*

9. Martin, T., Schacht, S., Riesen, P. and Paschen, M (2018). Efficient Implementation of a Numerical Model for Flexible Net Systems. *Ocean Engineering, Vol. 150, p. 272-279.*

10. Martin, T. and Shevchuk, I. (2018). Implementation and Validation of Semi-implicit WENO Schemes using OpenFOAM. *Computation, Vol. 6(1), doi: 10.3390/computation6010006.*

Related conference papers authored or co-authored by the candidate but not included in the thesis:

1. Martin, T., Kamath, A., Wang, G. and Bihs, H. (2021). Modelling Open Ocean Aquaculture Structures using CFD and a Simulation-based Screen Force Model. *9th International Conference on Computational Methods in Marine Engineering (MARINE2021), Under Review.*

2. Kamath, A., Martin, T. and Bihs, H. (2021). Numerical Simulation of A Floating Moored Buoy in Waves using Direct Forcing Immersed Boundary Method in REEF3D. *ASME 2021 40th International Conference on Ocean, Offshore and Arctic Engineering (OMAE2021), Accepted.*

3. Wang, G., Martin, T., Huang, L. and Bihs, H. (2021). A Numerical Study of the Hydrodynamics of an Offshore Fish Farm using REEF3D. *ASME 2021 40th International Conference on Ocean, Offshore and Arctic Engineering (OMAE2021), Accepted.*

4. Martin, T., Wang, G. and Bihs, H. (2020). Numerical Modelling of the interaction of moving Fish Nets and Fluid. *ASME 2020 39th International Conference on Ocean, Offshore and Arctic Engineering (OMAE2020) Volume 6: Ocean Space Utilization.*

5. Wang, G., Martin, T., Huang, L. and Bihs, H. (2020). Numerical Simulation of Hydrodynamics around Net Meshes using REEF3D. *ASME 2020 39th International Conference on Ocean, Offshore and Arctic Engineering (OMAE2020) Volume 6: Ocean Space Utilization.*

6. Martin, T., Kamath, A. and Bihs, H. (2019). Numerical Modelling of Net Motion in Waves and Current Using CFD. *ASME 2019 38th International Conference on Ocean, Offshore and Arctic Engineering (OMAE2019), Volume 6: Ocean Space Utilization.*

7. Aggarwal, A., Martin, T., Shirinov, S., Bihs, H. and Kamath, A. (2019). Numerical Study of Breaking Waves and Associated Wave Forces on a Jacket Substructure for Offshore Wind Turbines. *ASME 2019 38th International Conference on Ocean, Offshore and Arctic Engineering (OMAE2019), Volume 2: CFD and FSI.*

8. Bihs, H., Wang, W., Martin, T. and Kamath, A. (2019). REEF3D::FNPF: A Flexible Fully Nonlinear Potential Flow Solver. *ASME 2019 38th International Conference on Ocean, Offshore and Arctic Engineering (OMAE2019), Volume 2: CFD and FSI.*

9. Kamath, A., Martin, T. and Bihs, H. (2019). Numerical Modelling of Wave Interaction With an FPSO Under Different Incident Wave Conditions. *ASME 2019 38th International Conference on Ocean, Offshore and Arctic Engineering (OMAE2019), Volume 7A: Ocean Engineering.*

10. Martin, T., Kamath, A. and Bihs, H. (2019). Numerical Modelling of the Interaction between a Fish Net and Fluid using CFD. *8th International Conference on Computational Methods in Marine Engineering (MARINE2019).*

11. Dempwolff, L.-C., Martin, T., Kamath, A. and Bihs, H. (2019). Numerical and Experimental Investigation of Moored-Floating Structures in Regular Waves. *VIII International Conference on Computational Methods in Marine Engineering (MARINE2019).*

12. Martin, T., Bihs, H., Kamath, A. and Arntsen, Ø.A. (2019). Simulation of Floating Bodies in Waves and Mooring in a 3D Numerical Wave Tank using REEF3D. *4th International Conference in Ocean Engineering (ICOE2018).*

13. Martin, T., Kamath, A. and Bihs, H. (2018). Numerical Simulation of Interactions between Water Waves and a Moored-Floating Breakwater. *Proceedings of 36th Conference on Coastal Engineering (ICCE2018).*

14. Martin, T., Kamath, A. and Bihs, H. (2018). Modelling and Simulation of Moored-floating Structures using the Tension-Element-Method. *ASME 2018 37th International Conference on Ocean, Offshore and Arctic Engineering (OMAE2018), Volume 2: CFD and FSI.*

Chapter 1

Introduction

1.1 Background and motivation

According to the 2020 report on world fisheries and aquaculture from the Food and Agriculture Organization of the United Nations (FAO) [35], the global fish production was approximately 179 million tonnes in 2018 and aquaculture accounted for 46% of the total production with 16% from marine aquaculture. Further, the demand for aquatic food products is expected to increase by 16% until 2050 [37]. Captured fishing has no potential for increase in production because 90% of the wild captured species are already overfished or fully fished [27]. Marine aquaculture is therefore an important industry to meet the demand for aquatic resources in the future.

Norway is the leading producer of marine aquaculture products in Europe and the second major exporter of fishery products. The Norwegian fish farm industry has seen strong growth over the last decades and its sustained growth is seen as crucial for the Norwegian economy. In order to serve the rising demand and stay competitive on the market, fish farms are increasing in size. Recently [97], the worlds largest fish farm with a height of 68 m, a diameter of 110 m and space for up to 6000 tonnes of salmon was installed in Norway. Installing such structures near the coast creates severe ecological issues through excrement and medicament pollution as well as the problem of taking too much space [51]. Therefore, the focus of the aquaculture industry recently shifted to the open ocean where the local ecosystems are more robust. Another issue tackled by this development is the biosecurity of the fish from aquatic animal diseases. According to the FAO [35], this is one of the most serious constraints to the expansion and development of a more sustainable aquaculture. The more intense water circulation in open ocean cages can reduce the risk of disease spreading by replenishing the oxygen levels, clearing pollutants and avoiding the development of sea-lice. Thus, a more sustainable aquaculture might be enabled for the future.

The marine environment is characterised by harsh and uncertain conditions with episodes of extreme weather representing challenging conditions to operate in. Traditional fish farms can operate in currents of 0.1 m/s to 0.6 m/s, whereas at higher current speeds, nets with higher solidity are used to reduce the forces acting on the fish [27]. This is however increasing the drag forces on the net which requires more robust cage designs. Also, the increasingly larger dimensions of the farms pose a large economic risk in case of structural failures and fish escape [103]. These failures might be due to extreme loads on the floating structure or net, breaking of the mooring lines leading to differential forcing on the structure and buckling, or fatigue damage due to wave action [66]. Therefore, the severe environmental loads from high energy sea states including waves necessitates accurate analysis and calculation for the design of reliable and economical marine fish farm structures [43]. This led to the development of interest in the field of open ocean aquaculture (OOA) which is concerned with the adaptation of fish cages for the operation in environments with significant exposure to wave action and severe sea conditions [37].

In the light of this major shift in design, fish cage structures have evolved over decades and several designs made of different materials can be found. Traditional designs are composed of a floating collar structure and a porous elastic structure enclosing the fish. The cage is moored using a single point mooring system [30] or multiple mooring lines [41] consisting of catenary or taut leg configurations. The floating collar is usually a circular construction of high-density plastic with a diameter of $50-60$ m with the enclosing structure mounted on it. Alternative design choices adapted from offshore related fields of engineering arose during recent years to account for the increased structural loads [27]. This includes semi-submerged designs, mobile floating cages with one or multiple nets attached and more traditional floating flexible cages with a more robust dimensioning (see Fig. 1.1). The disadvantages of flexible designs in the offshore environment are the large deformation of the net due to waves and currents, difficult working conditions during bad weather and the difficulty of placing feed and monitoring systems due to space constraints [99]. In comparison, rigid frames lead to a fixed volume during operation [99]. Semi-submersible cages have additionally the advantage of relatively small vertical motions because of their relatively large mass and a low centre of gravity. Thus, it can be designed with a large natural period to avoid wave resonance effects [48]. In addition, the system is less exposed to large wave loads by submerging the cages during bad weather periods [27].

The structural and environmental challenges in the operation of open ocean aquaculture structures can be thoroughly studied and addressed with a detailed understanding of the fluid dynamics in and around the structure and the structural response of the floating frame, net and mooring system. Numerical modelling is a relatively inexpensive and flexible way of assessing the dynamics of this fluid-structure interaction (FSI) if appropriate approaches are chosen during establishing the frameworks. In the past, mostly

segregated numerical studies on either the motion of the structure [40, 70, 108] or the flow circulation around the structure [17] were performed. The first numerical investigations of OOA structures without considering the fluid-structure interaction were presented in [41, 42] using a finite element method for the net and linear potential theory for the excitation forces due to current and waves. The considered structure was a spar buoy with an octagonal rim held together by tensioned stays woven into the net. The authors stressed the importance of non-linear effects of extreme waves and fluid-structure interaction for the correct prediction of the structural dynamics. Thus, a separated approach to study these problems can be concluded to be misleading due to the non-linear relationship between the structural and fluid dynamics [44]. Recent computational methods developed for investigating the interaction of the flow and aquaculture systems relied on linear potential theory for the load calculation and empirical formulae for estimating the velocity reduction through the net. The most comprehensive study applying these methods was performed by Kristiansen and Faltinsen [67]. They validated a lumped mass net model coupled to a dynamic beam equation for the floater, linear wave theory to approximate the excitation forces and the formula of Løland [75] to account for the shading effect of the net against experiments of a traditional aquaculture structure. A reasonable agreement could be achieved for small wave steepness and low current which is in accordance with linear theory. For the same type of structure, Shen et al. [100] validated their numerical model, which is based on the same assumptions, against measurements in both regular and irregular waves. They concluded that in severe sea states, the deformation of the net is of a more limiting factor in the design choices than the stresses in the floater. Xu et al. [117] compared a numerical model based on potential theory, a rigid floater for submersible and moored floating net cages and a velocity reduction based on the formula of Løland [75] with physical model tests. The authors highlighted that the lowering of the structure resulted in smaller deformations of the net and reduced mooring line tension forces compared with the floating configuration. Also, varying wave steepness has minor effects on the structural loads in this condition. Finally, Li et al. [74] presented a numerical analysis of the concept of a vessel-shaped cage system using a panel method, linear wave theory and an empirical description of the velocity reduction through the net as the basis. No validation against measurements was provided. However, it was concluded that a deformable net model is necessary and non-linear effects have to be taken into account if offshore environmental conditions are to be investigated. These conditions are characterised by large loads on the structure and hence, strong non-linear fluid-structure interaction.

The existing numerical approaches cannot be regarded as appropriate for investigating OOA structures due to the lack of accurate load prediction in sea conditions or the neglect of the non-linear fluid-structure interaction during operation. In contrast, computational fluid dynamics (CFD) offers a two-way coupled numerical approach that can be applied to understand the environmental loads and structural response by modelling

the hydrodynamic forces affecting the dynamics of the floating structure, the flexible net and mooring system, and their effect on the surrounding fluid. To the best of the authors' knowledge, the only numerical approach so far was the two-dimensional model presented by Chen and Christensen [23]. They solved the incompressible Navier-Stokes equations in a two-dimensional numerical wave tank and coupled it to a lumped mass net model using a porous medium approach. They validated their model against experiments for a net attached to a moored-floating cylinder in waves and current and showed promising results. However, the approach was not tested for three-dimensional structures such as OOA structures. This results in the lack of an appropriate high-fidelity model to study the relevant fluid dynamics regarding offshore fish cage structures.

(a) Traditional floating flexible cage (reproduced from [27]).

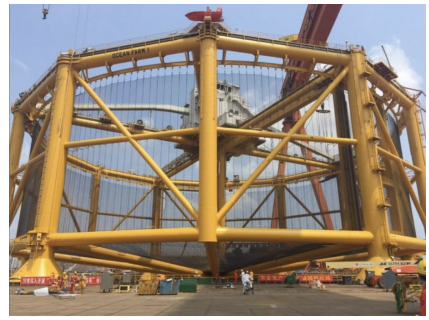

(b) Semi-submersible rigid cage (reproduced from [27]).

(c) Mobile floating cage (reproduced from [118]).

Figure 1.1: Classification of aquaculture cages for open ocean conditions.

1.2 Objectives, scope and limitations

The main objective of this thesis is the development of a complete numerical model for simulating open ocean aquaculture systems in strong current and waves. The expected environmental conditions, as well as the development of new designs concentrating on rigid structures with attached nets, necessitates the usage of advanced tools such as computational fluid dynamics (CFD) solvers. Thus, the incompressible Navier-Stokes equations are solved to account for viscous fluids, and the interaction of the fluid with a free surface and structures is modelled in a two-way coupled manner. This enables the investigation of both, the structural response of the cages and the flow field in and around the cages. As the basis of this development, the open-source CFD solver REEF3D [11] is chosen as it has proven its capability of simulating complex wave hydrodynamic problems including breaking waves [12].

In order to achieve the primary goal of the PhD project, suitable numerical models for all components of the system are developed. As illustrated in Fig. 1.2, the system includes a rigid floating structure, a mooring system as well as nets as an elastic porous enclosure holding the fish. This yields the following secondary objectives coping with the development of the necessary numerical models:

- Development of a rigid-body FSI solver for the rigid floating structure based on the fluid dynamics solver REEF3D. This requires the implementation of a rigid body dynamics model as well as a coupling algorithm to fulfil the boundary conditions at the interface between fluid and rigid structure. (**Paper 4**)

- Development of a numerical mooring model: The model shall combine flexibility with efficiency in order to cope with the demands of OOA systems as well as not constraining the complete solver unnecessarily. Hydrodynamic transparency is assumed because typical mooring systems consist of rather thin lines. The hydrodynamic effects on the lines shall however be respected by the model. (**Paper 1**)

- Development of a structural dynamics solver for the net: A non-linear dynamics solver accounting for large motions and non-linear material laws shall be implemented for the distinct characteristics of net structures. External forces due to gravity, inertia and drag have to be included in the model to account for the loads of the modelled sea states. (**Paper 3**)

- Development of a coupling methodology to account for the interaction of elastic porous structures and fluid: A new approach is required to account for the interaction of fluid and net structure in large deformed configurations. (**Paper 2**)

Finally, the complete solver is applied to open ocean aquaculture structures in waves and current to provide a proof of concept (**Paper 4 & 5**).

This research presents the development of a novel numerical model concentrating on open ocean aquaculture designs of today and the future. Therefore, traditional flexible fish cages, as well as closed flexible fish bags, are not in the scope of this thesis. It is however noticed that the presented approaches could be applied to these concepts as well. Further, an extensive study of the water circulation inside the cages including various types of structural designs and environmental configurations is left for future research.

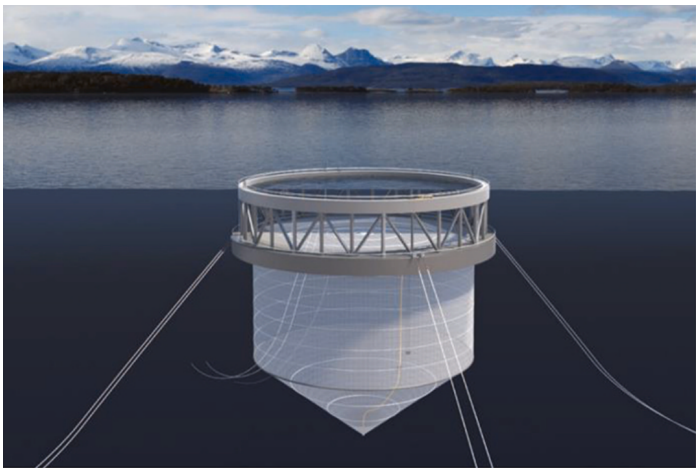

Figure 1.2: Illustration of the components of a typical open ocean aquaculture cage (reproduced from [118]).

1.3 Structure of the thesis

This thesis is submitted as a collection of four international journal articles and one conference article. The thesis begins with a brief overview of the current state of the art of the different aspects involved in the developments presented in this thesis (chapter 2). The complete numerical framework evolving from the work performed during this PhD is outlined in chapter 3. Afterwards, the major results of the articles are presented in chapter 4. Finally, chapter 5 presents the conclusions and an outlook for future work. The journal and conference articles are appended in chapter A.

Chapter 2

Current state of the art

2.1 Numerical wave tanks based on CFD

In the field of CFD, the interaction of floating structures and complicated free surfaces, including irregular and breaking waves, is modelled by solving the three-dimensional incompressible Navier-Stokes equations together with suitable approaches to generate, propagate and absorb waves.

Interface tracking methods, which are based on a Lagrangian tracking of the complete fluid [96] or markers identifying the free surface [56, 107], are highly accurate due to the transport of a permanent sharp surface and the geometrical calculation of the interface curvature from the mesh. On the contrary, the interface is sensitive to the spacing between the particles which necessitates dynamic re-meshing and affects the conservation of the liquid volume. Further, topological modifications as merging or breakage of interfaces have to be handled by sub-grid models which complicate their usage in numerical wave tanks.

Therefore, interface capturing or implicit methods are the most common way of interface handling for this type of application. They avoid the requirement of a Lagrangian grid by describing surfaces as a scalar field advected on the same Eulerian grid as the flow properties. Topological changes are handled automatically and undesired deformation and reparation of surface elements can be circumvented. Here, the interface is defined as an immersed boundary and taken as the locus of capillary forces and material discontinuities expressed as jump conditions. The treatment of the appearing singularities is provided by additional modifications using the continuum surface force method of Brackbill et al. [15] or the ghost fluid method [36].

The volume of fluid (VOF) method of Hirt and Nichols [58] captures the interface motion by transporting a scalar field, which presents the volume fraction of one phase, using an advection equation. The scalar function has a jump from zero to one at the interface for which reason the solution of the equation is prone to numerical instabilities

and smearing. The sharpness of the profile has to be ensured by applying geometrical reconstructions or artificial compression techniques. Also, a large number of cells per wave height is commonly necessary to capture the free surface propagation sufficiently because the location of the free surface is only approximated from the scalar function. Common geometrical reconstructions are based on the piecewise linear interface calculation (PLIC) [98] which reconstructs the interface in each cut cell by a plane so that the surface is represented by a sequence of polygons with small discontinuities in between. In [65], this approach was successfully implemented in a numerical wave tank. Compressive VOF methods were developed to improve the reconnection of the surface and reduce the computational costs by avoiding the explicit reconstruction procedure. The sharpness of the interface is ensured through high-resolution convection schemes with flux corrections or artificial compression terms. Both types were used in the past to implement a numerical wave tank, amongst others the CFD code ReFRESCO [110] and the OpenFOAM toolboxes of Jacobsen et al. [60] and Higuera et al. [57].

In contrast to VOF methods, Osher and Sethian [85] proposed an implicit method based on a signed distance function for indicating the free surface. This function has a smooth distribution and is zero at the interface. Fewer cells are necessary due to the exact information about the location of the free surface from the distance information at each grid point. The function is propagated in space and time using the local fluid velocities and the linear advection equation. The discretisation of the convection term attracts special attention due to the hyperbolic nature of the equation. The application of stable but low-order convection schemes introduces too much numerical dissipation resulting in smeared solutions. Therefore, high-order schemes are proposed to preserve the sharpness of the interface. Even low-dissipative schemes cannot guarantee the conservation of the signed distance function for which reason redistancing strategies were introduced. Here, the PDE based algorithm of Sussman et al. [104] was mostly applied. Amongst others, the open-source CFD code REEF3D [11] utilised this method in combination with a fifth-order accuracy weighted essentially non-oscillatory (WENO) scheme [62] for the implementation of a numerical wave tank. The code was successfully applied in the field of coastal and ocean engineering including breaking waves [4] and wave forces [12, 63] on fixed structures.

2.2 Modelling the interaction of rigid floating structures and fluid

Various approaches for modelling the interaction of the fluid and a rigid floating structure were proposed in the past. They rely either on an explicit or implicit representation of the structure in the fluid domain. Explicit methods are also known as body-fitted grids. First explicit approaches were based on Arbitrary Lagrangian-Eulerian (ALE)

methods [94]. Here, a single Eulerian grid is fitted around the rigid structure. The grid then dynamically adapts to the motion of the structure by distorting and merging the grid lines in the vicinity of the body. This approach raises the theoretical possibility of applying refined layers of cells around the structure to resolve the boundary layer flow. However, this is prone to a loss of numerical accuracy and stability due to suboptimal re-meshing and requires relatively large computational resources [120]. The potential for irregular grids can be prevented by relying either on completely Lagrangian descriptions of fluid and structures such as mesh-free SPH (Smoothed Particle Hydrodynamics) models [31] or dynamic overset grids [14, 20, 24]. In overset grid methods, usually two different Eulerian grids are considered. One grid remains fixed during the simulation, whereas another grid is fitted to the floating body. The position of the body-fitted grid adapts to the motion of the structure and hence, remains undisturbed. An interpolation mechanism is necessary for transferring the data between the overlapping grid points. A complete solution for the fluid properties can be found on the background grid by including the interpolations into the system matrix as shown by Hanaoka [55]. The size of the overlapping region is related to the stencil size of the discretisation which affects the efficiency for high-order numerical methods in three dimensions. In particular, moving boundary problems amplify this increase of computational costs [114].

Implicit methods were developed in order to overcome the computational challenges of explicit methods and are well suited for simulations including complex, three-dimensional structures and moving bodies. Most implicit approaches today are based on the immersed boundary method (IBM) originally developed for simulating elastic membranes in fluids [90, 91]. Here, a single Eulerian grid is applied, and the boundary conditions at the fluid-structure interface are respected implicitly by the equations solved on this grid. In ghost-cell immersed boundary methods, the numerical stencils around the structure is modified and ghost-cells are defined inside the solid domain to account for the presence of the interface. Berthelsen and Faltinsen [6] developed this procedure for fixed bodies using stencils in the principal directions of the domain. Thus, the modifications reduce to evaluations of Lagrangian polynomials near the body. Bihs and Kamath [10] extended this approach for floating and falling bodies using first-order interpolations of the velocity. In contrast, Calderer et al. [18] utilised the normal directions of the interface to modify the pressure stencils. The challenges in these methods are the accurate calculation of the forces on the structure because no explicit location for the evaluation exists, and oscillations in the pressure solution because the continuity equation is not satisfied locally when the interface passes a cell boundary [114]. As an alternative group of approaches, the direct forcing methods originally presented by Fadlun et al. [32] were proposed. Here, an additional source term is incorporated into the momentum equation of the fluid to account for the boundary conditions at the fluid-structure interface. This term is calculated on the grid points of the fluid domain using a reconstructed solution from the fluid domain and the known velocity at the nearby solid

surface. Uhlmann [109] showed that this procedure can lead to force spikes because the reconstruction stencil changes steadily. Recently, Yang and Stern [119] presented a hybrid method of this approach and an overset grid so that the reconstruction stencils remain constant in time. Promising results could be shown in two-dimensional benchmark cases but the aforementioned challenges of overset grids remain unsolved. Alternatively, a continuous version of the direct forcing method can be utilised. Uhlmann [109] proposed to calculate the forcing term on Lagrangian markers directly located on the surface of the structure. The terms are then distributed on the Eulerian domain using the interpolation procedure of the original immersed boundary method. The introduced smearing effectively removes force spikes but still keeps the nominal order of accuracy for the coupling problem. Additional computational costs arise from the back- and forth-transformations between the Eulerian grid and the Lagrangian markers. These costs can be avoided by using a completely Eulerian calculation as derived by Yang [121]. Here, the Eulerian grid is split into a fluid and solid domain. The momentum equation is solved in the whole domain including a forcing term to account for the boundary conditions. This additional term is calculated from the rigid body velocities at each grid point and smeared over the fluid-solid interface using a smoothed Heaviside step function. The function is determined using spline interpolations over Lagrangian markers which move with the rigid body velocity. The author validated the model against two-dimensional benchmark cases and showed high stability and accuracy. However, it can be assumed that the extension to three-dimensional structures compromises the efficiency due to the large number of marker points and increases the complexity due to the difficulty of spline interpolations in three dimensions. In this thesis, this continuous direct forcing approach is modified to enable its applicability for OOA structures.

2.3 Modelling the dynamics of mooring lines

Most mooring models rely on numerical methods [29] due to the non-linear second-order partial differential equations (PDE) describing the motion of these lines in space and time. These equations were solved using finite difference methods [2, 49, 59, 81] and finite element methods [1, 16, 47]. Palm et al. [87] improved the solution using a discontinuous Galerkin finite element method to account for the hyperbolic nature of the PDEs. This method is stable, of arbitrary order of accuracy and capable of simulating any type of loads including snap loads. The main disadvantage of fully dynamic mooring models is the necessity of stable initial conditions and the restriction of the time step imposed by the material stiffness. Thus, the time step due to the mooring dynamics can be several magnitudes smaller than the time step due to the CFL condition of the fluid solver. This either restricts the efficiency of the whole simulation or raises the need for interpolation in time [86]. Analogous methods based on truss elements [54,

112, 115] were proposed to remove the dependency on the initial condition, but the time step restriction remained. Here, force equilibria are solved at each point between the elements instead of the governing equations. Mooring modelling was further simplified by deriving an analytical solution under the assumption of negligible time dependence. Amongst others, Faltinsen [33] presented a catenary solution for elastic ropes. Generally, analytical solutions are restricted in their form and not suitable for tense or arbitrary shaped systems.

2.4 Modelling the dynamics of nets

The nets utilised in aquaculture span a large area and consist of a large number of twines with non-linear material properties [70]. Further, large motions and deformations are expected for these structures in offshore conditions. The directions of the deformation are related to the directions of the twines which distinguishes nets from e.g. continuous membranes and fabric structures [106]. This complicates the derivation of the constitutive laws for nets and prevents the derivation of a classical finite element approach based on a variational formulation [92, 106]. Tronstad [106] overcame this issue by deriving the stiffness matrix for a four-node membrane element based on connecting multiple non-linear truss elements. He successfully performed steady-state simulations including hydrodynamic loads from current. Similarly, Priour [93] developed a triangular element for static equilibria assuming a constant tension distribution in each element. Later, he extended the elements for quasi-static calculations by including hydrodynamic loads from current [92]. Tsukrov et al. [108] utilised a one-dimensional truss element with three degrees of freedom and a Lagrangian approach to model the non-linear dynamics of nets. Here, each truss accounts for a portion of the area of the physical net.

As an alternative, Lader and Fredheim [70] introduced the lumped mass method which represents the discrete structure as massless bars connected by mass knots. The solution of the dynamics of the knots was found in terms of their acceleration from Newton's second law. Runge-Kutta time integration was applied to calculate the knot velocities and positions from the accelerations. A minor modified version of the original approach was successfully applied to simulate net walls [9] and cylinders [7] in steady flow conditions. The constitutive equations, relating the forces to the deformations, are not automatically satisfied after each time step. This can lead to stability issues unless very small time steps are used. The time step restriction is also necessary due to the explicit time integration. In [80], an implicit quasi-static net model was proposed where the force equilibrium is solved for each knot with additional constraints on the connectivity of the bars. The missing time-stepping reduces the cost and simplifies the coupling to the fluid solver. However, the lack of dynamic effects prevents the application to large deformation problems including snap loads. A dynamic implicit method was proposed by LeBris and Marichal [72]. They derived a system for solving the dynamics of the

net under consideration of the kinematic relation between knot position and bar length. Here, inelastic material was assumed. This leads to unacceptable high condition numbers due to zero entries on the main diagonal of the system matrix. Marichal [76] and Vincent [111] included elastic material properties in the model to overcome this issue. However, their derivation relied on linear material assumptions, and linearisation was utilised in the derivation. In this thesis, these drawbacks are omitted by including a non-linear material law and avoiding linearisations.

2.5 Modelling the fluid-structure interaction for nets

In contrast to conventional membranes, nets have a high porosity and consist of multiple individual twines which are passed by the fluid. The length scale of the flow around each twine is significantly smaller than the length scale of the flow around the whole floating structure. This prevents the resolution of the net on the same numerical grid as the fluid domain, and an alternative representation of the FSI between net and fluid has to be introduced. One possible representation is the definition of a porous medium around the net. The fluid momentum equation is solved in the whole domain including an additional resistance coefficient in the porous zone. This approach is based on the work of Patursson et al. [89]. They incorporated a stiff net sheet as a porous medium in the fluid domain. The governing volume- and Reynolds-averaged Navier-Stokes equations are solved using a finite volume method. The research was mostly focused on the correct determination of the porous resistance coefficients, which were approximated from available experimental data. Bi et al. [9] and Zhao et al. [124] followed the same approach but used a theoretical force model for determining the coefficients. Chen and Christensen [21, 22] extended the general idea for complete net cages and included a more comprehensive determination of these coefficients. They provided an extensive validation of their approach for stiff net walls and cages in both current and waves. A Morison type force model which neglects important dependencies on the angle of attack in their derivations was utilised.

In contrast, Yao et al. [122] presented a hybrid finite volume method to incorporate the fluid-structure coupling into their CFD solver. The resistance forces of the net were distributed by assigning them to cells containing portions of the numerical net. The net was represented by a lumped mass method consisting of knots and bars in between. The distribution process requires the calculation of the intersection of each bar with each cell of the fluid grid and is thus computationally expensive. This drawback is amplified for rectilinear grids and polyhedral cell shapes where intersections can only be found by comparison to each cell face. They also introduced the idea of choosing the unknown force coefficients by fitting them with experimental data. Details about the fitting process and fitting results for the drag coefficients were not presented.

Chapter 3

Proposed numerical framework

In the following, an overview of the complete numerical framework developed within the PhD project is presented. The model arises from the proposed methods and findings of the attached journal articles. It consists of a two-phase numerical wave tank which is mostly based on the CFD code REEF3D::CFD [11, 116] (section 3.1), a rigid-body FSI algorithm for modelling the interaction of rigid structures and fluid (section 3.2), a structural solution for mooring lines (section 3.3) and an implicit solver for the structural dynamics of nets (section 3.4). Details regarding the coupling of the net solver to the fluid solver and the rigid body solver are also given. The final section 3.5 provides an overview of the interconnection of the different modules.

3.1 Two-phase numerical wave tank

The dynamics of an incompressible, viscous fluid is described by the conservation of mass and momentum. These conservation laws are defined as the three-dimensional Navier-Stokes equations solved in the convective form and continuity equation:

$$\begin{aligned} \nabla \cdot \mathbf{u} &= 0, \\ \frac{\partial \mathbf{u}}{\partial t} + \mathbf{u} \cdot \nabla \mathbf{u} &= -\frac{1}{\rho} \nabla p + \nabla \cdot \left(\nu \left[\nabla \mathbf{u} + \nabla \mathbf{u}^T \right] \right) + \mathbf{g}. \end{aligned} \tag{3.1}$$

Here, $\mathbf{u}$ is the velocity vector, ρ is the density, p represents the pressure contribution, ν is the sum of the kinematic and turbulent viscosity and $\mathbf{g}$ is the gravitational acceleration vector. The effect of turbulence is incorporated by adding turbulent viscosity to the diffusion term using the Boussinesq approximation and a modified k-ω turbulence model (see Bihs et al. [11] for details). Following a one-fluid approach, the two phases, air and water, are covered by a single set of equations but space and time dependent material distributions as proposed by Brackbill et al. [15]. The transition between the phases is

implicitly represented by the zero level set of the smooth signed distance function Φ [85]. The first-order hyperbolic equation

$$\frac{\partial \Phi}{\partial t} + \mathbf{u} \cdot \nabla \Phi = 0, \tag{3.2}$$

is solved to propagate Φ in space and time. After each time step, the reinitialisation equation of Sussman et al. [104] is solved in pseudo-time to keep the signed distance properties of Φ. The density and viscosity is then calculated using

$$\begin{aligned} \rho(\Phi) &= \rho_w H(\Phi) + \rho_a (1 - H(\Phi)), \\ \nu(\Phi) &= \nu_w H(\Phi) + \nu_a (1 - H(\Phi)), \end{aligned} \tag{3.3}$$

with w indicating water, a indicating air and H the smoothed Heaviside step function defined as

$$H(\Phi) = \begin{cases} 0 & \text{if } \Phi < -\varepsilon, \\ \frac{1}{2}\left(1 + \frac{\Phi}{\varepsilon} + \frac{1}{\pi} sin(\frac{\pi \Phi}{\varepsilon})\right) & \text{if } |\Phi| \leq \varepsilon, \\ 1 & \text{if } \Phi > \varepsilon. \end{cases} \tag{3.4}$$

Here, ε is defined as $2.1\Delta x$ with Δx the characteristic length between the grid points in the vicinity of each evaluation point [11].

The set of equations (3.1) - (3.2) is solved on a staggered rectilinear grid using finite differences. Fifth-order accurate weighted essentially non-oscillatory (WENO) schemes [61, 62] adapted to non-uniform point distances are applied for convection terms, and diffusion terms are discretised with second-order accurate central differences. Convection and source terms are temporally treated explicitly with the third-order accurate TVD Runge-Kutta scheme of Shu and Osher [102], and an implicit Euler method is applied for the temporal discretisation of the viscous term. This effectively removes a quadratic reciprocal dependency on the grid point distance from the CFL condition [11]. An incremental pressure-correction algorithm [105] is added to the code for the purpose of incorporating fluid-structure interactions explicitly and used for solving system (3.1). Here, a velocity field is predicted from the momentum equation using the pressure gradients of the previous step in each k-th Runge-Kutta sub-step:

$$\begin{aligned} \frac{\mathbf{u}^{(*)} - \beta_k \mathbf{u}^{(n)}}{\alpha_k \Delta t} = \frac{1}{\Delta t}\mathbf{u}^{(k-1)} - \mathbf{u}^{(k-1)} \cdot \nabla \mathbf{u}^{(k-1)} - \frac{\nabla p^{(k-1)}}{\rho} \\ + \frac{1}{\alpha_k} \nabla \cdot \left(\nu \left[\nabla \mathbf{u} + \nabla \mathbf{u}^T\right]\right)^{(*)} + \mathbf{g}, \end{aligned} \tag{3.5}$$

with $\alpha_k = 1.0, 1/4, 2/3$, $\beta_k = 0.0, 3/4, 1/3$ and $k = 1, 2, 3$. Afterwards, the Poisson equation

$$\nabla \cdot \left(\frac{1}{\rho} \nabla p_{\text{corr}}\right) = \frac{1}{\alpha_k \Delta t} \nabla \cdot \mathbf{u}^{(*)}, \tag{3.6}$$

is solved for the pressure correction term p_{corr} utilising a fully parallelized BiCGStab algorithm with geometric multigrid preconditioning from the HYPRE library [113]. An n-halo decomposition strategy and the message passing interface (MPI) handles inter-processor communication. The pressure and divergence free velocity fields are finally calculated from

$$p^{(k)} = p^{(k-1)} + p_{\text{corr}} - \rho\nu\,\nabla\cdot u^{(*)}, \tag{3.7}$$

$$\mathbf{u}^{(k)} = \mathbf{u}^{(*)} - \frac{\alpha_k \Delta t}{\rho}\nabla p^{(k)}. \tag{3.8}$$

The boundary conditions are enforced using the ghost-point approach. At the inlet, waves are generated by applying the relaxation method to the x- and z-component of the velocities and the level set function Φ. For a general variable γ it is given as [82]

$$\gamma(\hat{x}) = \Gamma(\hat{x})\gamma_{\text{analytical}} + (1-\Gamma(\hat{x}))\,\gamma_{\text{computed}}, \tag{3.9}$$

with Γ the relaxation function [60]

$$\Gamma(\hat{x}) = 1 - \frac{\mathrm{e}^{(\hat{x}^{3.5})} - 1}{\mathrm{e} - 1}, \tag{3.10}$$

and $\hat{x} \in [0,1]$ the relative x-coordinate in the relaxation zone. The same method is applied to damp potential reflections near the outlet of the tank.

3.2 Rigid-body FSI solver

A continuous direct forcing immersed boundary method is implemented to account for the presence of rigid floating objects in the fluid solver. At first, the floating object is transferred to the solver as an STL geometry consisting of multiple non-connected triangles. This information is sufficient to create a signed distance field Φ_s representing the geometry in the Eulerian fluid domain by applying a ray casting algorithm [13] to receive inside-outside information near the body and the reinitialisation algorithm of Sussman et al. [104]. The generated level set function Φ_s is used for distinguishing between the fluid and solid domain by extending (3.3):

$$\begin{aligned}\rho(\Phi,\Phi_s) &= \rho_s H(\Phi_s) + (1-H(\Phi_s))\cdot(\rho_w H(\Phi) + \rho_a(1-H(\Phi))),\\ \nu(\Phi,\Phi_s) &= (1-H(\Phi_s))\cdot(\nu_w H(\Phi) + \nu_a(1-H(\Phi))).\end{aligned} \tag{3.11}$$

The continuity of the forcing field can be ensured under consideration of the conservation law

$$\begin{aligned}\nabla\cdot\mathbf{u} &= 0,\\ \frac{\partial\mathbf{u}}{\partial t} + \mathbf{u}\cdot\nabla\mathbf{u} &= -\frac{1}{\rho}\nabla p + \mathbf{g} + \mathbf{f},\end{aligned} \tag{3.12}$$

with the forcing term

$$\mathbf{f} = \frac{\partial \mathbf{P}(\mathbf{u})}{\partial t} + \mathbf{P}(\mathbf{u}) \cdot \nabla \mathbf{P}(\mathbf{u}) + \frac{1}{\rho} \nabla p - \mathbf{g}, \tag{3.13}$$

which holds in the solid domain as proven in [121]. Here, $\mathbf{P}(\mathbf{u})$ represents the operator for projecting the velocity field into a divergence-free rigid body velocity field. Comparing (3.12) with (3.1) reveals that the only difference between these two systems is the term $\mathbf{f}$ and the diffusion term, respectively. Therefore, a single set of equations can be solved in the whole domain using (3.11) to distinguish the material properties in the three phases and the additional term $\mathbf{f}$ to account for the correct boundary conditions at the interface.

At a discrete level, $\mathbf{f}$ reads at the new time step $n+1$

$$\mathbf{f}^{(n+1)} = H(\Phi_s^{(n+1)}) \cdot \left(\frac{\mathbf{P}(\mathbf{u}^{(\mathbf{n+1})}) - \mathbf{P}(\mathbf{u}^{(\mathbf{n})})}{\Delta t} + \mathbf{P}(\mathbf{u}^{(\mathbf{n})}) \cdot \nabla \mathbf{P}(\mathbf{u}^{(\mathbf{n})}) + \frac{1}{\rho} \nabla p^{(n+1)} - \mathbf{g} \right). \tag{3.14}$$

The velocity at the new time step is unknown a priori. To overcome this issue and avoid expensive implicit calculations, the valid approximation $\mathbf{P}(\mathbf{u}^{(\mathbf{n})}) = \mathbf{u}^{(\mathbf{n})}$ is made and the pressure is taken from the previous time step as a good approximation. Then,

$$\mathbf{f}^{(n+1)} = H(\Phi_s^{(n+1)}) \cdot \left(\frac{\mathbf{P}(\mathbf{u}^{(\mathbf{n+1})}) - \mathbf{u}^{(\mathbf{n})}}{\Delta t} + \mathbf{u}^{(\mathbf{n})} \cdot \nabla \mathbf{u}^{(\mathbf{n})} + \frac{1}{\rho} \nabla p^{(n)} - \mathbf{g} \right), \tag{3.15}$$

and by comparing with (3.5), it can be identified that

$$\mathbf{f}^{(n+1)} = H(\Phi_s^{(n+1)}) \cdot \left(\frac{\mathbf{P}(\mathbf{u}^{(\mathbf{n+1})}) - \mathbf{u}^{(*)}}{\Delta t} \right). \tag{3.16}$$

A good approximation of the updated velocity field is $\mathbf{u}^{(*)}$ itself. Therefore, the predictor step (3.5) is first executed without the forcing term. Then, $\mathbf{f}^{(*)}$ is calculated from

$$\mathbf{f}^{(*)} = H(\Phi_s^{(*)}) \cdot \left(\frac{\mathbf{P}(\mathbf{u}^{(*)}) - \mathbf{u}^{(*)}}{\alpha_k \Delta t} \right), \tag{3.17}$$

and added to the predicted velocity field before solving the Poisson equation (3.6).

For the calculation of the rigid body velocity field, the translational position of the rigid body $\mathbf{x_i}$ is described in the inertia system, and the rotational motion is described in a body-fixed coordinate system using the Euler parameter vector $\mathbf{e} = (e_0, e_1, e_2, e_3)^T$

with the property $\mathbf{e}^T\mathbf{e} = 1$. Their relation to the physically more relevant Tait-Bryan angles ϕ, θ, ψ is given as (c is *cos* and s is *sin*) [50]

$$\begin{aligned}
e_0 &= c\left(\frac{\phi}{2}\right)\cdot c\left(\frac{\theta}{2}\right)\cdot c\left(\frac{\psi}{2}\right) + s\left(\frac{\phi}{2}\right)\cdot s\left(\frac{\theta}{2}\right)\cdot s\left(\frac{\psi}{2}\right),\\
e_1 &= s\left(\frac{\phi}{2}\right)\cdot c\left(\frac{\theta}{2}\right)\cdot c\left(\frac{\psi}{2}\right) - c\left(\frac{\phi}{2}\right)\cdot s\left(\frac{\theta}{2}\right)\cdot s\left(\frac{\psi}{2}\right),\\
e_2 &= c\left(\frac{\phi}{2}\right)\cdot s\left(\frac{\theta}{2}\right)\cdot c\left(\frac{\psi}{2}\right) + s\left(\frac{\phi}{2}\right)\cdot s\left(\frac{\theta}{2}\right)\cdot s\left(\frac{\psi}{2}\right),\\
e_3 &= c\left(\frac{\phi}{2}\right)\cdot c\left(\frac{\theta}{2}\right)\cdot s\left(\frac{\psi}{2}\right) - s\left(\frac{\phi}{2}\right)\cdot s\left(\frac{\theta}{2}\right)\cdot c\left(\frac{\psi}{2}\right).
\end{aligned} \tag{3.18}$$

The back-transformations are defined as

$$\begin{aligned}
\psi &= \arctan 2\left(2\cdot(e_1\cdot e_2 + e_3\cdot e_0), 1 - 2\cdot(e_2\cdot e_2 + e_3\cdot e_3)\right),\\
\theta &= \arcsin(2\cdot(e_0\cdot e_2 - e_1\cdot e_3)),\\
\phi &= \arctan 2(2\cdot(e_2\cdot e_3 + e_1\cdot e_0), 1 - 2\cdot(e_1\cdot e_1 + e_2\cdot e_2)).
\end{aligned} \tag{3.19}$$

The transformation of a vector in the body-fixed coordinate system to a corresponding vector in the inertial system is described by the orthogonal rotation matrix

$$\mathbf{R} = 2\begin{pmatrix}
\frac{e_0^2+e_1^2-e_2^2-e_3^2}{2} & e_1e_2 - e_0e_3 & e_0e_2 + e_1e_3\\
e_0e_3 + e_1e_2 & \frac{e_0^2-e_1^2+e_2^2-e_3^2}{2} & e_2e_3 - e_0e_1\\
e_1e_3 - e_0e_2 & e_0e_1 + e_2e_3 & \frac{e_0^2-e_1^2-e_2^2+e_3^2}{2}
\end{pmatrix}. \tag{3.20}$$

The kinematic equations for the rotational motion of the body in terms of the Euler parameters are given as

$$\dot{\mathbf{e}} = \frac{1}{2}\mathbf{G}^T\boldsymbol{\omega}, \tag{3.21}$$

with $\boldsymbol{\omega}$ the components of the angular velocity vector in the body-fixed coordinate system and

$$\mathbf{G} = \begin{pmatrix}
-e_1 & e_0 & e_3 & -e_2\\
-e_2 & -e_3 & e_0 & e_1\\
-e_3 & e_2 & -e_1 & e_0
\end{pmatrix}. \tag{3.22}$$

Introducing the momentum vector $\mathbf{h} = \mathbf{I}\boldsymbol{\omega}$ with $\mathbf{I}$ the moment of inertia tensor, (3.21) can be rewritten as

$$\dot{\mathbf{e}} = \frac{1}{2}\mathbf{G}^T\mathbf{I}^{-1}\mathbf{h}. \tag{3.23}$$

Following the derivation of Shivarama and Fahrenthold [101], a first-order ODE is derived for $\dot{\mathbf{h}}$ using a system Hamiltonian. Here, the constraint for the Euler parameters is fulfilled automatically. By setting the potential energy function to zero and assuming imposed moments $\mathbf{M_b}$ in the body-fixed system, the equations read

$$\dot{\mathbf{h}} = -2\mathbf{G}\dot{\mathbf{G}}^T\mathbf{h} + \mathbf{M_b}. \tag{3.24}$$

The translational motion of the rigid body is described by Newtons second law and transformed to a system of first-order differential equations. In combination with the equations (3.21) and (3.24), a system of thirteen first-order ODEs arises which is integrated with the same explicit scheme as the fluid solver above.

The body forces and momenta are calculated on the triangulated surface of N triangles by integrating the fluid properties over the structure surface Ω and using a trilinear interpolation:

$$\begin{aligned}
\mathbf{F_i} &= \int_\Omega (-\mathbf{n}p + \rho\nu\mathbf{n}\tau)\, d\Omega(\mathbf{x}) = \sum_{i=1}^{N} (-\mathbf{n}p + \rho\nu\mathbf{n}\tau)_i \cdot \Delta\Omega_i, \\
\mathbf{M_i} &= \int_\Omega \mathbf{r} \times (-\mathbf{n}p + \rho\nu\mathbf{n}\tau)\, d\Omega(\mathbf{x}) = \sum_{i=1}^{N} \mathbf{r}_i \times (-\mathbf{n}p + \rho\nu\mathbf{n}\tau)_i \cdot \Delta\Omega_i.
\end{aligned} \tag{3.25}$$

Here, $\mathbf{n}$ is the surface normal vector, τ is the viscous stress tensor and $\mathbf{r}$ represents the distance vector to the centre of gravity. The moments are transferred to the body-fixed coordinate system using the transformation matrix (3.20). Once the body velocities are calculated, the projection is finally calculated as

$$\mathbf{P}(\mathbf{u}^{(*)}) = \dot{\mathbf{x}}_\mathbf{i} + \omega_\mathbf{i} \times \mathbf{r}, \tag{3.26}$$

with $\dot{\mathbf{x}}_\mathbf{i}$ the translational and $\omega_\mathbf{i}$ the rotational rigid body velocity vector in the inertial reference frame.

3.3 Mooring dynamics solver

The dynamics of a mooring line neglecting bending stiffness is described as [87]

$$\gamma \frac{\partial^2 \mathbf{r}}{\partial t^2} = \frac{\partial F_T \mathbf{f}}{\partial s} + \mathbf{F}_e, \tag{3.27}$$

with $\mathbf{r}$ the coordinates of the line in the inertial system, s the coordinate along the line, γ the specific weight of the material, F_T the magnitude of the tension force, $\mathbf{f}$ the unit vector pointing in the direction of this force and $\mathbf{F}_e$ the external forces including gravitation ($\mathbf{F_G}$) and hydrodynamic effects ($\mathbf{F_H}$). Assuming small line motion in time and

steady-state flow of the fluid, respectively, (3.27) simplifies to

$$\frac{\partial F_T \mathbf{f}}{\partial s} = -\mathbf{F}_e. \tag{3.28}$$

In order to solve this force equilibrium, each mooring line is split into N equally distanced bars of length l_t with knots P in between. As shown in Fig. 3.1, the first and last knot, $P^{(0)}$ and $P^{(N)}$, are attached to the bottom and the floating object. Linear elasticity is assumed within this thesis.

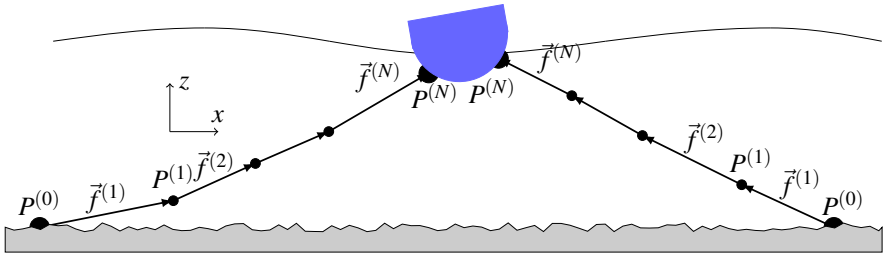

Figure 3.1: Discrete mooring lines: Inner knots (small black dots), Outer knots (big black dots), bars (black vectors).

The mass of the line is equally distributed on the adjacent knots which gives a gravity force contribution of

$$\mathbf{F_G}^{(j)} = \gamma \mathbf{g} \cdot \frac{\rho_m - \rho}{\rho_m} \cdot \frac{l_t^{(j)} + l_t^{(j+1)}}{2}, \quad j = 1, ..., N-1, \tag{3.29}$$

at any knot $P^{(j)}$. Here, ρ_m is the density of the mooring material and $\mathbf{g}$ is an unit vector pointing in negative z-direction. The hydrodynamic forces $\mathbf{F}_H$, arising from the slowly-varying relative motion between structure and surrounding fluid, are calculated as drag forces using Morison's formula [83] at each bar

$$\begin{aligned} \mathbf{F_H}^{(j)} = {} & l_t^{(j)} d_t^{(j)} \frac{\rho}{2} \cdot \\ & \left[c_t \left(\mathbf{u} \cdot \mathbf{f} \right) |\mathbf{u} \cdot \mathbf{f}| \cdot \mathbf{f} + c_n \left(\mathbf{u} - (\mathbf{u} \cdot \mathbf{f}) \mathbf{f} \right) |\mathbf{u} - (\mathbf{u} \cdot \mathbf{f}) \mathbf{f}| \right]^{(j)}, \\ & j = 1, ..., N, \end{aligned} \tag{3.30}$$

with c_n the drag coefficient in normal direction calculated as a function of the Reynolds number [26]

$$c_n(\mathrm{Re}) = \begin{cases} \dfrac{8\pi}{s\,\mathrm{Re}} \cdot \left(1.0 - 0.87\, s^{-2.0} \right) & \text{if } \mathrm{Re} < 1.0, \\ 1.45 + 8.55\, \mathrm{Re}^{-0.9} & \text{if } 1.0 \leq \mathrm{Re} < 30.0, \\ 1.1 + 4.0\, \mathrm{Re}^{-0.5} & \text{else}, \end{cases} \tag{3.31}$$

and c_t the drag coefficient in tangential direction. The hydrodynamic forces are assigned to knots by equally distributing their net amount.

Defining the tension forces acting at the knots in the direction of the adjacent bars, (3.28) is solved locally at each inner knot $P^{(j)}$ (see also Fig. 3.2):

$$\mathbf{f}^{(j+1)} F_T^{(j+1)} - \mathbf{f}^{(j)} F_T^{(j)} = -\left(\mathbf{F}_H^{(j)} + \mathbf{F}_G^{(j)}\right), \quad j = 1, ..., N-1. \tag{3.32}$$

A solution for the shape of the line and the distribution of tension forces is found by gathering (3.32) into a suitable linear system of equations. Both unknowns, $\mathbf{f}$ and F_T, are generally dependent on the direction of the bar unit vectors. However, $\mathbf{F}_H$ also depends on $\mathbf{f}$ according to (3.30). Therefore, an iterative method has to be chosen for solving the system. A successive approximation is utilised to ensure a converged solution. Further, Fig. 3.1 indicates that the discrete line consists of N bars but just $N-1$ inner knots. Therefore, (3.32) presents an undetermined system if solved for $\mathbf{f}$, and a geometrical constraint has to be introduced to close the system. This constraint is defined in such a way that it represents both, the physical boundary condition of the fixed end points $P^{(0)}$ and $P^{(N)}$ and the physical coherence of the line during the deformation (compare Fig. 3.3):

$$\sum_{j=1}^{N} \mathbf{f}^{(j)} l_t^{(j)} = \mathbf{x}\left(P^{(N)}\right) - \mathbf{x}\left(P^{(0)}\right). \tag{3.33}$$

Hence, the vector of the sum of all bar vectors has to be equal to the distance vector between the two end points $\mathbf{x}(P^{(0)})$ and $\mathbf{x}(P^{(N)})$. This is a conditional equation for a physical coherent solution of the problem.

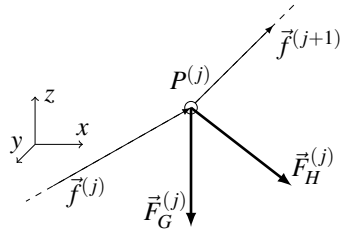

Figure 3.2: Force equilibrium at inner knot P^{ν}: Inner knot (white filled circle), bars (thin vectors), forces (thick vectors).

The resulting linear system of equations can be merged into a closed system of equations $\mathbf{A} \times \mathbf{F} = \mathbf{B}$ with the $(N \times 3)$ matrix $\mathbf{F}$ containing the unit bar vectors. For the first time step, less restrictive directions for the unit vectors and initial tension forces are set to fill the left- and right-hand sides. Thus, this model is independent of a predefined initial form of the cable and highly suitable for applications without this requirement.

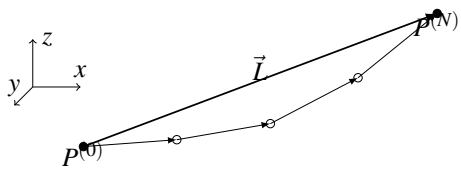

Figure 3.3: Geometrical constraint: Inner knots (white filled circles), Outer knots (black filled circles), bars (thin vectors), constraint vector (thick vector).

Based on the given values, the initial lengths and gravity forces of the bars are determined. The hydrodynamic forces are initialised using (3.30). The solution of the system is then found at any iterative step k using Gaussian elimination with pivoting. According to the definition, the lengths of the bar unit vectors equal unity. This condition is generally violated after each iteration for which reason the correction step

$$\left(\mathbf{f}^{(j)}\right)^{(k*)} = \frac{\left(\mathbf{f}^{(j)}\right)^{(k)}}{\left|\left(\mathbf{f}^{(j)}\right)^{(k)}\right|}, \quad j = 1,...,N, \tag{3.34}$$

has to be applied. Consistency is ensured by multiplying the columns of $\mathbf{A}$ by the Euclidean norm of the corresponding line of $\mathbf{F}^{(k)}$. As the next iteration starts, $\mathbf{F}^{(k*)}$ is utilised to fill the system. Convergence is formally proven in [52, 53] and typically reached within 100 iterations in the first time step and less than 50 afterwards. The algorithm stops after reaching the residual criterion

$$\max_j \left| \left|\left| \left(\vec{f}^{(j)}\right)^{(k)} \right|\right|_2 - 1 \right| < \text{tol}, \quad j = 1,...,N, \tag{3.35}$$

which corresponds to the conservation of all bar unit vectors within a tolerance typically chosen as 10^{-4}.

3.4 Net dynamics solver

The net is considered as a tensile structure consisting of a large number of square meshes forming a porous cylinder or sheet with two distinct stress directions. Therefore, it is discretised in a finite number of mass points (knots) connected by non-linear elastic bars pointing in the principal directions of the meshes. The initialisation process of Martin et al. [80] is applied to achieve this layout of the net. Also, a structural element is defined as the combination of four knots and their four connecting bars, and covers multiple physical meshes of the net (see Fig. 3.4). The specific number of meshes depends on

the solidity Sn of the net which is defined as

$$\mathrm{Sn} = \frac{2d_t}{l_t} - \left(\frac{d_t}{l_t}\right)^2, \tag{3.36}$$

for the considered nets (see [118] for alternative formulations). Here, d_t is the diameter and l_t is the length of each physical twine.

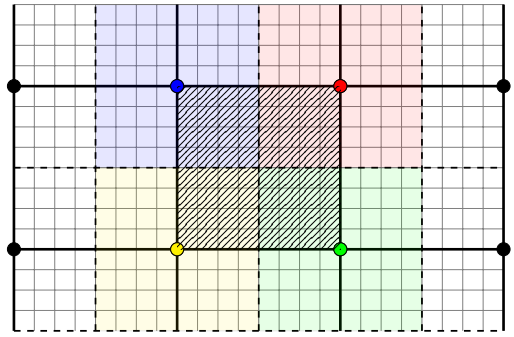

Figure 3.4: Illustration of the definitions for the net model: structural elements consist of four knots (thick dots) connected with bars (thick black lines). Each element (hatched area) covers multiple physical meshes (thin grey lines). The contribution of the structural elements to each knot is shown in matching colours.

A system of equations is sought for the dynamics of the knots. For this purpose, the equilibrium according to Newton's second law (see Fig. 3.4)

$$\mathbf{m}_i\, \ddot{\mathbf{x}}_i = \sum_{k=1}^{N_i} \mathbf{T}_{ik} + \mathbf{F}_{ex,i}, \tag{3.37}$$

is solved at each knot $\mathbf{x}_i$ and its N_i neighbouring knots. Here, dots indicate temporal derivatives, $\mathbf{F}_{ex}$ are external forces and $\mathbf{T}_{ij}$ represents the tension force vector of each bar:

$$\mathbf{T}_{ij} = T_{ij}\, \mathbf{b}_{ij} = T_{ij} \cdot \left(\frac{\mathbf{x}_j - \mathbf{x}_i}{|\mathbf{x}_j - \mathbf{x}_i|}\right), \tag{3.38}$$

with T_{ij} the tension force magnitude and $\mathbf{b}_{ij}$ the unit vector of the bar.
Following the assumptions of Morison et al. [83] for hydrodynamic transparent structures, the mass contributions of the surrounding $N_{S,i}$ structural elements is lumped at knot $\mathbf{x}_i$. Hence, the mass matrix $\mathbf{m}_i$ is approximated as

$$\mathbf{m}_i = \sum_{s=1}^{N_{S,i}} \begin{pmatrix} m_{\mathrm{air}} + m_{\mathrm{a}} n_x & 0 & 0 \\ 0 & m_{\mathrm{air}} + m_{\mathrm{a}} n_y & 0 \\ 0 & 0 & m_{\mathrm{air}} + m_{\mathrm{a}} n_z \end{pmatrix}_s, \tag{3.39}$$

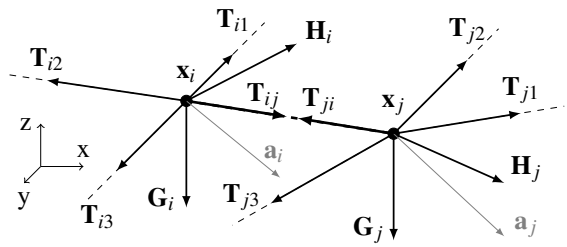

Figure 3.5: Illustration of the dynamic force equilibrium at the knots $\mathbf{x}_i$ and $\mathbf{x}_j$ showing only structural quantities.

with $m_{\text{air},s}$ the mass of the partial element in air and $\mathbf{n}_s$ the unit normal vector of the element pointing in relative velocity direction. The added mass $m_{a,s}$ is approximated as the mass of the water volume occupied by the screen under the assumption that the net is a mesh of multiple cylinders only. Here, the added mass is only applied in the normal direction of the structure. Similarly, the external forces from each structural element are assigned to the attached knots. An approximation of the forces has to be introduced because the net is not explicitly resolved in the computational domain of the fluid solver (see also section 3.5). The external force vector consists of static gravity and buoyancy forces as well as hydrodynamic forces. The latter consist of inertia forces $\mathbf{I}$ due to the fluid acceleration $\mathbf{a}_f$,

$$\mathbf{I}_i = \sum_{s=1}^{N_{S,i}} \begin{pmatrix} m_\text{a} + m_\text{a} n_x & 0 & 0 \\ 0 & m_\text{a} + m_\text{a} n_y & 0 \\ 0 & 0 & m_\text{a} + m_\text{a} n_z \end{pmatrix}_s \cdot \mathbf{a}_{f,s}, \tag{3.40}$$

and velocity related drag and lift forces $\mathbf{D}$ whose calculations are described in section 3.4.1.

An implicit solution for the structural dynamics problem is found at each new time step $(n+1)$ using the kinematic compatibility equation

$$\left(\mathbf{x_j}^{(n+1)} - \mathbf{x_i}^{(n+1)}\right)^2 = \left(l_{ij}^{(n+1)}\right)^2, \tag{3.41}$$

which relates the unknown position of the knots to the unknown tension forces. Assuming non-linear material, a constitutive equation is formulated as

$$T_{ij} = C_1 \varepsilon + C_2 \varepsilon^2 = C_1 \left(\frac{l_{ij}}{l_{0,ij}} - 1\right) + C_2 \left(\frac{l_{ij}}{l_{0,ij}} - 1\right)^2, \tag{3.42}$$

with l_{ij} the current length of the bar and $l_{0,ij}$ its unstretched length. Lader and Fredheim [70] found this relation to be valid with $C_1 = 1160\ N$ and $C_2 = 37300\ N$ for nylon

nets with squared meshes, which is used in the validation section below. Eq. (3.42) is reformulated for l_{ij} by eliminating the non-physical solution:

$$l_{ij} = \frac{l_0}{2C_2} \cdot \left(-C_1 + 2\,C_2 + \sqrt{C_1^2 + 4\,C_2\,T_{ij}} \right). \tag{3.43}$$

Further, the left-hand side of (3.41) is replaced by the dynamic equilibrium (3.37). This can be achieved by replacing the position vectors $\mathbf{x}^{(n+1)}$ with accelerations using high-order backward finite differences in time. The weight of each point included in the approximation is found iteratively using the algorithm of Fornberg [39] because of variable time steps in the coupled simulations. Thus, the velocity of the knot is expressed as

$$\frac{d\mathbf{x}^{(n+1)}}{dt} = \dot{\mathbf{x}}^{(n+1)} = \sum_{p=0}^{P} c_p \mathbf{x}^{(n+1-p)}, \tag{3.44}$$

with c_p the weights of the P points of the interpolation. The unknown velocity vectors $\mathbf{v}^{(n+1)}$ are approximated by repeating the derivation:

$$\frac{d^2\mathbf{x}^{(n+1)}}{dt^2} = \ddot{\mathbf{x}}^{(n+1)} = \sum_{p=0}^{P} c_p \dot{\mathbf{x}}^{(n+1-p)}. \tag{3.45}$$

Inserting (3.45) in (3.44) and then in (3.41), a non-linear function f is found for each bar b_{ij} after rearranging the expression:

$$\begin{aligned} f_{ij}\left(\mathcal{T}^{(n+1)}\right) = &\left(\sum_{k=1}^{N_j} \mathbf{m}_j^{-1} \mathbf{T}_{jk}^{(n+1)} - \sum_{k=1}^{N_i} \mathbf{m}_i^{-1} \mathbf{T}_{ik}^{(n+1)} + \mathbf{m}_j^{-1} \mathbf{F}_{ex,j}^{(n)} - \mathbf{m}_i^{-1} \mathbf{F}_{ex,i}^{(n)} + \dot{\mathbf{X}}_{ij} + \mathbf{X}_{ij} \right)^2 \\ &- \frac{c_0^4\, l_0^2}{4\, C_2^2} \cdot \left(-C_1 + 2C_2 + \sqrt{C_1^2 + 4C_2 T_{ij}^{(n+1)}} \right)^2 = 0, \end{aligned} \tag{3.46}$$

with $\mathcal{T}$ the unknown global vector of tension force magnitudes and the definitions

$$\mathbf{X}_{ij} = -c_0 \sum_{p=1}^{P} c_p \left(\mathbf{x}_j^{(n+1-p)} - \mathbf{x}_i^{(n+1-p)} \right), \tag{3.47}$$

$$\dot{\mathbf{X}}_{ij} = -\sum_{p=1}^{P} c_p \left(\dot{\mathbf{x}}_j^{(n+1-p)} - \dot{\mathbf{x}}_i^{(n+1-p)} \right). \tag{3.48}$$

A system of equations is formulated from (3.46) and solved using the improved Newton's method [28]

$$\begin{aligned} \mathcal{T}^{(*)} &= \mathcal{T}^{(n)} - \left[\mathcal{J}\left(\mathcal{T}^{(n)}\right) \right]^{-1} \mathcal{F}\left(\mathcal{T}^{(n)}\right), \\ \mathcal{T}^{(n+1)} &= \mathcal{T}^{(*)} - \left[\mathcal{J}\left(\mathcal{T}^{(n)}\right) \right]^{-1} \mathcal{F}\left(\mathcal{T}^{(*)}\right), \end{aligned} \tag{3.49}$$

with $\mathcal{F}$ the vector of the expressions (3.46) and $\mathcal{J}$ its Jacobian matrix (see [77] for the expression). In practice, (3.49) converges well if the initial condition is chosen properly. It is proposed to perform the first time step with the linearised version of this model because the solution of the linear system only depends on an approximation of the initial position of the structure. The convergence is checked using the L_2 norm of the tension force vector. After convergence is reached, the updated accelerations, velocities and positions of the knots are calculated from (3.37), (3.45) and (3.45).

3.4.1 Calculating the drag and lift forces on nets

Following the screen force model of Kristiansen and Faltinsen [68], the net area is distributed on adjoint knots as indicated in Fig. 3.4. Thus, the contributions of up to four structural elements add up to the hydrodynamic forces corresponding to a single knot. The surface integral at each element is approximated by a second-order accurate quadrature rule using its geometrical centre as the integration point. In the inertia system of the fluid, the velocity related hydrodynamic force vector $\mathbf{D}$ is split into drag and lift force components in normal ($\mathbf{n}_d$) and tangential ($\mathbf{n}_l$) direction of the local relative velocity vector $\mathbf{u}_{\text{rel,s}} = \mathbf{u}_{f,s} - \dot{\mathbf{x}}_s$:

$$\mathbf{D}_i = \sum_{s=1}^{N_{S,i}} \frac{\rho}{2} A_s u_{\text{rel,s}}^2 (c_d \mathbf{n}_d + c_l \mathbf{n}_l)_s. \tag{3.50}$$

Here, A_s is the area given as

$$A_s = \frac{l_1 l_2}{4} \cdot |\vec{b}_1 \times \vec{b}_2|, \tag{3.51}$$

with indices 1 and 2 referring to the two bars spanning the area and $\vec{b}$ the unit bar vectors. The coefficients c_d and c_l are calculated from a truncated Fourier series expanded for their dependency on the angle of attack α between fluid velocity vector and structural element vector:

$$c_d(\alpha) = c_{d,0} \sum_{k=1}^{\infty} a_{2k-1} \cos\left((2k-1)\alpha\right), \tag{3.52}$$

$$c_l(\alpha) = c_{l,\frac{\pi}{4}} \sum_{k=1}^{\infty} b_{2k} \cos\left(2k\alpha\right). \tag{3.53}$$

The definition of the constants $c_{d,0}$ and $c_{l,\frac{\pi}{4}}$ can be taken from [68]. In order to achieve general applicability, the Fourier coefficients a and b are found by fitting them to experimental data given in [89], [38] and [123].

This choice raises challenges because most force coefficients from experimental data is normalised by the undisturbed inflow velocity. However, the velocity at the

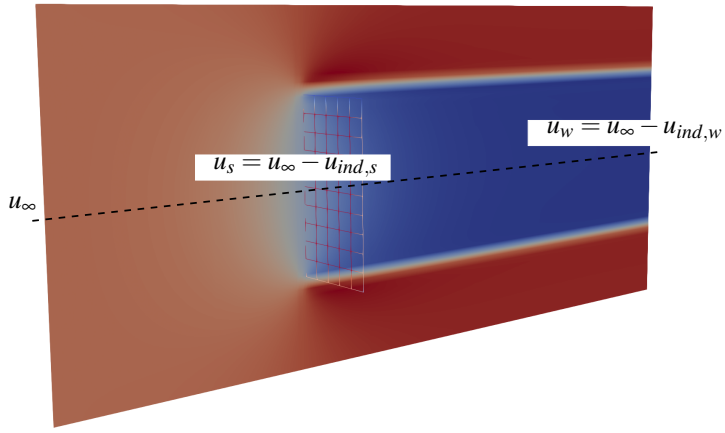

Figure 3.6: Illustration of velocity definitions in front and behind the net. Cross section shows the x-velocity distribution with velocity reduction behind the net.

location where the forces are evaluated in the numerical simulation is disturbed by the fluid-structure interaction close to the net as can be seen from Fig. 3.6. One possibility is to fit the coefficients to numerical data including the FSI. In the present model, a relation between the numerically interpolated velocity at the net and the undisturbed inflow velocity based on Froude's momentum theory [19] is used instead. It is based on the assumptions of potential flow that the induced velocities from the screen $u_{ind,s}$ and in the wake $u_{ind,w}$ are much smaller than the inflow velocity u_∞ and that no rotational velocities are induced (see Fig. 3.6 for definitions). Then, two Bernoulli equations can be stated:

$$p_\infty + \frac{\rho}{2} u_\infty^2 = p_{s,1} + \frac{\rho}{2}(u_\infty - u_{ind,s})^2, \tag{3.54}$$

$$p_{s,2} + \frac{\rho}{2}(u_\infty - u_{ind,s})^2 = p_w + \frac{\rho}{2}(u_\infty - u_{ind,w})^2. \tag{3.55}$$

Here, (3.54) is valid in front of the screen and (3.55) describes the fluid behind the screen. By combining these equations, the pressure jump at the screen is defined as

$$\Delta p = p_{s,2} - p_{s,1} = p_w - p_\infty + \rho\, u_{ind,w} \cdot \left(-u_\infty + \frac{u_{ind,w}}{2} \right). \tag{3.56}$$

It can be assumed that $p_w = p_\infty$ if start and end point are far away from the disturbance. Thus, (3.56) expresses the pressure jump in terms of inflow and induced velocities. Linearisation of the equation yields

$$\Delta p \approx -\rho\, u_{ind,w}\, u_\infty. \tag{3.57}$$

In addition, (3.54) can be used to approximate the pressure jump in front of the screen. The linearised expression is

$$p_{s,1} - p_\infty = \rho \; u_\infty \; u_{ind,s}. \tag{3.58}$$

Froude's hypothesis arises from (3.58) if the assumption is made that half of the pressure jump is in front and the other half behind the screen,

$$u_{ind,w} = 2u_{ind,s}, \tag{3.59}$$

i.e. the velocity at the screen is half the velocity between inflow and wake velocity (see Fig. 3.7). By inserting this result in (3.57) and using the definition of the screen velocity, it yields a new formula for u_s:

$$u_s = u_\infty - \frac{\Delta p}{2\rho u_\infty}. \tag{3.60}$$

The pressure jump Δp is due to the disturbance of the fluid through the presency of the net. Using the fluid velocity at the screen and the inflow velocity for the coefficient calculation, the jump can be expressed as

$$\Delta p = \frac{\rho}{2} c_d(u_\infty) u_s^2. \tag{3.61}$$

In combination with (3.60), the inflow velocity can finally be approximated from the known screen velocity as

$$u_\infty = \frac{c_d(u_\infty)}{2 \cdot \left(\sqrt{1 + c_d(u_\infty)} - 1 \right)} \cdot u_s, \tag{3.62}$$

which is solved using the Newton-Raphson method with $u_\infty = u_s$ as the initial guess. The converged solution of (3.62) gives then information about both, the undisturbed inflow velocity and the drag coefficient according to (3.52). The lift coefficient is finally calculated from (3.53) using this result.

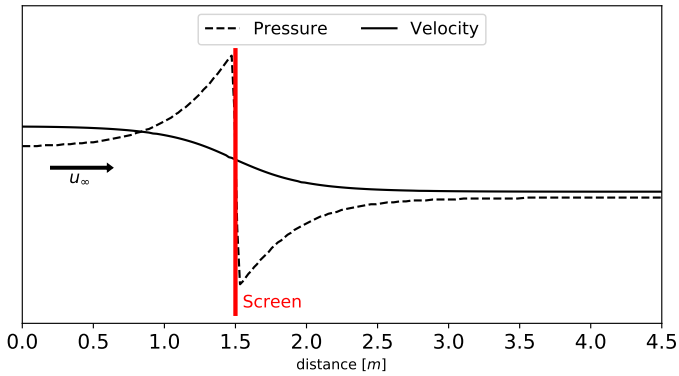

Figure 3.7: Illustration of velocity and pressure distribution in front and behind the net.

3.5 Coupling strategy

An overview of the proposed numerical model is shown in Fig. 3.8. A weak coupling of the free surface propagation, turbulence modelling, fluid dynamics and structural dynamics is chosen. The time step is adapted according to the CFL condition for two-phase flows taken from [11]. Here, the fluid and rigid body dynamics solver are weakly coupled through the common time step procedure based on an explicit Runge-Kutta method. The quasi-static mooring model is updated within each sub-step of the algorithm, and the arising mooring forces are added to the rigid body dynamics solver as external forces. Similarly, the effect of the net on the dynamics of the floating body is added to the external force vector. However, the dynamics of the net is only calculated once per time step before entering the FSI solution. The implicit time marching of the net model prevents additional restrictions on the time step size of the fluid solver. In the following, an overview of the mooring and net algorithm is given. Special attention is thereby given to the FSI between nets and fluid.

3.5.1 Incorporating the effects of mooring into the FSI solver

The algorithm of the quasi-static mooring model is illustrated in Fig. 3.9. As input parameters, the fluid velocity field and the locations of the mounting points are communicated to the algorithm. The geometrical constraint vector (3.33) is calculated from these, and the initial system of equations is generated. For the first time step, less restrictive directions for the unit vectors and initial tension forces are set to fill the left- and right-hand sides. Thus, this model is independent of a predefined initial form of the cable and highly suitable for applications without this requirement. The initial lengths

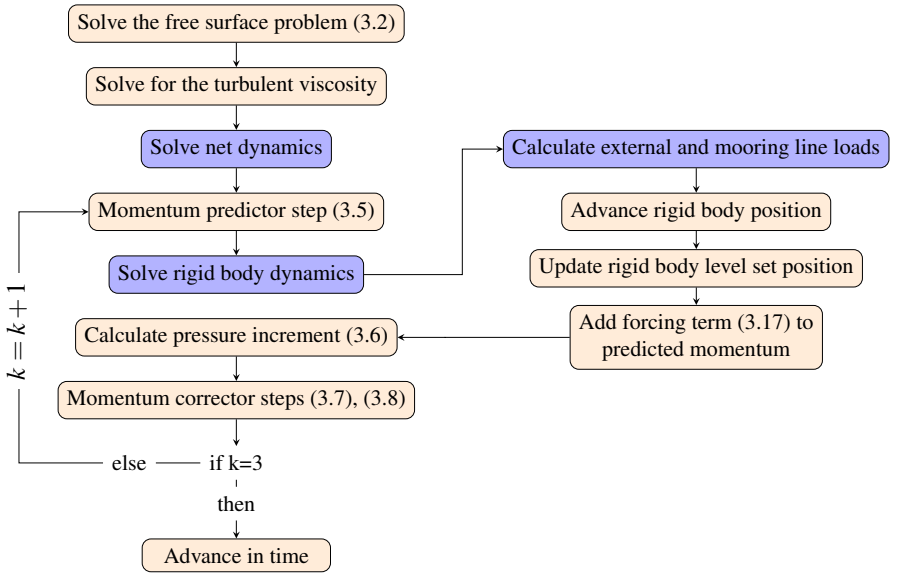

Figure 3.8: Flowchart of the proposed numerical model. Here, the index k defines the three Runge-Kutta sub-steps.

of the bars are calculated based on the given discretisation, and (3.29) yields the gravity force distribution. The hydrodynamic forces are initialised considering the fluid velocity field and (3.30). The velocities at the bars are linearly interpolated from the surrounding velocity grid points. This process is fully parallelised using MPI.

It is further noticed that the influence of the mooring line on the fluid is neglected because hydrodynamic transparency is assumed. This is justified by the focus on the motion of the body, which is not affected by the fluid disturbances due to the presence of the mooring lines. Thus, the communicated data from the mooring algorithm to the FSI solver only includes the tension forces and their angle of connection at the upper mounting point.

3.5.2 Incorporating the effects of flexible nets into the FSI solver

The length scale of the meshes of a net in aquaculture is typically smaller than the cage structure by order of magnitudes. Thus, a discretisation of the computational domain accounting for all structural components of the net is not practical. This raises the need for an alternative fulfilment of the boundary conditions at the fluid-structure interface because the physical fluid-structure interface is not present in the CFD simulation. A suitable coupling condition can be enforced starting from the Eulerian grid for the fluid

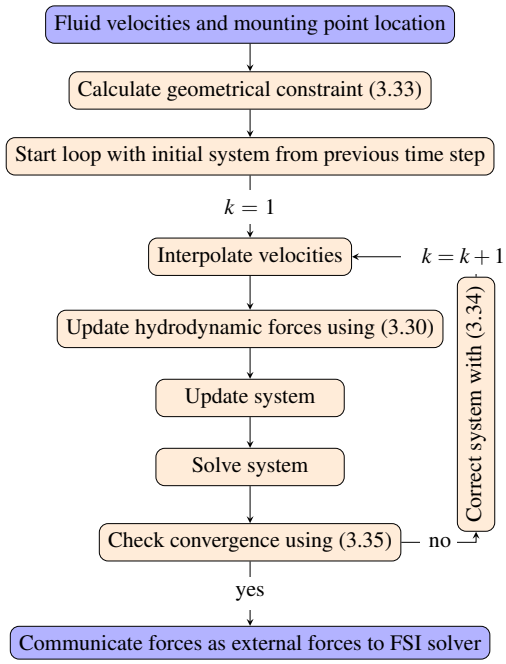

Figure 3.9: Flowchart of the quasi-static mooring model. Here, the index k defines the sub-iterations of the succesive approximation algorithm.

and a Lagrangian representation of the net. Conservation of momentum is assumed for any control volume enclosing the net. This implies that the energy transfer from the fluid to the net corresponds to the loss of the fluid momentum due to the disturbance of the net. This momentum loss can be physically identified as a pressure jump over an infinitesimally small distance through the net (compare Fig. 3.7) and is calculated from the external forces acting in (3.37).

The momentum loss $\mathbf{S}$ is assumed to be uniformly distributed over the net surface regardless of the difference between twines and voids. This implication requires uniformly distributed markers holding $\mathbf{S}$ and that the area which is covered by each marker is nearly equal to the grid size of the encircling fluid domain. However, it is not practical to evaluate the structural dynamics on a scale where the knots fulfil these requirements. Therefore, additional Lagrangian markers are introduced to distribute $\mathbf{S}$. They are defined by splitting the structural elements in triangles according to the Eulerian grid size in their vicinity. The Lagrangian markers are then defined in the geometrical centres of each triangle. An example of the distribution of the markers on the discrete net structure is shown in Fig. 3.10.

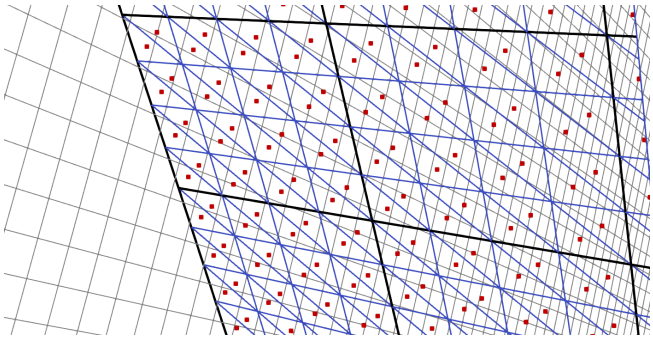

Figure 3.10: Illustration of the discrete net structure for the fluid-structure interaction. Black lines represent structural elements of the net, blue lines show the triangulated surface and the Lagrangian points are marked in red. The background shows the Eulerian fluid grid as thin grey lines in a perpendicular plane.

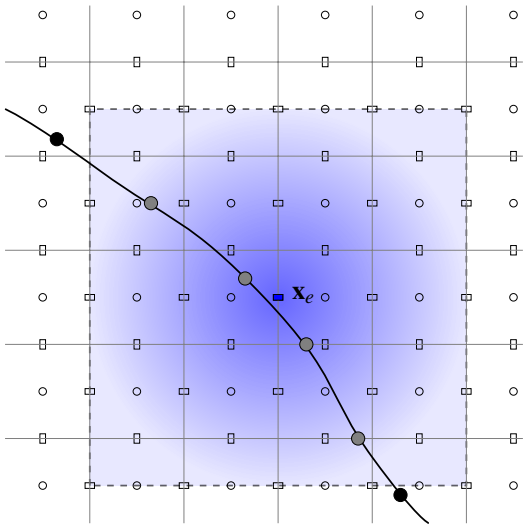

Figure 3.11: Definition of the kernel for determining the disturbance of the fluid at the velocity point $\mathbf{x}_e$ (blue). Blue shading illustrates the kernel weighting. The Eulerian grid points are shown as transparent dots and rectangles. The involved Lagrangian points of the net are coloured in grey.

The forces of each marker are distributed on the fluid grid points $\mathbf{x}_e$ as forcing terms using the interpolation

$$\mathbf{S}(\mathbf{x}_e) = \sum_{L=1}^{L_e} \frac{\mathbf{s}(\mathbf{x}_L)}{\Delta x \Delta y \Delta z} \mathrm{D}\left(\frac{x_e - x_L}{\Delta x}\right) \mathrm{D}\left(\frac{y_e - y_L}{\Delta y}\right) \mathrm{D}\left(\frac{z_e - z_L}{\Delta z}\right), \tag{3.63}$$

with L_e the number of markers within a kernel around $\mathbf{x}_e$ (see also Fig. 3.11). The kernel is defined as [91]

$$D(r) = \begin{cases} \frac{1}{4}\left(1 + \cos\left(\frac{\pi r}{2}\right)\right) & \text{if } |r| < 2.0, \\ 0.0 & \text{else.} \end{cases} \tag{3.64}$$

The forces vectors $\mathbf{s}(\mathbf{x}_L)$ at the marker with position $\mathbf{x}_L = (x_L, y_L, z_L)$ are calculated by integrating the external forces in (3.37) over the triangle area A_L:

$$\mathbf{s}(\mathbf{x}_L) = \left[\frac{\rho}{2} u_{\mathrm{rel}}^2 \cdot (c_d \mathbf{n}_d + c_l \mathbf{n}_l) + m_a \left(\mathbf{a_f} + \mathrm{diag}(n_x, n_y, n_z) \cdot (\mathbf{a_f} - \ddot{\mathbf{x}})\right) + \mathbf{G}\right]_L \cdot A_L. \tag{3.65}$$

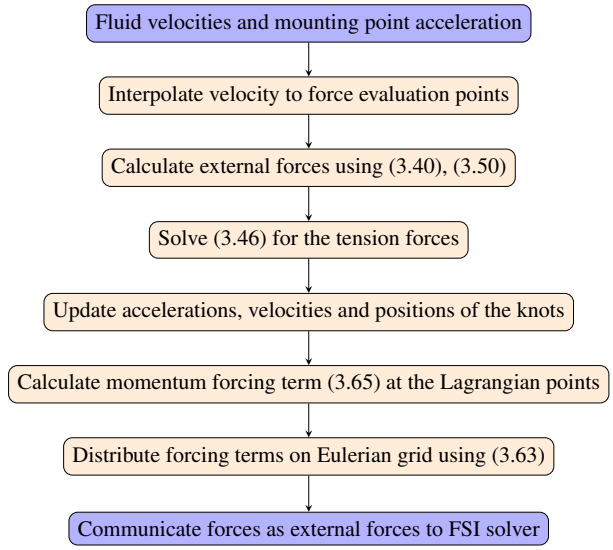

Figure 3.12: Flowchart of the dynamic net model.

The flowchart of the proposed dynamic net model is shown in Fig. 3.12. As input, the fluid velocity field and the positions of the mounting points of the previous time step are used. Here, the fields are interpolated to the points where the external forces are evaluated using the kernel function (3.64). Then, the external forces are evaluated,

and the new tension force distribution is calculated and used for updating the dynamic properties of the knots. Afterwards, the forcing terms (3.63) are determined on the Eulerian grid and the forces. The communicated data from the net model to the FSI solver includes the tension forces and their angle of attack at the mounting points. The momentum forcing terms are added to the momentum equations before solving the pressure correction step.

Two-way coupling is enabled by assigning the topmost knots to the rigid body motion. For this purpose, it is sufficient to replace the third or fourth terms of the dynamic equilibria (3.46) with the known acceleration of the rigid body at these points.

Chapter 4

Summary of validation cases

The numerical framework presented in chapter 3 is the result of the research published in the five appended articles. Here, each of the articles is concerned with one of the secondary objectives stated in chapter 1.2. All individually developed parts are ultimately merged into the new numerical model which is applied to OOA structures in paper 4 and 5. The most important validation cases for each of the appended articles are presented in the following. Conclusions arising from these can be found in the final part of this thesis (chapter 5).

4.1 Paper 1: Efficient quasi-static mooring model

The first paper is concerned with the development of a new approach for simulating the effect of mooring systems on floating structures. It is based on quasi-static assumptions and a discretisation into elastic bars and mass points connecting them. The introduction of successive approximation for this problem raises the possibility to converge to a physically relevant solution within a small number of iterations. Under consideration of the multiple inversions to reach convergence, the successive approximation arises as an efficient algorithm due to a significantly decreased matrix size in comparison to Newton-Raphson iterations, which requires the solution vector to contain a single column with directions of the unit bars as well as tension force magnitudes [73]. Further advantages of the proposed model are the lack of restrictions on time stepping and that the static shape of the line is not necessary to initialise the model.

The validation of the proposed mooring model includes comparisons of line shape and maximum tension forces with experimental data. First, the maximum tension force is analysed for a single mooring line attached to a buoy with prescribed heave motion. The mooring line consists of chains and wires of different material properties which can be found in the work of Chenga et al. [25]. Here, linear material is assumed. A preliminary static test is conducted to validate the forces for different positive offsets.

The resulting distribution is shown in Fig. 4.1a. The deviation between the numerical model and experiments is generally small but increases slightly with increasing offset. The error is below 0.2% for offsets smaller than 5 m and increases to $\approx 1.1\%$ for 30 m offset. Next, a simple harmonic heave motion with an amplitude of 15 m and a period of 10 s is prescribed to the top of the line. Good agreement with the measurements can be stated from comparing the distributions shown in Fig. 4.1b. Generally, the numerical model slightly under predicts the troughs and over predicts the crests by $\approx 2.5\%$ in peak height. A Fourier analysis of the time series indicates an error of less than 1% for the amplitude of the fundamental frequency.

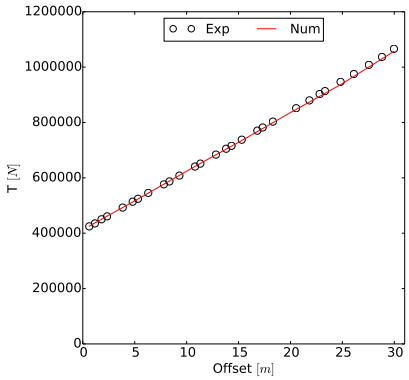

(a) Tension forces for different heave offsets.

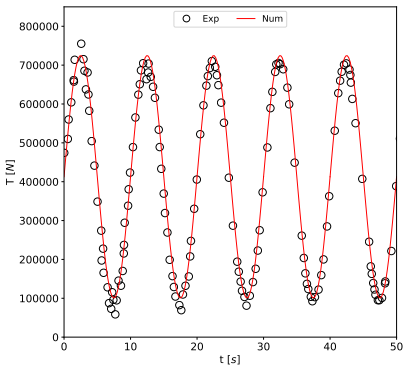

(b) Maximum tension force time series for the dynamic case.

Figure 4.1: Comparison of numerical and experimental results for the static analysis and the prescribed heave motion.

Next, the mooring model is validated through comparison to experimental results from wind channel measurements at the Institute of Ocean Engineering at the University of Rostock, Germany. The considered mooring system consists of a single rope with a length of $L_m = 1.82$ m, a diameter of $d_t = 0.004$ m, a specific weight of $\gamma = 0.089$ kg/m and Young's modulus of 7.9 GPa. The line is fixed at the coordinates $(x, y) = (0\,\text{m}, 0\,\text{m})$ and mounted to a moveable load cell on the top to measure maximum tension forces. The wind machine at the inlet of the channel generates a laminar flow of predefined velocity which the mooring system is exposed to. In the first set of experiments, three different locations of the upper mounting point are investigated without inflow. Numerical results are produced using the same input data as given above. The results in Fig. 4.2 show the distribution of the discrete line with 5, 10 and 50 bar elements and the comparison to the experimental data. Regardless of the considered distribution, the numerical model can accurately reproduce the experimental measurements. Small under-

and over-predictions can be found for the coarsest line discretisation and the hanging rope distribution in Fig. 4.2a which is overcome by increasing the number of elements slightly.

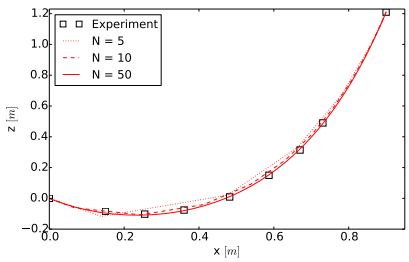

(a) Hanging rope distribution.

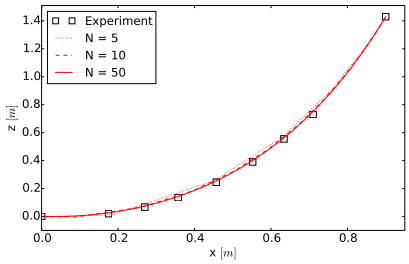

(b) Catenary rope distribution.

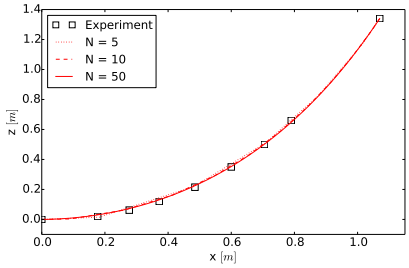

(c) Stretched rope distribution.

Figure 4.2: Numerical and experimental mooring line distributions without inflow.

The second set of experiments is conducted by applying inflow velocities of $v = 8$ m/s and $v = 18$ m/s on the stretched rope distribution of Fig. 4.2c. The results, shown in Fig. 4.3, indicate that the numerical model is capable of representing the physical deformation of ropes in stationary flow conditions. All line discretisations show qualitatively good agreements with the experiment. Further information on the accuracy is provided by presenting the numerical and experimental results for the maximum tension forces over different inflow velocities in Tab. 4.1. It can be seen that the model converges towards a value close to the experimental data as the number of bar elements increases. This is demonstrated by calculating an extrapolated value without discretisation error from the numerical results using Richardson extrapolation [95]. The remaining deviation from experiments is related to the modelling error. Here, a good agreement with the experiments can be stated because the maximum error is below 3% for $v = 8$ m/s.

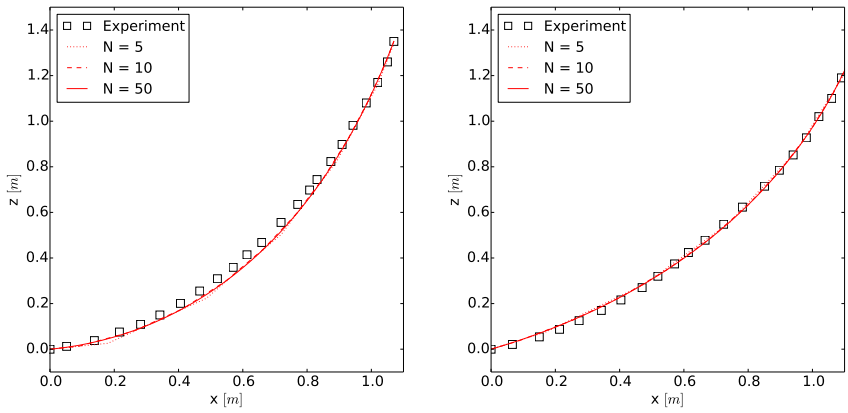

(a) Stretched rope distribution at $v = 8$ m/s.

(b) Stretched rope distribution at $v = 18$ m/s.

Figure 4.3: Numerical and experimental mooring line distributions for different inflow velocities.

Table 4.1: Numerical and experimental maximum tension forces for inflow velocities between $v = 0\ m/s$ and $v = 18\ m/s$. Values in $[N]$ if not defined differently.

$v\ [m/s]$	Exp	N=5	N=10	N=50	Extrapol.	Error [%]
0.0	1.54	1.61	1.57	1.56	1.56	1.45
8.01	1.65	1.74	1.71	1.70	1.70	2.93
11.97	1.90	1.93	1.90	1.89	1.89	-0.43
14.08	2.01	2.06	2.03	2.02	2.02	1.22
16.08	2.21	2.21	2.19	2.18	2.18	-0.94
18.05	2.40	2.39	2.37	2.36	2.36	-1.64

4.2 Paper 2: Improving the incorporation of porous tensile structures in CFD

In the second paper, a new approach for modelling the interaction of fluid and porous net structures is proposed. It arises from the analysis of the existing approach based on a porous medium model. This model is considered as a surrogate, sharing similar physical properties as the original interaction process. However, it does not imply any physical connection. This is illustrated by the necessity of arbitrarily [22] defining the added mass coefficient, originating from the derivation of the volume- and Reynolds-averaged Navier-Stokes (VRANS) equations, or neglecting it [89]. The closure model

for the VRANS equations is usually based on the Darcy-Forchheimer law and requires the predefinition of several coefficients which are dependent on fluid properties. Previous research [22, 124] neglected these dependencies and rather used the free coefficients for incorporating the disturbances of the net on the fluid. As pointed out by Chen and Christensen [22], it is challenging to incorporate all aspects of properties influencing the forces on a net into the calculation of these coefficients. Therefore, they defined them as normal and tangential constants throughout the porous medium. This leads to a zone of constant pressure loss rather than a thin sheet where the pressure drops immediately as in reality. Another challenge of porous medium models occurs for net cages and deformed nets in general. In [21], the utilisation of a porous medium for these cases is investigated where the authors proposed defining zones of certain thickness around each macro element of the net. The resulting prism volumes represent a continuous porous medium. This procedure might be interpreted as a type of overset grid. Besides the high computational cost of generating and parallelising this generally three-dimensional grid, a more severe problem occurs in the case of deformed elements. As shown in Fig. 4.4, overlapping regions and gaps can occur at possible intersections of zones. So far, this issue has not been addressed.

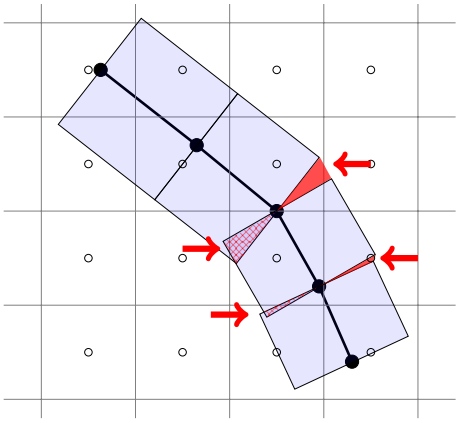

Figure 4.4: Two-dimensional illustration of the challenges in constructing a discrete porous zone (blue shaded) around a net wall (thick black lines and points) as proposed in [21]. Overlapping regions are indicated in hatched red; Holes are indicated as red triangles.

These drawbacks of the porous medium approach indicate theoretical, physical and computational limitations, and the necessity for an alternative coupling model arises. Therefore, a new coupling model based on Lagrangian-Eulerian considerations is proposed. The new approach avoids demanding volume handling and is straightforward to

be parallelised. It also incorporates more advanced hydrodynamic force calculations. This increases the actual physical information contained in the coupling process and, eventually, improves numerical tools for modelling this type of fluid-structure interaction. The chosen kernel in this publication leads to a free parameter to fulfil dimensional equality in the interpolation. It arises numerically with the transition from the hydrodynamic surface force at the screens to a volume force representation in the Eulerian grid. The parameter corresponds physically to the influence range of the net disturbance on the fluid and is linked to the deceleration of the flow behind the net and was determined from the data in [89]. In Paper 4, the parameter was successfully eliminated.

In order to validate the proposed coupling scheme, a fixed net panel of $1\ m \times 1\ m$ with a solidity of 0.184 is compared to the experimental data of Patursson et al. [89]. A steady current between 0.125 m/s and 0.75 m/s as well as several angles of attack α between 15° and 90° are considered. A slice of the domain through the middle plane is shown for $\alpha = 45°$ and 90° and $u_\infty = 0.5$ m/s in Fig. 4.5. The wake of the net has approximately the same width as the net panel. The fluid is accelerated around the panel. As the angle of attack increases, the fluid slows down in front of the net which leads to a decreasing velocity at the net itself. Behind the net, a nearly steady velocity field can be observed for both angles of attack.

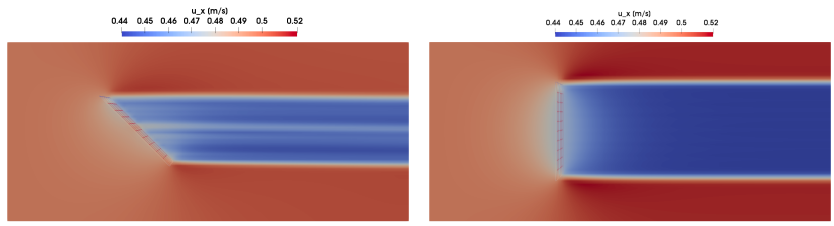

(a) $\alpha = 45°$. (b) $\alpha = 90°$.

Figure 4.5: Velocity field for the fixed net panel in steady current flow of $u_\infty = 0.5$ m/s.

Fig. 4.6 presents the numerical and experimental force coefficients for the different inflow velocities as a function of α. The computed drag coefficients (Fig. 4.6a) increase with decreasing inflow velocity and increasing angle of attack. The maximum deviation for C_D is 25% for $\alpha = 15°$ which might be due to neglecting the influence of the frame. For larger angles, the maximum deviation is reduced to 15%. The predicted lift coefficients in Fig. 4.6b indicate maximum lift forces for $\alpha = 45°$. At larger angles of attack, the flow separates at the frame, and the lift forces reduce. In general, the lift forces are smaller than the drag forces. The deviations are slightly larger than for the prediction for C_D with a maximum derivation of 27% for angles larger than 15°. These results describe an improvement over existing porous medium models [22] where deviations larger than

50% for C_L were reported. The velocity reduction behind the net is predicted well by the numerical model for $\alpha \geq 30^\circ$ as can be seen in Fig. 4.6c. The maximum deviations for U_r are in a similar range as the deviations for C_L. A tendency to a better agreement with experiments can be observed for the larger angles of attack.

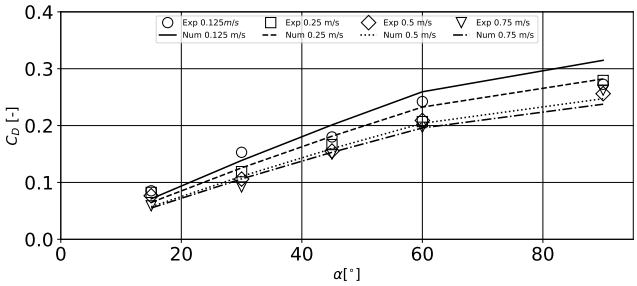

(a) Drag coefficient C_D.

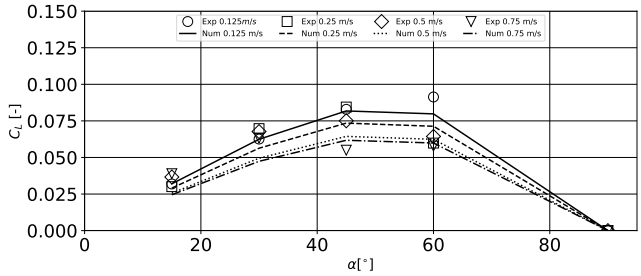

(b) Lift coefficient C_L.

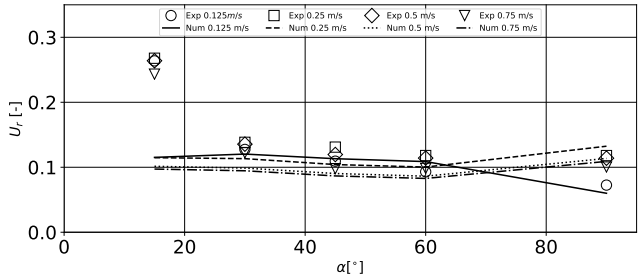

(c) Velocity reduction factor U_r.

Figure 4.6: Comparison of the numerical and experimental results for the fixed net panel in steady current flow.

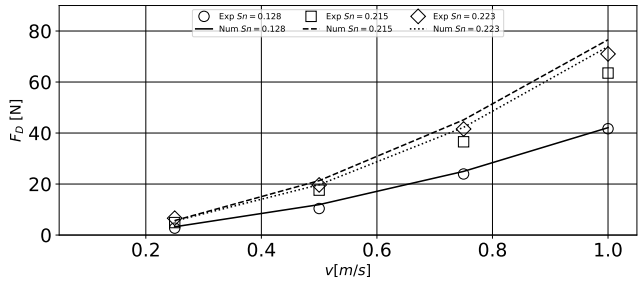

Figure 4.7: Comparison of the numerical and experimental drag forces on fixed net cage in steady current flow.

A validation case with more complicated geometry is conducted by replicating the experiments in [123]. Here, the drag forces on fully submerged fixed circular net structures are measured for constant inflow velocities between 0.25 m/s and 1.0 m/s and net geometries with the solidities $0.128, 0.215$ and 0.223. The predicted drag forces are compared to the experimental results in Fig. 4.7. In the experiments, the forces increase with the solidity and inflow velocity. In contrast, the numerical model computes slightly larger drag forces for $Sn = 0.215$ than for $Sn = 0.223$. The difference in solidity between the two nets seems to be small. However, the net with $Sn = 0.215$ contains meshes with half the length and half the diameter compared to the net with $Sn = 0.223$. Thus, the interaction between the twines increases for the net with $Sn = 0.215$. This effect is apparently not captured well by the screen force model because the deviations to the experiments are the largest for this net (up to 23% in deviation). The other net configurations are modelled within a range of a 20% deviation band which indicates a good capturing of the physics for the investigated range of inflow velocities and improvement over the results reported in [22].

The accuracy of the velocity reduction algorithm is tested against the experiments of Bi et al. [8]. They conducted PIV measurements of the fluid around a single and multiple fixed perpendicular net panels in varying current velocities. A knotless net with square meshes and $Sn = 0.243$ is used. The inflow velocities u_∞ are 0.056 m/s, 0.113 m/s, 0.17 m/s and 0.226 m/s. In a first measurement series, up to three additional panels of the same size and geometry are placed in the wake of the first panel. The distance between each panel is one panel length. The velocity is measured one panel length behind the last panel for each configuration. In a second series, the wake velocities are measured at different locations between and behind up to $N = 4$ net panels for $u_\infty = 0.17$ m/s. Fig. 4.8 presents the comparisons for the velocity reduction factor U_r with the experiments. As can be seen in Fig. 4.8a, the velocity reduction increases with the number of panels due to an increased resistance over the same distance. At the same time, U_r tends to decrease slightly if the inflow velocity is increased. The maximum

deviation is 27%, but most deviations are well below 10%. Generally, the deviations are the largest for the single net case. However, $N = 1$ also results in the smallest reduction factors which correspond to the highest sensitivity to errors. If the L_2 norms of deviation, which are $0.033, 0.044, 0.044$ and 0.026 for $N = 1-4$, are considered, it can be seen that the modelling deviation is similar for all cases. As reported in [8], downstream panels slightly influence the flow through upstream panels. This effect seems to be captured by the numerical model due to the qualitatively good agreement with the experimental distribution of U_r over x in Fig. 4.8b.

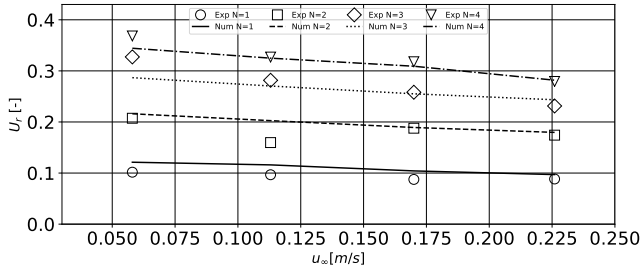

(a) Distribution of U_r over u_∞, measured 1.0 L behind the last panel.

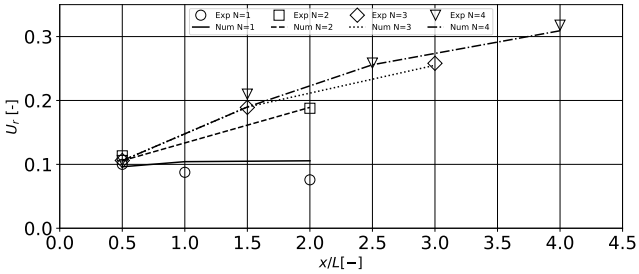

(b) Distribution of U_r over x/L for $u_\infty = 0.17$ m/s.

Figure 4.8: Comparison of the numerical and experimental velocity reduction factors for N fixed net panels in steady current flow.

Finally, the drag forces on a net panel in regular waves are compared with experiments presented in [71]. This allows testing of the proposed model in a space- and time-varying velocity field including a free surface. The numerical wave tank is defined as shown in Fig. 4.9. It has a length of 10 m, a height of 1.0 m and a width of 0.5 m. The water depth is set to 0.62 m. The tank is shortened in comparison to the experimental wave flume to save computational time. A two wavelength long numerical beach is placed at the end of the tank to absorb the wave energy. A wave relaxation zone of one

wavelength is defined at the inlet to generate waves. In the experiments, five different regular waves of different length, height and steepness are generated using a vertical piston wavemaker. Fifth-order Stokes wave theory is used to model these waves because the wavemaker signal is not available and the Ursell numbers are small. The input wave frequencies and heights are given in Tab. 4.2. The investigated net panels have the same width and height as the tank and solidities of $0.095, 0.22$ and 0.288. They are referred as net case $1-3$ in the following.

Table 4.2: Wave input parameters for the simulation of fixed net panels in waves (taken from [71]).

Wave case	1	2	3	4	5
Wave frequency f $[Hz]$	1.42	1.42	1.42	1.25	1.0
Wave height H $[m]$	0.045	0.064	0.084	0.104	0.167

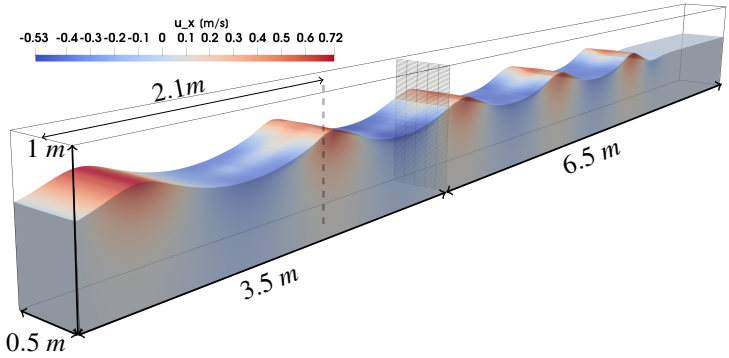

Figure 4.9: Computational domain for the simulation of a fixed net panel in regular waves. Colours show velocities in x-direction.

Lader et al. [71] suggest evaluating the wave energy by calculating the zeroth-order moment of the power spectrum due to the non-linearity of the wave. However, it is shown in this paper that the high-order components are less then $1/5$ of the leading wave frequency component in magnitude using a discrete Fourier transformation of the numerical wave signals. Thus, the contribution of the high-order components to the total wave energy is of minor interest, and it is justified to simplify the analysis to a comparison of the wave amplitudes. Following Lader et al. [71], a distinction between positive and negative amplitudes is made because of the asymmetry of the waves with higher crests and shallower troughs. As illustrated in Fig. 4.10b, the higher wave crests result in higher particle velocities and larger submerged net area. This corresponds to

larger drag forces on the net in the wave propagation direction. In contrast, the load changes sign in a wave trough situation (Fig. 4.10a), and a smaller net area is wetted.

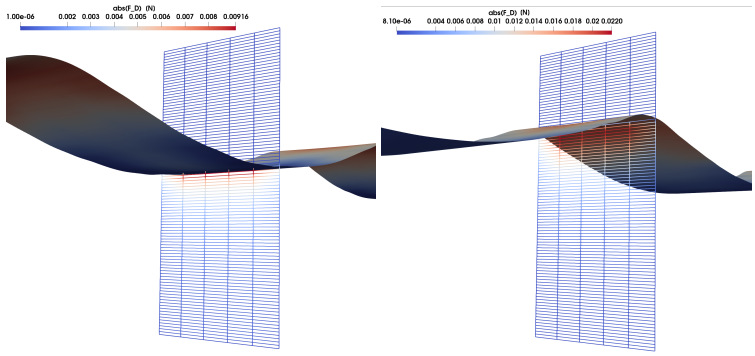

(a) Wave trough situation. (b) Wave crest situation.

Figure 4.10: Distribution of the drag force magnitudes on net panel with $Sn = 0.288$ in wave 5.

The most important components of the total wave forces act on the net with the regular wave frequency as shown in the Figs. 4.11a - 4.11e. Therefore, it is sufficient to compare the drag force amplitudes when the total wave forces are of interest. It is also noticed from these figures that the magnitude of the forces increases with the net solidity and wave amplitude. Both phenomena are expected from the validation cases. The forces are mostly under-predicted by up to 25% for the first net with $Sn = 0.095$ (compare Tab. 4.3). In comparison, the model over-predicts the forces for the nets with higher solidities. The positive forces on the net with the highest solidity are generally predicted with high accuracy (12% and less) whereas the negative forces show larger discrepancies (up to 30%). The intermediate solidity is generally predicted the least accurate with most deviations between 20% and 40%. Chen and Christensen [22] noticed similar challenges with their porous medium model and pointed to uncertainties in the experimental data. In addition, it is noticeable that the second net geometry consists of the shortest twines.

Table 4.3: Deviations [%] between numerical simulation and experimental data of Lader et al. [71] for the averaged positive $(+)$ and negative $(-)$ drag force amplitudes.

Sn	Wave case									
	1		2		3		4		5	
	+	-	+	-	+	-	+	-	+	-
0.095	11.4	19.1	25.1	−17.6	23.2	1.9	10.9	21.7	17.9	0.5
0.22	−80.5	−21.4	−31.2	−30.6	−29.2	−49.1	−59.8	−29.2	−41.1	−21.7
0.288	−12.4	−30.3	−3.2	−9.8	−3.2	−20.2	4.3	−30.4	−3.2	−55.8

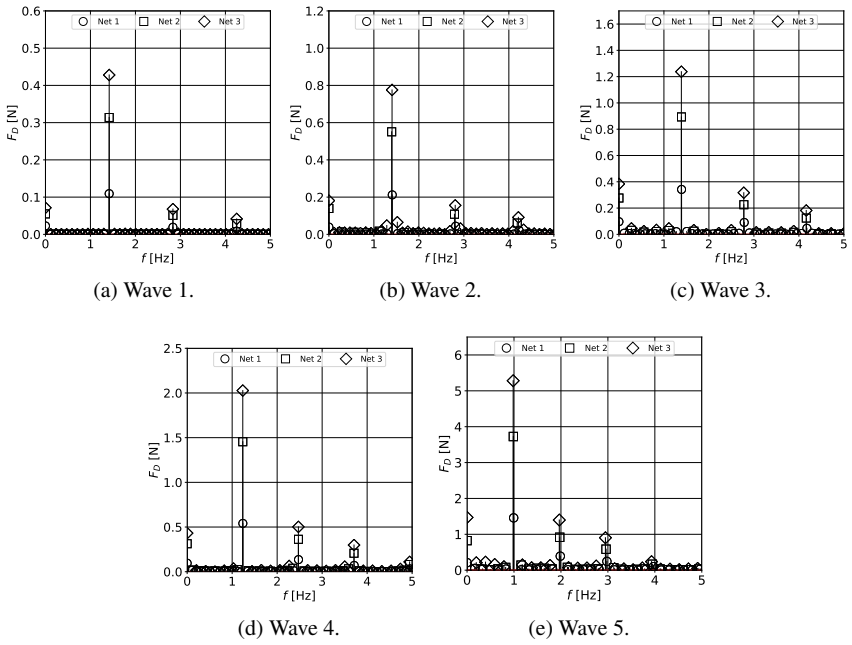

(a) Wave 1. (b) Wave 2. (c) Wave 3.

(d) Wave 4. (e) Wave 5.

Figure 4.11: Amplitude spectra of the numerical drag force time series for the five different wave cases.

4.3 Paper 3: A non-linear implicit structural model for solving the dynamics of nets

In this paper, a new methodology for modelling the non-linear dynamics of porous tensile structures and their interaction with the surrounding fluid was proposed. An efficient structural model was derived for arbitrary deformations and non-linear material. It is based on solving Newton's second law for the unknown tension forces. The fluid loading on the structure was calculated using the screen force model as proposed in paper 2. High-order backward finite differences were included to approximate the structural motion. Finally, a single matrix-vector problem arose which was solved using an accelerated Newton's method. In contrast to existing explicit algorithms, the implicit time and deformation handling increases stability and effectively removes strong time step restrictions from the fluid solver. Two-way coupling was provided by including the loss of fluid momentum due to passing a porous sheet in the Navier-Stokes equations as a source term. As initially developed in paper 2, it was determined from a kernel inte-

gration of the hydrodynamic and body forces over multiple Lagrangian points which follow the structural deformation. However, the interpolation was chosen such that the previously necessary parameter κ could be omitted.

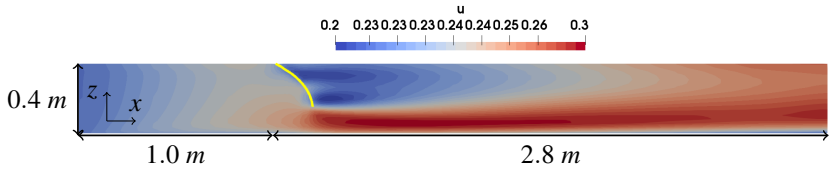

Figure 4.12: Slice through the centre of the computational domain for the simulation of a porous sheet in steady current incident from the left. The deformed sheet is shown in yellow. The contours show the velocity in x-direction for the case with $u_\infty = 0.226$ m/s.

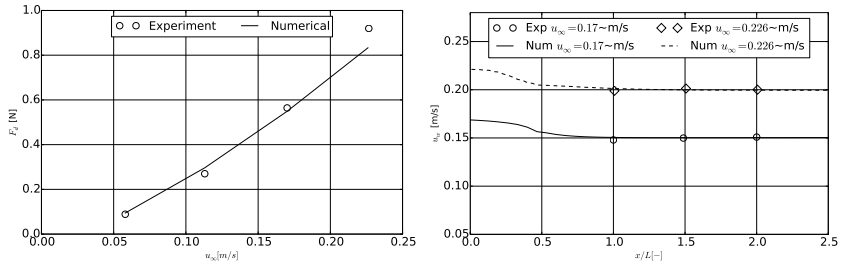

(a) Drag forces for different inflow velocities.

(b) Velocity profile along the x-axis through the centre of the sheet. $x/L = 0$ corresponds to the x-position of the fixed top of the sheet.

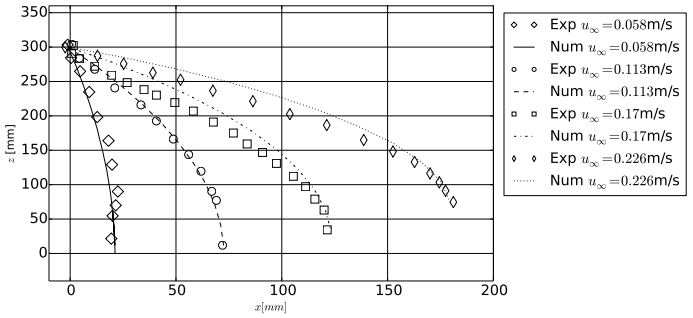

(c) Distribution of the deformed centre line for different inflow velocities.

Figure 4.13: Comparison of the numerical and experimental results for a porous sheet in steady current flow.

First, the deformation of a porous sheet in steady current flow is presented following the experimental setup by Bi et al. [9]. The sheet has a size of 0.3 m $\times$ 0.3 m with solidity $S = 0.243$. The top is fixed during the experiments and a steel bar with a mass of 73 g in air is attached to the bottom of the structure. The computational domain, shown in Fig. 4.12, replicates the physical experiment. Fig. 4.13 shows the distribution of the centre line of the sheet, the global drag forces and velocity distribution through the structure for inflow velocities u_∞ between 0.056 m/s and 0.226 m/s.

The experimental results for the deformation are extracted from pictures of the whole structure presented in their paper and therefore, prone to some degree of uncertainties. Based on that, the comparison in Fig. 4.13c shows a satisfying performance of the numerical model. For larger velocities, the model tends to predict a larger curvature in the middle part of the sheet. This also affects the calculated global drag forces shown in Fig. 4.13a. Here, deviations below 10% are shown for the lower range of investigated inflow velocities, but a 20% under-prediction is given for the largest velocity. This is probably linked to the slightly different deformation causing larger lift forces but smaller drag forces. Additionally, Fig. 4.13b shows the distribution of the velocity through and behind the sheet for two inflow velocities. As the flow passes the structure, a velocity drop is visible due to a loss of fluid momentum. The magnitude and position of the velocity reduction are well presented by the proposed model irrespective of the inflow velocity.

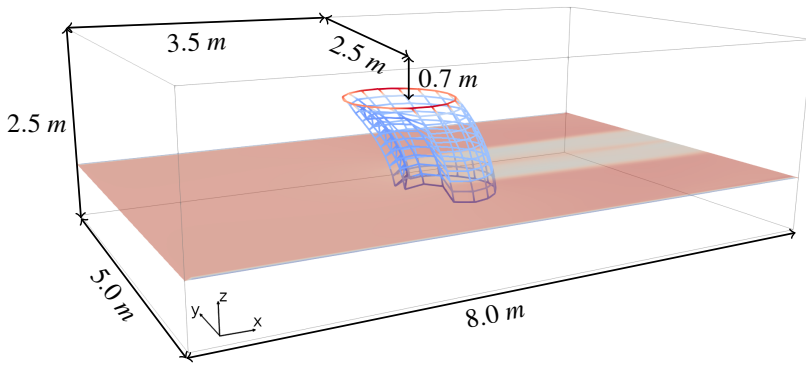

Figure 4.14: Computational domain for the simulation of a porous cylinder in steady current flow. The current propagates in positive x-direction.

Another validation case concentrated on the deformation of a porous cylinder in steady current flow. The setup and measurements are taken from [69]. The cylinder has a diameter of 1.435 m, a height of 1.44 m and consists of meshes with $d_t = 0.0018$ m and $l_t = 0.018$ m, which corresponds to a solidity of $S = 0.19$. It is numerically represented

by 17×10 structural elements. The top is fixed during the experiments and 16 cylindrical weights of $0.4, 0.6$ and 0.8 kg each are attached to the bottom row of the cylinder. The computational domain together with the placement of the centre top position of the cylinder is shown in Fig. 4.14. The inflow velocity u_∞ varies between 0.13 m/s and 0.56 m/s. As the results, Fig. 4.15 shows the global drag and lift forces and volume and area reduction coefficients for the different inflow velocities and attached weights. The reduction coefficients represent the ratio of the volume and area of the deformed structure to the initial structure and are calculated as proposed in [69] to be consistent with the experiments. Their accurate prediction demands a correct force calculation and proper velocity reduction through the front part of the cylinder since both influence the deformed shape.

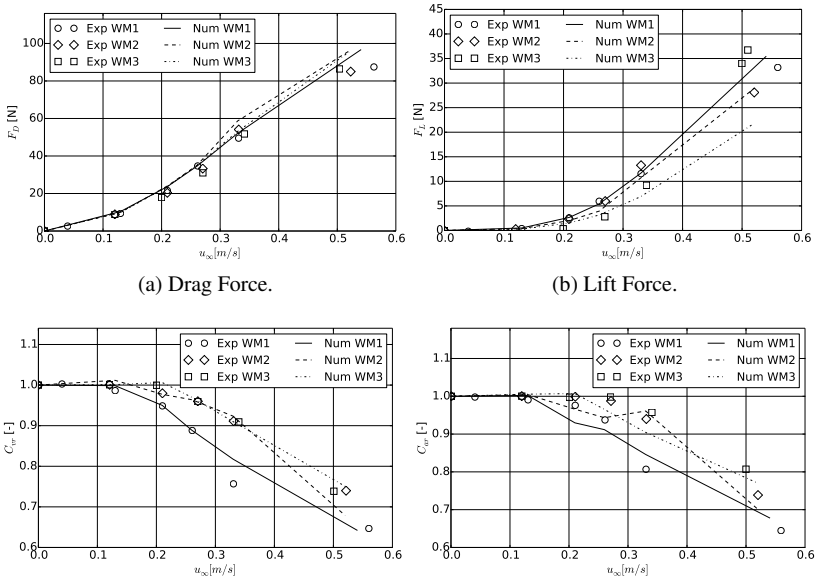

(a) Drag Force.

(b) Lift Force.

(c) Volume reduction coefficient.

(d) Area reduction coefficient.

Figure 4.15: Numerical and experimental results for the simulation of a porous cylinder in steady current flow. WM1 corresponds to 16×0.4 kg additional weight, WM2 corresponds to 16×0.6 kg additional weight and WM3 corresponds to 16×0.8 kg additional weight.

The global forces on the structure, shown in Fig. 4.15a and Fig. 4.15b, increase with increasing inflow velocity, and the influence of the changing weights is only of importance for velocities larger than 0.33 m/s. For smaller velocities, the numerical

model agrees well with the experiments due to consistent deviations below 10%. For the largest inflow velocity, the lift force is under-predicted. Here, the simulations show consistent results as the lift forces with the largest additional weight is generally the lowest due to the smallest deformation. In contrast, the experimental data shows the largest lift force for this configuration without providing a physical explanation for this phenomenon. The volume and area reduction (Figs. 4.15c and 4.15d) is negligible for inflow velocities smaller than 0.2 m/s. For larger velocities, the numerical model accords well with the experiments by predicting increasing volume and area reduction with increasing velocity. The largest deviation is observed for the predicted area reduction coefficient for velocities between 0.23 m/s and 0.27 m/s. A possible explanation is a slightly different deformation process of the numerical cage in comparison to the physical one. In the experiment, the deformation at this velocity seems to be related to a bending of the cylinder, whereas the cage also deforms through a reduced diameter numerically. However, a large uncertainty associated with accessing the area reduction by tracking only three points has to be considered. As expected, the largest deformation of the cylinder is predicted for the lowest additional weight.

4.4 Paper 4: Development of an immersed boundary method to simulate moored-floating objects in waves

A new numerical framework for modelling the motion of moored-floating structures in waves and current based on a continuous direct forcing immersed boundary method was proposed in this paper. The interactions of floating structures, mooring, nets and fluid are incorporated as two-way coupling problems. The presented rigid-body FSI algorithm is validated against measurements of a horizontal moored-floating cylinder in waves. The two-dimensional setup, shown in Fig. 4.16, replicates the experiments of Kristiansen [66]. A cylinder with diameter 0.1 m, the same length as the width of the tank and a mass of 3.94 kg/m is placed in the tank. A mooring system, consisting of ropes and springs with stiffness 151.2 N/m^2 and pre-tension 38.1 N/m, is attached to the cylinder. The other end of the lines is coupled to a pulley 2.43 m away from the cylinder at a height of 0.136 m above the free surface. The waves are generated in a wave generation zone of one wavelength, and a numerical beach damps the waves at the end of the tank. The mooring system is modelled as two springs mounted at the centre of the cylinder.

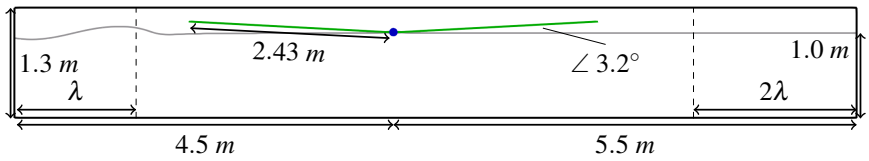

Figure 4.16: Two-dimensional domain for the simulation of a moored-floating cylinder in waves. The cylinder is shown in blue, the mooring lines in green and λ is the wavelength.

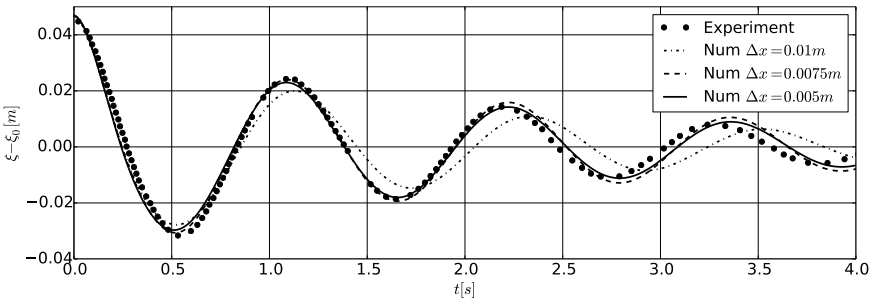

(a) Comparison of the time series of the surge decay test.

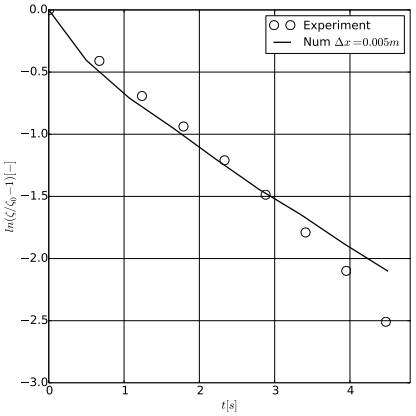

(b) Comparison of the decay rate for the surge decay test.

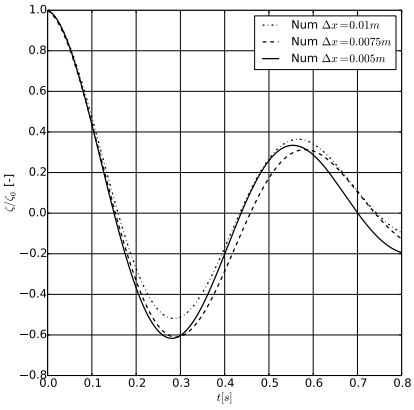

(c) Numerical heave decay test without mooring system.

Figure 4.17: Comparison of the numerical and experimental results for the decay tests of a moored-floating cylinder.

First, a convergence study is conducted using decays test of the moored-floating cylinder (see Fig. 4.17). In the experiments, only a surge decay of the moored-floating cylinder is reported. The comparison of the time series using numerical grids with $\Delta x = 0.01, 0.0075$ and 0.005 m is presented in the Figs. 4.17a and 4.17b. For all chosen grid sizes, the numerical model captures the first peak well. Numerical damping results in under-prediction of the subsequent amplitude for coarser grids. Similar observations are indicated for the free heave test (Fig. 4.17c). Although the medium grid seems to accurately predict the amplitudes, further refinement is needed for a convergence of the phase. As a consequence, the finest grid size is chosen for further testing.

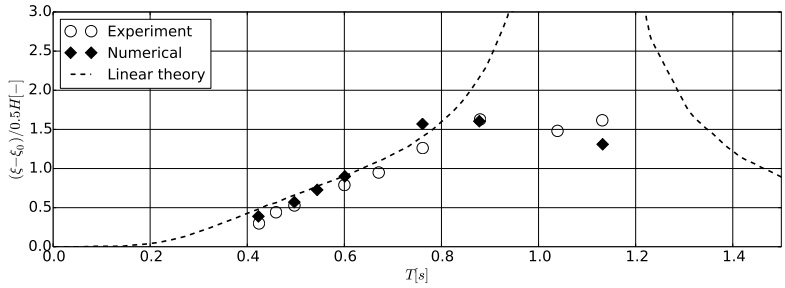

(a) Surge motion.

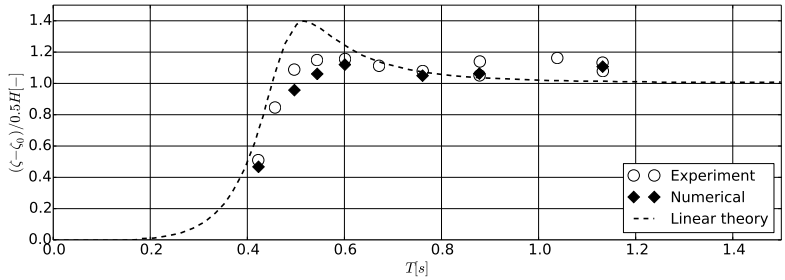

(b) Heave motion.

Figure 4.18: Comparison of the response amplitude operators (RAO) between the numerical model and the experiments for the moored-floating cylinder in regular waves. The linear solution is taken from [66].

Next, the motion responses in surge and heave in regular waves with a constant steepness of $1/14$ are compared. The waves have periods of $0.497, 0.544, 0.601, 0.761$ and 0.878 s and are modelled as 2nd-order Stokes waves in the numerical simulations. A more robust indication of the object's behaviour can be investigated through the amplitude responses over the wave periods as shown in Fig. 4.18. In general, the deviations

are between 5% and 10%. In shorter waves, the surge motion oscillates with the encounter frequency plus a sub-harmonic component at half the frequency. Further, the model follows the linear relation between the wave period and surge amplitude response present for short waves. The object thereby damps the waves almost completely as the wave height in the wake is significantly reduced. The heave motion gradually increases as the waves increase in height. Here, linear theory significantly over-predicts the heave response, whereas the numerical solution agrees well with the experiment. In longer wave periods, the heave response amplitude reaches a value slightly above 1 as the cylinder follows the surface of the long waves. Highly non-linear fluid-structure interaction occurs in these conditions. Around the surge resonance frequency, the numerical model predicts amplitudes close to the experiments, whereas theoretical formulae typically overestimate the response.

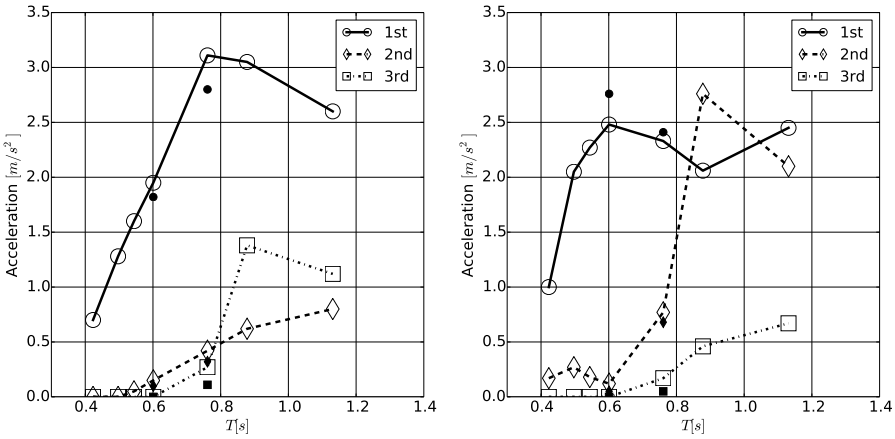

(a) Acceleration amplitudes in surge direction over wave period.

(b) Acceleration amplitudes in heave direction over wave period.

Figure 4.19: Fourier amplitudes of the first three harmonic components of the acceleration obtained from the numerical model for the moored-floating cylinder in regular waves. Experimental results are shown as black markers of corresponding shape.

Further analysis of the wave excitation forces is conducted by comparing the significant amplitude components of the acceleration signal. This is justified by the direct link of acceleration and hydrodynamic load through Newton's second law. The resulting linear, second and third harmonic components of the acceleration amplitudes are provided in Fig. 4.19 using discrete Fourier analyses. In surge direction, the excitation is mainly driven by the linear component. High-order components become more relevant for longer waves, in particular around the surge resonance. This increase might be

caused by wave overtopping and viscous effects due to flow separation. For the vertical accelerations, second-order harmonics exceed the linear part for wave periods between 0.8 s and 1.0 s. It is noticed by Kristiansen [66] that this effect occurs because the second component occurs at a frequency close to the natural heave frequency of the system. As a consequence, the disregard of these high-order components can lead to a significant under-estimation of the loads on and stresses in the structure.

The complexity is further increased by attaching a net to a moored-floating cylinder encountering propagating waves as physically investigated in [5]. A net with solidity 0.23 and sinker weight 1.64 kg is attached at the bottom of the net. Tension forces acting in the topmost twines are reported for regular waves with a wave steepness of $1/14$ and wave periods between 0.4 s and 1.3 s. Fig. 4.20 compares the predicted maximum tension forces with the experimental data. For small waves, the maximum tension forces are of similar magnitude as in a hydrostatic fluid due to the small motion of the cylinder in these waves. As the wave height increases and the wave period approaches the eigenperiod of the system, the maximum tension forces are approximately five times higher than in the hydrostatic condition and snap loads occur. These loads arise from the relative motion between the cylinder and sinker. Typically, when the cylinder is in a wave trough, the maximum elongation of the net reduces and the net becomes slack (see Fig. 4.21a). When the wave trough passes and the cylinder is accelerated upwards by the following wave crest, the net accelerates but its motion is restricted by the sinker mass. Thus, a large force is observed in the net which might lead to damage to the net in practice. The behaviour of the system changes for very long waves. Here, both the cylinder and the sinker follow the curvature of the waves, and the occurrence of snap loads becomes less likely. The numerical model quantitatively agrees very well with the experimental data in short and long waves. The snap loads tend to be over-predicted by up to 15%.

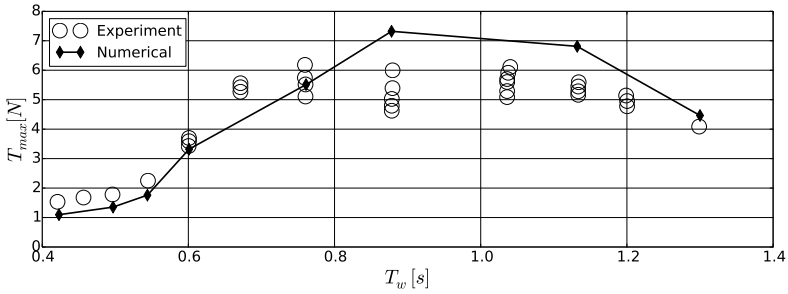

Figure 4.20: Comparison of the numerical and experimental maximum tension forces in the topmost twines over the wave period T_w for the moored-floating cylinder with net in regular waves.

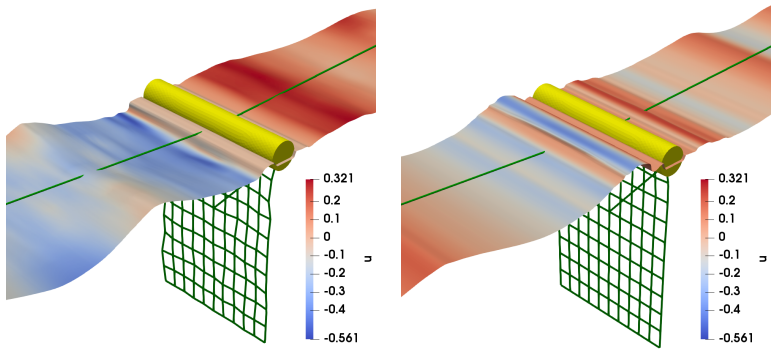

(a) Wave trough situation with slack net. (b) Wave crest situation with a taut net.

Figure 4.21: Two typical situations during the simulation of a moored-floating cylinder with net in a regular wave with $T = 0.761$ s. Colours show velocity on free surface in x-direction.

4.5 Paper 4: Application to the simulation of a semi-submersible OOA structure in regular and irregular waves

Semi-submersible offshore fish cages are characterised by being attached to a pre-tensioned mooring system which holds the structure in place but also influences the seakeeping properties of the system. Therefore, the accurate prediction of the dynamic responses to a variety of sea states is of importance and exemplarily investigated for a structure in the style of Ocean Farm 1 adapted from [125]. The structure is assumed to be rigid and consists of 8 pontoons with straight columns attached. The columns are connected at three different heights via additional thinner columns so that a hexadecagon with a diameter of approximately 1 m is formed. An additional pontoon and column is placed in the middle of the structure slightly below the others and connected to the other columns with thin pipes. In comparison to the model of Zhao et al. [125], the thinnest pipes are not considered because of their negligible contribution for the loading and minor influence on the fluid. The draught of the model is 0.28 m in the simulations and reached by adjusting the overall mass of the structure and a free heave decay test. Uniform mass distribution is then assumed to calculate the moments of inertia for the rotational motions of the structure. A characteristic of this semi-submersible OOA design is that the net is fastened more tightly to the structure than in traditional aquaculture cage systems [27]. As a consequence, the deformation of the net is neglected in the

numerical model. The external forces on the net are added to the rigid body solver and used for determining the shading effect as before. The net covers the complete structure and is assembled using a cylinder for the side walls and a cone for the bottom. Each part of the net consists of twines with a length of 8 mm and thickness of 0.6 mm resulting in a solidity of 0.145.

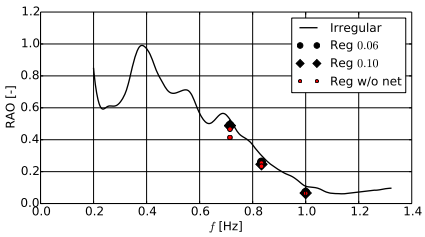

(a) Heave motion.

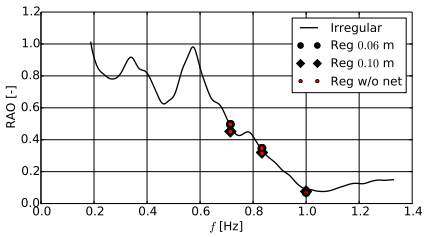

(b) Surge motion.

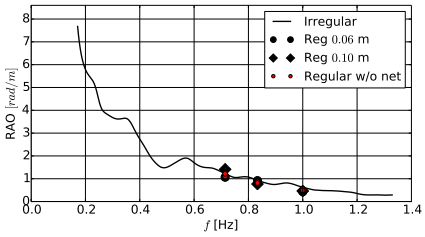

(c) Pitch motion.

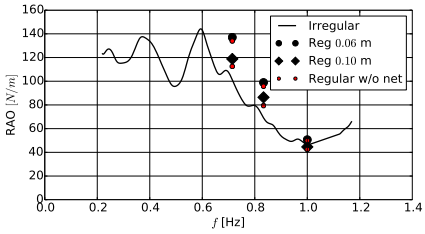

(d) Maximum front line tension forces.

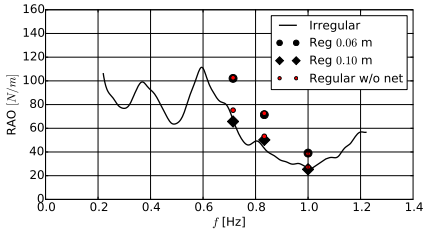

(e) Maximum aft line tension forces.

Figure 4.22: RAO of the semi-submersible OOA structure using regular and irregular wave input. For comparison, the motions without considering the net are shown in red.

A mooring system is attached to the structure for the simulations in waves. The experimental setup includes four mooring lines, each consisting of a rope with a linear spring at the end. The stiffness of the lines is calculated as 195 N/m based on the

reported relation between force and line elongation. Further, the pretension is set as 1.91 N. A grid with $\Delta x = 0.008$ m around the structure is conducted for the simulations including waves after performing the convergence test for the decay motion of the structure (see [79]). The grid points outside the inner box are stretched at a ratio of 1.02 towards the domain boundaries until the maximum grid point distance of 0.05 m is reached. The resulting grid has 16 M points. The simulations include regular waves with height $H = 0.06$ m, 0.1 m and period $T_w = 1.0\ s, 1.2\ s, 1.4\ s$, which are taken from the experiment. Additional simulations without the net are conducted to study the importance of the net for the motion of the structure. Further, the response of the structure in irregular waves is simulated to gain a deeper understanding of the structural response. Several JONSWAP spectra with a significant wave height of 0.1 m and peak periods between 0.5 s and 3.5 s are chosen for this purpose. Each spectrum is generated by superposing multiple linear wave components as described in [3]. Power and cross power spectra are calculated using an FFT analysis, and the linear transfer functions (RAO), as well as the coherences γ, are subsequently determined. The results of the simulations are shown in Fig. 4.22 as the response amplitude operators of the structure and maximum front and aft mooring line forces.

As shown in Fig. 4.22a, the heave amplitude increases with decreasing wave frequency and increasing wave amplitude. The maximum heave response is expected at $f = 0.4$ Hz. Further, the results indicate a highly damped system as the response to high-frequency excitations is small [41]. Similar observations can be stated for the surge motion in Fig. 4.22b. The surge motion increases non-linearly with decreasing wave frequency and approaches values closer to one in very long waves with $f < 0.6$ Hz as the structure increasingly follows the wave envelope. Also, the regular wave tests reveal larger surge motion for steeper waves due to increased wave energy. Here, the net plays a minor role as the motion without the net shows similar amplitudes. However, the horizontal forces on the net account for about 30% of the total horizontal forces on the system. This indicates that the horizontal forces are generally small, amongst others caused by the low solidity of the net, and that the surge response of the system is mainly dominated by the mooring system. This possible explanation is substantiated by observing the free surface travelling through the structure in Fig. 4.23. The fluid is accelerated along and wakes are developed behind each member of the structure. In contrast, the damping effect of the net is not visible.

For the rotational motion of the structure (Fig. 4.22c), a strong increase of the pitch amplitude indicates a possible resonance close to the lowest investigated wave frequencies. The response in pitch is relatively small for wave frequencies larger than 0.6 Hz compared to the translational motions. This might be caused by a rather horizontally than vertically acting mooring system. The maximum tension forces in the front and aft mooring lines increase naturally with increased structural motion and reach local maxima close to the maxima of the heave and surge responses. This strengthens the

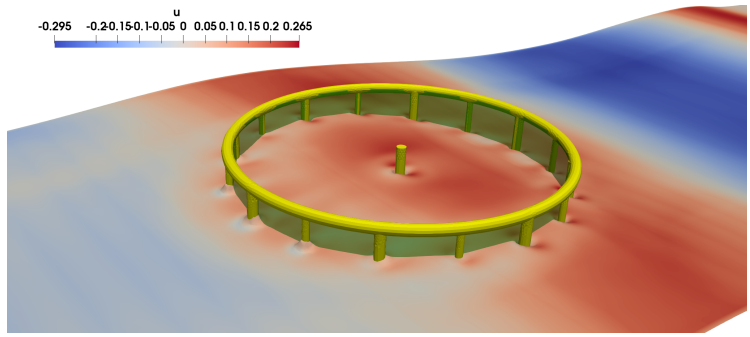

Figure 4.23: Free surface contour showing x-velocities in a wave crest situation for the simulation of the semi-submersible OOA structure in a regular wave with height 0.1 m and period 1.4 s.

argument that mooring reaction forces are the driving excitation forces for the dynamics of the OOA structure. Generally, the front line forces are larger than the forces in the aft due to the undisturbed impact of the wave loads. The difference between the front and aft forces tends to increase with larger encountered wave periods, whereas the wave steepness mostly affects the aft mooring line as steeper waves travel less disturbed through the upper part of the structure. Further, the simulations without the net reveal that the aft forces tend to decrease if the net is present, as already observed experimentally. This might be caused by the shielding and damping effect of the net. Generally, it is noticed that the results from the regular wave tests mostly coincide with the irregular test results, which indicates that both wave inputs are valid approaches to determine the response of OOA structures.

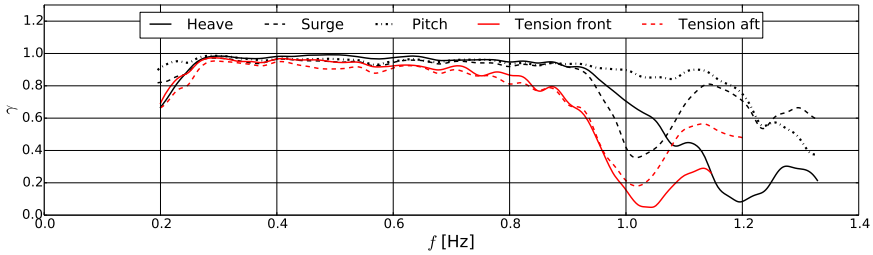

Figure 4.24: Coherence of the semi-submersible OOA structure using irregular wave input.

The obtained transfer functions are based on the assumption that the considered system is linear. The coherences for the motions and tension forces are presented in

Fig. 4.24 to investigate the validity of this assumption. The shown distributions hint at a linear system for wave frequencies between 0.3 Hz and 0.8 Hz because γ is close to unity. The translational motions tend to become non-linear at smaller frequencies than the pitch motion which has a coherence close to one up to $f = 1.1$ Hz. The strongest non-linear effects, caused by the coupling to the wave loads and all degrees of freedom, are expected for the tension forces.

4.6 Paper 4 & 5: Application to the simulation of a mobile floating OOA structure in current and waves

As a second application, the mobile floating offshore aquaculture facility Havfarm 2, developed by Nordlaks and NSK Ship Design [84], is investigated. The main structure is represented by a large, slender ship-shaped hull with several net cages attached (Fig. 4.25). The design process faces challenges due to the complex interaction of multiple nets with the fluid and the resulting water quality change in the cages. The quality is expected to improve with increasing discharge through each net. For this purpose, Havfarm 2 is equipped with a dynamic positioning (DP) system which can change the heading angle between incident flow and structure. However, this increases the external loads which have to be withstood by all components involved. The DP system will be further applied to vary the location of the farm, dependent on the sea state and weather forecast. Hence, the manoeuvrability of the farm and thus, the prediction of global forces is important for the operation of Havfarm 2.

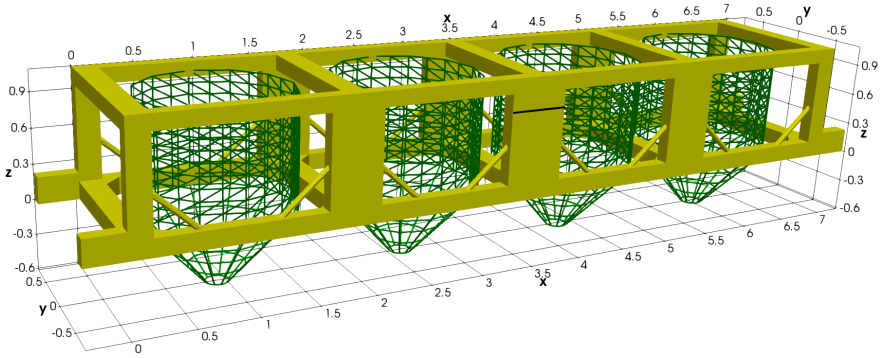

Figure 4.25: Geometry of the floating OOA structure. Rigid structure in model scale 1:40 is shown in yellow and nets in green. The design draft is indicated by the black line at the centre column. All measures are in metres.

Model tests were performed in the ocean basin of SINTEF Ocean, Trondheim, Norway, in a 1 : 40 model scale to investigate the fluid-structure interaction experimentally. Amongst others, towing tests with different heading angles between the structure and towing direction were conducted and are taken as a reference here. The prototype of Havfarm 2 consists of multiple rectangular beams forming four equally sized box-shaped spaces. In each of these, a cylindrical net with solidity 0.22 is tightly fastened to the rigid structure. They are simulated as non-deforming nets moving with the rigid structure as explained above. Further, a flexible conical net with the same solidity is attached to the bottom of each cylinder, which requires dynamic modelling. A sinker weight of 2 kg is pre-tensioning this part of the net during the towing tests.

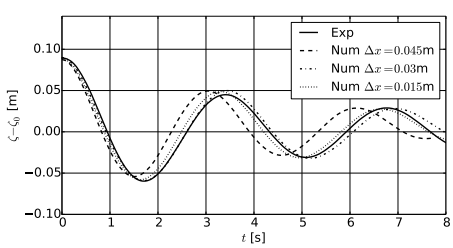

(a) Time series of the heave decay test.

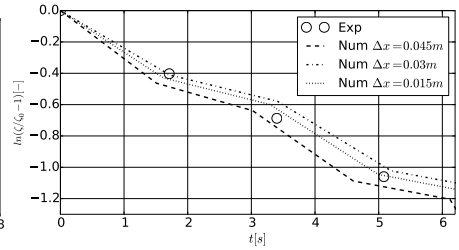

(b) Decay rate for the heave decay test.

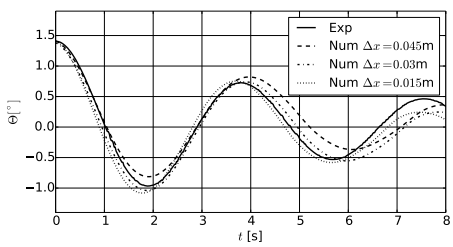

(c) Time series of the pitch decay test.

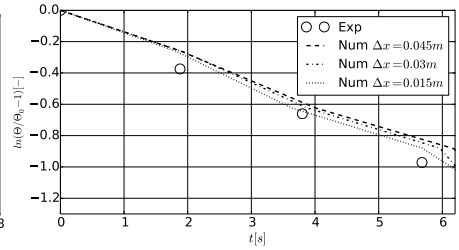

(d) Decay rate for the pitch decay test.

Figure 4.26: Numerical and experimental results for the free decay tests of the floating OOA structure.

Prior to this, a grid convergence study is conducted using the decay tests in pitch and heave. A refinement box with a uniform grid size of $\Delta x = \Delta y = \Delta z = 0.045, 0.03$ and 0.015 m is placed in a rectangular domain of $15 \times 10 \times 10$ m. The chosen domain size is justified by placing numerical beaches at all domain boundaries to absorb the energy induced by the structural motion. The water height is 8 m. The grid size is gradually coarsened towards the domain boundaries with a ratio of 1.1. The OOA structure including the attached nets is placed in the centre of the refinement box with an initial

displacement of $\Delta z = 0.09$ m for the heave decay test and $\Delta\Theta = 1.4^\circ$ for the pitch decay test. Small displacements of the other degrees of freedom in the model tests are respected in the simulations as well.

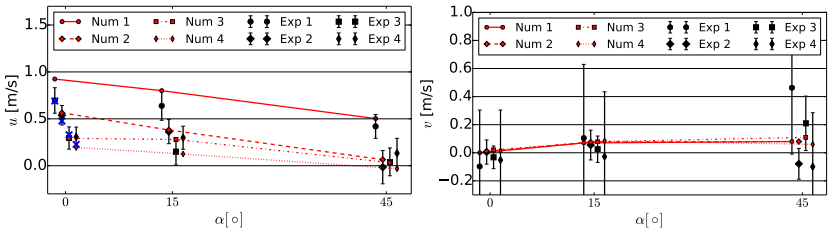

(a) Velocities in x-direction for $u_\infty = 0.83$ m/s. (b) Velocities in y-direction for $u_\infty = 0.83$ m/s.

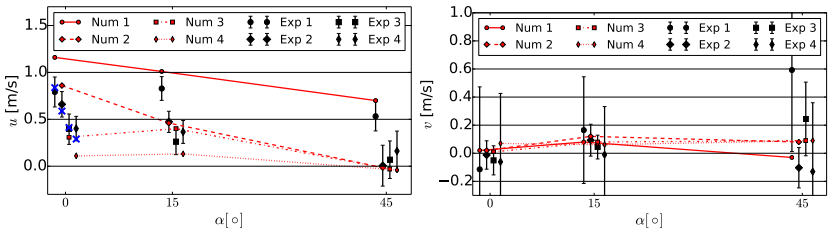

(c) Velocities in x-direction for $u_\infty = 1.0$ m/s. (d) Velocities in y-direction for $u_\infty = 1.0$ m/s.

Figure 4.27: Numerical and experimental results for the mean velocities inside the cages for different inflow velocities u_∞ and angles of attack $\alpha = 0^\circ, 15^\circ$ and 45°. Cage 1 is in the front and cage 4 in the back. The bars indicate the variation of the measurements in terms of one standard deviation. Additionally, theoretical results for $\alpha = 0^\circ$ using the formula of Løland [75] are indicated in blue.

The time series of the decay tests are compared to the measurements in Fig. 4.26. On the coarsest grid, a too-large heave frequency and a relatively large peak deviation are predicted (see Fig. 4.26a). A grid size of 0.03 m around the structure improves the results, especially for the first peaks. Further convergence of the solution towards the experimental data is seen for the finest grid size. In Fig. 4.26b, the decay rate is plotted as the damping ratio over time. The numerical solution can replicate the measured damping on all grids. Similarly, the time series and decay rate for the simulated pitch decay test is presented in the Figs. 4.26c-4.26d. The pitch frequency converges towards the reported value with decreasing grid size. The first three peaks are captured well with the two finer grids, whereas an under-prediction is present at the last peak. A further refinement might improve the results, but it should also be noticed that the angles itself are already very small in magnitude. Hence, small deviations in the setup can have

significant effects on the results. It is further noticed that small differences between the numerical and experimental geometry exist because of the neglect of very thin bracings. As for the heave decay test, the decay rate is predicted well by the numerical model, and the convergence of the results with increasing grid size is visible. Based on these results, a grid size of 0.03 m is chosen around the structure for the analyses below.

The box is placed in the middle of a tank of the dimensions $30 \times 20 \times 10$ m with a smooth growth of the grid size towards the boundaries. The water depth is chosen as 8.0 m to avoid interaction with the bottom of the domain. Constant inflows of 0.83 m/s and 1.0 m/s are predefined at the inlet and the flow freely leaves the tank at the outlet. The structure is rotated relative to the inlet with heading angles of $0°, 15°$ and $45°$. The structure can freely heave, roll and pitch during the simulations. However, the motions are not investigated further because the heave motion remains small and the rotational motions are below $1.0°$ for all cases.

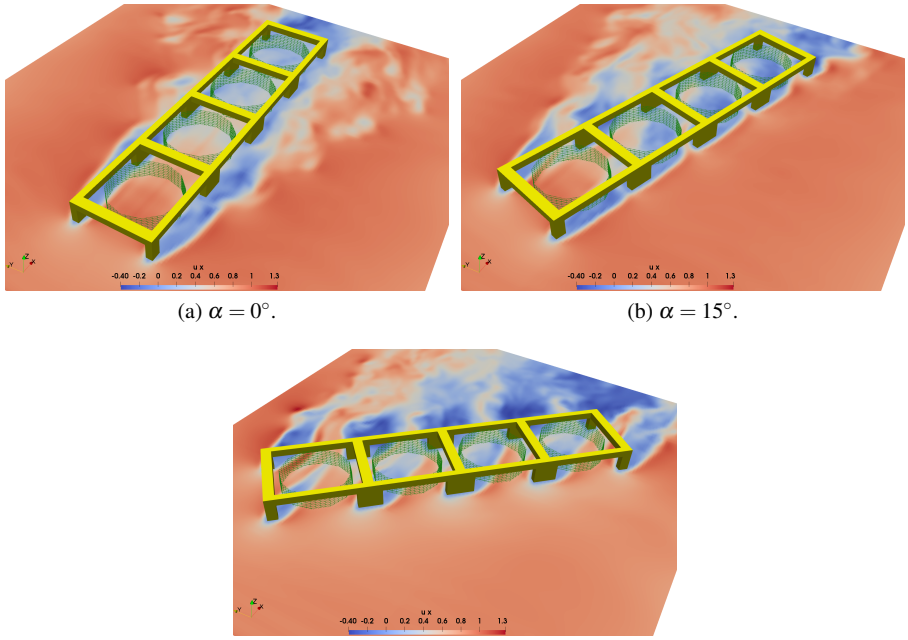

(a) $\alpha = 0°$.

(b) $\alpha = 15°$.

(c) $\alpha = 45°$.

Figure 4.28: Slices of the x-y plane at $z = 7.9$ m for the simulation of the floating OOA structure with different angles of attack α and $u_\infty = 0.83$ m/s. The contours show the velocity in x-direction.

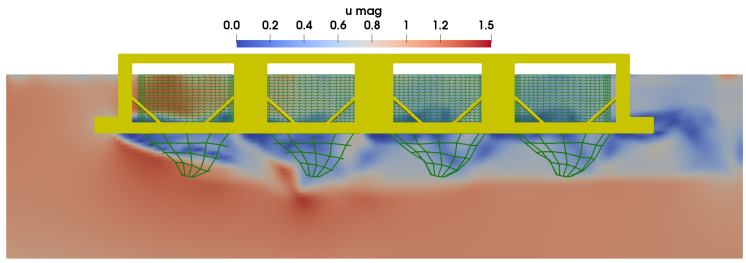

(a) $\alpha = 0°$.

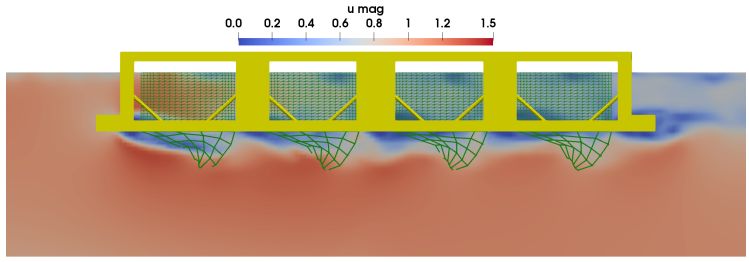

(b) $\alpha = 15°$.

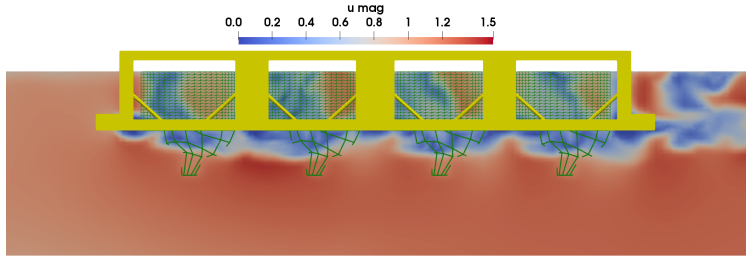

(c) $\alpha = 45°$.

Figure 4.29: Slices in the centre x-z plane along the longitudinal axis of the floating OOA structure for different angles of attack α and $u_\infty = 1.0$ m/s. The contours show the velocity magnitudes.

The mean velocities inside each net, 0.1 m below the free surface, are computed and compared to the experimental data in Fig. 4.27. The measurements showed large oscillations for which reason the variations are included in terms of one standard deviation. Additionally, slices of the x-y plane around the structure at this height are shown in Fig. 4.28 to reach a further understanding of the results. It is at first noticed that the computed x-velocities are mostly within the chosen interval of the experimental results. The values also coincide well with the theoretical formula for the velocity reduction through

net panels by Løland [75]. This formula is however limited to the case of $\alpha = 0°$. For the front cage and small heading angles, the simulations predict an accelerated flow resulting in velocities higher than the inflow velocities. This is also visible in the Figs. 4.28a and 4.28b, where the two vertical beams in the front form a narrow channel passed by the flow. At these angles, the shading effects of the nets result in decreasing velocities in the cages behind. The flow separation at each beam becomes increasingly important for the flow field in each cage with increasing angles (see Fig. 4.28c). At large heading angles, the interaction between the cages becomes less significant. Thus, the differences between the predicted velocities in the different cages as well as the x-velocities itself become small as shown both experimentally and numerically. The mean y-velocities are generally smaller than the mean x-velocities, and the fluid oscillates more in this direction, especially for the front cage and large heading angles. A possible physical explanation is the development of an oscillating wake behind each beam. This causes the recirculation zones passing the probe points in the centre of each cage periodically.

The analysis of the velocity inside the upper part of the cages reveals that the intended improvement of water quality through increased discharge cannot be achieved by increasing the heading angle. However, this changes for the lower, flexible part of the cage. Fig. 4.29 shows the velocity distribution in the centre x-z plane along the longitudinal axis of the structure for different angles of attack α. As expected, the shading effect of the nets causes the increasing deceleration of the flow along the structure for $\alpha = 0°$ (see Fig. 4.29a). Thus, a lower discharge and less deformation are predicted for the cages in the back. By increasing the heading angle (Figs. 4.29b and 4.29c), the flow in front of each cage is less disturbed by the wake of cages placed in the front. As a result, similar deformation and discharge are predicted for all cages which consequentially indicates improved water quality in the back cages.

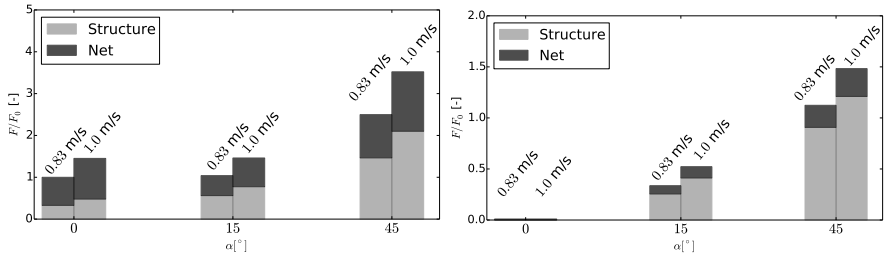

(a) Forces in x-direction.

(b) Forces in y-direction.

Figure 4.30: Numerically predicted mean forces for the floating OOA structure. Values are normalised using the total forces in x-direction for $u_\infty = 0.83$ m/s.

The water quality control through the rotation of the structure has the drawback of increased loads. In order to quantify this, Fig. 4.30 presents the loads on the net and the structure in x- and y-direction for the different cases. In general, the forces increase with increasing inflow velocity. Also, the loads on the nets are generally more crucial to consider in x- than in y-direction and are even dominant at small heading angles in x-direction. The increase of the loads on the nets is further less dependent on the heading angle than the rigid structure forces. This is caused by the symmetry of the cage geometry in comparison to the changing structural area exposed to the undisturbed inflow. Thus, the structural forces become the dominant factor for large heading angles. The same conclusion can be drawn in y-direction (Fig. 4.30b). The increase for larger heading angles is caused by the increased area but might also be influenced by intensified vortex shedding.

Table 4.4: Measured mean frequencies for the motion of the OOA structure in waves. G1 and G3 are the two wave gauges. All measured values in Hz.

$H[m]$	f	α	$G1$	$G3$	$Surge$	$Heave$	$Roll$	$Pitch$	Yaw
0.1125	0.421	0	0.424	0.424	–	0.424	–	0.425	–
0.1125	0.421	15	0.424	0.424	–	0.425	0.425	0.424	0.425
0.1125	0.421	45	0.424	0.424	0.425	0.425	0.425	0.425	0.424
0.1125	0.294	0	0.291	0.291	0.291	0.291	–	0.291	–
0.1125	0.294	15	0.291	0.292	0.294	0.291	0.293	0.291	0.291
0.1125	0.294	45	0.292	0.291	0.293	0.291	0.294	0.293	0.294

Table 4.5: Numerically calculated main frequencies for the motion of the OOA structure in waves. G1 and G3 are the two wave gauges. All measured values in Hz.

$H[m]$	f	α	$G1$	$G3$	$Surge$	$Heave$	$Roll$	$Pitch$	Yaw
0.1125	0.421	0	0.422	0.422	–	0.419	–	0.421	–
0.1125	0.421	15	0.422	0.422	–	0.424	0.421	0.422	0.422
0.1125	0.421	45	0.421	0.422	0.421	0.420	0.421	0.420	0.422
0.1125	0.294	0	0.293	0.294	0.293	0.294	–	0.294	–
0.1125	0.294	15	0.293	0.294	0.295	0.294	0.292	0.293	0.295
0.1125	0.294	45	0.293	0.294	0.293	0.294	0.293	0.294	0.294

Next, the dynamic response of the OOA structure in waves is investigated. Two regular waves with a height of $H = 0.1125$ m and the frequencies of $f = 0.421$ Hz (wave 1) and $f = 0.294$ Hz (wave 2) were considered in the experiment. A numerical wave tank is established to reproduce the physical setup (see Fig. 4.25). At the inlet, a relaxation zone [11] is defined to generate the waves as second-order Stokes waves.

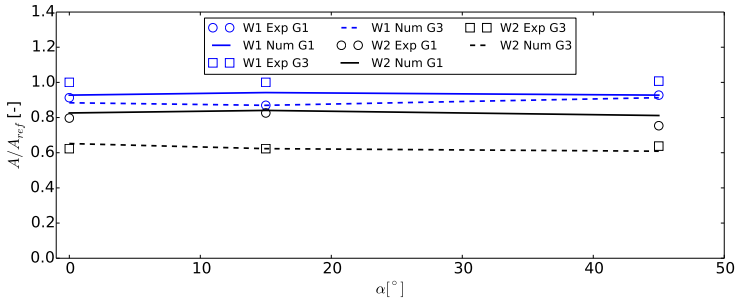

(a) Wave amplitude at the two wave gauges.

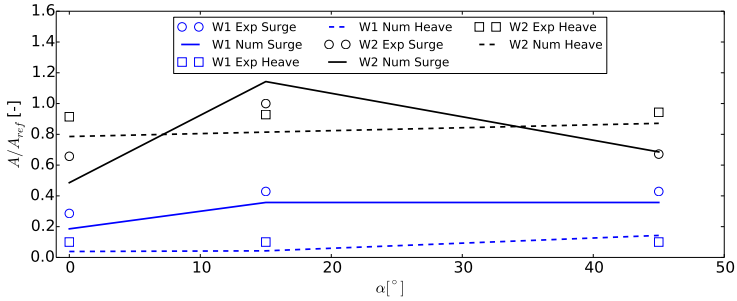

(b) Amplitudes of the translational motions.

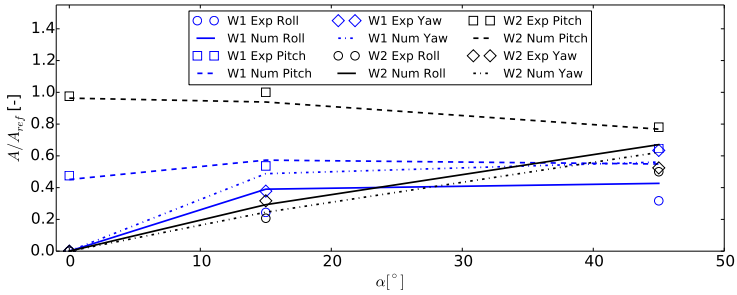

(c) Amplitudes of the rotational motions.

Figure 4.31: Numerical and experimental results for the mean wave amplitudes and mean response amplitudes for different heading angles α. The amplitudes are calculated using a FFT and normalised with the largest measured amplitude. The two wave inputs are indicated in blue (wave 1) and black (wave 2).

A numerical beach at the end of the tank damps the waves such that reflections can be avoided. The structure is placed in the middle of the tank with heading angles between

0 and 90°. Four mooring lines are horizontally attached to the sides of the structure to keep the structure in the centre of the tank. The lines are modelled as springs with predefined pre-tension in accordance with the experimental setup.

At first, the waves are validated at two different wave gauges. G1 is located 1.5 m in front of the structure and G3 is located 1.5 besides the centre of the structure. The measured frequencies are summarised in the Tabs. 4.4 and 4.5, and the amplitudes can be found in Fig. 4.31a. The model tests measure a minor increase of the frequency for the short wave and a minor decrease in the frequency for the long wave. In contrast, the simulation predicts wave frequencies very close to the input signal. The maximum deviation is less than 1%. Similar accuracy is achieved for the amplitudes except for the short wave at G3 were an under-prediction of about 7% is present.

The translational motions surge and heave, as well as the rotational motions around all three axes, are considered next. The frequencies can be found in Tabs. 4.4 and 4.5, whereas the Figs. 4.31b and 4.31c compare the amplitudes obtained from a FFT analysis of the time series signal. The simulated results show motion frequencies close to the wave frequency and the experimental results. Further, the heave and surge amplitudes are larger for the longer wave which has a wavelength of twice the structural length. Generally, a good agreement between experimental and numerical results can be stated for the translational motions with deviations of less than 15% for all cases.

The amplitudes of the rotational motions are presented in Fig. 4.31c. The largest rotations are observed around the y-axis (pitch) with up to 0.8°. Pitch is also larger in the long wave because the wave crest reaches the front of the structure while at the same time a wave trough is present at the aft. In comparison, two wave crests are at both ends of the structure in the shorter wave with a wavelength similar to the structure (compare Fig. 4.32). The pitch motion tends to decrease with increasing heading angle due to the shortening of the structural dimensions in wave direction. In contrast, the rotations around the body fixed x- and z-axis increase with α due to the same reason. In general, the numerical model agrees well with the experiments at small heading angles as the deviations are below 5%. Larger differences are observed for the roll motion at $\alpha = 45\%$ (about 15%) which might be caused by a slightly different attachment position of the mooring lines in the experiments.

Finally, the mean force amplitudes of the four different nets are analysed in Fig. 4.33. No experimental data is available for this property. If no heading angle is present, the forces are largest in x-direction whereas the forces in y-direction are close to zero. Despite the circular motion of the fluid particles in the given waves, the forces in z-direction are smaller due to the small bottom surface of the net compared to the vertical surfaces. Also, the forces are larger in the short wave than in the long wave. This might be due to the smaller structural motions in wave 1 leading to a more direct inflow into the cages. The force magnitudes tend to decrease with increasing heading angles due to a stronger blockage effect through the rigid structure. It is further noticed that no

clear pattern of the force direction and magnitude can be found for the different net cage positions. This indicates that the structural motion, including its blockage effects at different heading angles, has an important effect on the expected net forces, whereas the shielding effect of the nets plays an insignificant role for the nets in the aft of the OOA structure.

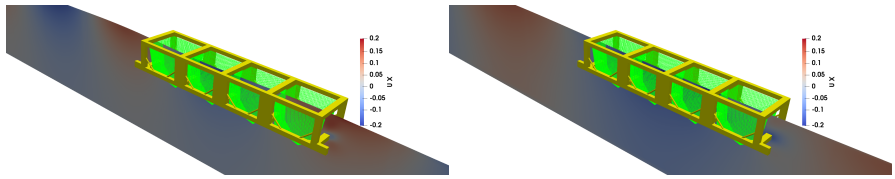

(a) Short wave (wave 1). (b) Long wave (wave 2).

Figure 4.32: X-velocity profiles under the free surface in the plane through the centre of the structure for $\alpha = 15°$ and the two different wave inputs. The waves propagate from the left to the right.

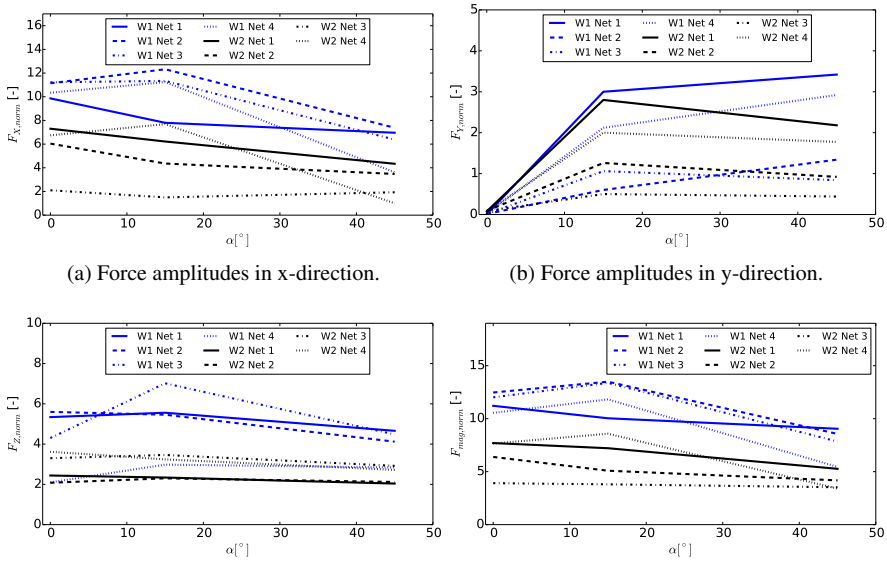

(a) Force amplitudes in x-direction. (b) Force amplitudes in y-direction.

(c) Force amplitudes in z-direction. (d) Force magnitude amplitudes.

Figure 4.33: Numerical results for the mean net force amplitudes for different heading angles α. The results are normalised with the smallest force in x-direction at net 4.

Chapter 5

Concluding remarks

In this thesis, a new numerical framework for modelling elastic porous and floating structures in viscous two-phase flows was developed and applied to open ocean aquaculture. It is based on the solution of the incompressible Reynolds-averaged Navier-Stokes equations using the finite difference method and the level set method to account for the propagating free surface. A new mooring model for constraining the motion of floating structures was presented. It is based on quasi-static assumptions and a discretisation into elastic bars and mass points connecting them. The introduction of successive approximation for this problem raised the possibility to converge to a physically relevant solution within a small number of iterations. Any restriction on time-stepping was removed and no initial shape of the line is necessary. It is noticed that this approach converges towards a simple spring model for completely taut mooring lines. In case of bottom contact, the coupling to a catenary solution is recommended. An implicit structural model was derived for the arbitrary deformation of porous tensile structures with a non-linear material law. For this purpose, Newton's second law was solved for the unknown tension forces at knots presenting the lumped mass of the structure. Elastic bars connecting the knots enabled the correct distribution of tension forces within nets used in aquaculture. A new approach for calculating the fluid loads on the structure was proposed as the structure is not directly resolved in the fluid. Here, fluid properties were interpolated on the structural domain using a kernel function, and the hydrodynamic forces were approximated using a screen force model. High-order backward finite differences were included to approximate the structural motion. Finally, a single matrix-vector problem arose which was solved using an accelerated Newton's method. In contrast to existing explicit algorithms, the implicit time and deformation handling increase stability and effectively remove strong time step restrictions from the fluid solver. Two-way coupling between fluid and net structure was provided by including the loss of fluid momentum, due to passing the porous sheet, in the Navier-Stokes equations using a forcing term. It was determined from a kernel integration of the hydrodynamic and body forces over multiple Lagrangian points which follow the structural deformation. This represents

an innovative extension of the classical forcing approach for porous and hydrodynamic transparent structures. Also, the issue of transferring existing force models to coupled numerical simulations was discussed for the first time. The coupling process influences the flow velocity at the net which had to be corrected to match the undisturbed velocity used for computing force coefficients. An intrinsic formula was derived to couple these velocities using Froude's momentum theory.

The different modules were validated individually and combined to evaluate their accuracy and practicability. The mooring model was validated against experiments of static line distributions, dynamic motion of tensed lines and the response of a moored-floating barge. The accuracy of the model was assessed, and the applicability as well as efficiency was highlighted. The numerical coupling algorithm was extensively validated against existing experiments for fixed net panels, multiple panels and cages with varying geometries and solidities in current and regular waves. For all cases, both qualitative and quantitative analysis were performed. Overall, the proposed model performed reasonably for all presented cases because deviation bands of less than 10% could be achieved regularly and physical explanations were given elsewhere. Elastic porous sheets and cylinders with varying geometries and solidities in current and regular waves were validated afterwards. Deviation bands of less than 10% were regularly achieved which indicates a proper calculation of the loads, the wake velocity field and the structural response. Benchmark tests were performed in order to determine the accuracy of the FSI solver. A moored-floating cylinder was analysed in waves, and important non-linearities in the response of the system could be captured in comparison to traditional linear methods. Finally, the complete numerical framework was applied to OOA structures in waves and current. The response of a semi-submersible OOA structure in regular and irregular waves was investigated. Here, the importance of incorporating the net into the investigation for larger wave heights and periods, due to the increased wave energy and the non-linear growth of the drag forces on the net, could be shown. Another application concentrated on the flow around a mobile floating OOA structure in steady current flow and long waves. The numerical study revealed that the considered structural design resulted in complex flow patterns with separation and recirculation zones interacting with the upper part of the cages which complicates the proper adjustment of the discharge through the cages by changing the heading angle.

Thus, the proposed framework enables the study of the effects of waves and current on the motion of OOA systems taking into account the fluid-structure interaction around and inside the cages, the motion of the rigid structure as well as the deformation of the net. Here, the important interactions of floating structures, mooring, nets and fluid are incorporated as two-way coupling problems.

The proposed CFD-based framework can be further advanced within future work:

- Several modules of the proposed framework were verified in the enclosed articles. However, particularily the complete numerical framework as a whole has to be verified and further validated.

- The validation process indicates a possible limitation of the screen force model for nets with small twine lengths due to its assumptions. In particular, the applicability of the strip theory on each twine and the derived formula for the characteristic cross-flow velocity at the twines (see [34]) might have a constraint which has to be discussed further.

- The RANS turbulence model from [11] is used to account for turbulence in this thesis, and the validation process indicates that this choice is appropriate for the correct modelling of mean quantities such as loads and velocity reduction. However, it is observed in measurements inside and behind fish cages [64] that increased cross-flow and thus cross-flow forces are to be expected. Further, it is postulated that larger vortices are decomposed while passing the physical net which might reduce the turbulent kinetic energy through dissipation. Thus, a dissipation term would have to be included in a RANS model to account for this effect. At the same time, a reconnection of eddies in the wake-field is possible so that a counteracting production term is necessary to account for the increased turbulence in the vortex streets behind the twines. The quantification of these effects and their inclusion in the numerical framework is initiated in forthcoming studies [46].

- The Fourier coefficients of the proposed hydrodynamic force model are based on a non-linear regression of available experimental work. As an alternative, CFD simulations can be conducted at a case to case level in order to improve the prediction of the drag and lift forces for the specific geometrical properties of each net and in specific fluid conditions. This simulation-based screen force model is currently developed in the research group [45].

- The new algorithm to model the effect of nets on the fluid dynamics can also be applied to model the interaction of fluid and slender elastic structures such as mooring lines, pipes or vegetation. This requires an additional model to account for the large deformation of flexible structures with bending and torsion stiffness. The author of this thesis initiated this development in a forthcoming publication [78].

- A more realistic representation of OOA structures should include the biomass to study their effect on the fluid and structural dynamics. Kleber and Su [64] recently concluded from physical measurements that the fish reduce the velocity magnitudes but do not play a significant role for the expected flow patterns or turbulence rates in and behind the cages. A starting point for the detailed simulation of single fish could be the recent work of Patel et al. [88], whereas the inclusion of the complete shoal would require some surrogate modelling such as a Lagrangian particles and deforming porous media.

Bibliography

[1] O.M. Aamo and T.I. Fossen. “Finite Element Modelling of Moored Vessels”. In: *Mathematical and Computer Modelling of Dynamical Systems* 7(1) (2001), 47–75.

[2] C.M. Ablow and S. Schechter. “Numerical Solution of Undersea Cable Dynamics”. In: *Ocean Engineering* 10 (1983), 443–457.

[3] A. Aggarwal et al. “Characteristics of breaking irregular wave forces on a monopile”. In: *Applied Ocean Research* (2019). DOI: 10.1016/j.apor.2019.06.003.

[4] M. Alagan-Chella et al. “Breaking characteristics and geometric properties of spilling breakers over slopes”. In: *Coastal Engineering* 95 (2015), 4–19.

[5] M. Bardestani and O.M. Faltinsen. “A two-dimensional approximation of a floating fish farm in waves and current with the effect of snap loads”. In: *Proceedings of the ASME 2013 32nd International Conference on Ocean, Offshore and Arctic Engineering* (2013).

[6] P.A. Berthelsen and O.M. Faltinsen. “A local directional ghost cell approach for incompressible viscous flow problems with irregular boundaries”. In: *Journal of Computational Physics* 227 (2008), 4354–4397.

[7] C.-W. Bi et al. “A numerical analysis on the hydrodynamic characteristics of net cages using coupled fluid–structure interaction model”. In: *Aquaculture Engineering* 59 (2014), 1–12.

[8] C.-W. Bi et al. “Experimental investigation of the reduction in flow velocity downstream from a fishing net”. In: *Aquaculture Engineering* 57 (2013), 71–81.

[9] C.-W. Bi et al. “Numerical simulation of the interaction between flow and flexible nets”. In: *Journal of Fluids and Structures* 45 (2014), 180–201.

[10] H. Bihs and A. Kamath. “A combined level set/ghost cell immersed boundary representation for floating body simulations”. In: *Int. J. Numer. Meth. Fluids* 83 (2017), 905–916.

[11] H. Bihs et al. “A new level set numerical wave tank with improved density interpolation for complex wave hydrodynamics”. In: *Computers & Fluids* 140 (2016), 191–208.

[12] H. Bihs et al. “Breaking-wave interaction with tandem cylinders under different impact scenarios”. In: *Journal of Waterway, Port, Coastal, and Ocean Engineering* 142(5) (2016).

[13] H. Bihs et al. “Complex geometry handling for a cartesian grid based solver”. In: *MekIT, Ninth national conference on Computational Mechanics* (2017).

[14] I. Borazjani et al. “A parallel overset-curvilinear-immersed boundary framework for simulating complex 3D incompressible flows”. In: *Computers & Fluids* 77 (2013), 76–96.

[15] J.U. Brackbill, D.B. Kothe, and C. Zemach. “A Continuum Method for Modeling Surface Tension”. In: *Journal of Computational Physics* 100(2) (1992), 335–354.

[16] Brad Buckham, Frederick R. Driscoll, and Meyer Nahon. “Development of a Finite Element Cable Model for Use in Low-Tension Dynamics Simulation”. In: *Journal of Applied Mechanics* 71 (4) (2004), 476–485.

[17] C.M. Bui, T.X. Ho, and L.H. Khieu. “Numerical study of a flow over and through offshore fish cages”. In: *Ocean Engineering* 201 (2020). DOI: 10.1016/j.oceaneng.2020.107140.

[18] A. Calderer, S. Kang, and F. Sotiropoulos. “Level set immersed boundary method for coupled simulation of air/water interaction with complex floating structures”. In: *Journal of Computational Physics* 277 (2014), 201–227.

[19] J.S. Carlton. *Marine Propellers and Propulsion*. Fourth edition. Butterworth-Heinemann, Oxford, UK, 2019.

[20] P.M. Carrica, R.W. Noack, and F. Stern. “Ship motions using single-phase level set with dynamic overset grid”. In: *Computers & Fluids* 36 (2007), 1415–1433.

[21] H. Chen and E.D. Christensen. “Development of a numerical model for fluid-structure interaction analysis of flow through and around an aquaculture net cage”. In: *Ocean Engineering* 142 (2017), 597–615.

[22] H. Chen and E.D. Christensen. “Investigations on the porous resistance coefficients for fishing net structures”. In: *Journal of Fluids and Structures* 65 (2016), 76–107.

[23] H. Chen and E.D. Christensen. “Simulating the hydrodynamic response of a floater net system in current and waves”. In: *Journal of Fluids and Structures* 79 (2018), 50–75.

[24] H. Chen et al. “Application of an overset mesh based numerical wave tank for modelling realistic free-surface hydrodynamic problems”. In: *Ocean Engineering* 176 (2019), 97–117.

[25] Y. Chenga et al. “Nonlinear analysis for ship-generated waves interaction with mooring line/riser systems”. In: *Marine Structures* 59 (2018), 1–24.

[26] Y.-I. Choo and M.J. Casarella. “Hydrodynamic Resistance of Towed Cables”. In: *J. Hydronautics* 5 (4) (1971), 126–131.

[27] Y.I. Chu et al. “Review of cage and containment tank designs for offshore fish farming”. In: *Aquaculture* (2020). DOI: 10.1016/j.aquaculture.2020.734928.

[28] C. Chun. “Iterative Methods Improving Newton’s Method by the Decomposition Method”. In: *Computers and Mathematics with Applications* 50 (2005), 1559–1568.

[29] J. Davidson and J. Ringwood. “Mathematical modelling of mooring systems for wave energy converters-A review”. In: *Energies* 10 (2017). DOI: 10.3390/en10050666.

[30] J. DeCew et al. “Modeling of dynamic behavior of a single-point moored submersible fish cage under currents”. In: *Aquacultural Engineering* 43(2) (2010), 38–45.

[31] J.M. Domínguez et al. “SPH simulation of floating structures with moorings”. In: *Coastal Engineering* 153 (2019). DOI: 10.1016/j.coastaleng.2019.103560.

[32] E. A. Fadlun et al. “Combined Immersed-Boundary Finite-Difference Methods for Three-Dimensional Complex Flow Simulations”. In: *Journal of Computational Physics* 161 (2000), 35–60.

[33] O.M. Faltinsen. *Sea Loads on Ships and Offshore Structures*. Cambridge University Press, Cambridge, 1990.

[34] O.M. Faltinsen and A.N. Timokha. *Sloshing*. Cambridge University Press, 2009.

[35] FAO. *The State of World Fisheries and Aquaculture 2020. Sustainability in action.* 2020. DOI: 10.4060/ca9229en.

[36] R. Fedkiw et al. “A non-oscillatory Eulerian approach to interfaces in multimaterial flows (the Ghost Fluid Method)”. In: *Journal of Computational Physics* 152 (1999), 457–492.

[37] J.G. Ferreira et al. “Modelling of interactions between inshore and offshore aquaculture”. In: *Aquaculture* (2014), 154–164.

[38] H.M Føre et al. “Loads on net panels with different solidities”. In: *Proceedings of the ASME 2020 39th International Conference on Ocean, Offshore and Arctic Engineering* (2020).

[39] B. Fornberg. “Calculation of Weights in Finite Difference Formulas”. In: *SIAM Rev.* 40 (3) (1998), 685–691.

[40] A. Fredheim. *Current Forces on Net Structures*. Ph.D. thesis, NTNU Trondheim, Norway. 2005.

[41] D.W. Fredriksson et al. “Fish cage and mooring system dynamics using physical and numerical models with field measurements”. In: *Aquacultural Engineering* 27 (2003), 117–146.

[42] D.W. Fredriksson et al. “Moored fish cage dynamics in waves and currents”. In: *IEEE Journal of Oceanic Engineering* 30(1) (2005), 28–36.

[43] S.X. Fu et al. “Hydroelastic analysis of flexible floating interconnected structures”. In: *Ocean Engineering* 34 (2007), 1516–1531.

[44] S. Fu et al. “Experimental investigation on hydrodynamics of a fish cage floater-net system in oscillatory and steady flows by forced oscillation tests”. In: *Journal of Ship Research* 58(1) (2014), 20–29.

[45] W. Gang et al. “An improved screen force model based on CFD simulations of the hydrodynamic loads on knotless net panels”. In: *Applied Ocean Research* Under review (2020).

[46] W. Gang et al. “Modelling the flow around and wake behind net panels using Improved Delayed Detached Eddy Simulations”. In: *Ocean Engineering* Under review (2020).

[47] D. L. Garrett. “Dynamic Analysis of Slender Rods”. In: *Journal of Energy Resources Technology* 104(4) (1982), 302–306.

[48] DNV GL. *Global performance analysis of deepwater floating structures*. In: DNVGL- RP-F205. Det Norske Veritas and Germanischer Lloyd, Norway. 2010.

[49] J. Gobat and M. Grosenbaugh. *Dynamics in the trouchdown region of catenary moorings*. In: Proceedings of the 11th International Offshore and Polar Engineering Conference, Stavanger, Norway, 2001.

[50] H. Goldstein, C. P. Poole, and J. L. Safko. *Classical Mechanics*. Addison-Wesley, Boston, USA, 2001.

[51] K. Grigorakis and G. Rigos. “Aquaculture effects on environmental and public welfare – The case of Mediterranean mariculture”. In: *Chemosphere* 855 (2011), 899–919.

[52] W. Hackmann. “Mathematische Begründung von Verfahren zur Berechnung von Form und Zugkraft in Fadenzugsystemen”. In: *ZAMM* 63 (1983), 173–184.

[53] W. Hackmann. “Zur Lösung der Grundgleichungen des Fadens bei gleichförmiger Bewegung in einer Flüssigkeit”. In: *ZAMM* 62 (1982), 191–199.

[54] M. Hall and A. Goupee. “Validation of a lumped-mass mooring line model with DeepCwind semisubmersible model test data”. In: *Ocean Engineering* 104 (2015), 590–603.

[55] A. Hanaoka. *An overset grid method coupling an orthogonal curvilinear grid solver and a Cartesian grid solver*. Ph.D. thesis, University of Iowa, USA. 2013.

[56] F. Harlow and J. Welch. “Numerical calculation of time dependent viscous incompressible flow of fluid with a free surface”. In: *Physics of Fluids* 8 (1965), 2182–2189.

[57] P. Higuera, J.L. Lara, and I.J. Losada. “Realistic wave generation and active wave absorption for Navier–Stokes models: Application to OpenFOAM”. In: *Coastal Engineering* 71 (2013), 102–118.

[58] C.W. Hirt and B.D. Nichols. “Volume of fluid (VOF) method for dynamics of free boundaries”. In: *Journal of Computational Physics* 39 (1981), 201–225.

[59] C.-C. Huang, H.-J. Tang, and J.-Y. Liu. “Dynamical analysis of net cage structures for marine aquaculture: Numerical simulation and model testing”. In: *Aquacultural Engineering* 35 (2006), 258–270.

[60] N.G. Jacobsen, D.R. Fuhrman, and J. Fredsöe. “A wave generation toolbox for the open-source CFD library: OpenFoam”. In: *International Journal for Numerical Methods in Fluids* 70(9) (2012), 1073–1088.

[61] G.S. Jiang and D. Peng. “Weighted ENO schemes for Hamilton Jacobi equations”. In: *SIAM Journal of Scientific Computing* 21 (2000), 2126–2143.

[62] G.S. Jiang and C.W. Shu. “Efficient implementation of weighted ENO schemes”. In: *Journal of Computational Physics* 126(1) (1996), 202–228.

[63] A. Kamath et al. “CFD investigations of wave interaction with a pair of large tandem cylinders”. In: *Ocean Engineering* 108 (2015), 738–748.

[64] P. Kleber and B. Su. “Turbulence and flow field alterations inside afish sea cage and its wake”. In: *Applied Ocean Research* 98 (2020). DOI: 10.1016/j.apor.2020.102113.

[65] Kleefsman, K.M.T., Fekken, G., Veldman, A.E.P., Iwanowski, B. and Buchner, B. “A Volume-of-Fluid based simulation method for wave impact problems”. In: *Journal of Computational Physics* 206 (2005), 363–393.

[66] D. Kristiansen. *Wave induced effects on floaters of aquaculture plants*. Ph.D. thesis, NTNU Trondheim, Norway. 2010.

[67] T. Kristiansen and O. M. Faltinsen. "Experimental and numerical study of an aquaculture net cage with floater in waves and current". In: *Journal of Fluids and Structures* 54 (2015), 1–26.

[68] T. Kristiansen and O. M. Faltinsen. "Modelling of current loads on aquaculture net cages". In: *Journal of Fluids and Structures* 34 (2012), 218–235.

[69] P.F. Lader and B. Enerhaug. "Experimental Investigation of Forces and Geometry of a Net Cage in Uniform Flow". In: *IEEE Journal of Oceanic Engineering* 30.1 (2005), 79–84.

[70] P.F. Lader and A. Fredheim. "Dynamic properties of a flexible net sheet in waves and current - A numerical approach". In: *Aquacultural Engineering* 35 (3) (2006), 228–238.

[71] P.F. Lader et al. "Experimental Investigation of Wave Forces on Net Structures". In: *Applied Ocean Research* 29 (3) (2007), 112–127.

[72] F. LeBris and D. Marichal. "Numerical and experimental study of submerged supple nets applications to fish farms". In: *Journal of Marine Science Technology* 3 (1998), 161–170.

[73] H. Leitzke. *Berechnung von Form und Kräften biegeschlaffer, räumlicher Zugsysteme*. Ph.D. thesis, University of Rostock, Germany. 1983.

[74] L. Li et al. "Numerical Analysis of a Vessel-Shaped Offshore Fish Farm". In: *Journal of Offshore Mechanics and Arctic Engineering* 140 (2018). DOI: 10.1115/1.4039131.

[75] G. Løland. *Current forces on and flow through fish farms*. Ph.D. thesis, NTH Trondheim, Norway. 1991.

[76] D. Marichal. *Cod-end numerical study*. In: Proceedings of the 3rd International Conference on Hydroelasticity in Marine Technology, Oxford, UK., 2003.

[77] T. Martin and H. Bihs. "A non-linear implicit approach for modelling the dynamics of porous tensile structures interacting with fluids". In: *Journal of Fluids and Structures* (100) (2021). DOI: 10.1016/j.jfluidstructs.2020.103168.

[78] T. Martin and H. Bihs. "A Numerical Solution for Modelling Mooring Dynamics, Including Bending and Shearing Effects, Using a Geometrically Exact Beam Model". In: *Journal of Marine Science and Engineering* 9 (5) (2021). DOI: 10.3390/jmse9050486.

[79] T. Martin, A. Tsarau, and H. Bihs. “A numerical framework for modelling the dynamics of open ocean aquaculture structures in viscous fluids”. In: *Applied Ocean Research* (106) (2021). DOI: 10.1016/j.apor.2020.102410.

[80] T. Martin et al. “Efficient implementation of a numerical model for flexible net structures”. In: *Ocean Engineering* 150 (2018), 272–279.

[81] S. Mavrakos et al. “Deep water mooring dynamics”. In: *Marine Structures* 9 (1996), 181–209.

[82] S. Mayer, A. Garapon, and L.S. Sörensen. “A fractional step method for unsteady free-surface flow with applications to non-linear wave dynamics”. In: *International Journal for Numerical Methods in Fluids* 28 (1998), 293–315.

[83] J. Morison et al. “The force exerted by surface waves on piles”. In: *Pet. Trans. Amer. Inst. Min. Eng.* 186 (1950), 149–154.

[84] Nordlaks. https://www.nordlaks.no/havfarm/om-havfarm-prosjektet. accessed 08.06.2020.

[85] S. Osher and J.A. Sethian. “Fronts propagating with curvature-dependent speed: Algorithms based on Hamilton-Jacobi formulations”. In: *Journal of Computational Physics* 79 (1988), 12–49.

[86] J. Palm. *Mooring Dynamics for Wave Energy Applications*. Ph.D. thesis, Chalmers University of Technology, Gothenburg, Sweden. 2017.

[87] J. Palm, C. Eskilsson, and L. Bergdahl. “An hp-adaptive discontinuous Galerkin method for modelling snap loads in mooring cables”. In: *Ocean Engineering* 144 (2017), 266–276.

[88] N.K. Patel, A.P. Singh Bhalla, and N.A. Patankar. “A new constraint-based formulation for hydrodynamically resolved computational neuromechanics of swimming animals”. In: *Journal of Computational Physics* 375 (2018), 684–716.

[89] Ø. Patursson et al. “Development of a porous media model with application to flow through and around a net panel”. In: *Ocean Engineering* 37 (2010), 314–324.

[90] C. S. Peskin. “Flow patterns around the heart valves: A numerical method”. In: *Journal of Computational Physics* 10 (2) (1972), 252–271.

[91] C. S. Peskin. “Numerical analysis of blood flow in the heart”. In: *Journal of Computational Physics* 25 (3) (1977), 220–252.

[92] D. Priour. *A Finite Element Method for Netting*. First edition. Springer Netherlands, 2013.

[93] D. Priour. “Calculation of net shapes by the finite element method with triangular elements”. In: *Commun. Numer. Meth. Engng.* 15 (1999), 757–765.

[94] B. Ramaswamy, M. Kawahara, and T.Nakayama. “Lagrangian finite element method for the analysis of two-dimensional sloshing problems”. In: *International Journal for Numerical Methods in Fluids* 6 (1986), 659–670.

[95] P.J. Roache. “Quantification of Uncertainty in Computational Fluid Dynamics”. In: *Annu.Rev. Fluid Mech.* No. 29 (1997), 123–160.

[96] G. Ryskin and L. Leal. “Numerical solution of free boundary problems in fluid mechanics. part I The finite-difference technique”. In: *Journal of Fluid Mechanics* 148 (1984), 1–17.

[97] SalMar. `https://www.salmar.no/en/offshore-fish-farming-a-new-era/`. accessed 08.02.2021.

[98] R. Scardovelli and S. Zaleski. “Interface reconstruction with least-square and split Eulerian–Lagrangian advection”. In: *International Journal for Numerical Methods in Fluids* 41 (2003), 251–274.

[99] D. Scott and J. Muir. *Offshore cage systems: a practical overview*. In: Option Mediterraneennes-International Centre for Advanced Mediterranean Agronomic Studies. 2000.

[100] Y. Shen et al. “Numerical and experimental investigations on mooring loads of a marine fish farm in waves and current”. In: *Journal of Fluids and Structures* 79 (2018), 115–136.

[101] R. Shivarama and E.P. Fahrenthold. “Hamilton’s Equations With Euler Parameters for Rigid Body Dynamics Modeling”. In: *J. Dyn. Sys., Meas., Control* 126 (2004), 124–130.

[102] C.W. Shu and S. Osher. “Efficient implementation of essentially non-oscillatory shock-capturing schemes”. In: *Journal of Computational Physics* 77(2) (1988), 439–471.

[103] I.M. Strand et al. “Experimental study of current forces and deformations on a half ellipsoidal closed flexible fish cage”. In: *Journal of Fluids and Structures* 65 (2016), 108–120.

[104] M. Sussman, P. Smereka, and S. Osher. “A level set approach for computing solutions to incompressible two-phase flow”. In: *Journal of Computational Physics* 114 (1994), 146–159.

[105] L.J.P. Timmermans, P.D. Minev, and F.N. Van De Vosse. “An approximate projection scheme for incompressible flow using spectral elements”. In: *International Journal for Numerical Methods in Fluid* 22 (1996), 673–688.

[106] H. Tronstad. *Nonlinear hydroelastic analysis and design of cable net structures like fishing gear based on the finite element method*. Ph.D. thesis, NTNU Trondheim, Norway. 2000.

[107] G. Tryggvason et al. "A Front-Tracking Method for the Computations of Multiphase Flow". In: *Journal of Computational Physics* 169 (2) (2001), 708–759.

[108] I. Tsukrov et al. "Finite element modeling of net panels using a consistent net element". In: *Ocean Engineering* 30 (2003), 251–270.

[109] M. Uhlmann. "An immersed boundary method with direct forcing for the simulation of particulate flows". In: *Journal of Computational Physics* 209 (2005), 448–476.

[110] G. Vaz, F. Jaouen, and M. Hoekstra. "Free-surface viscous flow computations. Validation of URANS code FreSCo". In: *Proceedings of the ASME 2009 28th International Conference on Ocean, Offshore and Arctic Engineering* (2009). DOI: 10.1115/OMAE2009-79398.

[111] B. Vincent. *A new generation of tools for trawls dynamic numerical simulation*. In: Proceedings of the 4th International Workshop on Methods for Development and Evaluation of Maritime Technologies, Rostock, Germany, 1999.

[112] G. Vissio et al. *Expanding ISWEC Modelling with a Lumped-Mass Mooring Line Model*. In: Proceedings of the European Wave and Tidal Energy Conference, Nantes, France, 2015.

[113] H. van der Vorst. "BiCGStab: A fast and smoothly converging variant of Bi-CG for the solution of nonsymmetric linear systems". In: *SIAM Journal of Scientific Computing* 13 (1992), 631–644.

[114] A. Vreman. "Immersed boundary and overset grid methods assessed for Stokes flow due to an oscillating sphere". In: *Journal of Computational Physics* 423 (2020). DOI: 10.1016/j.jcp.2020.109783.

[115] T. Walton and H. Polachek. "Calculation of transient motion of submerged cables". In: *Math. Comp.* 14 (1959), 27–46.

[116] W. Wang et al. "A Comparison of Different Wave Modelling Techniques in An Open-Source Hydrodynamic Framework". In: *Journal of Marine Science and Engineering* 8 (7), 526 (2020). DOI: 10.3390/jmse8070526.

[117] T.-J. Xu et al. "Analysis of hydrodynamic behavior of a submersible net cage and mooring system in waves and current". In: *Applied Ocean Research* 42 (2013), 155–167.

[118] Z. Xu and H. Qin. "Fluid-structure interactions of cage based aquaculture: From structures to organisms". In: *Ocean Engineering* 217 (2020). DOI: 10.1016/j.oceaneng.2020.107961.

[119] J. Yang and F. Stern. “A non-iterative direct forcing immersed boundary method for strongly-coupled fluid-solid interactions”. In: *Journal of Computational Physics* 295 (2015), 779–804.

[120] J. Yang and F. Stern. “Sharp interface immersed-boundary/level-set method for wave-body interactions”. In: *Journal of Computational Physics* 228 (2009), 6590–6616.

[121] L. Yang. “One-fluid formulation for fluid–structure interaction with free surface”. In: *Comput. Methods Appl. Mech. Engrg.* 332 (2018), 102–135.

[122] Y. Yao et al. “Numerical modeling of current loads on a net cage considering fluid–structure interaction”. In: *Journal of Fluids and Structures* 62 (2016), 350–366.

[123] J.M. Zhan et al. “Analytical and experimental investigation of drag on nets of fish cages”. In: *Aquacultural Engineering* 35 (1) (2006), 91–101.

[124] Y.-P. Zhao et al. “Numerical Simulation of Interaction Between Waves and Net Panel Using Porous Media Model”. In: *Engineering Applications of Computational Fluid Mechanics* 8.1 (2014), pp. 116–126.

[125] Y. Zhao et al. “Experimental Investigations on Hydrodynamic Responses of a Semi-Submersible Offshore Fish Farm in Waves”. In: *Journal of Marine Science and Engineering* 7 (2019). DOI: 10.3390/jmse7070238.

Appendix A

Appended publications

Paper 1 Martin, T., Kamath, A. and Bihs, H. (2021). Accurate modelling of the interaction of constrained floating structures and complex free surfaces using a new quasi-static mooring model. *Int. J. Numer. Meth. Fluids, Vol. 93(2), pp. 504–526, doi: 10.1002/fld.4894.*

Paper 2 Martin, T., Kamath, A. and Bihs, H. (2020). A Lagrangian approach for the coupled simulation of fixed net structures in a Eulerian fluid model. *Journal of Fluids and Structures, Vol. 94, doi: 10.1016/j.jfluidstructs.2020.102962.*

Paper 3 Martin, T. and Bihs, H. (2021). A non-linear implicit approach for modelling the dynamics of porous tensile structures interacting with fluids. *Journal of Fluids and Structures, Vol. 100, doi: 10.1016/j.jfluidstructs.2020.103168.*

Paper 4 Martin, T., Tsarau, A. and Bihs, H. (2021). A numerical framework for modelling the dynamics of open ocean aquaculture structures in viscous fluids. *Applied Ocean Research, Vol. 106, doi: 10.1016/j.apor.2020.102410.*

Paper 5 Martin, T. and Bihs, H. (2021). A CFD approach for modelling the fluid-structure interaction of offshore aquaculture cages and waves. *ASME 40th International Conference on Ocean, Offshore and Artic Engineering, OMAE2021, Accepted.*

Paper 1

Accurate modelling of the interaction of constrained floating structures and complex free surfaces using a new quasi-static mooring model

Martin, T., Kamath, A. and Bihs, H. (2021).
International Journal of Numerical Methods in Fluids, Vol. 93(2), pp. 504–526,
doi: 10.1002/fld.4894.

Accurate modelling of the interaction of constrained floating structures and complex free surfaces using a new quasi-static mooring model

Tobias Martin* Arun Kamath Hans Bihs

Department of Civil and Environmental Engineering, Norwegian University of Science and Technology (NTNU), 7491 Trondheim, Norway

Postprint
published in *Int. J. Numer. Meth. Fluids*, 2021, Vol. **93**, pp. 504–526,
DOI: 10.1002/fld.4894.

Abstract

A new approach for the coupled simulation of moored floating structures in a numerical wave tank using CFD is subject of this paper. A quasi-static mooring model is derived by dividing the cable into finite elements and solve force equilibria in each time step. A successive approximation is applied to solve the problem most efficiently. Here, the unknown internal and external forces are separated, and the system is corrected iteratively using the intermediate results for the unit vectors until convergence is reached. An improved algorithm based on the directional ghost cell immersed boundary method is utilised for modelling floating objects in a three-dimensional numerical wave tank. It is based on an implicit representation of the body on a stationary grid using a level set function. The motion of the rigid body is described using Euler parameters and Hamiltonian mechanics. Dynamic boundary conditions are enforced by modifying the ghost points in the vicinity of the structure. A special procedure for staggered grids is included in the paper. The mooring model is coupled to the fluid-structure interaction solver to simulate physically constrained floating bodies in waves. Several validation cases provide an overview of the accuracy of the mooring model and the floating algorithm. Additionally, the comparison of the numerical results for the motion of a moored floating barge in regular waves with experiments is presented.

Keywords: Numerical Methods, Fluid-Structure Interaction, Mooring, CFD, Immersed Boundary Method, Rigid Body Dynamics

*Corresponding author, tobias.martin@ntnu.no

1 Introduction

Floating offshore and coastal constructions are exposed to a challenging environment with intense fluid-structure interaction. Their safety is often related to fixing their position, which is usually achieved by mounting an appropriate mooring system. Therefore, the computer-aided design process requires not just the solution of a two-phase problem for the fluid and an accurate determination of the rigid body dynamics but also a mooring model.

Taking the Navier-Stokes equations as the basis of the calculations, several attempts have been proposed to solve fluid-structure interactions. In Arbitrary Lagrangian-Eulerian methods [37], the fluid properties are described on a fixed Eulerian grid which is fitted to the moving body. As the body changes its position, the mesh has to be recalculated dynamically. This approach raises the theoretical possibility to resolve the boundary layer around the structure by applying fine layers of cells but is prone to loss of numerical accuracy and stability due to suboptimal re-meshing, especially for large body motions. To prevent irregular grids, re-meshing can be avoided using either completely Lagrangian methods such as meshless SPH (Smoothed Particle Hydrodynamics) models [15] or dynamic overset grids [7, 10]. In overset methods, several moving meshes which are arranged on a fixed base grid are considered. Hence, body-fitted cell alignments remain possible. An interpolation mechanism handles the data transfer between the overlapping grid points, and an overall solution for the fluid properties can be found by including these interpolations into the system matrix [23]. The size of the overlapping region is related to the stencil size of the discretisation. This complicates the implementation and affects the efficiency for high-order numerics. Alternative approaches are based on immersed boundary methods [35]. They require just one Eulerian grid, and the body is described implicitly. Direct forcing methods [17] incorporate the fluid-structure interaction as an additional source term in the Navier-Stokes equations. The term represents the amount of momentum between the actual fluid-solid interface and the nearest cell centres under consideration of the boundary conditions. Evaluating this term usually includes several iterations with multiple pressure solution processes. A non-iterative and more efficient approach was recently presented by Yang and Stern [48]. Following the work of Calderer et al. [9], an easier way of respecting the boundary conditions can be found. Instead of an additional term, modified stencils are considered. In the vicinity of the body, interpolation stencils are modified by including their closest distance to the body. Berthelsen and Faltinsen [4] further simplified this procedure for fixed bodies by using the closest distances in the local directions of the stencils. In doing so, the necessary interpolations become straightforward evaluations of Lagrangian polynomials in the principal directions of the grid. Bihs and Kamath [5] utilised this advantage to develop a local ghost-cell immersed boundary method for moving bodies. Their research was mainly focused on falling objects, and the algorithm was based on first-order interpolations and force and geometry property calculations using the level set representation of the body. A possibly under-resolved level set function has a significant effect on the accuracy of the results, which is particularly severe for floating objects depending on the equilibrium of forces. Therefore, this paper presents several improvements of the original solver by reducing the dependency on the level set function to the most useful parts. Thus, the simulation of floating objects in complex waves is enabled for the first time using a local ghost-cell immersed boundary method.

The dynamics of mooring lines is described by a non-linear partial differential equation of second order in both space and time even if bending stiffness is neglected. Therefore, the

general solution can just be found numerically. Davidson and Ringwood [14] present a review of a wide range of possible discretisation methodologies. They are based on finite differences [2, 24], finite elements [1] or spring elements [22]. Palm et al. [34] pointed out the hyperbolic nature of the equations and applied an hp-adaptive discontinuous Galerkin method. Their method is stable, of arbitrary order of accuracy and capable of simulating snap loads. The main disadvantage of fully dynamic mooring models is the necessity of stable initial conditions and the restriction of the time step imposed by the material stiffness. Thus, the time step due to the mooring dynamics can be several magnitudes smaller than the time step due to the CFL condition of the fluid solver. This either restricts the efficiency of the whole simulation or raises the need for interpolation in time [33]. If the purpose of the simulation is more concentrated on the FSI problem and less on the details of the mooring dynamics or the expected motion of the lines are small in any case, simplifications of the original equations are appropriate. By neglecting the dynamic effects, dependencies of mass, damping and fluid acceleration on the system are omitted. In this case, the mooring line shape and tension is often found analytically using the catenary solution [18]. This solution is restricted in its form and not suitable for tense or arbitrary shaped systems. Therefore, a quasi-static solution presents a suitable compromise because it combines the flexibility of a generically formulated numerical approach with similar efficiency and simplicity as an analytical solution.

This paper aims at developing such a quasi-static mooring model, which is disregarded in research so far. The finite element method for tensile structures [29], which is based on a discrete representation of the structure using knots connected with trusses, is taken as the basis of the presented developments. Here, a linear system of equations is generated using force equilibria at each knot of the discrete line and a geometrical constraint preventing unphysical correlation of tension forces and bar deformation. Important hydrodynamic effects on the lines are respected using Morison forces from the surrounding fluid solution. The presented mooring model is coupled to the new floating algorithm within the framework of the open-source CFD solver REEF3D. The coupling process is straightforward and adds significantly less computational time to the overall simulation than dynamic models due to the missing time step restriction. Further, the transition from a hyperbolic problem based on initial and boundary conditions to a boundary value problem makes the new mooring model a more flexible approach.

In section 2.1, the CFD model is briefly described. Afterwards, details about the improved floating algorithm and new mooring model are given in the sections 2.2 and 2.3. Section 3 presents several verification and validation cases. First, section 3.1 provides the validation of the new mooring model against measurements of the prescribed motion of a single line and wind channel experiments with a line mounted between two fixed points. Afterwards, the rigid body dynamics solver is investigated and the complete FSI solver is validated for fluid-structure interactions of a floating and moored floating barge in regular waves in the sections 3.3 and 3.4. The paper concludes with an application to a more complex moored semi-submersible platform in section 4 and final remarks in section 5.

2 Numerical models

2.1 Computational fluid dynamics solver

In this paper, the incompressible continuity and Reynolds-averaged Navier-Stokes (RANS) equations are solved in the whole domain. They are given as

$$\frac{\partial u_i}{\partial x_i} = 0, \tag{1}$$

$$\frac{\partial u_i}{\partial t} + u_j \frac{\partial u_i}{\partial x_j} = -\frac{1}{\rho}\frac{\partial p}{\partial x_i} + \frac{\partial}{\partial x_j}\left((\nu + \nu_t)\cdot\left(\frac{\partial u_i}{\partial x_j} + \frac{\partial u_j}{\partial x_i}\right)\right) + g_i. \tag{2}$$

Here, u_i with $i = 1, 2, 3$ are the velocity components in the coordinate directions, ρ is the fluid density, p presents the pressure contribution, ν and ν_t are the kinematic and turbulent viscosity, and g_i is the gravity acceleration vector. The additional viscosity is evaluated from the k-ω turbulence model with a modified source term to account for free surfaces [6]. The material properties of the two phases are determined for the whole domain in accordance to the continuum surface force model of Brackbill et al. [8]. The equations are discretised on a rectilinear and staggered grid using a finite difference method (FDM). Chorin's projection method for incompressible flows is applied to resolve the velocity-pressure coupling [13]. The pressure is obtained as the solution of a Poisson equation from the continuity equation. The fully parallelized BiCGStab algorithm [46] with PFMG pre-conditioner [3] from the iterative linear system solvers of HYPRE are exploited. Temporal terms are discretised applying the third-order accurate Total Variation Diminishing (TVD) Runge-Kutta scheme [41]. An adaptive time-stepping control according to the CFL condition is used. Diffusion terms are treated implicitly to overcome their restrictions on this condition. The Convection term in (2) is discretised in a non-conservative form to increase numerical stability [42]. The fifth-order accurate weighted essentially non-oscillatory (WENO) scheme of Jiang and Shu [27] is chosen to reconstruct the fluxes. The scheme is adapted to non-conservative terms under consideration of the work of Zhang and Jackson [50].

The free surface is implicitly captured by the level set method of Osher and Sethian [32]. A smooth signed distance function ϕ, defined as the closest distance to the interface, is convected in the fluid velocity field using the linear advection equation

$$\frac{\partial \phi}{\partial t} + u_i \frac{\partial \phi}{\partial x_i} = 0. \tag{3}$$

The convection term is discretised by the fifth-order accurate Hamilton-Jacobi WENO method of Jiang and Peng [26]. In order to conserve the signed distance property, the level set function is reinitialized after each time step using the PDE-based reinitialization equation of Sussman et al. [42].

All simulations are executed in the numerical wave tank of the open-source CFD solver REEF3D [6]. Waves are generated by applying the relaxation method to the x- and z-component of the velocities and the level set function ϕ. For a general variable ε it is given as [30]

$$\varepsilon(x) = \Gamma(x)\varepsilon_{\text{analytical}} + (1 - \Gamma(x))\varepsilon_{\text{computed}}, \tag{4}$$

with Γ the relaxation function taken from [25]. The same method is applied to damp potential reflections near the outlet of the tank. Extensive validation of the described numerical wave tank can be found in [6].

2.2 Improved rigid body dynamics and fluid-structure coupling

In the following, the rigid body dynamics solver and its coupling to the fluid model is described. In comparison to the previous algorithm [5], the improved model calculates geometrical properties of a rigid body from a triangulated surface instead of a level set function approximation. This can be computed more efficiently by surface integrations if the assumption of a homogeneous material with density ρ_s holds. Given the approximation of the bodies' surface S as

$$S = \bigcup_{i=1}^{N} S_i, \tag{5}$$

where S_i is assumed to be triangular, the properties are defined as

$$\rho_s \int_V \nabla \cdot f(\vec{x}) dV = \rho_s \int_S (\vec{n} \cdot \vec{k}) f(\vec{x}) dS = \rho_s \sum_{i=1}^{N} (\vec{n}_i \cdot \vec{k}) \int_{S_i} f(\vec{x}) dS. \tag{6}$$

Here, $\nabla \cdot f(\vec{x}) = 1$ returns the body mass, $\nabla \cdot f(\vec{x}) = x, y, z$ present the centre of mass coordinates in an inertial system and $\nabla \cdot f(\vec{x}) = x^2, y^2, z^2, xy, yz, xz$ compute the moments of inertia. Further, $\vec{n}_i$ is the face normal vector of triangle S_i, and $\vec{k}$ is a unit vector in the x, y or z-direction dependent on the chosen integration of the function. Numerical integrations in (6) can be avoided by parametrising the triangles and analytically integrating over a standard triangle as given in [16].

The translational motion of the rigid body is described by Newtons second law as

$$\ddot{\vec{x}}_s = \frac{\vec{F}_{\vec{x}}}{\rho_s V}. \tag{7}$$

The position $\vec{x}_s$ and velocity $\dot{\vec{x}}_s$ of the bodies centre of gravity can be determined by numerically integrating (7).

The orientation in a fixed coordinate system is described by the four Euler parameters $\vec{e} = (e_0\ e_1\ e_2\ e_3)^T$ which are related to the physically more relevant Tait-Bryan angles Φ, Θ, Ψ via (c is cos and s is sin) [19]

$$e_0 = c\left(\frac{\Phi}{2}\right) \cdot c\left(\frac{\Theta}{2}\right) \cdot c\left(\frac{\Psi}{2}\right) + s\left(\frac{\Phi}{2}\right) \cdot s\left(\frac{\Theta}{2}\right) \cdot s\left(\frac{\Psi}{2}\right), \tag{8}$$

$$e_1 = s\left(\frac{\Phi}{2}\right) \cdot c\left(\frac{\Theta}{2}\right) \cdot c\left(\frac{\Psi}{2}\right) - c\left(\frac{\Phi}{2}\right) \cdot s\left(\frac{\Theta}{2}\right) \cdot s\left(\frac{\Psi}{2}\right), \tag{9}$$

$$e_2 = c\left(\frac{\Phi}{2}\right) \cdot s\left(\frac{\Theta}{2}\right) \cdot c\left(\frac{\Psi}{2}\right) + s\left(\frac{\Phi}{2}\right) \cdot s\left(\frac{\Theta}{2}\right) \cdot s\left(\frac{\Psi}{2}\right), \tag{10}$$

$$e_3 = c\left(\frac{\Phi}{2}\right) \cdot c\left(\frac{\Theta}{2}\right) \cdot s\left(\frac{\Psi}{2}\right) - s\left(\frac{\Phi}{2}\right) \cdot s\left(\frac{\Theta}{2}\right) \cdot c\left(\frac{\Psi}{2}\right). \tag{11}$$

In practice, this choice overcomes eventual issues due to the Gimbal lock effect. The back-transformation can be calculated using

$$\Psi = \arctan 2\left(2 \cdot (e_1 \cdot e_2 + e_3 \cdot e_0), 1 - 2 \cdot (e_2 \cdot e_2 + e_3 \cdot e_3)\right), \tag{12}$$

$$\Theta = \arcsin(2 \cdot (e_0 \cdot e_2 - e_1 \cdot e_3)), \tag{13}$$

$$\Phi = \arctan 2(2 \cdot (e_2 \cdot e_3 + e_1 \cdot e_0), 1 - 2 \cdot (e_1 \cdot e_1 + e_2 \cdot e_2)). \tag{14}$$

The four Euler parameters are depend as $\vec{e}^{\,T}\vec{e} = 1$. The transformation of a vector in the body-fixed coordinate system to a corresponding vector in the inertial system is described by the orthogonal rotation matrix

$$\mathbf{R} = 2\begin{pmatrix} \frac{e_0^2+e_1^2-e_2^2-e_3^2}{2} & e_1e_2 - e_0e_3 & e_0e_2 + e_1e_3 \\ e_0e_3 + e_1e_2 & \frac{e_0^2-e_1^2+e_2^2-e_3^2}{2} & e_2e_3 - e_0e_1 \\ e_1e_3 - e_0e_2 & e_0e_1 + e_2e_3 & \frac{e_0^2-e_1^2-e_2^2+e_3^2}{2} \end{pmatrix}. \tag{15}$$

Based on this, the kinematic equations for the rotational motion of the body in terms of the Euler parameters are given as

$$\dot{\vec{e}} = \frac{1}{2}\mathbf{G}^T\vec{\omega}, \tag{16}$$

with $\vec{\omega}$ the components of the angular velocity vector in the body-fixed coordinate system and

$$\mathbf{G} = \begin{pmatrix} -e_1 & e_0 & e_3 & -e_2 \\ -e_2 & -e_3 & e_0 & e_1 \\ -e_3 & e_2 & -e_1 & e_0 \end{pmatrix}. \tag{17}$$

Introducing the momentum vector $\vec{h} = \mathbf{I}\vec{\omega}$ with $\mathbf{I}$ the moment of inertia tensor, (16) can be rewritten as

$$\dot{\vec{e}} = \frac{1}{2}\mathbf{G}^T\mathbf{I}^{-1}\vec{h}. \tag{18}$$

Following the derivation of Shivarama and Fahrenthold [40], a first-order ODE can be derived for $\dot{\vec{h}}$ using a system Hamiltonian. Here, the constraint for the Euler parameters is fulfilled automatically. By setting the potential energy function to zero and assuming imposed moments $\vec{M}'_{\vec{x}}$ in the body-fixed system, the equations read

$$\dot{\vec{h}} = -2\mathbf{G}\dot{\mathbf{G}}^T\vec{h} + \vec{M}'_{\vec{x}}. \tag{19}$$

The moments are obtained from the inertia system using the transformation matrix (15). In total, (7), (16) and (19) forms a system of thirteen first-order ODEs which can be solved using any type of numerical integration method. An advantage of the derivation based on Hamiltonian mechanics is the energy based formulation. Thus, conservation of energy can be tracked easily in the absence of external forces. This is used later to choose a suitable numerical integration method.

An implicit description of the floating body is found efficiently by defining a level set function such that the zero level set describes the surface of the body using the triangulated

body representation. A ray-tracing algorithm [49] is applied first to get the shortest distances in each coordinate direction between the zero level set and each grid point. The signed distance property for the level set function is ensured by the above-mentioned reinitialization process. The method avoids explicit calculations for getting the intersections between the contour and the grid but lacks accuracy for calculating the surface area. Thus, the algorithm determines the body forces by applying a linear interpolation between the grid point values and integrating over the discrete surface

$$\vec{F}_{\vec{x}} = \int_{\Omega} (-\vec{n}p + \mu\vec{n}\vec{\tau}) \; dS(\vec{x}) = \sum_{i=1}^{N} (-\vec{n}p + \mu\vec{n}\vec{\tau})_i \cdot \Delta S_i, \tag{20}$$

with $\vec{n}$ the surface normal vectors, μ the dynamic viscosity, $\vec{\tau}$ the viscous stress tensor and N the number of surface representing triangles. Further, ΔS is the area of each triangle. This is in contrast to the previous force calculation based on the level set and the Dirac delta function.

The proposed FSI model is a weakly coupling algorithm with the possibility for sub-iterations. As already indicated in [5], the overall accuracy or stability is only marginally influenced by these sub-iterations and so can usually be omitted. Key steps in the new algorithm are the ghost cell interpolations, which are adapted from the ghost cell immersed boundary method of Berthelsen and Faltinsen [4], to incorporate the boundary conditions of the solid. For this purpose, the staggered evaluation points for the velocity are defined as either fluid, interpolation or ghost points as indicated in Fig. 1a. Pressure points, which coincide with the cell centres of the original grid, are defined as fluid points if they are in the fluid and as ghost points elsewhere. The pressure values of ghost points are extrapolated in the different coordinate directions from calculated fluid values and the boundary condition for the pressure gradient at the interface which reads

$$\left.\frac{\partial p}{\partial x_i}\right|_{\Gamma} = -\frac{1}{\rho} \cdot \frac{Du_{i,\Gamma}}{Dt}, \quad i = 1, 2, 3, \tag{21}$$

with $u_{i,\Gamma}$ the bodies' velocities at the interface which are given in [5]. Equation (21) simplifies to the common zero gradient boundary condition for non-moving bodies. The pressure ghost cells are used during the solution of the Poisson equation and force calculations. A slightly different approach is implemented for the velocity components on the staggered grids. As can be seen in Fig. 1a, interpolation points are defined as an additional class of points. The velocity values at these points are determined from a linear interpolation using a fluid point and the known velocity of the solid at the interface in the principal direction (see Fig. 1b). Thus, the correct boundary conditions are implicitly respected by the momentum calculations in the predictor step. In comparison to other immersed boundary methods, this directional approach avoids modification of the fluid stencils or the setup of additional stencils in the vicinity of the body. The indicated problems of solid cells becoming fluid cells and the resulting missing velocity information [44, 47] are circumvented by assigning a velocity to the ghost points in the body. This velocity equals the body velocity at the corresponding ghost point. The presented approach is easily extendable to higher-order interpolations but preliminary tests did not show significant improvements in accuracy or stability.

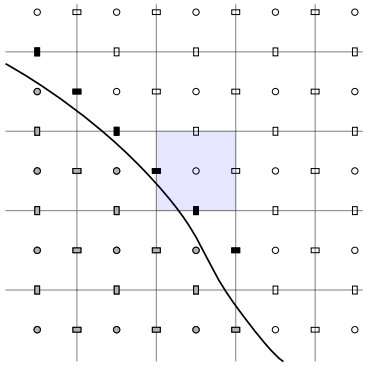

(a) Overview of categorisation strategy.

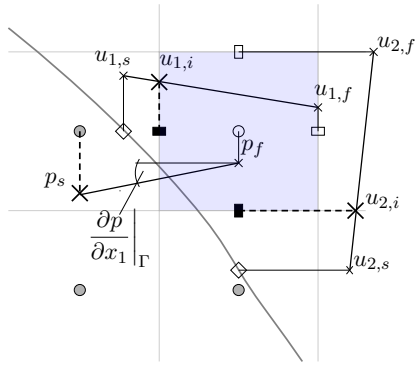

(b) Exemplary directional interpolations of the velocities u_1 and u_2 and extrapolation of the pressure in x_1 direction using the known pressure gradient at the boundary $\frac{\partial p}{\partial x_1}_\Gamma$.

Figure 1: Details of the directional ghost cell interpolation method for one cell (blue): fluid points (white), interpolation points (black), ghost points (gray).

2.3 New quasi-static numerical approach for solving mooring dynamics

The development of the new quasi-static mooring model based on finite elements which were originally developed for quasi-static modelling of more complex tensile structures [28, 29].

The dynamics of a mooring line neglecting bending stiffness is described as [34]

$$\gamma \frac{\partial^2 \vec{r}}{\partial t^2} = \frac{\partial F_T \vec{f}}{\partial s} + \vec{F}_e, \tag{22}$$

with γ the specific weight of the material, F_T the magnitude of the tension force, $\vec{f}$ the unit vector pointing in the direction of this force and $\vec{F}_e$ external forces including gravitation and hydrodynamic effects. Assuming small line motion in time and steady-state flow of the fluid, respectively, (22) simplifies to

$$\frac{\partial F_T \vec{f}}{\partial s} = -\vec{F}_e. \tag{23}$$

In order to solve this force equilibrium, each mooring line is split into N equally distanced bars of length l_t with knots P in between. As shown in Fig. 2, the first and last knot, $P^{(0)}$ and $P^{(N)}$, are attached to the bottom and the floating object.

The mass of the line is equally distributed on the adjacent knots which gives a gravity force contribution of

$$\vec{F_G}^{(j)} = \gamma \vec{g} \cdot \frac{\rho_m - \rho}{\rho_m} \cdot \frac{l_t^{(j)} + l_t^{(j+1)}}{2}, \quad j = 1, ..., N-1, \tag{24}$$

at any knot $P^{(j)}$. Here, ρ_m is the density of the mooring material and $\vec{g}$ is an unit vector pointing in negative $z-$direction. Hydrodynamic forces $\vec{F}_H$, arising from the slowly-varying

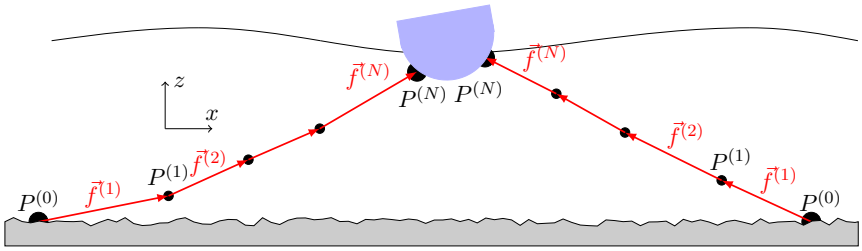

Figure 2: Discrete mooring lines: Inner knots (small black dots), Outer knots (big black dots), bars (red vectors).

relative motion between structure and surrounding fluid, are calculated as drag forces using Morison's formula at each bar

$$\vec{F_H}^{(j)} = l_t^{(j)} d_t^{(j)} \frac{\rho}{2} \cdot \left[c_t \left(\vec{v} \cdot \vec{f} \right) \left| \vec{v} \cdot \vec{f} \right| \cdot \vec{f} + c_n \left(\vec{v} - \left(\vec{v} \cdot \vec{f} \right) \vec{f} \right) \left| \vec{v} - \left(\vec{v} \cdot \vec{f} \right) \vec{f} \right| \right]^{(j)} , \quad j = 1, ..., N, \tag{25}$$

with c_n and c_t the drag coefficients in normal and tangential direction. The hydrodynamic forces are assigned to knots by equally distributing the net amount. As indicated in [29], hydrodynamic forces can also be written as the partial sum of hydrodynamic drag, lift and shear forces. The coefficients then depend particularly on the local angle between the fluid and bar unit vector and have to be found experimentally for each mooring configuration. However, using (25) with coefficients for slender cylindrical shapes is more practical for general applications. Choo and Casarella [12] derived a formula for c_n as a function of the Reynolds number

$$c_n(\mathrm{Re}) = \begin{cases} \frac{8\pi}{s\ \mathrm{Re}} \cdot \left(1.0 - 0.87\ s^{-2.0}\right) & \text{if } \mathrm{Re} < 1.0 \\ 1.45 + 8.55\ \mathrm{Re}^{-0.9} & \text{if } 1.0 \leq \mathrm{Re} < 30.0 \\ 1.1 + 4.0\ \mathrm{Re}^{-0.5} & \text{else.} \end{cases} \tag{26}$$

For c_t, typical values can be found in literature.

Further, it is given that the tension forces act at the knots in the direction of the adjacent bars such that (23) can be solved locally at each inner knot $P^{(j)}$ (see also Fig. 3):

$$\vec{f}^{(j+1)} F_T^{(j+1)} - \vec{f}^{(j)} F_T^{(j)} + \vec{F}_H^{(j)} + \vec{F}_G^{(j)} = \vec{0}, \quad j = 1, ..., N-1. \tag{27}$$

A solution for the shape of the line and the distribution of tension forces can be found by gathering (27) into a suitable linear system of equations. Both sought unknowns are generally dependent on the direction of the bar unit vectors. However, $\vec{F}_H$ also depends on $\vec{f}$ according to (25), whereas $\vec{F}_G$ is related to the length of the bars which is a function of tension forces. This elasticity of the material is respected by representing l_t as a polynomial of F_T such as

$$l_{t,(k+1)}^{(j)} = \left[l_t^{(j)} \cdot \left\{ 1.0 + \sum_{p=1}^{P} K_p(j) \cdot \left(\frac{F_T^{(j)} + F_T^{(j-1)}}{2} \right)^p \right\} \right]_{(k)} , \quad j = 1, ...N, \tag{28}$$

with K_p the stiffness constants and k the iteration index. Hooke's law is considered in the applications shown below by only using K_1. An iterative method has to be chosen for solving the system because all components of (27) are related to each other. As proven by Hackmann [20, 21], a successive approximation can be found to ensure a converged solution. For this purpose, (27) is rearranged such that internal and external forces are separated

$$\vec{f}^{(j+1)} F_T^{(j+1)} - \vec{f}^{(j)} F_T^{(j)} = -\left(\vec{F}_H^{(j)} + \vec{F}_G^{(j)}\right), \quad j = 1, ..., N-1. \tag{29}$$

Fig. 2 indicates that the discrete line consists of N bars but just $N-1$ inner knots. Therefore, (29) presents an undetermined system if solved for $\vec{f}$. A geometrical constraint is introduced in order to close the system. This constraint can be chosen in such a way that it represents both the physical boundary condition of fixed end points $P^{(0)}$ and $P^{(N)}$, and the physical coherence of the line during deformation:

$$\sum_{j=1}^{N} \vec{f}^{(j)} l_t^{(j)} = \vec{x}(P^{(N)}) - \vec{x}(P^{(0)}). \tag{30}$$

This means that the vector of the sum of all bar vectors has to be equal to the distance vector between the two end points $\vec{x}(P^{(0)})$ and $\vec{x}(P^{(N)})$, which is a conditional equation for a physical coherent solution of the problem.

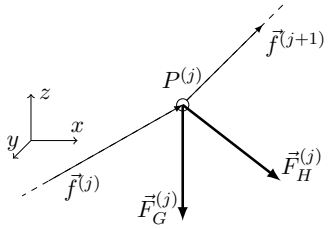

Figure 3: Force equilibrium at inner knot P^ν: Inner knot (white filled circle), bars (thin vectors), forces (thick vectors).

The resulting linear system of equations can now be formulated with the unit bar vectors as the $(N \times 3)$ solution matrix $\mathbf{F}$ because of the dependencies in (30). Under consideration of (29) and (30), the system reads

$$\underbrace{\begin{pmatrix} \mathbf{T} \\ \mathbf{L} \end{pmatrix}}_{\mathbf{A}} \cdot \mathbf{F} = \underbrace{\begin{pmatrix} -(\mathbf{H}+\mathbf{G}) \\ \vec{x}(P^{(N)}) - \vec{x}(P^{(0)}) \end{pmatrix}}_{\mathbf{B}}, \tag{31}$$

with the $(N \times N)$ matrix $\mathbf{A}$ containing the $(N-1 \times N)$ sub-matrix of unknown tension forces $\mathbf{T}$ and the $(1 \times N)$ vector of the bar lengths $\mathbf{L}$. On the right hand side, $\mathbf{B}$ is filled with the $(N-1 \times 3)$ sub-matrices of hydrodynamic and static forces $\mathbf{H}$ and $\mathbf{G}$ and the vector connecting the two end points.

The solution process of the mooring model is illustrated in Fig. 4. As input parameters, the fluid velocity field and the current locations of the mounting points are communicated

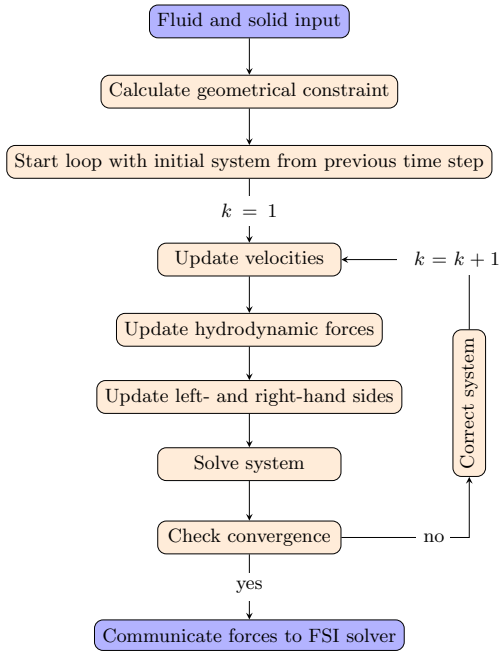

Figure 4: Illustration of the quasi-static mooring algorithm.

to the algorithm. The geometrical constraint vector is calculated from these and an initial system of equations is generated. For the first time step, less restrictive directions for the unit vectors and initial tension forces are set to fill the left- and right-hand sides. Thus, this model is independent of a predefined initial form of the cable and highly suitable for applications without this requirement. Based on the given values, (28) returns the initial lengths of the bars and (24) yields the gravity force matrix $\mathbf{G}$. The hydrodynamic force matrix $\mathbf{H}$ is initialised considering the fluid velocity field and (25). The velocities at the bars are calculated from the surrounding velocity cells and a weighted interpolation. This process is fully parallelised using MPI. The solution of (31) at any iterative step k is determined by Gaussian elimination with pivoting as

$$\mathbf{F}^{(k)} = \left(\mathbf{A}^{(k)}\right)^{-1} \cdot \mathbf{B}^{(k)}. \tag{32}$$

The lengths of bar unit vectors have to be equal to one by definition after being calculated from (32)

$$\max_j \left| \left|\left| \left(\vec{f}^{(j)}\right)^{(k)} \right|\right|_2 - 1 \right| = 0, \quad j = 1, ..., N. \tag{33}$$

As this condition is generally not fulfilled, a correction step according to

$$\left(\vec{f}^{(j)}\right)^{(k*)} = \frac{\left(\vec{f}^{(j)}\right)^{(k)}}{\left|\left(\vec{f}^{(j)}\right)^{(k)}\right|}, \quad j = 1, ..., N, \tag{34}$$

is performed. Consistency is given by multiplying the columns of $\mathbf{A}$ by the Euclidean norm of the corresponding line of $\mathbf{F}^{(k)}$. As the next iteration starts, $\mathbf{F}^{(k*)}$ is inserted in (28), (24) and (25) to fill the system again. Convergence is formally proven in [20, 21] and typically reached within 100 iterations in the first time step and less than 50 afterwards. The algorithm stops after reaching the residual criterion

$$\max_j \left| \left|\left| \left(\vec{f}^{(j)}\right)^{(k)} \right|\right|_2 - 1 \right| < \text{tol}, \quad j = 1, ..., N, \tag{35}$$

which corresponds to the conservation of all bar unit vectors within a tolerance typically chosen as 10^{-4}. In this paper, the influence of the mooring system on the fluid is neglected because hydrodynamic transparency is assumed. This is justified by the focus on the motion of the body, which is not affected by the fluid disturbances due to the presence of the mooring lines. Thus, the communicated data from the mooring algorithm to the FSI solver only includes the tension force and angle of attack at the upper mounting point. The force is added to the calculated fluid forces on the floating body (see also Fig. 5).

Alternatively, (29) can be solved using Newton-Raphson iterations. As shown in [28], the solution vector then contains a single column with directions of the unit bars and tension forces. Under consideration of the multiple inversions to reach convergence, the successive approximation arises as the more efficient algorithm due to a significantly decreased matrix size. Additionally, the boundary condition is not directly included in a Newton-Raphson method such that its fulfilment is not guaranteed without sufficient convergence.

3 Validation process

3.1 Validation of the mooring model

The validation of the proposed mooring model includes comparisons of line shape and maximum tension forces with experimental data. First, the maximum tension force is analysed for a single mooring line attached to a buoy with prescribed heave motion. The mooring line consists of chains and wires of different material properties which can be found in the work of Chenga et al. [11]. Here, linear material is assumed. A preliminary static test is conducted to validate the forces for different positive offsets. The resulting distribution is shown in Fig. 6a. The deviation between the numerical model and experiments is generally small but increases slightly with increasing offset. The error is between -0.2% for offsets smaller than 5 m and increases to $\approx 1.1\%$ for 30 m offset. Next, a simple harmonic heave motion with an amplitude of 15 m and a period of 10 s is prescribed to the top of the line. Good agreement with the measurements can be stated from comparing the distributions shown in Fig. 6b. Generally, the numerical model slightly under predicts the troughs and over predicts the crests by $\approx 2.5\%$ in peak height. A Fourier analysis of the time series indicates an error of less than 1% for the amplitude of the fundamental frequency.

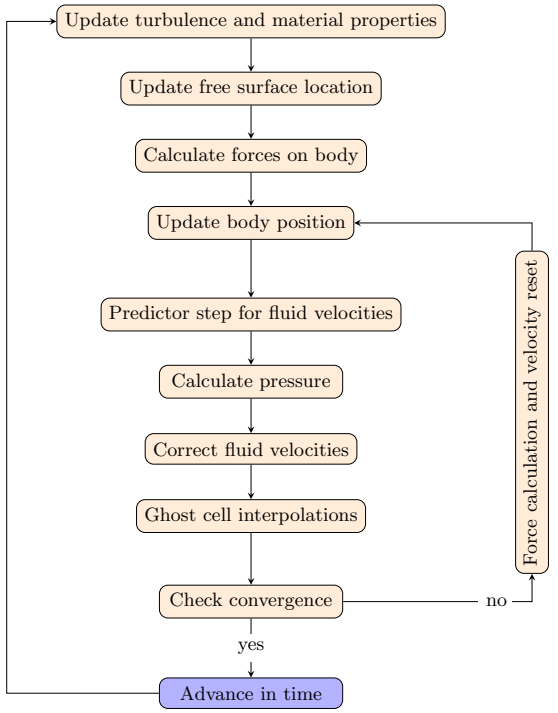

Figure 5: Illustration of the fluid-structure interaction algorithm for simulating moored floating structures in waves.

Next, the mooring model is validated by comparison to experimental results from wind channel measurements at the Institute of Ocean Engineering at the University of Rostock, Germany. The considered mooring system consists of a single rope with a length of $L_m = 1.82$ m, a diameter of $d_t = 0.004$ m, a specific weight of $\gamma = 0.089$ kg/m and Young's modulus of 7.9 GPa. The line is fixed at the coordinates $(x, y) = (0\text{ m}, 0\text{ m})$ and mounted to a moveable load cell on the top to measure maximum tension forces. The wind machine at the inlet of the channel generates a laminar flow of predefined velocity which the mooring system is exposed to. A touch probe moves laterally along the deformed rope to record coordinates during static tests. Dynamic deformations are recorded using side view pictures.

In the first set of experiments, three different locations of the upper mounting point are investigated without inflow. Numerical results are produced using the same input data as given above. The results in Fig. 7 show the distribution of the discrete line with 5, 10 and 50 bar elements and the comparison to the experimental data. Regardless of the considered distribution, the numerical model can accurately reproduce the experimental measurements. Small under and over predictions can be found for the coarsest line discretisation and the hanging rope distribution in Fig. 7a which is overcome by increasing the number of elements slightly. The second set of experiments is conducted by applying inflow velocities of $v = 8$ m/s

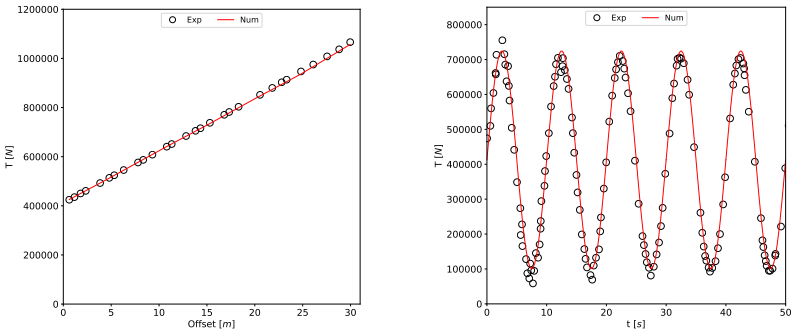

(a) Tension forces for different heave offsets.

(b) Maximum tension force time series for the dynamic case.

Figure 6: Comparison of numerical and experimental results for the static analysis and the prescribed heave motion.

and $v = 18$ m/s on the stretched rope distribution of Fig. 7c. The drag coefficients are calculated from (35), and $c_t = 0.35$ is chosen from literature [45]. The results, shown in Fig. 8, indicate that the numerical model is capable of representing the physical deformation of ropes in stationary flow conditions. All line discretisations coincide with the experiment accurately. Further information on the accuracy is provided by presenting the numerical and experimental results for the maximum tension forces over different inflow velocities in Tab. 1. It can be seen that the model converges towards the experimental data as the number of bar elements increases. This is demonstrated by calculating an extrapolated value without discretisation error from the numerical results using Richardson extrapolation [39]. The remaining deviation from experiments is related to the model error. Here, a good agreement with the experiments can be stated because the maximum error is below 3% for $v = 8$ m/s.

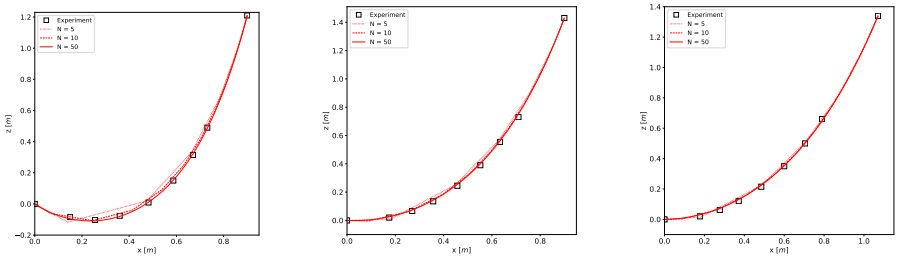

(a) Hanging rope distribution.

(b) Catenary rope distribution.

(c) Stretched rope distribution.

Figure 7: Numerical and experimental mooring line distributions without inflow.

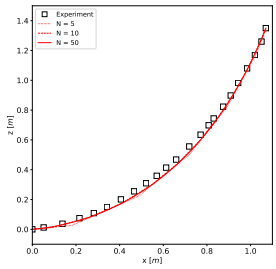

(a) Stretched rope distribution at $v = 8$ m/s.

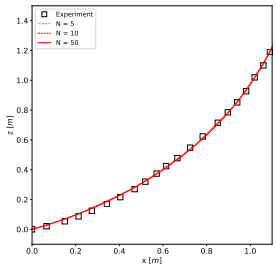

(b) Stretched rope distribution at $v = 18$ m/s.

Figure 8: Numerical and experimental mooring line distributions for different inflow velocities.

Table 1: Numerical and experimental maximum tension forces for inflow velocities between $v = 0\ m/s$ and $v = 18\ m/s$. Values in $[N]$ if not defined differently.

$v\ [m/s]$	Exp	N=5	N=10	N=50	Extrapol.	Error [%]
0.0	1.54	1.61	1.57	1.56	1.56	1.45
8.01	1.65	1.74	1.71	1.70	1.70	2.93
11.97	1.90	1.93	1.90	1.89	1.89	-0.43
14.08	2.01	2.06	2.03	2.02	2.02	1.22
16.08	2.21	2.21	2.19	2.18	2.18	-0.94
18.05	2.40	2.39	2.37	2.36	2.36	-1.64

3.2 Validation of the rigid body dynamics solver

The derived solver for the rigid body dynamics simulation is validated. A major advantage of the chosen Hamiltonian approach is the direct availability of the kinetic energy of the system T in runtime. In canonical form, it is calculated as (compare [40]):

$$T = \frac{1}{2}(\mathbf{G}^T h)^T \mathbf{G}^T I^{-1} \mathbf{G}\mathbf{G}^T h. \tag{36}$$

In absence of external forces, (36) is constant in time. Considering the time evolution of the phase space of fixed energy states, the volume of this space should remain constant according to Liouville's theorem. This condition is ensured by using time-reversible, symplectic methods. The second-order Verlet algorithm conserves energy in the mean [43] and has, hence, advantages over forward integration methods such as Runge-Kutta schemes. For system (16) and (19), the advance from time step n to $n+1$ is calculated using

$$h^* = h^{(n)} + \frac{\Delta t}{2} L(e, h^*), \tag{37}$$

$$e^{(n+1)} = e^{(n)} + \frac{\Delta t}{2} L(e^{(n)}, h^*), \tag{38}$$

$$h^{(n+1)} = h^{(n)} + \frac{\Delta t}{2} L(e^{(n+1)}, h^*). \tag{39}$$

Both, (37) and (39) are implicit equations which need time-consuming sub-iterations. Therefore, a fast forward method might be the better option in terms of efficiency. In the following, the motion of a rigid body [40] with the principal moments of inertia of $400, 307.808$ and $200\ kg\ m^2$ and an initial momentum of $\vec{h}_0 = (346.410, 0.0, 200.0)^T$ N ms shall be investigated with the second-order accurate Verlet and the fourth-order accurate Runge-Kutta scheme.

First, torque-free motion is assumed. The Verlet scheme benefits from its time-reversibility as can be seen in Tab. 2. It shows the error in energy conservation for different time step sizes after a 20 s simulation. The method conserves the original energy of the system up to machine precision irrespective of the chosen step size. In comparison, the Runge-Kutta method converges with the expected rate of $p \approx 4$ and needs smaller time steps to conserve energy.

Table 2: Convergence of the error in energy conservation in $[J]$ using the fourth-order Runge-Kutta and the second-order Verlet scheme.

Scheme	$\Delta t = 1$	$\Delta t = 0.1$	$\Delta t = 0.01$	p
RK4	28.21	0.0043	5.57e-08	3.82
Verlet	1.99e-13	3.13e-13	3.13e-13	-

In a second example, a constant torque of 10 Nm around the x-axis is imposed. This implies a change of the kinetic energy as indicated in Tab. 3. Both schemes show the expected rate of convergence. Therefore, the Runge-Kutta scheme converges faster than the Verlet scheme which leads to a bigger discrepancy of the latter method to the converged energy of $528.520\ J$ for small time steps. The time consumption of both methods is compared in Tab. 4. Here, the time consumed with the biggest time steps is taken as the reference. As expected, the Runge-Kutta scheme is not just faster than the Verlet scheme but also scales much better for smaller time-stepping due to its explicit nature. In combination with the results from Tab. 3, it can be concluded that the Runge-Kutta scheme is the more efficient choice for the calculation of the rigid body motions. In practice, the time steps are relatively small due to the velocity restriction in the fluid so that the lack of energy conservation is not seen as critical.

Table 3: Convergence of the total kinetic energy in $[J]$ using the fourth-order Runge-Kutta and the second-order Verlet scheme.

Scheme	$\Delta t = 1$	$\Delta t = 0.1$	$\Delta t = 0.01$	p
RK4	237.78	528.47	528.52	3.77
Verlet	574.25	529.37	528.56	1.74

Table 4: Time increase for different time step sizes using the fourth-order Runge-Kutta and the second-order Verlet scheme.

Scheme	$\Delta t = 1$	$\Delta t = 0.1$	$\Delta t = 0.01$
RK4	1 ($0.021s$)	1.372	4.26
Verlet	1 ($0.070s$)	5.67	51.72

3.3 Validation of the floating algorithm

A validation case for the floating algorithm without mooring is presented. The numerical simulation of a free floating barge in waves is compared to the experimental data of Ren et al. [38]. The 2D setup is illustrated in Fig. 9 and consists of a wave tank with a length of 20 m, a height of 0.8 m and a water depth of $d = 0.4$ m. A 0.3 m $\times$ 0.2 m barge with density $\rho_s = 500$ kg/m^3 is placed in the tank at $(x, z) = (7.0\text{ m}, 0.4\text{ m})$. Regular waves are modelled as second-order Stokes waves in a wave generation zone at the inlet. The wave generation zone is one wavelength long. The incoming waves have a height of $H = 0.04$ m, a period of $T = 1.2$ s and a wavelength of $\lambda = 1.936$ m. Wave reflections are prevented by placing a numerical beach of two wavelengths at the outlet. The numerical methods described in section 2.1 are applied. The convergence is investigated using three different mesh configurations with the smallest cell sizes $\Delta x = 0.012\text{ m}, 0.01\text{ m}, 0.007$ m, leading to $80, 120$ and 200 thousand cells. Stretching functions are used to coarsen the cell size in x-direction towards the inlet and outlet and z-direction towards bottom and top.

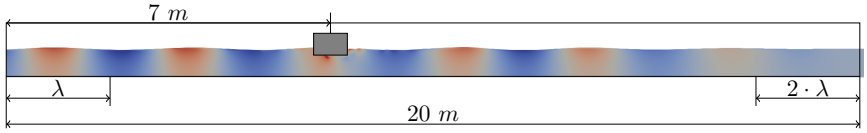

Figure 9: Numerical setup for the simulation of a 2D barge in a wave tank.

In a first step, the time series for the wave elevation η at $x = 5.5$ m and the surge motion ξ, the heave motion ζ and the pitch motion θ of the free floating barge are compared with the measurements for the time period between $t/T = 6$ and $t/T = 12$ (Fig. 10). It shows the results for the medium grid and CFL$= 0.1$. In Fig. 10a, the wave elevation in front of the barge is presented. Good agreement with the experiments can be stated. Similarly, the heave motion in Fig. 10b reproduces the measurements but shows minor under- and overshoots. The pitch motion is shown in Fig. 10c. The numerically predicted frequency follows the experiment, but some deviations can be observed for the amplitudes of the motion. Both, experiments and the simulation show minor irregularities for the amplitudes at different time instances. Fig. 10d presents the surge motion over time. A very good agreement of the numerical simulation with the experiments can be seen.

As a further step, the spatial and temporal convergence of the model is calculate based on the procedure described above. In case of an oscillatory converging behaviour, the average of the two extreme values is taken as the extrapolated value. The presented error then corresponds to the discrepancy between this value and the experimental results. A constant CFL number of 0.1 is chosen for the spatial convergence test, and the medium grid is considered for the temporal convergence test. The mean frequency and amplitude are considered to be the variables of interest for this study. Special attention is given to the surge motion because a high-frequency motion superimposes the mean drift of the body due to Stokes drift forces. The latter presents the most important parameter in practice and is investigated in terms of its gradient in the space-time domain.

The spatial convergence study is presented in Tab. 5 and Tab. 6. For the mean periods, all variables show oscillatory convergence. The resulting extrapolated values under predict

the measurements by up to 4%. In comparison, the main amplitude tends to over predict the experiments by up to 10%. For the mean drift in the surge motion, the coarsest grid clearly under-resolves the physics leading to a large over prediction. Thus, the extrapolated value and the resulting error is misleading. If the average value of the two finer grids for the surge motion is considered instead, the error would be 9% which is in a similar order as the predicted errors of other motions.

The temporal convergence study is shown in Tab. 7 and Tab. 8. All variables converge except the heave period which shows an oscillatory diverging behaviour. However, all the calculated periods are very close to the experiment and, therefore, the average value is still assumed to be valid. The general agreement of the numerical values with the measurements is within 8%. Hence, mean periods tend to be predicted more accurately than mean amplitudes. It might also be noticed that the proposed model computes stable results even for higher CFL numbers.

Table 5: Spatial convergence of the numerical mean period (dimensionless) in comparison to the experimental results. For the surge motion, the high-frequency component is analysed here.

Motion	Coarse	Medium	Fine	Extrapol.	Exp	Error [%]
η	0.951	1.046	0.997	0.974	0.998	2.4
ζ	0.992	1.012	0.995	0.994	0.997	0.3
θ	1.018	1.051	1.027	1.023	1.059	3.5

Table 6: Spatial convergence of the numerical mean amplitude (dimensionless) in comparison to the experimental results. For the surge motion, the mean drift is considered.

Motion	Coarse	Medium	Fine	Extrapol.	Exp	Error [%]
η	0.0567	0.0558	0.0546	0.0531	0.0513	-3.4
ζ	0.0580	0.0593	0.0587	0.0584	0.0615	5.3
θ	0.0437	0.0394	0.0426	0.0432	0.0388	-10.2
ξ	0.1008	0.0763	0.0812	0.0911	0.0715	-21.5

Table 7: Temporal convergence of the numerical mean period (dimensionless) in comparison to the experimental results.

Motion	CFL 0.5	CFL 0.3	CFL 0.1	Extrapol.	Exp	Error [%]
η	1.021	1.036	1.046	1.048	0.998	-4.7
ζ	1.001	0.999	1.012	1.004	0.997	-0.7
θ	1.027	1.047	1.051	1.051	1.059	0.8

Table 8: Temporal convergence of the numerical mean amplitude (dimensionless) in comparison to the experimental results. For the surge motion, the mean drift is considered.

Motion	CFL 0.5	CFL 0.3	CFL 0.1	Extrapol.	Exp	Error [%]
η	0.0587	0.0571	0.0558	0.0554	0.0513	-7.4
ζ	0.0621	0.0604	0.0593	0,0591	0.0615	4.1
θ	0.0426	0.0409	0.0394	0.0387	0.0388	0.3
ξ	0.0774	0.0683	0.0763	0.0769	0.0715	-7.0

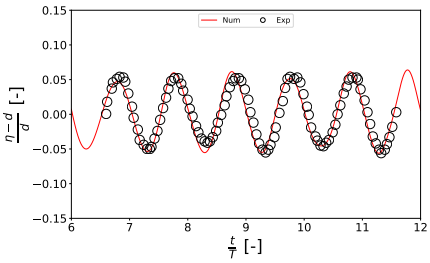

(a) Wave elevation over time at $x = 5.5$ m.

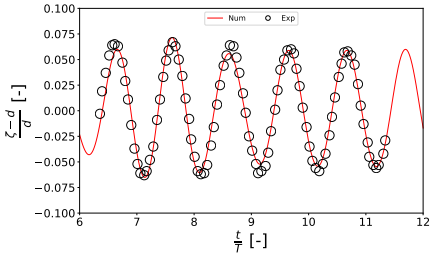

(b) Heave motion over time.

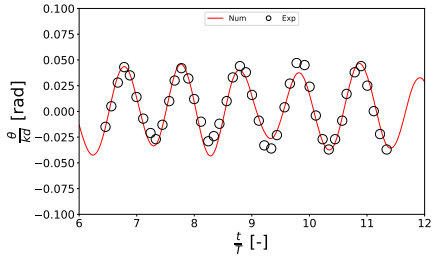

(c) Pitch motion over time.

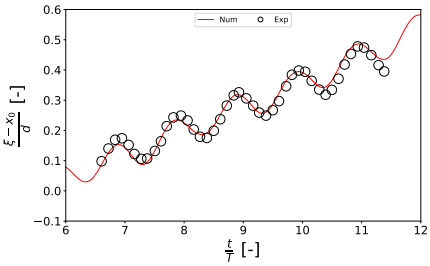

(d) Surge motion over time.

Figure 10: 3DOF motion of the two-dimensional barge over time. Comparison of numerical and experimental results for $\Delta x = 0.01$ m and CFL$= 0.1$.

3.4 Validation of the complete moored floating algorithm

The three degrees of motion of a moored floating barge in waves is investigated. Experiments were conducted at the wave flume of the Ludwig-Franzius-Institute Hannover, Germany. The investigated barge Is made of a material with a uniform density of 680 kg/m^3. It has a length of 0.3 m and a height of 0.15 m. The incoming waves have a height of $H = 0.03$ m and periods of $T = 1.2$ s and $T = 1.6$ s, respectively. Both waves are modelled using the second-order Stokes theory. Fig. 11 illustrates the two-dimensional numerical domain. The tank is 20 m long, and the water height is fixed to $d = 0.85$ m. The centre of the barge is initially located at $(x, z) = (10\text{ m}, 0.823\text{ m})$. Based on the results of the previous simulations, a cell size of 0.012 m and CFL$= 0.5$ are considered. Two mooring lines are fixed to the barge at still water

level. The distance between the centre of the barge and the bottom mounting point of the lines is 4.15 m along the x-axis. Both lines have a length of $L_m = 4.07$ m, a diameter of $d_t = 0.94$ mm and a stiffness of $K_1 = 10e5$ N^{-1}. Their weight is negligible in water. A wave gauge is placed 2 m in front of the centre of the barge to calculate the incident and reflected waves.

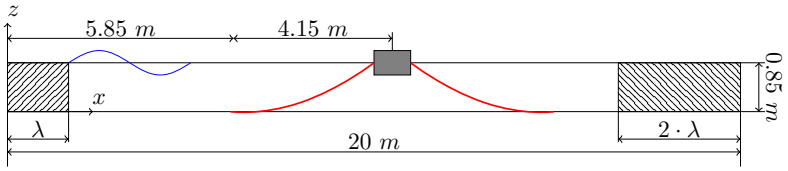

Figure 11: Numerical setup for the simulation of a 2D moored floating barge in a wave tank.

The predicted and measured mean period and amplitude, as well as the discrepancy for the wave elevation and the three degrees of motion, are given in Tab. 9 and Tab. 12. For the wave with $T = 1.2$ s, it is noticed that the numerical model generally under predicts both period and amplitude, for all motions. For the mean period, very good agreement with the experiments can be observed as the error band is below 4%. At the same time, the numerical amplitudes deviate from the measurements by up to 29% for the heave motion. As the period of the waves increases, improved prediction of the periods can be observed (below 2%), and the maximum amplitude error is 35% for the surge motion.

Table 9: Numerical and experimental results and error [%] between numerical and experimental mean period and amplitude for the original simulation of a moored floating barge in waves with $T = 1.2$ s.

Motion	Exp		Num		Error	
	Period [s]	Amplitude [m]	Period [s]	Amplitude [m]	Period	Amplitude
η	1.22	0.015	1.20	0.013	1.505	14.012
ζ	1.23	0.018	1.19	0.013	3.363	28.978
θ	1.21	8.857	1.18	5.605	2.154	26.717
ξ	1.22	0.016	1.19	0.012	1.805	23.136

Table 10: Error [%] between numerical and experimental mean period and amplitude for the simulation with a shifted centre of gravity in z-direction with $T = 1.2$ s.

Motion	CG +3 mm		CG −3 mm	
	Period	Amplitude	Period	Amplitude
η	1.591	7.151	1.941	32.452
ζ	3.268	21.095	3.750	27.568
θ	1.164	41.296	2.894	4.665
ξ	3.231	28.260	2.988	31.751

Both simulations indicate a reduction of accuracy in comparison to the free floating case. A source of error is possibly small measurement errors in one of the sub-systems, which then adds

Table 11: Error [%] between numerical and experimental mean period and amplitude with varying stiffness constants with $T = 1.2$ s.

Motion	EA +5%		EA −5%	
	Period	Amplitude	Period	Amplitude
η	1.697	16.854	1.662	29.674
ζ	3.288	27.910	3.571	30.415
θ	1.371	26.889	1.146	39.142
ξ	3.393	25.794	2.963	27.619

up for this complicated fluid-structure interaction problem. In order to analyse this suspected sensitivity, reported parameters are varied slightly and compared to the original results. First, the location of the centre of gravity is shifted in the positive and negative z-direction by 3 mm which might be linked to imperfect manufacturing of the barge. Tab. 10 and Tab. 13 present the resulting errors. For $T = 1.2$ s, the chosen modification has no significant effect on the mean periods but considerably affects the simulated mean amplitudes. The error for the heave motion is reduced from 28% to 21%, and the mean wave amplitude prediction is improved by 50% if the centre of gravity is slightly higher. In contrast, a lower centre of gravity improves the pitch amplitude prediction from 26% to below 5% deviation from the experiments. For $T = 1.6$ s, considering a higher centre of gravity has no significant effect on the computations. However, the decrease of the centre improves the pitch amplitude which is also observed for the shorter wave. These findings indicate a strong sensitivity of the motion to the correct location of the centre of gravity. At the same time, the strong coupling between the different motions is highlighted. An additional investigation of the influence of the stiffness constant is shown in Tab. 11 for the shorter wave. The results indicate no significant difference if the value is increased by 5% but a higher difference is noticed if the stiffness constant is reduced by 5%.

The time series of the tension forces in the top of the front and back mooring line are shown in Fig. 12 for both waves. As the experiment did not consider force measurements only the numerical results are provided. The alternating occurrence of force peaks can be observed and is explained through a strong back and forth motion of the barge as indicated in Fig. 13. The relatively tense initial configuration of the mooring lines results in snap-like reaction forces as the barge is moving in and against wave direction in wave crest and trough situations. Generally, the forces increase with the increase of the wave period due to higher wave forces acting on the moored floating body.

Table 12: Numerical and experimental results and error [%] between numerical and experimental mean period and amplitude for the original simulation of a moored floating barge in waves with $T = 1.6$ s.

Motion	Exp		Num		Error	
	Period [s]	Amplitude [m]	Period [s]	Amplitude [m]	Period	Amplitude
η	1.61	0.016	1.59	0.014	1.155	12.817
ζ	1.62	0.016	1.59	0.014	1.798	11.524
θ	1.62	2.158	1.59	3.379	1.757	−26.595
ξ	1.61	0.029	1.60	0.0185	0.769	35.903

Table 13: Error [%] between numerical and experimental mean period and amplitude for the simulation with a shifted centre of gravity in z-direction with $T = 1.6$ s.

Motion	CG +3 mm		CG −3 mm	
	Period	Amplitude	Period	Amplitude
η	1.185	14.220	0.839	12.919
ζ	1.692	12.670	1.849	10.060
θ	9.537	−30.673	0.789	−14.231
ξ	1.571	35.449	1.097	41.024

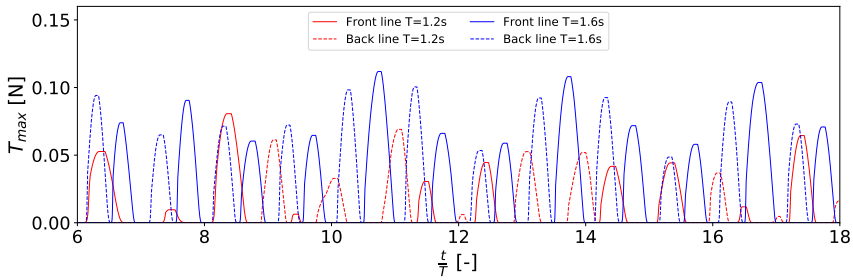

Figure 12: Tension forces in the top of the front and back mooring line over time. Forces for $T = 1.2$ s are marked in red; forces for $T = 1.6$ s are marked in blue. Solid lines indicate the front lines; dashed lines indicate the lines behind the body.

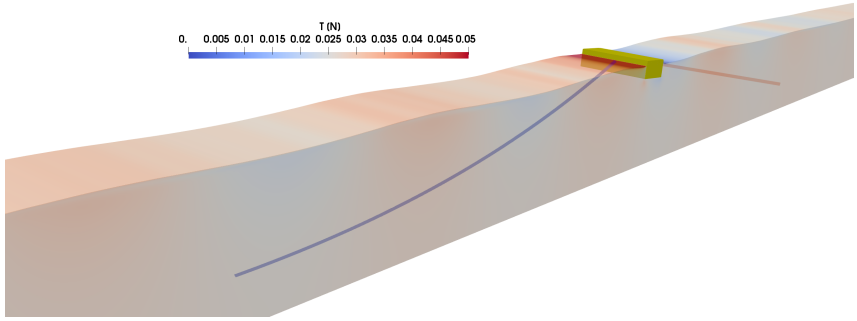

Figure 13: Fluid-structure interaction of a barge in waves. Situation with one slack and one taut mooring line.

4 Application to a moored floating semi-submersible platform

The range of applications of the proposed moored floating FSI algorithm is broad and can include both, mooring system analysis and restricted motion analysis. Exemplarily, the analysis of a moored floating semi-submersible platform is presented. The geometry and

properties of the platform are taken from [36] and shown in Fig. 14. The model consists of two rectangular floaters and six cylindrical columns placed symmetrically on the floaters. The height of the cylinders is such that they pierce the free surface at any time. The platform has a mass of $m_s = 34.58$ kg, and the principal moments of inertia are $(I_{xx}, I_{yy}, I_{zz}) = (3.227\ kg\ m^2, 5.23\ kg\ m^2, 6.0246\ kg\ m^2)$. The centre of gravity is 0.086 m above keel, and the draft is 0.2 m. The platform is placed in the middle of a three-dimensional wave tank with a length of 10 m, a width of 2 m, a height of 3 m and a water height of $d = 1.9$ m (see Fig. 15). Active wave generation [31], which prescribes the velocities and the free surface as Dirichlet boundary conditions at the inlet, is utilised. A numerical beach is placed at the outlet to prevent reflections. Six mooring lines are attached centred under the cylinders: two front and back lines, respectively, with the same length and two shorter middle lines. Their properties can be found in Tab. 14. Six different cases are considered: Three head wave conditions with $H = 0.1$ m and $\lambda = 0.9735$ m, 1.947 m and 3.894 m, and three beam wave conditions with the same wave input. Both, free floating and moored floating configurations are investigated.

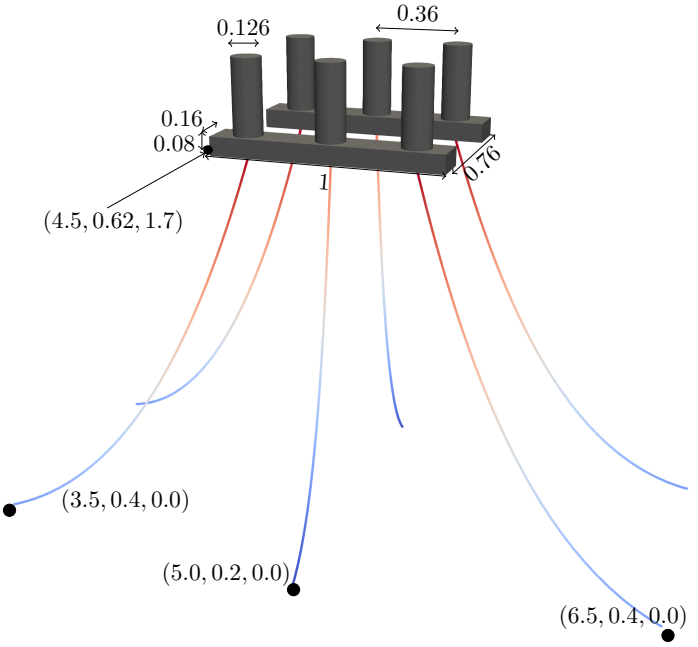

Figure 14: Geometry of the mooring system and the semi-submersible platform. All measures in metre.

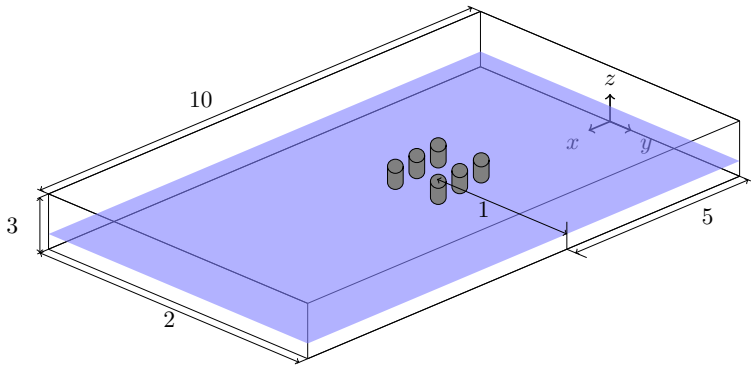

Figure 15: Dimensions of the numerical wave tank for the simulation of a moored semi-submersible platform in regular waves. All measures in metre.

Table 14: Properties of the mooring system attached to the semi-submersible platform.

Line	γ $[kg/m]$	ρ_m $[kg/m^3]$	K_1 $[1/N]$	d $[m]$	L $[m]$
Front & back	0.05	1100	10000	0.00085	2.15
Middle	0.05	1100	10000	0.00085	1.8

In Fig. 16a, the mean periods and amplitudes of the wave elevation 1.5 m in front of the platform are shown. It can be seen that the influence of the body on the wave periods is small, but the amplitude is influenced by the wave direction and length. As the wavelength decreases, the amplitude of the wave decreases. For head waves, the amplitude decreases if a mooring system is attached, whereas the amplitude increases in long beam waves due to stronger reflections. The same investigation is presented in Fig. 16b for the heave motion. Without any restriction, the heave amplitudes and periods decrease with decreasing wavelength. When the platform is moored, strongly non-linear interactions lead to the smallest periods for the intermediate wavelength, whereas the amplitude decreases with the length of the incident wave. As a tendency, the heave amplitudes are higher in head than in beam waves. For the pitch motion in Fig. 16c, a general increase of the amplitude is observed if the mooring system is attached. In head waves, the pitch period increases with mooring. In contrast, the period decreases for beam waves. Overall, the most significant influence of the mooring system is on the pitch motion of the platform in head waves and on the heave motion in beam waves. An explanation for these observations is shown in Fig. 17 which depicts the moored floating platform in head and beam wave crest situations for a wavelength of 1.947 m. In head waves (Fig. 17a), the two front lines get tensed, whereas the middle line is tensed in beam waves (Fig. 17a). The angle of attack at the mounting point is larger at the front lines than at the middle lines. This leads to larger horizontal forces in the front lines and larger vertical forces in the middle lines, and, accordingly, to higher influences of rolling and heave motions.

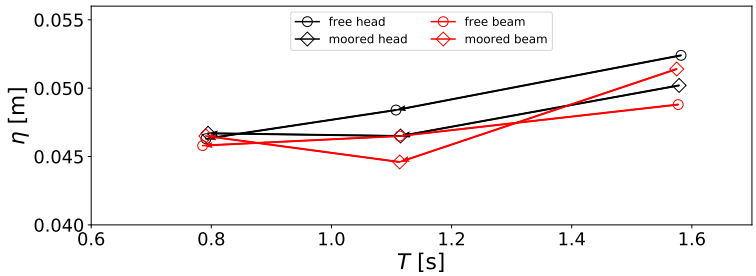

(a) Free surface elevation at $(x, y) = (3.5\ m, 1\ m)$.

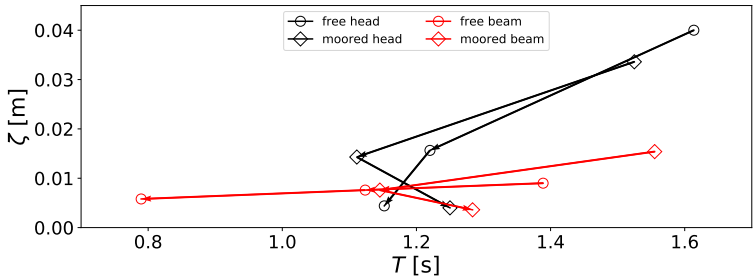

(b) Heave motion.

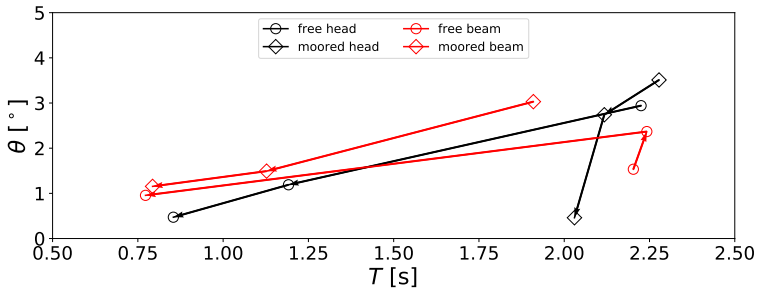

(c) Pitch motion.

Figure 16: Mean amplitudes over mean period for the motions of the three-dimensional moored floating semi-submersible platform. Black lines indicate head waves, red lines beam waves. Free floating motion is marked with (○), moored floating with (◇). Arrows point from the longest to the shortest incoming wave.

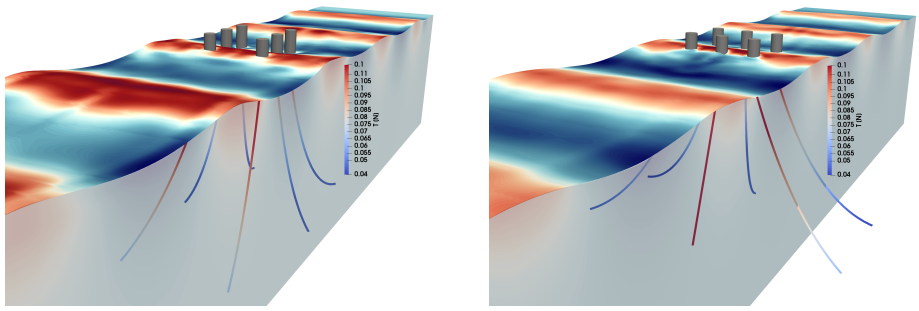

(a) Head wave condition.

(b) Beam wave condition.

Figure 17: Tension force distribution in mooring system for a wave crest situation. The incoming wavelength is 1.947 m.

5 Conclusion

A new approach for simulating the effect of mooring systems on floating structures is presented. It is based on quasi-static assumptions and a discretisation into elastic bars and mass points connecting them. The introduction of successive approximation for this problem raises the possibility to converge to a physically relevant solution within a small number of iterations. Any restriction on time stepping is removed and no initial shape of the line has to be given. It is also noticed that the method was originally developed for nets [29] and direct coupling of both system matrices is now possible for applications in aquaculture technology.

An improved non-iterative weakly-coupled model has been proposed for the accurate and efficient simulation of fluid-structure interaction problems including the physical constraint of mooring systems. The basis of these developments is a previously presented FSI algorithm [5] which adapted a directional ghost cell immersed boundary method for moving bodies. The simplicity of this algorithm, due to the absence of an iterative algorithm and the usage of a ghost cell method, is now combined with several improvements to increase the overall accuracy. The rigid body dynamics solver is based on Euler parameters and Hamiltonian mechanics. Thus, the gimbal lock leading to a loss of a degree of freedom for Euler angles is avoided and arbitrary bodies and motions can be modelled. The resulting system is of the first order and free of constraints or Lagrangian multipliers. This enables the application of simple but high-order numerical integration techniques. A further advantage of a Hamiltonian is the energy-based formulation. In the validation process, this could be utilised to investigate the applicability of explicit methods like the Runge-Kutta method. It was shown that even relatively large time steps lead to sufficient conservation of energy such that conservative but less efficient methods do not have to be used. Further, the computation of areas, moments of inertia and forces is improved by considering the original triangulated surface of the body. The integration process of the geometrical quantities is simplified by mapping and solving it analytically. Similarly, the introduction of linear interpolations and the explicit distinction between pressure and velocity grids leads to a more reliable formulation. The new FSI solver is validated for a challenging free floating case in regular waves. Convergence in time and space is shown, and all physically important aspects of the motion are captured by the proposed model.

The comparison of the physically constrained motion of a floating barge in waves with experiments underlines the accuracy of the coupled solver. Very good agreement exists for the mean periods. The complexity of this problem is highlighted by investigating the influence of small inaccuracies in the body's centre of gravity position on the results. It is shown that the prediction of the mean amplitudes for heave and pitch is highly dependent on this position. Additionally, the interaction of the different body motions and the mooring lines changes eventually. The application to a semi-submersible platform indicates the possibility of time-domain analyses including the coupled dynamics of waves, rigid bodies and mooring systems.

Acknowledgements

The authors are grateful for the grants provided by the Research Council of Norway under the HAVBRUK2 project (no. 267981). This research was supported in part with computational resources at NTNU provided by NOTUR (Norwegian Metacenter for Computational Sciences, http://www.notur.no) under project no. NN2620K.

References

[1] O.M. Aamo and T.I. Fossen. "Finite Element Modelling of Moored Vessels". In: *Mathematical and Computer Modelling of Dynamical Systems* Volume 7(1) (2001), 47–75.

[2] C.M. Ablow and S. Schechter. "Numerical Solution of Undersea Cable Dynamics". In: *Ocean Engineering* Volume 10 (1983), 443–457.

[3] S.F. Ashby and R.D. Flagout. "A parallel mulitgrid preconditioned conjugate gradient algorithm for groundwater flow simulations". In: *Nuclear Science and Engineering* Volume 124(1) (1996), 145–159.

[4] P.A. Berthelsen and O.M. Faltinsen. "A local directional ghost cell approach for incompressible viscous flow problems with irregular boundaries". In: *Journal of Computational Physics* Volume 227 (2008), 4354–4397.

[5] H. Bihs and A. Kamath. "A combined level set/ghost cell immersed boundary representation for floating body simulations". In: *Int. J. Numer. Meth. Fluids* Volume 83 (2017), 905–916.

[6] H. Bihs et al. "A new level set numerical wave tank with improved density interpolation for complex wave hydrodynamics". In: *Computers & Fluids* Volume 140 (2016), 191–208.

[7] Iman Borazjani et al. "A parallel overset-curvilinear-immersed boundary framework for simulating complex 3D incompressible flows". In: *Computers & Fluids* 77 (2013), pp. 76–96.

[8] J.U. Brackbill, D.B. Kothe, and C. Zemach. "A Continuum Method for Modeling Surface Tension". In: *Journal of Computational Physics* Volume 100(2) (1992), 335–354.

[9] A. Calderer, S. Kang, and F. Sotiropoulos. "Level set immersed boundary method for coupled simulation of air/water interaction with complex floating structures". In: *Journal of Computational Physics* Volume 277 (2014), 201–227.

[10] P.M. Carrica, R.W. Noack, and F. Stern. "Ship motions using single-phase level set with dynamic overset grid". In: *Computers & Fluids* Volume 36 (2007), 1415–1433.

[11] Y. Chenga et al. "Nonlinear analysis for ship-generated waves interaction with mooring line/riser systems". In: *Marine Structures* Volume 59 (2018), 1–24.

[12] Y.-I. Choo and M.J. Casarella. "Hydrodynamic Resistance of Towed Cables". In: *J. Hydronautics* Volume 5 (4) (1971), 126–131.

[13] A. Chorin. "Numerical solution of the Navier-Stokes equations". In: *Mathematics of Computation* Volume 22 (1968), 745–762.

[14] J. Davidson and J. Ringwood. "Mathematical modelling of mooring systems for wave energy converters-A review". In: *Energies* Volume 10 (2017), p. 666.

[15] J.M. Domínguez et al. "SPH simulation of floating structures with moorings". In: *Coastal Engineering* Volume 153 (2019). DOI: 103560.

[16] D. H. Eberly and K. Shoemake. *Game Physics*. Taylor Francis, London, UK., 2010.

[17] E. A. Fadlun et al. "Combined Immersed-Boundary Finite-Difference Methods for Three-Dimensional Complex Flow Simulations". In: *Journal of Computational Physics* 161 (2000), pp. 35–60.

[18] O.M. Faltinsen. *Sea Loads on Ships and Offshore Structures*. Cambridge University Press, Cambridge, 1990.

[19] H. Goldstein, C. P. Poole, and J. L. Safko. *Classical Mechanics*. Addison-Wesley, Boston, USA, 2001.

[20] W. Hackmann. "Mathematische Begründung von Verfahren zur Berechnung von Form und Zugkraft in Fadenzugsystemen". In: *ZAMM* Volume 63 (1983), 173–184.

[21] W. Hackmann. "Zur Lösung der Grundgleichungen des Fadens bei gleichförmiger Bewegung in einer Flüssigkeit". In: *ZAMM* Volume 62 (1982), 191–199.

[22] M. Hall and A. Goupee. "Validation of a lumped-mass mooring line model with DeepCwind semisubmersible model test data". In: *Ocean Engineering* Volume 104 (2015), 590–603.

[23] A. Hanaoka. *An overset grid method coupling an orthogonal curvilinear grid solver and a Cartesian grid solver*. Ph.D. thesis, University of Iowa, USA. 2013.

[24] C.-C. Huang, H.-J. Tang, and J.-Y. Liu. "Dynamical analysis of net cage structures for marine aquaculture: Numerical simulation and model testing". In: *Aquacultural Engineering* Volume 35 (2006), 258–270.

[25] N.G. Jacobsen, D.R. Fuhrman, and J. Fredsöe. "A wave generation toolbox for the open-source CFD library: OpenFoam". In: *International Journal for Numerical Methods in Fluids* Volume 70(9) ([2012).

[26] G.S. Jiang and D. Peng. "Weighted ENO schemes for Hamilton Jacobi equations". In: *SIAM Journal of Scientific Computing* Volume 21 (2000), 2126–2143.

[27] G.S. Jiang and C.W. Shu. "Efficient implementation of weighted ENO schemes". In: *Journal of Computational Physics* Volume 126(1) (1996), 202–228.

[28] H. Leitzke. *Berechnung von Form und Kräften biegeschlaffer, räumlicher Zugsysteme.* Ph.D. thesis, University of Rostock, Germany. 1983.

[29] T. Martin et al. "Efficient implementation of a numerical model for flexible net structures". In: *Ocean Engineering* Volume 150 (2018), 272–279.

[30] S. Mayer, A. Garapon, and L.S. S örensen. "A fractional step method for unsteady free-surface flow with applications to non-linear wave dynamics". In: *International Journal for Numerical Methods in Fluids* Volume 28 (1998), 293–315.

[31] A. Moreno Miquel et al. "Analysis of Different Methods for Wave Generation and Absorption in a CFD-Based Numerical Wave Tank". In: *Journal of Marine Science and Engineering* 6 (2) (2018). DOI: 10.3390/jmse6020073.

[32] S. Osher and J.A. Sethian. "Fronts propagating with curvature-dependent speed: Algorithms based on Hamilton-Jacobi formulations". In: *Journal of Computational Physics* Volume 79 (1988), 12–49.

[33] J. Palm. *Mooring Dynamics for Wave Energy Applications.* Ph.D. thesis, Chalmers University of Technology, Gothenburg, Sweden. 2017.

[34] J. Palm, C. Eskilsson, and L. Bergdahl. "An hp-adaptive discontinuous Galerkin method for modelling snap loads in mooring cables". In: *Ocean Engineering* Volume 144 (2017), 266–276.

[35] C. S. Peskin. "Flow patterns around the heart valves". In: *Journal of Computational Physics* 10 (1972), pp. 252–271.

[36] J.A. Pinkster. *Low frequency second order wave exciting forces on floating structures.* Ph.D. thesis, Delft University of Technology, Faculty of Marine Technology, The Netherlands. 1979.

[37] B. Ramaswamy, M. Kawahara, and T.Nakayama. "Lagrangian finite element method for the analysis of two-dimensional sloshing problems". In: *International Journal for Numerical Methods in Fluids* Volume 6 (1986), 659–670.

[38] B. Ren et al. "Nonlinear simulations of wave-induced motions of a freely floating body using WCSPH method". In: *Applied Ocean Research* Volume 50 (2015), 1–12.

[39] P.J. Roache. "Quantification of Uncertainty in Computational Fluid Dynamics". In: *Annu.Rev. Fluid Mech.* No. 29 (1997), pp. 123–160.

[40] R. Shivarama and E. P. Fahrenthold. "Hamilton's Equations With Euler Parameters for Rigid Body Dynamics Modeling". In: *Journal of Dynamic Systems Measurement and Control* Volume 126(1) (2004), 124–130.

[41] C.W. Shu and S. Osher. "Efficient implementation of essentially non-oscillatory shock-capturing schemes". In: *Journal of Computational Physics* Volume 77(2) (1988), 439–471.

[42] M. Sussman, P. Smereka, and S. Osher. "A level set approach for computing solutions to incompressible two-phase flow". In: *Journal of Computational Physics* Volume 114 (1994), 146–159.

[43] S. Toxvaerd. "Hamiltonians for discrete dynamics". In: *Physcial Review E* Volume 50 (3) (1994), 2271–2274.

[44] H.S. Udaykumar et al. “A sharp interface cartesian grid method for simulating flows with complex moving boundaries”. In: *Journal of Computational Physics* Volume 174 (2001), 174–345.

[45] Det Norske Veritas. *Offshore Standard DNV-OS-E301 - Position Mooring*. Technical report, Norway. 2010.

[46] H. van der Vorst. “BiCGStab: A fast and smoothly converging variant of Bi-CG for the solution of nonsymmetric linear systems”. In: *SIAM Journal of Scientific Computing* Volume 13 (1992), 631–644.

[47] J. Yang and E. Balaras. “An embedded-boundary formulation for large-eddy simulation of turbulent flows interacting with moving boundaries”. In: *Journal of Computational Physics* Volume 215 (2006), 12–40.

[48] J. Yang and F. Stern. “A non-iterative direct forcing immersed boundary method for strongly-coupled fluid-solid interactions”. In: *Journal of Computational Physics* Volume 295 (2015), 779–804.

[49] J. Yang and F. Stern. “Robust and efficient setup procedure for complex triangulations in immersed boundary simulations”. In: *Journal of Fluids Engineering* Volume 135(10) (2014), 1–11.

[50] J. Zhang and T. L. Jackson. “A high-order incompressible flow solver with WENO”. In: *Journal of Computational Physics* Volume 228 (2009), 146–159.

Paper 2

A Lagrangian approach for the coupled simulation of fixed net structures in a Eulerian fluid model.

Martin, T., Kamath, A. and Bihs, H. (2020).
Journal of Fluids and Structures, Vol. 94, doi: 10.1016/j.jfluidstructs.2020.102962.

A Lagrangian approach for the coupled simulation of fixed net structures in a Eulerian fluid model

Tobias Martin* Arun Kamath Hans Bihs

Department of Civil and Environmental Engineering, Norwegian University of Science and Technology (NTNU), 7491 Trondheim, Norway

Postprint
published in *Journal of Fluids and Structures*, 2020, Vol. **94**,
DOI: 10.1016/j.jfluidstructs.2020.102962.

Abstract

A Lagrangian approach for the coupled numerical simulation of fixed net structures and fluid flow is derived. The model is based on solving the Reynolds-averaged Navier-Stokes equations in a Eulerian fluid domain. The equations include disturbances to account for the presence of the net. For this purpose, forces on the net are calculated using a screen force model and are distributed on Lagrangian points to represent the geometry of the net. In comparison to previous approaches based on porous media representations, the new model includes a more physical derivation and simplifies the necessary numerical procedure. Hence, it is also suitable for arbitrary geometries and large scale simulations. An extensive validation section provides insight into the performance of the new model. It includes the simulation of steady currents through single and multiple fixed net panels and cages, and wave propagation through a net panel. Different solidities, inflow velocities and angles of attack are considered. The comparison of loads on and velocity reductions behind the net with available measurements indicates superior performance of the proposed model over existing approaches for a wide range of applications.

Keywords: Hydroelasticity, Net structure, Fluid-structure interaction, CFD, Drag forces

1 Introduction

Aquaculture has seen strong growth recently due to its potential for covering the rising global food demand. Offshore fish production becomes relevant as the size of the structures increases and greater concerns about the environmental impact on the nearshore zone arise. In the open sea, severe environmental loadings from high energy sea states necessitate the accurate analysis of motion and fatigue for the design of reliable and economical fish farm structures.

*Corresponding author, tobias.martin@ntnu.no

The enclosure of a fish cage consists of a large number of square or rhombic meshes forming a flexible or stiff net cylinder or panel. Patursson et al. [29] performed measurements of drag and lift forces on a fixed net panel and the velocity reduction behind the net for different inflow velocities and angles of attack. They observed that the force coefficients are more dependent on the angle of attack than on the Reynolds number and that the velocity reduction is less dependent on the angle of attack. Similarly, Bi et al. [5] conducted experiments on the velocity profile behind multiple net panels in a current tank. Their results indicate that the velocity reduction behind the net is a function of the net solidity due to a changing shielding effect. In [6], an experimental study on the deformation of a net wall in different current velocities was presented. Lader and Enerhaug [21] analysed the forces and deformation of a complete net cage in a current. They found a strong coupling between occurring forces and deformation and concluded that existing simple drag formulae for stiff net panels are not suitable for calculating the forces on flexible cage structures. Less research is focused on experiments including waves. Lader et al. [23, 24] studied wave forces on net panels in a small wave flume and compared the results with different wave force models. They showed the increasing influence of the net on the wave forces with increasing wave steepness. A complete study of a net cage in current and waves including an elastic floater, mooring and net was presented in [19], where the authors investigated the validity of different rational hydrodynamic load models for more complex wave situations.

Besides experimental studies, numerical simulations using computational fluid dynamics (CFD) can be applied to understand the structural and environmental challenges in the operation of the whole structure. It allows for the investigation of the forces on and the fluid dynamics in and around the cage. Mostly separate numerical studies on either the motion of the structure or the fluid around the structure were performed in the past [15, 22, 36]. However, a segregated approach is not valid for offshore conditions due to the strong non-linear fluid-structure interaction. Resolving a physical net in a computational domain which also covers the surrounding ocean is not feasible considering the significant difference in length scales and the available computational power. One possibility to overcome this limitation is the application of the potential theory which is based on disproportional assumptions [19]. The introduction of an advanced procedure which decouples the resolution dependence of the fluid from the net representation is eventually the more elaborated and efficient solution. Here, the introduction of an appropriate coupling model is the main issue of concern.

Yao et al. [38] presented a hybrid finite volume method to incorporate the fluid-structure coupling into their CFD solver. The resistance forces of the net were distributed by assigning them to cells containing portions of the numerical net. The net was represented by a lumped mass method consisting of knots and bars in between. The distribution process requires the calculation of the intersection of each bar with each cell of the fluid grid and is thus computationally expensive. This drawback is amplified for rectilinear grids and polyhedral cell shapes where intersections can only be found by comparison to each cell face. They also introduced the idea of choosing the unknown force coefficients by fitting them with experimental data. Details about the fitting process and fitting results for the drag coefficients were not presented. In contrast, the most dominant approach is based on the work of Patursson et al. [29]. They incorporated a stiff net sheet as a porous medium in the fluid domain. The governing volume- and Reynolds-averaged Navier-Stokes equations are solved using a finite volume method. The research was mostly focused on the correct determination of the porous resistance coefficients, which were approximated from available experimental data. Bi et al.

[6] and Zhao et al. [40] followed the same approach but used a theoretical force model for determining the coefficients. Chen and Christensen [11, 12] extended the general idea for complete net cages and included a more comprehensive determination of these coefficients. They provided an extensive validation of their approach for stiff net walls and cages in both current and waves. A Morison type force model which neglects important dependencies on the angle of attack in their derivations was utilised.

The usage of a porous medium model for incorporating the interaction of fluid and net into a CFD solver comes with several drawbacks which will be presented in section 2. This leads to the proposition of a new coupling model which is the subject of this paper. The new model utilises a screen force model to calculate the forces on the net accurately and distributes their influence on the fluid using Lagrangian points. Section 3 introduces the governing equations and the applied numerical solver. Details about the net and hydrodynamic force model which are necessary for the further understanding of the proposed model are also presented. The derivation of the new coupling methodology can be found in section 4. In section 5, a discussion of the overall numerical model is presented, while section 6 is devoted to several validation cases of fixed net walls and cages in varying wave and current conditions. Conclusions arising from the previous sections are given in section 7.

2 Review of the porous medium approach for coupling net and fluid in CFD solvers

The porous medium model is considered as a surrogate sharing similar physical properties as the original interaction process, but it does not imply any physical connection. This is illustrated by the necessity of arbitrarily [12] defining the added mass coefficient, originating from the derivation of the volume- and Reynolds-averaged Navier-Stokes (VRANS) equations, or neglecting it [29]. The closure model for the VRANS equations is usually based on the Darcy-Forchheimer law and requires the predefinition of several coefficients which are dependent on fluid properties. Previous research [12, 40] neglected these dependencies and rather used the free coefficients for incorporating the disturbances of the net on the fluid. As pointed out by Chen and Christensen [12], it is challenging to incorporate all aspects of properties influencing the forces on a net into the calculation of these coefficients. Therefore, they defined them as normal and tangential constants throughout the porous medium. This leads to a zone of constant pressure loss rather than a thin sheet where the pressure drops immediately as in reality.

Another challenge of porous medium models occurs for net cages and deformed nets in general. In [11], the utilisation of a porous medium for these cases is investigated where the authors proposed defining zones of certain thickness around each macro element of the net. The resulting prism volumes represent a continuous porous medium. This procedure might be interpreted as a type of overset grid. Besides the high computational cost of generating and parallelising this generally three-dimensional grid, a more severe problem occurs in the case of deformed elements. As shown in Fig. 1, overlapping regions and gaps can occur at possible intersections of zones. So far, this issue has not been addressed.
In order to keep the validity of the porous medium model, a solution of this geometrical problem is sought in preparation of the current paper. The idea was based on defining a point cloud of certain distance to the net elements. A Delaunay triangulation was then applied

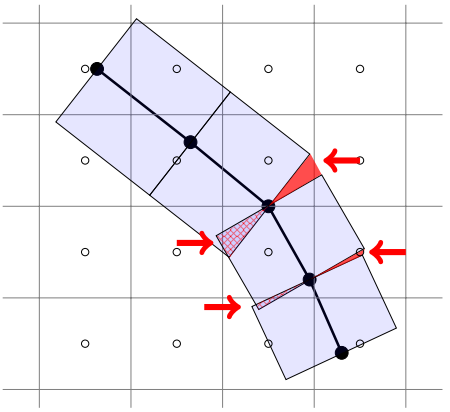

Figure 1: Two-dimensional illustration of the challenges in constructing a discrete porous zone (blue shaded) around a net wall (thick black lines and points) as proposed in [11]. Overlapping regions are indicated in hatched red; Holes are indicated as red triangles.

for generating a continuous volume enclosing the original net, and a level set function was defined around the volume and used for calculating normal vectors. These could be utilised for the calculation of the resistance coefficients in arbitrary directions. As a consequence of the Delaunay triangulation, concave shapes which occur inside a circular cage cannot be handled properly. This demonstrates the non-applicability of this approach in practice. Further, the triangulation process is computationally very demanding and challenging to parallelise. The correct assignment of the porous media closure terms to the surrounding grid cells is another unsolved problem arising in porous medium models, i.e. how to determine the portion of a particular porous zone in a fluid cell.

These drawbacks of the porous medium approach indicate theoretical, physical and computational limitations, and the necessity for an alternative coupling model arises. Therefore, a new coupling model based on Lagrangian-Eulerian considerations is proposed in this paper. The new approach avoids demanding volume handling and is straightforward to be parallelised. It also incorporates more advanced hydrodynamic force calculations. This increases the actual physical information contained in the coupling process and, eventually, improves numerical tools for modelling this type of fluid-structure interaction.

3 Numerical model

3.1 Fluid model

The basis of the new development in this paper is the open-source CFD solver REEF3D [7, 8]. It solves the continuity and Reynolds-averaged Navier-Stokes (RANS) equations for

incompressible fluids which can be written in indices notation as

$$\frac{\partial u_i}{\partial x_i} = 0, \tag{1}$$

$$\frac{\partial u_i}{\partial t} + u_j \frac{\partial u_i}{\partial x_j} = -\frac{1}{\rho}\frac{\partial p}{\partial x_i} + \frac{\partial}{\partial x_j}\left(\nu\left(\frac{\partial u_i}{\partial x_j} + \frac{\partial u_j}{\partial x_i}\right)\right) + g_i, \tag{2}$$

with u_i the velocity components, p representing the pressure and g_i the gravity acceleration vector. The kinematic viscosity ν contains the turbulent viscosity which is calculated from turbulent properties using the Boussinesq approximation. If the free surface is considered, the density ρ and ν have to be distinguished in the two phases. Following the ideas in [9], the material properties at any location are defined as

$$\rho = \rho_w H(\phi) + \rho_a(1 - H(\phi)), \tag{3}$$

$$\nu = \nu_w H(\phi) + \nu_a(1 - H(\phi)), \tag{4}$$

with w indicating water and a air properties. ϕ defines a signed distance function introduced below. H presents a smoothed Heaviside step function chosen as

$$H(\phi) = \begin{cases} 0 & \text{if } \phi < -\epsilon \\ \frac{1}{2}\left(1 + \frac{\phi}{\epsilon} + \frac{1}{\pi} sin(\frac{\pi\phi}{\epsilon})\right) & \text{if } |\phi| \leq \epsilon \\ 1 & \text{if } \phi > \epsilon, \end{cases} \tag{5}$$

with $\epsilon = 2.1\Delta x$ and Δx the characteristic length scale of the discrete domain.

The location of the free water surface is represented implicitly by the zero level set of a smooth signed distance function ϕ [28]. The gradients of ϕ satisfy the Eikonal equation $|\nabla\phi| = 1$. The motion of the free surface is captured by solving the linear advection equation with the fluid velocities u_i convecting ϕ. A reinitialisation step has to be incorporated after each time step to preserve the Eikonal equation. In the given framework, the reinitialization equation of Sussman et al. [35] is solved with an artificial time-stepping for this purpose.

Numerical solutions of the equations are sought using finite difference methods on rectilinear grids. The coupling of pressure and velocity during the solution of the system (1) and (2) is ensured by staggering the locations of velocity and pressure information. A fifth-order accurate weighted essentially non-oscillatory (WENO) scheme [16, 17] adapted to non-uniform cell sizes is applied to convection terms. Diffusion terms are discretised using second-order accurate central finite differences. The solution process follows the projection method for incompressible flows of Chorin [13]. In a first step, the momentum equations without pressure gradients are solved for predicting the velocities $u_i^{(*)}$:

$$\frac{u_i^{(*)} - u_i^{(n)}}{\Delta t} = -u_j \frac{\partial u_i}{\partial x_j} + \frac{\partial}{\partial x_j}\left(\nu \cdot \left(\frac{\partial u_i}{\partial x_j} + \frac{\partial u_j}{\partial x_i}\right)\right) + g_i. \tag{6}$$

In this study, the third-order accurate TVD Runge-Kutta scheme [34]

$$\begin{aligned} u_i^{(1)} &= u_i^{(n)} + \Delta t\ \mathbf{L}\left(u_i^{(n)}\right), \\ u_i^{(2)} &= \frac{3}{4}u_i^{(n)} + \frac{1}{4}u_i^{(1)} + \frac{1}{4}\Delta t\ \mathbf{L}\left(u_i^{(1)}\right), \\ u_i^{(*)} &= \frac{1}{3}u_i^{(n)} + \frac{2}{3}u_i^{(2)} + \frac{2}{3}\Delta t\ \mathbf{L}\left(u_i^{(2)}\right), \end{aligned} \tag{7}$$

is applied for solving Eq. (6) in time. In a second step, a Poisson equation is defined for the pressure:

$$\frac{\partial}{\partial x_i}\left(\frac{1}{\rho}\frac{\partial p^{(n+1)}}{\partial x_i}\right) = \frac{1}{\Delta t}\frac{\partial u_i^{(*)}}{\partial x_i}. \tag{8}$$

It is solved using the fully parallelized BiCGStab solver with geometric multigrid preconditioning of the HYPRE library [37]. Adaptive time stepping controls the time steps according to the required CFL condition. A divergence free velocity field is finally found by correcting the predicted velocities in accordance with

$$u_i^{(n+1)} = u_i^{(*)} - \frac{\Delta t}{\rho}\frac{\partial p^{(n+1)}}{\partial x_i}. \tag{9}$$

An n-halo domain decomposition strategy is implemented in the CFD solver. Here, the domain is split into several subdomains, and data is transferred to neighbouring subdomains using several layers of ghost cells. Convection term containing equations require three layers due to the application of the fifth-order accurate WENO scheme. Otherwise, one layer is sufficient because at most second-order accurate spatial discretization schemes are applied. High-performance computation is enabled by using the message passing interface (MPI) for inter-processor communication.

3.2 Net model

The development of the quasi-static net model implemented in the fluid solver is thoroughly described in [26]. The initialisation process of the net model is applied in this study to calculate hydrodynamic forces on the fixed net. Thus, a discrete representation of the net is assumed. It consists of several knots connected with elastic bars. Each macro element is defined by four knots and four bars. It can represent several meshes depending on the solidity of the net. Assuming square meshes, the solidity S can be approximated as in [15]:

$$S = \frac{2d_t}{l_t} - \left(\frac{d_t}{l_t}\right)^2, \tag{10}$$

with d_t the diameter and l_t the length of each twine. An example of a discrete net is shown in Fig. 2.

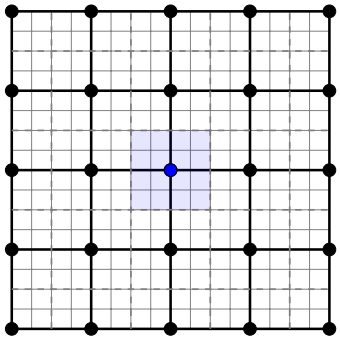

Figure 2: Illustration of a discrete representation of a physical net (thin lines): black dots represent knots, thick black lines represent bars. Dashed lines show the distribution of the screens for the force calculation. For example, the blue areas correspond to the blue knot.

3.3 Hydrodynamic force model

In contrast to previous research on this subject, the proposed model includes the dependency on all important properties for calculating hydrodynamic forces. Following the screen force model of Kristiansen and Faltinsen [20], the net area is distributed on adjoint knots as indicated in Fig. 2. Thus, the contributions of up to four panel parts (screens) add up to the hydrodynamic forces corresponding to a single knot. The surface integral of each screen is approximated by a second-order accurate quadrature rule using its geometrical centre as the integration point. On each screen, two force vectors $\vec{F}_D$ and $\vec{F}_L$ are defined in the normal and tangential direction to the inflow velocity vector, which can be identified as drag and lift force directions $\vec{n}_d$ and $\vec{n}_l$:

$$\vec{F}_D = \frac{\rho}{2} C_D A u_{rel}^2 \vec{n}_d, \tag{11}$$

$$\vec{F}_L = \frac{\rho}{2} C_L A u_{rel}^2 \vec{n}_l, . \tag{12}$$

Here, A is the area of the screen given as

$$A = \frac{l_1 l_2}{4} \cdot |\vec{b}_1 \times \vec{b}_2|, \tag{13}$$

with indices 1 and 2 referring to the two bars spanning the area and $\vec{b}$ the unit bar vectors. Further, u_{rel} represents the magnitude of the relative velocity vector $\vec{u}_{rel}$ between the inflow velocity u_∞ and the velocity of the panel which is zero in this paper. The two necessary directions are determined as follows

$$\vec{n}_d = \frac{\vec{u}_{rel}}{|\vec{u}_{rel}|}, \tag{14}$$

$$\vec{n}_l = \frac{(\vec{u}_{rel} \times \vec{n}_s) \times \vec{n}_s}{|(\vec{u}_{rel} \times \vec{n}_s) \times \vec{n}_s|}, \tag{15}$$

where $\vec{n}_s$ is the unit normal vector of the screen pointing in the same direction as $\vec{u}_{rel}$. The unknown force coefficients C_D and C_L are calculated from a truncated Fourier series expanded for their dependency on the angle of attack α

$$C_D(\alpha) = C_{D,0} \sum_{n=1}^{\infty} a_{2n-1} \cos\left((2n-1)\alpha\right), \tag{16}$$

$$C_L(\alpha) = C_{L,\frac{\pi}{4}} \sum_{n=1}^{\infty} b_{2n} \cos\left(2n\alpha\right). \tag{17}$$

In [20], details about the calculation of the constants $C_{D,0}$ in Eq. (16) and $C_{L,\frac{\pi}{4}}$ in Eq. (17) are given. However, they kept the determination of the Fourier coefficients a and b open for discussion. In accordance with the idea of Yao et al. [38], optimum coefficients are found by fitting them to experimental data. Currently, the available amount of measurements for drag and lift forces on nets is rather small and specific for nets with low solidity. High solidity measurements as provided in [4] are important contributions for future adjustments, in particular with regards to bio-fouled nets.

The chosen fitting data is taken from the measurements and data provided by Patursson et al. [29]. Additionally, data from Zhan et al. [39] is included for the drag force prediction. In total, the data set spans solidities between 0.128 and 0.317 and inflow velocities between 0.159 m/s and 1.0 m/s. It also includes the whole range of possible angles of attack ($0° - 90°$). Non-linear fitting is accomplished using the downhill simplex method [27] with constraints to keep the results physically bounded and fulfil the condition $C_D(\alpha = 0) = C_{D,0}$. Solidity, twine diameter, inflow velocity and angle of attack are defined as fitting parameters. The optimum is sought and compared for up to four Fourier coefficients for C_D and three Fourier coefficients for C_L. Tab. 1 shows the resulting coefficients for the best fit. The mean absolute percentage error (MAPE) for the C_D fitting problem is 17.3%, 8.5% and 35.1% for the two data sets in [29] and the data in [39] if three coefficients are used. However, the fit would be just slightly worse if just two coefficients, as proposed in [20], are used. For C_L, the best MAPE is 20.9% and 14.2% for the data in [29] if the series is truncated after two coefficients. As indicated in [38], a better fit can be achieved if b_2 is set larger than one. Thus, the applied Fourier series is

$$C_D(\alpha) = C_{D,0} \cdot \left[0.9725 \cos\left(\alpha\right) + 0.0139 \cos\left(3\alpha\right) + 0.0136 \cos\left(5\alpha\right)\right], \tag{18}$$

$$C_L(\alpha) = C_{L,\frac{\pi}{4}} \cdot \left[1.2291 \cos\left(2\alpha\right) + 0.1116 \cos\left(4\alpha\right)\right]. \tag{19}$$

Table 1: Calculated Fourier coefficients using a multidimensional optimisation method with bounded constraints.

a_1	a_3	a_5	a_7	b_2	b_4	b_6
0.9725	0.0139	0.0136	0.0	1.2291	0.1116	0.0

4 New Lagrangian-Eulerian coupling algorithm

A new methodology for modelling the interaction of net and fluid is proposed in this section. This method aims to provide better physical representation, higher modelling flexibility and

lower computational cost in comparison to porous media representations. It is based on a Lagrangian-Eulerian approach as it is originally developed for impermeable membranes [30] and applied to e.g. parachute modelling [3]. In section 4.1, a Lagrangian model to represent the net is described, followed by the coupling process to the fluid in section 4.2. A general problem from this coupling is the modified velocity near the net. In contrast to previous research, this paper proposes a physical correction for this problem in section 4.3. The resulting model creates a free parameter which is used for adapting the correct velocity reduction behind the net. Section 4.4 is devoted to provide details about it.

4.1 Lagrangian representation of the net

A Lagrangian representation of the net is found as a first step. In order to keep flexibility, no assumption about the ratio between the Eulerian cell size of the fluid and the macro element size representing the net is stated. The disturbance of the fluid by the net should be nearly equally distributed over the area of the net. Hence, the distance between Lagrangian points is connected to the cell size of the surrounding Eulerian grid. In case the grid is rather coarse, the numerical representation of the net as macro elements is sufficient. However, the macro elements should be refined if the grid is refined. The most efficient way of automating this process is to divide the net elements into triangles and compare their average length with a reference cell size (see Fig. 3). If the length exceeds the reference length, the triangle is split into four smaller triangles using the centre of each side as an additional vertex. Further iterations are executed until the criterium is fulfilled. The Lagrangian points are then set in the geometrical centre of each triangle.

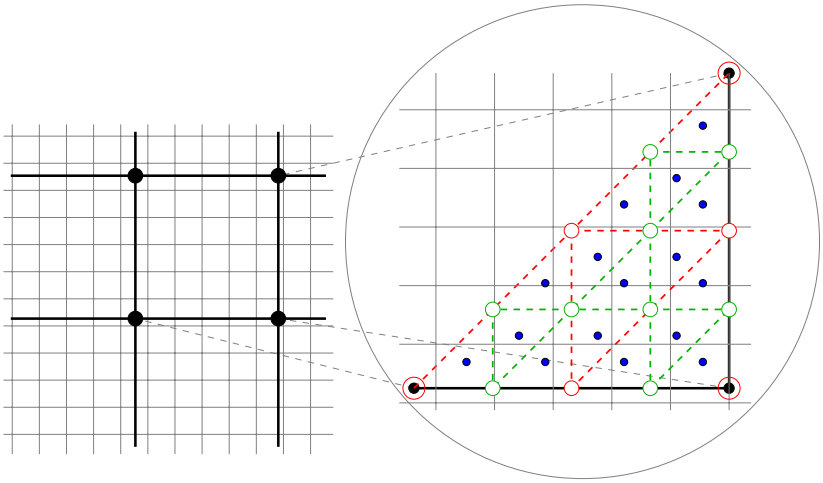

Figure 3: Illustration of the procedure for obtaining a Lagrangian representation of one half of a net element (thick lines and points) in a Eulerian fluid domain (thin grey lines). Red lines and dots indicate the triangles after the first triangulation loop, green lines and dots result from the second loop. The resulting Lagrangian points are shown in blue.

4.2 Coupling process

A coupling condition can be enforced starting from the Eulerian grid for the fluid and the Lagrangian points representing the net. Conservation of momentum is assumed for any control volume enclosing the net. It results in the condition that the energy transfer from the fluid to the net corresponds to the loss of the fluid momentum due to the disturbance of the net. This momentum loss can be physically identified as a pressure jump over an infinitesimally small distance through the net. Looking into the procedure of the projection method from above, a modification of Eq. (8) can incorporate this change. It leads to the updated Poisson equation

$$\frac{\partial}{\partial x_i}\left(\frac{1}{\rho}\frac{\partial p^{(n+1)}}{\partial x_i}\right) = \frac{1}{\Delta t}\frac{\partial}{\partial x_i}\left(u_i^{(*)} - F_i\right), \tag{20}$$

and the new velocity correction step

$$u_i^{(n+1)} = u_i^{(*)} - F_i - \frac{\Delta t}{\rho}\frac{\partial p^{(n+1)}}{\partial x_i}, \tag{21}$$

with $F_i = F(\vec{x}_e)_i$ being one component of the momentum loss vector due to the presence of the net at point $\vec{x}_e$ of the Eulerian grid. Following the idea of Peskin [30], it can be calculated from

$$F(\vec{x}_e)_i = \sum_{l=1}^{L} D(\vec{x}_e, \vec{x}_l) \cdot f(\vec{x}_l)_i, \tag{22}$$

where $f(\vec{x}_l)_i$ is the i-th component of the hydrodynamic screen force vector at the Lagrangian point $\vec{x}_l$ and L is the number of Lagrangian points within a defined Kernel D around $\vec{x}_e$. A modification of Eq. (22) is proposed to have a more flexible choice for the diameter of the kernel. For this purpose, $F(\vec{x}_e)_i$ is calculated using the inverse distance weighting

$$F(\vec{x}_e)_i = \frac{\sum_{l=1}^{L} w_{e,l} \cdot f(\vec{x}_l)_i}{\sum_{l=1}^{L} w_{e,l}}, \tag{23}$$

with the dimensionless weights

$$w_{e,l} = \frac{1}{|\vec{x}_e - \vec{x}_l|^2}. \tag{24}$$

The chosen distribution of F over a certain volume of the fluid grid is illustrated in 2D in Fig. 4. Special attention has to be given to the staggered grid arrangement. For example, the x-component of the force is distributed only on the grid of the x-velocity component.

Finally, the forces at each Lagrangian point $\vec{f}(\vec{x}_l)$ in the principal direction of the Eulerian grid are calculated. By comparing to the described screen forces in Eq. (11) and Eq. (12), they can be expressed as the integrand of the surface integral:

$$f(\vec{x}_l)_i = F_{D,i}(\vec{x}_l) + F_{L,i}(\vec{x}_l) = \frac{\rho}{2} u_{rel}^2 \cdot \left(C_D n_{d,i} + C_L n_{l,i}\right). \tag{25}$$

A dimensional analysis of Eq. (23), Eq. (25) and Eq. (20) shows equality only if $\vec{f}(\vec{x}_l)$ is divided by a length. The necessary parameter κ with dimension $[1/m]$ arises from the transition from a surface force to a volume force and is the diameter of the influence sphere of each Lagrangian point. In subsection 4.4, κ is determined to represent the correct velocity reduction behind the net. The momentum loss vector is finally calculated as

$$F(\vec{x}_e)_i = \frac{1}{\kappa} \cdot \frac{\sum_{l=1}^{L} w_{e,l} \cdot f(\vec{x}_l)_i}{\sum_{l=1}^{L} w_{e,l}}. \tag{26}$$

It is noticed that the new coupling algorithm theoretically does not fulfil the law of momentum conservation because the net forces are calculated on the original macro elements but the disturbances on the fluid are determined from a usually finer triangulated surface. This choice is made for efficiency reasons and motivated by the valid assumption of small velocity changes within one net screen. It is in particular reasonable if in both steps the velocities are interpolated using the same inverse distance weighting algorithm.

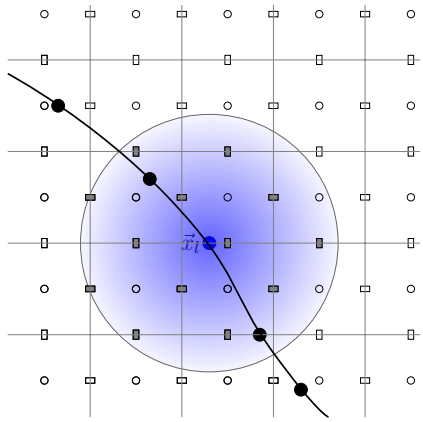

Figure 4: Distribution of the force $\vec{F}(\vec{x}_l)$ of point $\vec{x}_l$ (blue) on the Eulerian grid points (white dots and rectangles). Blue shading illustrates inverse weighting for surrounding fluid points. The influenced velocity nodes are coloured in grey.

4.3 Improving the velocity prediction

A challenge arising from the numerical representation of the net within the fluid domain is the disturbed velocity field around the net. As shown in Fig. 5, the velocity at the net differs from the undisturbed inflow velocity due to the discrete interpolation (Eq. (23)). In previous research [29], this was overcome by fitting the porous medium coefficients numerically which implicitly respects this difference in velocity. In the current model, the force coefficients are determined based on the assumption of undisturbed velocities in front of the net in accordance with most force models. Thus, a relationship between the numerically interpolated velocity at the net and the undisturbed inflow velocity has to be derived.

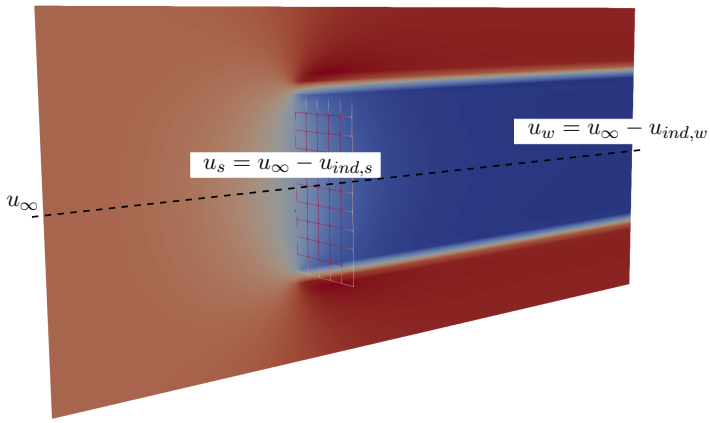

Figure 5: Illustration of velocity definitions in front and behind the net. Cross section shows the x-velocity distribution with velocity reduction behind the net.

One possibility is the approach of Løland [25] which is based on the linearised turbulent wake equations of Schlichting [33]. A more proven concept is based on Froude's momentum theory [10]. In the research area of hydrodynamics, it is applied to include the discrete disturbance of a propeller disk in a fluid domain. Here, the balance of momentum before and behind an infinitesimally thin rotating screen has to be calculated. In the following, this approach is elaborated for net applications. Besides the assumptions valid for potential flows, it is assumed that the induced velocities from the screen $u_{ind,s}$ and in the wake $u_{ind,w}$ are much smaller than the inflow velocity u_∞ and no rotational velocities are induced (see Fig. 5 for definitions). Then, two Bernoulli equations can be stated:

$$p_\infty + \frac{\rho}{2} u_\infty^2 = p_{s,1} + \frac{\rho}{2}(u_\infty - u_{ind,s})^2, \tag{27}$$

$$p_{s,2} + \frac{\rho}{2}(u_\infty - u_{ind,s})^2 = p_w + \frac{\rho}{2}(u_\infty - u_{ind,w})^2. \tag{28}$$

Eq. (27) is valid in front of the screen and Eq. (28) describes the fluid behind the screen. By combining these equations, the pressure jump at the screen is defined as

$$\Delta p = p_{s,2} - p_{s,1} = p_w - p_\infty + \rho\ u_{ind,w} \cdot \left(-u_\infty + \frac{u_{ind,w}}{2}\right). \tag{29}$$

It can be assumed that $p_w = p_\infty$ if start and end point are far away from the disturbance. Thus, Eq. (29) expresses the pressure jump in terms of inflow and induced velocities. Linearisation of the equation yields

$$\Delta p \approx -\rho\ u_{ind,w}\ u_\infty. \tag{30}$$

In addition, Eq. (27) can be used to approximate the pressure jump in front of the screen. The linearised expression is

$$p_{s,1} - p_\infty = \rho\ u_\infty\ u_{ind,s}. \tag{31}$$

Froude's hypothesis arises from Eq. (31) if the assumption is made that half of the pressure jump is in front and the other half behind the screen,

$$u_{ind,w} = 2u_{ind,s}, \tag{32}$$

i.e. the velocity at the screen is half the velocity between inflow and wake velocity (see Fig. 6). By inserting this result in Eq. (30) and using the definition of the screen velocity, it yields a new formula for u_s:

$$u_s = u_\infty - \frac{\Delta p}{2\rho u_\infty}. \tag{33}$$

The pressure jump Δp is due to the disturbance forces from Eq. (25) normal to the screen. Using the fluid velocity at the screen and the inflow velocity for the coefficient calculation, the jump can be expressed as

$$\Delta p = \frac{\rho}{2} C_D(u_\infty) u_s^2. \tag{34}$$

In combination with Eq. (33), the inflow velocity can finally be approximated from the known screen velocity as

$$u_\infty = \frac{C_D(u_\infty)}{2 \cdot \left(\sqrt{1 + C_D(u_\infty)} - 1\right)} \cdot u_s. \tag{35}$$

In the later validation process, Eq. (35) is solved using the Newton-Raphson method with $u_\infty = u_s$ as an initial guess.

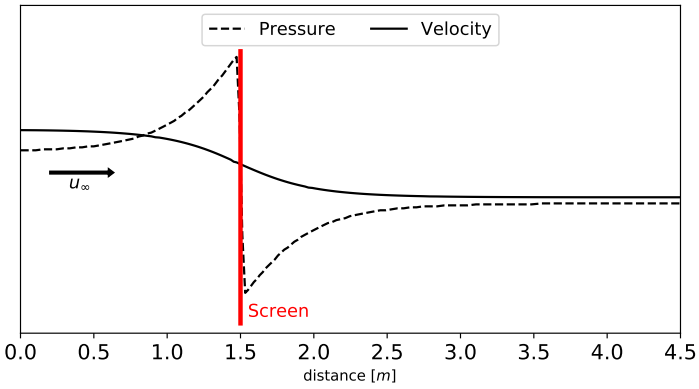

Figure 6: Illustration of velocity and pressure distribution in front and behind the net.

4.4 Estimating the velocity reduction through the net

The derivation of the new coupling algorithm in section 4.2 leads to a free parameter κ to fulfil dimensional equality. It arises numerically with the transition from the hydrodynamic surface

force at the screens to a volume force representation in the Eulerian grid. The parameter corresponds physically to the influence range of the net disturbance on the fluid and is linked to the deceleration of the flow behind the net. In porous medium models, the parameter was determined implicitly through coupling it to the resistance coefficients. Thus, a single fitting was used for both, the velocity reduction and the force calculation. In the new proposed model, these two effects can be investigated separately through the introduction of the velocity reduction correction in the previous section.

A physical determination of κ for approximating the correct velocity reduction behind nets is preferable. However, the available measurements are not sufficient for conclusions at this stage of research. Rudi et al. [32] performed measurements of the velocity reduction behind vertical net sheets, but the data is not publicly available. Patursson et al. [29] measured the same effect but only for a single net solidity. Their results indicate that the dependency of the reduction on the inflow velocity is marginal. The dependency on the angle of attack is also less significant for angles larger than 30°. For smaller angles, the frame of the net wall modifies the solidity of the actual sheet, and the reduction increases disproportionally. The highest influence is expected due to changing net solidity, but more numerical and physical experiments have to be conducted to find correlations. In general, the velocity reduction is documented using the velocity reduction factor U_r which is given as

$$U_r = 1.0 - \frac{u_w}{u_\infty}. \tag{36}$$

As pointed out by Løland [25], this parameter is very sensitive with respect to the measured wake velocity. This further complicates the accurate prediction of the velocity reduction numerically. As a starting point and unless stated otherwise, the validation cases are computed using $\kappa = 0.07$ which is determined from comparing U_r with the data in [29].

5 Summary of the proposed model

A flowchart illustrating the proposed Lagrangian-Eulerian fluid-structure interaction (FSI) algorithm is provided in Fig. 7. Three steps are executed in addition to the original fluid solution algorithm [8]. Each time step starts with the calculation of the free surface using the level set method, and material properties are updated as given in Eq. (3) - Eq. (5). These steps can be omitted in a one-phase simulation. The projection method initially performs the predictor step (Eq. (6)) for the velocities. The hydrodynamic loads on the discrete net structure are computed using Eq. (11) and Eq. (12). In case of a moving net algorithm, the net is then advanced in time. Based on the new position of the net, the position of the Lagrangian points describing the net in the fluid are corrected, and disturbances are distributed on the Eulerian grid by applying Eq. (23). Finally, the modified Poisson equation (20) is solved, and the velocity field is corrected to be divergence-free.

The choice of the kernel radius remains from the previous sections. In the given implementation, it has a minor influence on the results as long as the recommended distance between the Lagrangian points is used. In case of a ghost cell approach as described above, the given number of additional cell layers needed for solving the RANS equations is adequate to store all information needed for the local kernel interpolations. Thus, the only inter-processor communication is the distribution of the disturbance field before the solution of the Poisson equation. This reduces the computational costs significantly and simplifies the parallelisation process.

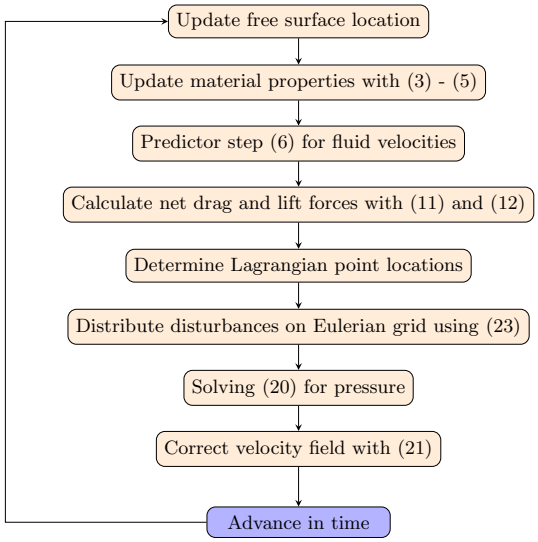

Figure 7: Flowchart of the presented Lagrangian-Eulerian FSI algorithm.

Regarding turbulence modelling, the proposed model consisting of macro elements prevents the resolution of turbulence interactions between net and fluid. Chen and Christensen [12] hypothesised that vortices smaller than the mesh size convect freely through the net, whereas larger vortices are split. Simultaneously, the wake of the individual twines and knots is characterised by separated vortices and strong interaction between them. It is in the interest of the research community to investigate these effects more thoroughly [23] because the turbulence influences the flow transported to the back part of the net cage and the fish inside the cage. The most promising approach for incorporating these effects into a RANS model is their expression as additional generation and dissipation terms in the equation for the turbulent kinetic energy (TKE). This requires an extensive study on TKE changes due to inflow turbulence intensity, angles of attack and net geometry, and is not restricted only to numerical investigations since experimental validation data has to be available as well. It exceeds the scope of this paper to include such investigations. Instead, the indications in [12], that the turbulence might have minor effects on integral quantities like the total load on a net in practice, are taken into account. Further, the incorporation of experimental data into the derivation of the numerical model presumably includes the influence of turbulent effects for the loads. Hence, turbulence modelling is neglected in the following validation section.

6 Validation process

Results from the new solver are compared to available experimental data for total forces on fixed net sheets and cages. The numerical forces on the net are determined by integrating the discrete forces from Eq. (11) and Eq. (12) over the whole net area. The quantitative validation of the results is performed by calculating the percent deviation between the numerical result

Φ_{num} and the measured value Φ_{exp}:

$$\text{Deviation} = \frac{\Phi_{\text{exp}} - \Phi_{\text{num}}}{\Phi_{\text{exp}}} \cdot 100. \tag{37}$$

The sign of the deviation is kept for analysing the over- and under-predictions of the model.

6.1 Forces and velocity reduction for a fixed net panel in steady current flow

A fixed net panel is compared to the experimental data of Patursson et al. [29] in a steady current of different velocities and under several angles of attack α. Here, the drag and lift force coefficients and the velocity reduction factor behind the net as given in Eq. (36) are considered. For the latter, the wake velocity is measured 2.5 m behind the net. The comparability of the velocity at that specific point is not valid because of the continuous numerical representation of the net in the fluid domain. Therefore, velocity probes are arranged in the form of a disc around the measured point and the average value is compared with that from the experiment. This should provide a better impression of the numerical accuracy because it takes the discrete approach of macro elements into account.

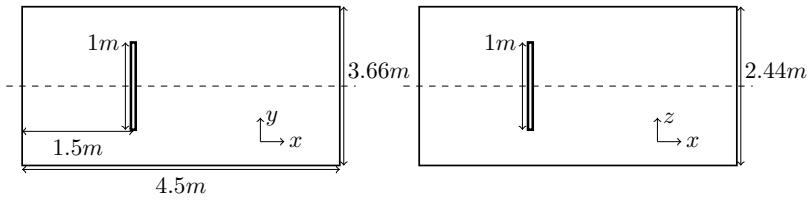

Figure 8: Computational domain for the simulation of a fixed net panel in steady current flow. Top view is shown on the left, side view is shown on the right.

The net is fixed in a frame of 1.0 m × 1.0 m and has a solidity of 0.184. The frame is not considered in this study due to missing geometrical data. This is in accordance with previous calculations [12, 29]. Four different angles of attack, i.e. $\alpha = 15°, 30°, 45°, 90°$ and four different inflow velocities between 0.125 m/s and 0.75 m/s are investigated. Here, 90° corresponds to perpendicular inflow conditions. The computational domain is 4.5 m × 3.66 m × 2.44 m, and the geometrical centre of the net is kept at (1.5 m, 1.83 m, 1.22 m) for all angles of attack (see also Fig. 8).

A spatial convergence test is conducted for the configuration $\alpha = 45°$ and $u_\infty = 0.5$ m/s. The validation process as given in [31] is applied to check convergence. For this purpose, three grids with 0.423 million, 1.22 million and 3.45 million cells with a gradual refinement towards the net are considered. The deviation for C_D and C_L are oscillatory converging, and the deviation of U_r is monotonically converging. As can be seen in Tab. 2, the differences between the results on the different grids are generally small. Therefore, it is decided to utilise the coarsest grid for the following computations. Temporal convergence is not investigated because the simulations result in steady-state conditions.

A slice of the domain through the middle plane is shown for $\alpha = 45°$ and 90° and $u_\infty =$ 0.5 m/s in Fig. 9. The wake of the net is visible and has approximately the same width as

Table 2: Convergence test for the fixed net wall in steady current flow. Table shows the deviations [%] for the drag and lift coefficients and the velocity reduction for the three different grids.

	Coarse	Medium	Fine
C_D	-6.48	-4.90	-6.41
C_L	-17.16	-14.52	-15.57
U_r	7.64	7.09	6.86

the net panel. The fluid is accelerated around the panel. As the angle of attack increases, the fluid slows down in front of the net which leads to a decreasing velocity at the net itself. Behind the net, a nearly steady velocity field can be observed for both angles of attack.

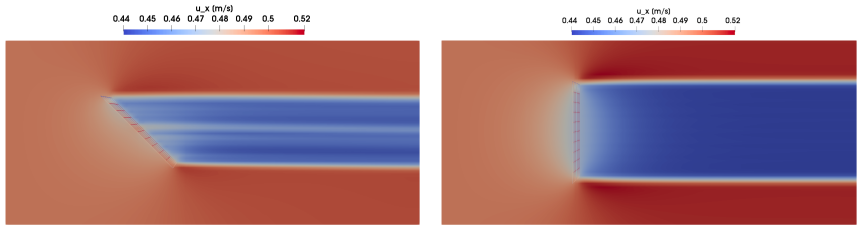

(a) $\alpha = 45°$. (b) $\alpha = 90°$.

Figure 9: Velocity field for the fixed net panel in steady current flow of $u_\infty = 0.5$ m/s.

Fig. 10 presents the numerical and experimental force coefficients for the different inflow velocities as a function of α. The computed drag coefficients (Fig. 10a) increase with decreasing inflow velocity and increasing angle of attack. This agrees qualitatively with the measurements. The predicted lift coefficients in Fig. 10b indicate maximum lift forces for $\alpha = 45°$. At larger angles of attack, the flow separates at the frame, and the lift forces reduce. In general, the lift forces are smaller than the drag forces. The velocity reduction behind the net is predicted well by the numerical model for $\alpha \geq 30°$ as can be seen in Fig. 10c. At smaller angles of attack, the deviations are as expected due to the choice of κ in section 4.4.

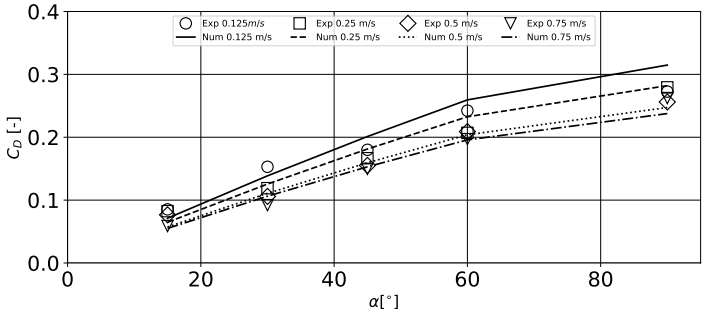

(a) Drag coefficient C_D.

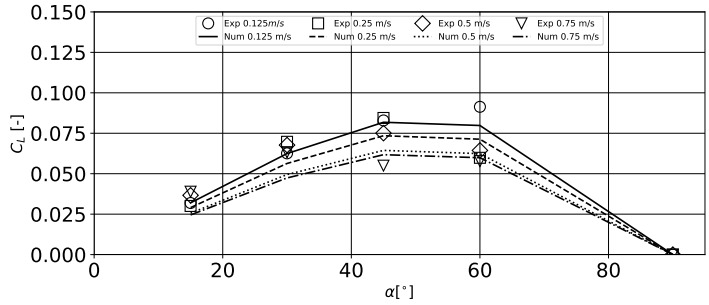

(b) Lift coefficient C_L.

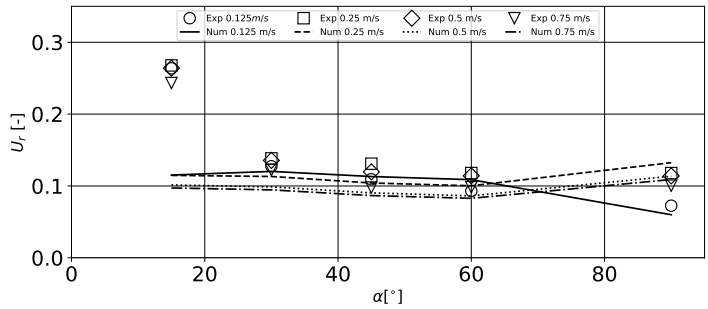

(c) Velocity reduction factor U_r.

Figure 10: Comparison of the numerical and experimental results for the fixed net panel in steady current flow.

The quantitative determination of the numerical results is presented in the Tabs. 3, 4 and 5. They present the deviations for all three properties at different fluid velocities and angles of attack. The maximum deviation in computing C_D is 25% for $\alpha = 15°$ which might be due to neglecting the influence of the frame. For larger angles, the maximum deviation is reduced to 15%. The L_2 norms of the deviation for the four different inflow velocities are

0.05, 0.04, 0.02 and 0.03, which indicates a good approximation of the model over the whole range of Reynolds numbers. Similar behaviour can be seen for C_L, where the L_2 norms of deviation are 0.01, 0.02, 0.02 and 0.02. However, the deviations are slightly larger than for the prediction for C_D with a maximum derivation of 27% for angles larger than 15°. These results describe an improvement over existing porous medium models [12] where deviations larger than 50% for C_L were reported. The maximum deviations for U_r are in a similar range as the deviations for C_L. The chosen constant κ seems to approximate the velocity reduction well over the considered range of angles of attack and Reynolds numbers. A tendency to better agreement to experiments can be observed for the larger angles of attack which coincides with the comments in section 4.4.

Table 3: Deviations [%] for the drag force coefficients between numerical simulation and experimental data of Patursson et al. [29].

α [°]	u_∞ [m/s]			
	0.125	0.25	0.5	0.75
15	16.53	21.40	25.09	6.49
30	9.39	−5.52	−4.60	−15.46
45	−11.76	−8.79	−2.71	−2.18
60	−7.06	−12.34	2.42	0.59
90	−15.47	−0.98	3.44	9.41

Table 4: Deviations [%] for the lift force coefficients between numerical simulation and experimental data of Patursson et al. [29].

α [°]	u_∞ [m/s]			
	0.125	0.25	0.5	0.75
15	−0.36	3.38	30.11	36.95
30	0.23	19.22	26.92	25.13
45	1.35	13.0	14.20	−12.33
60	12.63	−19.22	3.05	−3.61

Table 5: Deviations [%] for the velocity reduction factors between numerical simulation and experimental data of Patursson et al. [29].

α [°]	u_∞ [m/s]			
	0.125	0.25	0.5	0.75
15	56.32	57.16	61.55	60.04
30	5.63	18.18	27.16	22.65
45	−3.45	20.49	24.43	11.45
60	−16.87	15.05	24.45	15.75
90	−17.30	−12.20	0.34	−8.59

6.2 Drag forces on a fixed net panel in steady current flows

Further experiments on fixed net panels in current are presented by Zhan et al. [39]. Several net geometries with square meshes are investigated. This gives a better understanding of the proposed model for a variety of net solidities.

The net panel has a width of 1.3 m and a height of 0.7 m. Three angles of attack, i.e. $\alpha = 30°, 60°, 90°$ and four different inflow velocities between 0.25 m/s and 1.0 m/s are considered. The solidities of the net Sn are $0.128, 0.215$ and 0.223. The same computational domain, net position and grid as given in section 6.1 is used for the simulations.

The measurements are limited to drag forces. Fig. 11 presents the numerical and experimental drag force coefficients as a function of α. As observed before, the forces increase with decreasing inflow velocity and increasing angle of attack. The forces also rise with increasing solidity due to a growing number of twines or increase of twine diameter. The quantification of the results are presented in the Tabs. 6, 7 and 8. The largest deviations are calculated for $\alpha = 30°$ irrespective of the solidity and for all angles at $u_\infty = 0.25$ m/s, with a maximum deviation of 31%. A general trend of under- or over-prediction cannot be stated. This indicates the appropriate capturing of the physics by the proposed approach in the applied range of Reynolds numbers, angles of attack and net geometries. This impression is strengthened by considering the similarity of the L_2 norms of the deviation, which are 0.12, 0.09 and 0.10.

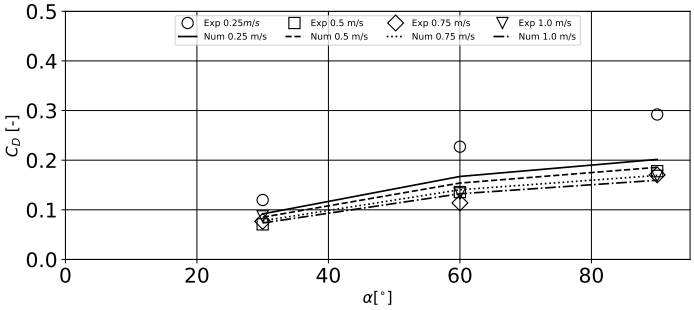

(a) $Sn = 0.128$.

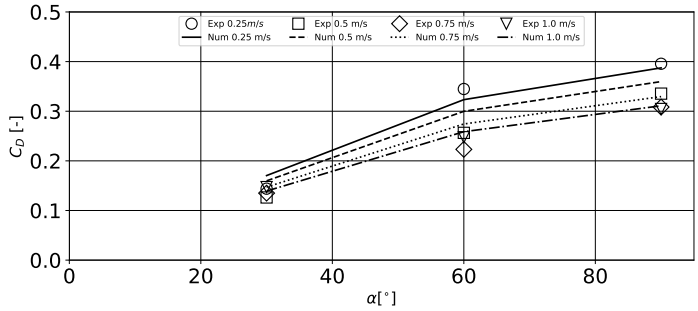

(b) $Sn = 0.215$.

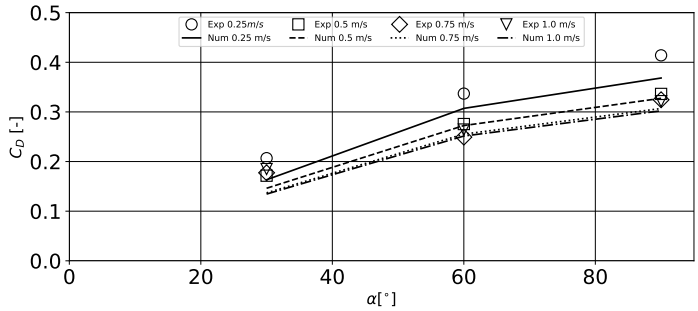

(c) $Sn = 0.223$.

Figure 11: Comparison of numerical and experimental drag coefficients for the fixed net panel in steady current flow.

Table 6: Deviations [%] for the drag force coefficients between numerical simulation and experimental data of Zhan et al. [39] for a net wall with $Sn = 0.128$.

α [°]	u_∞ [m/s]			
	0.25	0.5	0.75	1.0
30	23.40	−20.32	−1.57	15.35
60	26.39	−13.35	−23.32	0.66
90	31.02	−4.33	0.67	5.25

Table 7: Deviations [%] for the drag force coefficients between numerical simulation and experimental data of Zhan et al. [39] for a net wall with $Sn = 0.215$.

α [°]	u_∞ [m/s]			
	0.25	0.5	0.75	1.0
30	−18.34	−26.54	22.81	5.43
60	6.23	−16.91	−22.91	−4.49
90	2.10	−7.24	−6.83	−2.11

Table 8: Deviations [%] for the drag force coefficients between numerical simulation and experimental data of Zhan et al. [39] for a net wall with $Sn = 0.223$.

α [°]	u_∞ [m/s]			
	0.25	0.5	0.75	1.0
30	21.06	14.77	22.81	27.29
60	8.84	1.10	−2.43	4.97
90	11.04	2.64	5.43	6.06

6.3 Drag forces on a fixed net cage in steady current flows

A validation case with more complicated geometry is conducted in this section. In [39], the drag forces on fully submerged fixed circular net structures are measured for different inflow velocities and net geometries. The cage has a height of 0.7 m and a diameter of 0.414 m. The inflow velocities vary from 0.25 m/s to 1.0 m/s, and solidities of $0.128, 0.215$ and 0.223 are considered. The dimensions of the computational domain are illustrated in Fig. 12.

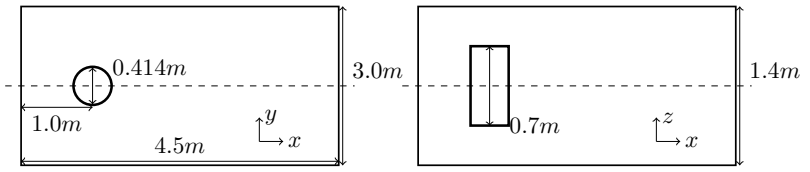

Figure 12: Computational domain for the simulation of a fixed net cage in steady current flow. The top view is shown on the left, the side view is shown on the right.

The predicted drag forces are compared to the experimental results in Fig. 13 and Tab. 9. In the experiments, the forces increase with the solidity and inflow velocity. In contrast, the numerical model computes slightly larger drag forces for $Sn = 0.215$ than for $Sn = 0.223$. The difference in solidity between the two nets seems to be small. However, the net with $Sn = 0.215$ contains meshes with half the length and half the diameter compared to the net with $Sn = 0.223$. Thus, the interaction between the twines increases for the net with $Sn = 0.215$. This effect is apparently not captured well by the screen force model because the deviations to the experiments are the largest for this net (up to 23% in deviation). The other net configurations are modelled within a range of a 20% deviation band, and the L_2 norms of deviation are 1.94 N and 3.15 N. This indicates a good capturing of the physics for the investigated range of inflow velocities and improvement over the results reported in [12].

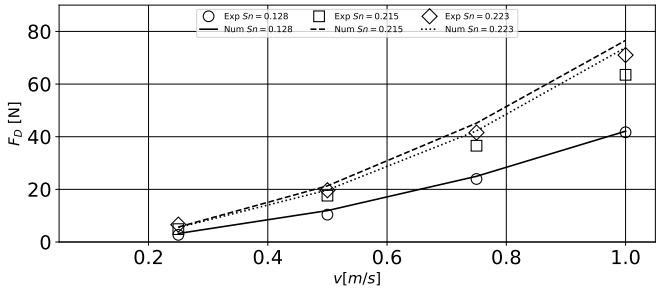

Figure 13: Comparison of the numerical and experimental drag forces on fixed net cage in steady current flow.

Table 9: Deviations [%] for the drag forces between numerical simulation and experimental data of Zhan et al. [39] for a net cage in current.

Sn	u_∞ [m/s]			
	0.25	0.5	0.75	1.0
0.128	−19.54	−14.68	−4.24	−0.94
0.215	−16.10	−21.14	−23.50	−20.58
0.223	16.86	−0.42	−1.54	−4.06

The considered experiments do not include measurements of the velocity reduction in and behind the cage. A typical velocity distribution is shown in Fig. 14 for $Sn = 0.128$ and $u_\infty = 0.5$ m/s. A gradual deceleration of the flow through the net cage is observed, whereas parts of the flow are accelerated along the sides of the cylindrical structure which leads to larger velocities than the inflow velocity outside the wake of the net cage.

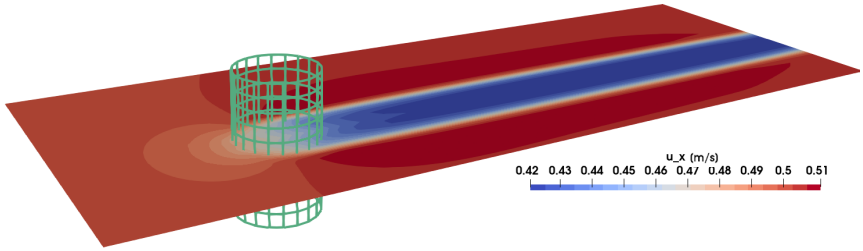

Figure 14: Numerical result for the x-velocity profile in the middle slice for the fixed net cage with $Sn = 0.128$ in steady current flow of $u_\infty = 0.5$ m/s.

6.4 Drag forces on a fixed net panel in regular waves

Lader et al. [24] presented an experimental study on the interaction of regular waves and net panels of different geometries. This allows testing of the proposed model in a space- and time-varying velocity field including a free surface. As pointed out by Kristiansen and Faltinsen [20], the screen force model is also applicable to wave cases because the KC number is large, i.e. quasi-steady flow conditions.

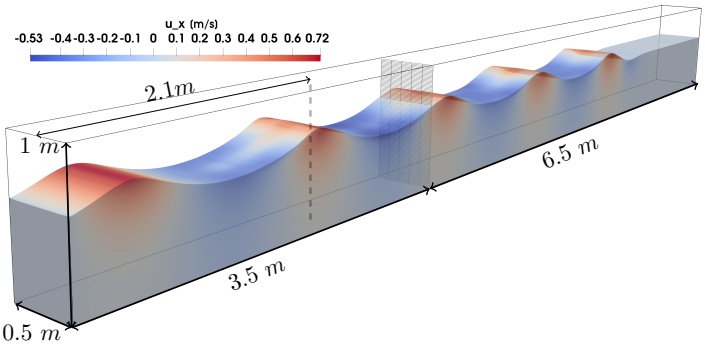

Figure 15: Computational domain for the simulation of a fixed net panel in regular waves. Colours show velocities in x-direction.

Table 10: Wave input parameters for the simulation of fixed net panels in waves (taken from [24]).

Wave case	1	2	3	4	5
Wave frequency f $[Hz]$	1.42	1.42	1.42	1.25	1.0
Wave height H $[m]$	0.045	0.064	0.084	0.104	0.167

The numerical wave tank is defined as shown in Fig. 15. It has a length of 10 m, a height of 1.0 m and a width of 0.5 m. The water depth is set to 0.62 m. The tank is shortened in comparison to the experimental wave flume to save computational time. A two wavelength long numerical beach is placed at the end of the tank to absorb the wave energy. A wave relaxation zone of one wavelength is defined at the inlet to generate waves. The numerical wave tank was thoroughly described in [8] and successfully validated for regular [18], irregular [2] and breaking waves [1]. In the experiments, five different regular waves of different length, height and steepness are generated using a vertical piston wavemaker. Fifth-order Stokes wave theory is used to model these waves because the wavemaker signal is not available and the Ursell numbers are small. The input wave frequencies and heights are given in Tab. 10. The investigated net panels have the same width and height as the tank and solidities of $0.095, 0.22$ and 0.288. They are referred as net case 1-3 in the following. The panel is placed 3.5 m in the tank. The time series for the drag forces and the wave elevation 1.4 m in front of the net are recorded for further analyses. A section of the series is compared to the measured time series in the Figs. 16 - 20.

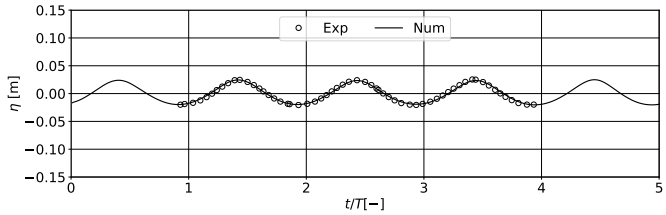

(a) Surface elevation at the wave gage.

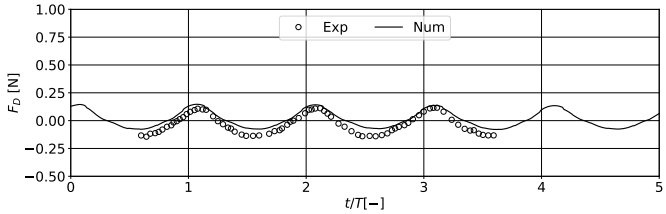

(b) Drag force for net case 1.

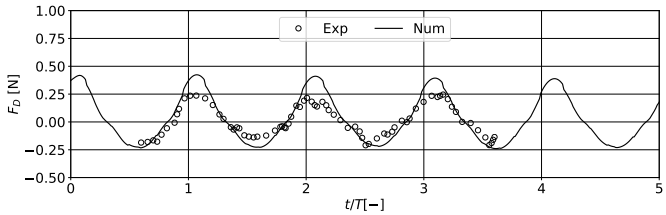

(c) Drag force for net case 2.

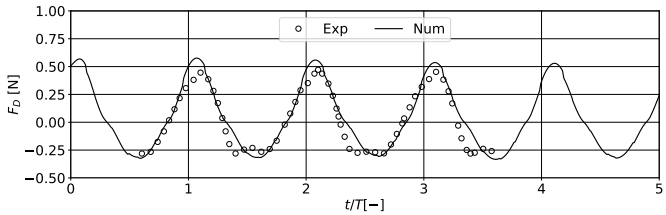

(d) Drag force for net case 3.

Figure 16: Numerical and experimental time series of surface elevation η and drag forces for wave case 1 with $f = 1.42\ Hz$ and $H = 0.045$ m.

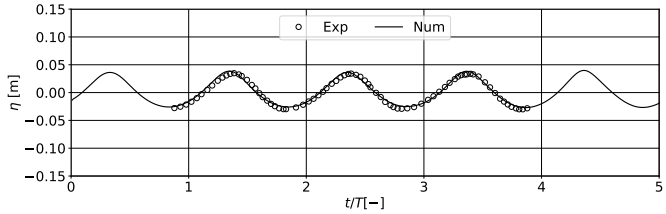

(a) Surface elevation at the wave gage.

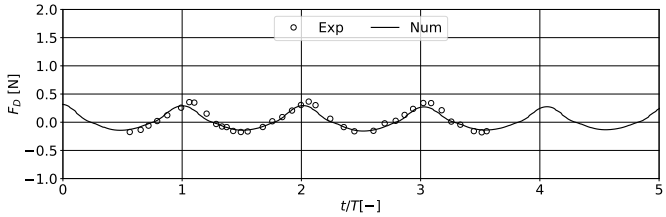

(b) Drag force for net case 1.

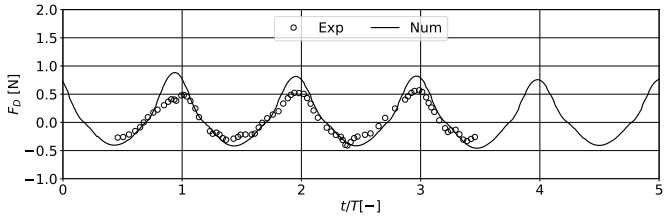

(c) Drag force for net case 2.

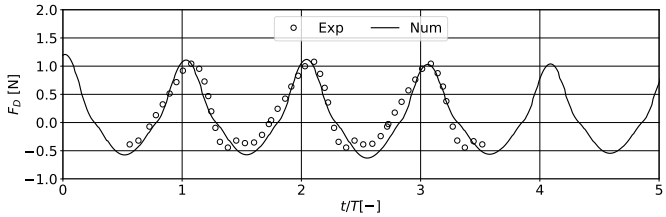

(d) Drag force for net case 3.

Figure 17: Numerical and experimental time series of surface elevation η and drag forces for wave case 2 with $f = 1.42\ Hz$ and $H = 0.064$ m.

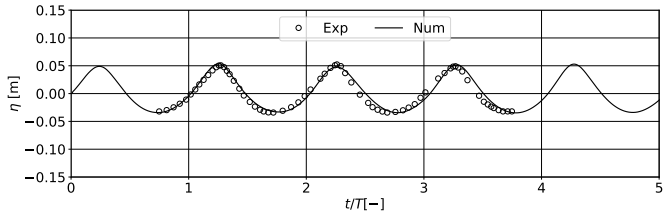

(a) Surface elevation at the wave gage.

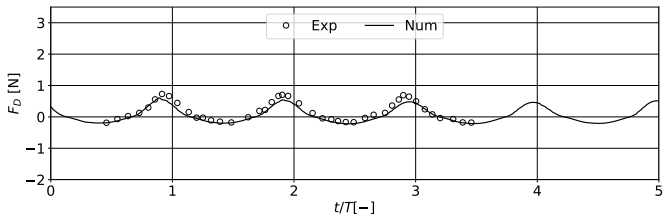

(b) Drag force for net case 1.

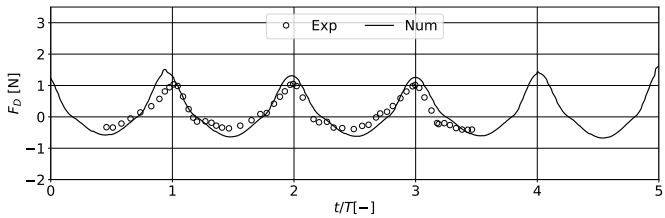

(c) Drag force for net case 2.

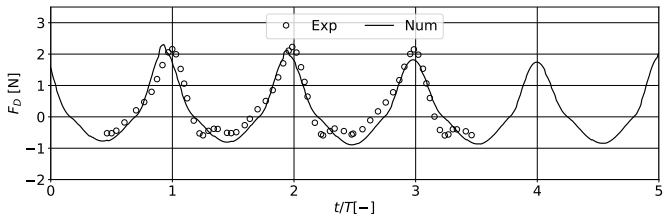

(d) Drag force for net case 3.

Figure 18: Numerical and experimental time series of surface elevation η and drag forces for wave case 3 with $f = 1.42\ Hz$ and $H = 0.084$ m.

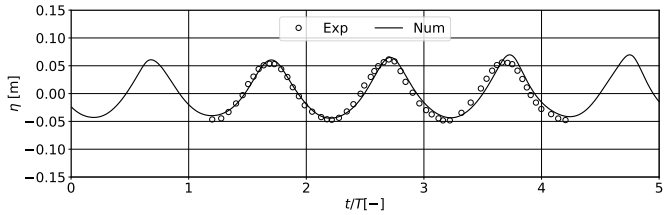

(a) Surface elevation at the wave gage.

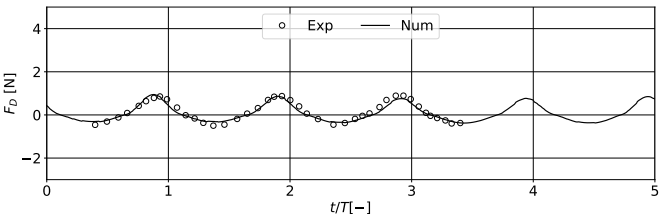

(b) Drag force for net case 1.

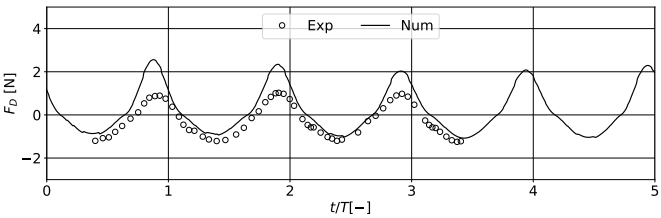

(c) Drag force for net case 2.

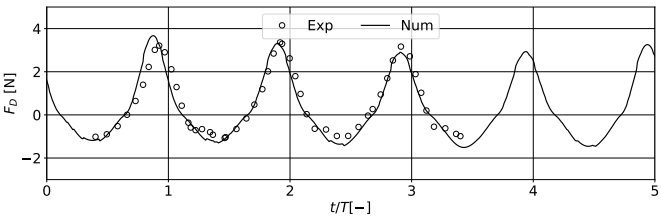

(d) Drag force for net case 3.

Figure 19: Numerical and experimental time series of surface elevation η and drag forces for wave case 4 with $f = 1.25\ Hz$ and $H = 0.104$ m.

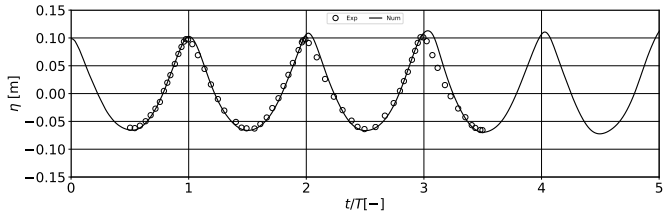

(a) Surface elevation at the wave gage.

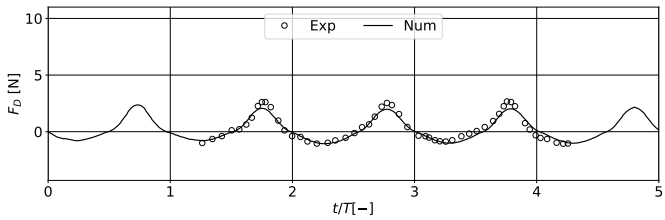

(b) Drag force for net case 1.

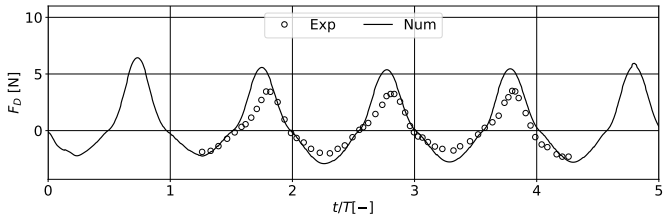

(c) Drag force for net case 2.

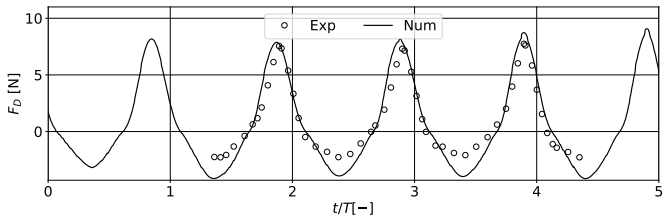

(d) Drag force for net case 3.

Figure 20: Numerical and experimental time series of surface elevation η and drag forces for wave case 5 with $f = 1.0\ Hz$ and $H = 0.167$ m.

In general, the numerically predicted wave propagation matches well with the experiments (Figs. 16a - 20a). Lader et al. [24] suggest evaluating the wave energy by calculating the zeroth-order moment of the power spectrum due to the non-linearity of the wave. Fig. 21 shows the amplitude spectra of the five simulated wave signals into their frequency components. They indicate the adequate representation of the low-order component (Stokes drift) and several

high-order components with multiple times the leading wave frequency. However, all these amplitude components are at most 1/5 of the leading wave frequency component. Thus, their contribution to the total wave energy is of minor interest, and it is justified to simplify the analysis to a comparison of the wave amplitudes. Following Lader et al. [24], a distinction between positive and negative amplitudes is made because of the asymmetry of the waves with higher crests and shallower troughs. As illustrated in Fig. 22b, the higher wave crests result in higher particle velocities and larger submerged net area. This corresponds to larger drag forces on the net in the wave propagation direction. In contrast, the load changes sign in a wave trough situation (Fig. 22a), and a smaller net area is wetted.

The most important components of the total wave forces act on the net with the regular wave frequency as shown in the Figs. 23a - 23e. Therefore, it is sufficient to compare the drag force amplitudes when the total wave forces are of interest. It is also noticed from these figures that the magnitude of the forces increases with the net solidity and wave amplitude. Both phenomena are expected from the validation cases.

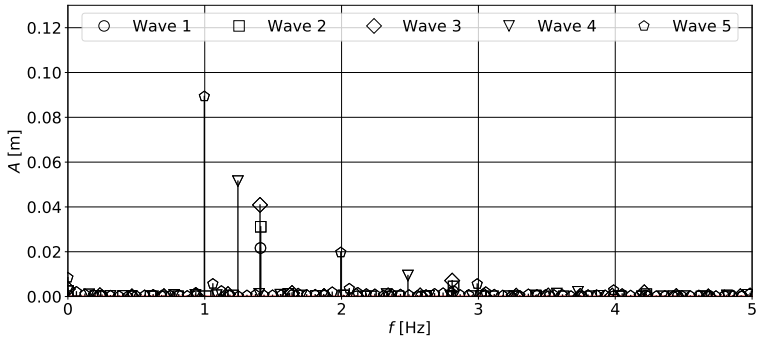

Figure 21: Amplitude spectra of the numerical wave elevation time series for the five different wave cases.

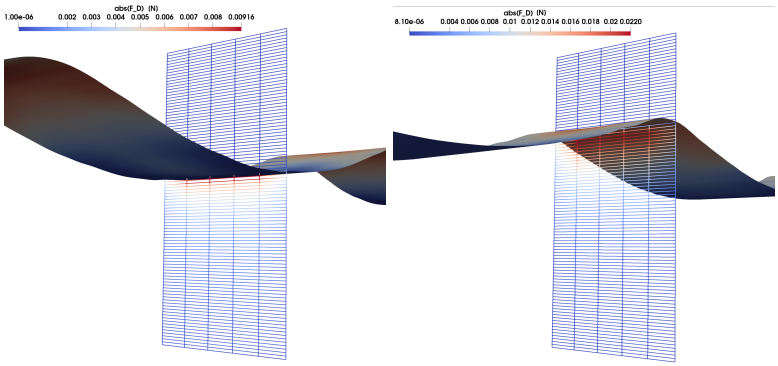

(a) Wave trough situation. (b) Wave crest situation.

Figure 22: Distribution of the drag force magnitudes on net panel with $Sn = 0.288$ in wave 5.

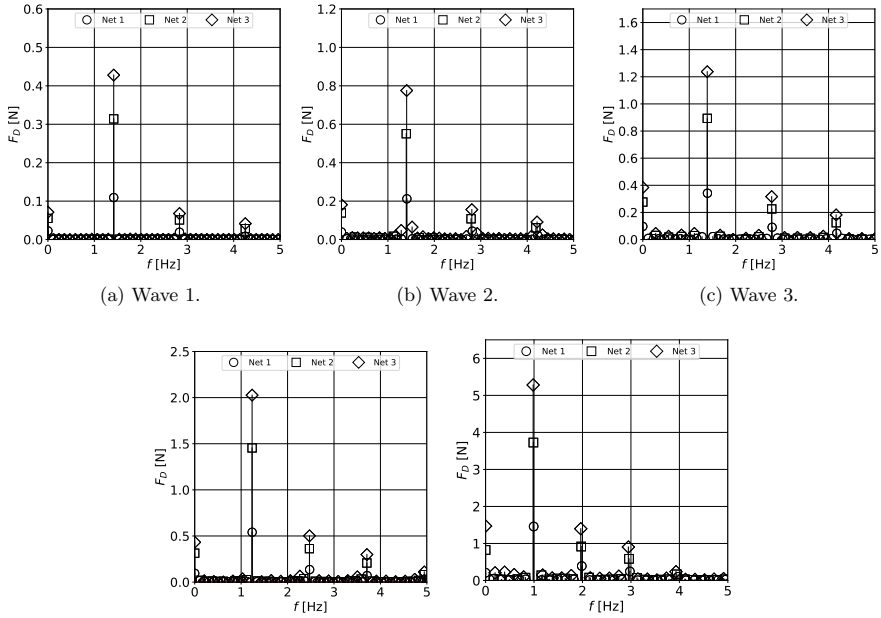

(a) Wave 1. (b) Wave 2. (c) Wave 3.

(d) Wave 4. (e) Wave 5.

Figure 23: Amplitude spectra of the numerical drag force time series for the five different wave cases.

The quantification of the predicted wave and force amplitudes is performed considering the

deviation for the positive and negative side separately. For the wave propagation, this corresponds to values of less than 13% for all wave crest amplitudes and less than 12% for all wave trough amplitudes. The deviations for the drag forces are presented in Tab. 11. The forces are mostly under-predicted by up to 25% for the first net with $Sn = 0.095$. In comparison, the model over-predicts the forces for the nets with higher solidities. The positive forces on the net with the highest solidity are generally predicted with high accuracy (12% and less) whereas the negative forces show larger discrepancies (up to 30%). The intermediate solidity is generally predicted the least accurate with most deviations between 20% and 40%. Chen and Christensen [12] noticed similar challenges with their porous medium model and pointed to uncertainties in the experimental data. In addition, it is noticeable that the second net geometry consists of the shortest twines. This confirms the observation in section 6.3 where the net cage in steady current with the shortest twines was most challenging for the model.

Table 11: Deviations [%] between numerical simulation and experimental data of Lader et al. [24] for the averaged positive (+) and negative (−) drag force amplitudes.

Sn	Wave case									
	1		2		3		4		5	
	+	-	+	-	+	-	+	-	+	-
0.095	11.4	19.1	25.1	−17.6	23.2	1.9	10.9	21.7	17.9	0.5
0.22	−80.5	−21.4	−31.2	−30.6	−29.2	−49.1	−59.8	−29.2	−41.1	−21.7
0.288	−12.4	−30.3	−3.2	−9.8	−3.2	−20.2	4.3	−30.4	−3.2	−55.8

6.5 Velocity reduction behind multiple net panels in steady current flows

A final validation case is the comparison to the experiments of Bi et al. [5]. They conducted PIV measurements of the fluid around a single and multiple fixed net panels in varying currents. They were carried out in a wave-current flume at the State Key Laboratory of Coastal and Offshore Engineering at the Dalian University of Technology, China. The flume has the dimensions 22 m × 0.45 m × 0.6 m and a water depth of 0.4 m. The net panel is $L = 0.3$ m long and wide. It is placed in the centre of the flume normal to the flow direction. A knotless net with square meshes and $Sn = 0.243$ is used. The inflow velocities u_∞ are 0.056 m/s, 0.113 m/s, 0.17 m/s and 0.226 m/s. In a first measurement series, up to three additional panels of the same size and geometry are placed in the wake of the first panel. The distance between each panel is one panel length. The velocity is measured one panel length behind the last panel for each configuration. In a second series, the wake velocities are measured at different locations between and behind up to $N = 4$ net panels for $u_\infty = 0.17$ m/s. An illustration of the computational domain is shown in Fig. 24. The length of the domain is 3.8 m which is long enough to avoid eventual reflections from the outlet. All probe points are taken from the experiment at which the origin is located in the middle of the first panel. The same argument as given in section 6.1 is used for the calculation of the wake velocity. Therefore, several probes with the same x location are computed, averaged and compared to the experiment. In contrast to the previous cases, $\kappa = 0.05$ is applied. Thus, the influence of the net is higher than in section 6.1 which is physically linked to a higher solidity. As the main results, Fig. 25 and the Tabs. 12 and 13 show the qualitative and quantitative comparisons for the velocity reduction factor U_r with the experiments. Further, the variation of the drag forces on the different net panels for different inflow velocities is provided in Fig. 26.

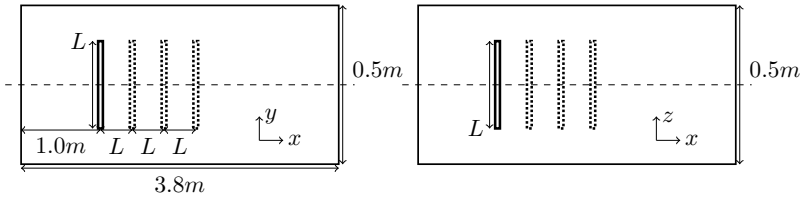

Figure 24: Computational domain for the simulation of multiple fixed net panels in steady current flow. Top view is shown on the left, side view is shown on the right. Origin of the coordinate system is on the intersection of the middle line and the first panel.

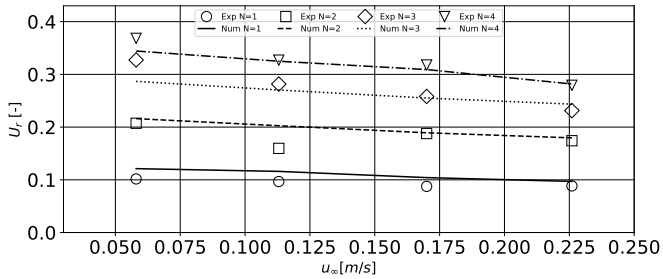

(a) Distribution of U_r over u_∞, measured 1.0 L behind the last panel.

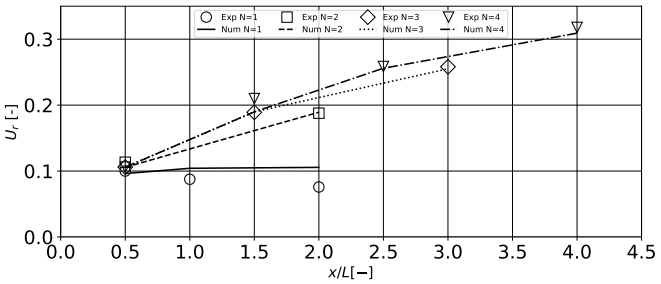

(b) Distribution of U_r over x/L for $u_\infty = 0.17$ m/s.

Figure 25: Comparison of the numerical and experimental velocity reduction factors for N fixed net panels in steady current flow.

As can be seen in Fig. 25a, the velocity reduction increases with the number of panels due to an increased resistance over the same distance. At the same time, U_r tends to decrease slightly if the inflow velocity is increased as can also be seen in the previous results (Fig. 10c). The quantitative analysis in Tab. 12 indicates a maximum deviation of 27%, but most deviations are well below 10%. Generally, the deviations are the largest for the single net case. However, $N = 1$ also results in the smallest reduction factors which correspond to the highest sensitivity to errors. If the L_2 norms of deviation, which are $0.033, 0.044, 0.044$ and 0.026 for

$N = 1 - 4$, are considered, it can be seen that the modelling deviation is similar for all cases. A further explanation can be obtained from Fig. 25b which presents the U_r distribution over $x/L = 0$ to $x/L = 4$ for $u_\infty = 0.17$ m/s and $N = 1 - 4$. In comparison to the velocity in the vicinity of the net, U_r slightly decreases over x. This effect implies an acceleration of the fluid which might be due to enhanced turbulence in the wake-field. In the numerical model, this would have to be incorporated by increasing the turbulence production through the net in the turbulence model. If multiple panels are arranged in such a way that the wake cannot evolve freely, as given in these computations, an increase of U_r can be observed (see also Fig. 27). As reported in [5], downstream panels slightly influence the flow through upstream panels which is also captured by the numerical model. This is confirmed by reporting the deviations in Tab. 13. All deviations are within a 10% deviation band for $N > 1$, and the L_2 norms of deviations are $0.034, 0.008, 0.003$ and 0.022 for $N = 1 - 4$.

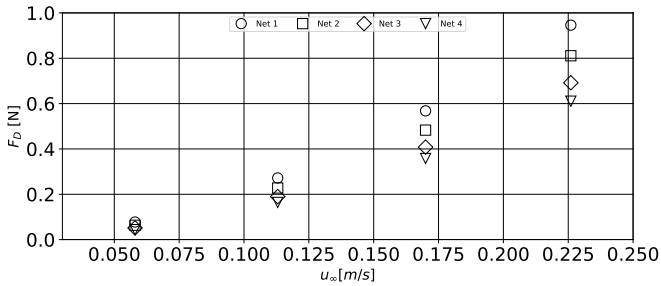

Figure 26: Numerical drag forces on four fixed net panels for varying steady inflow velocities.

The numerically predicted drag forces on the panels for different u_∞ and $N = 4$ are shown in Fig. 26. No measurements are available for comparison. The forces increase quadratically as a function of u_∞ for all nets as expected. Further, they decrease with the position of the corresponding net because of a decreased inflow velocity. It is also interesting to note that the difference in the calculated F_D between the first and the last net increases with u_∞. Thus, the importance of incorporating the velocity reduction behind a net increases with the inflow velocity.

Table 12: Deviations [%] for the velocity reduction factors measured 1.0 L behind the last net for different inflow velocities and varying number of panels N. The numerical results are compared to the experimental data of Bi et al. [5].

N	u_∞ [m/s]			
	0.058	0.113	0.17	0.226
1	−19.19	−19.94	−19.01	−9.71
2	−4.21	−26.90	−0.75	−3.10
3	12.41	3.97	1.18	−5.26
4	6.53	0.65	2.76	−0.88

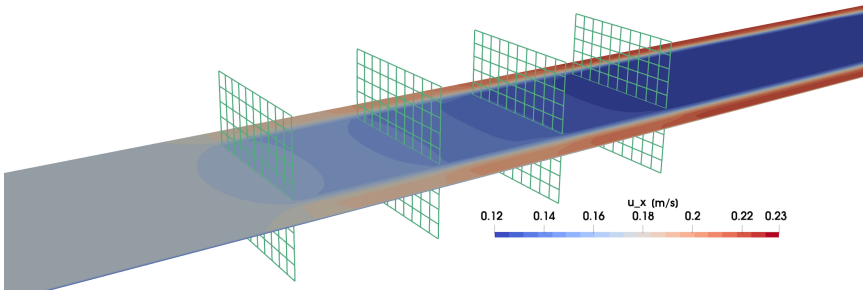

Figure 27: Numerical result for the x-velocity profile in the middle slice for 4 nets with $Sn = 0.243$ in steady current flow of $u_\infty = 0.17$ m/s.

Table 13: Deviations [%] for the velocity reduction factors at different x/L positions and varying number of panels N. The numerical results are compared to the experimental data of Bi et al. [5].

N	x/L [−]						
	0.5	1.0	1.5	2.0	2.5	3.0	4.0
1	3.80	−19.01	-	−39.47	-	-	-
2	6.75	-	-	−0.75	-	-	-
3	0.29	-	−0.29	-	-	1.18	-
4	0.29	-	9.60	-	1.04	-	2.76

7 Conclusions

The presented paper introduces a new method for modelling the flow through fish nets. The new approach is based on momentum disturbances incorporated into the Reynolds-averaged Navier-Stokes equations. The procedure is derived and discussed extensively. All necessary forces are calculated using the screen force model for plane net panels. This model has advantages over Morison type force models due to the incorporation of the angle between fluid and net into its formulation. The unknown force coefficients are determined from experimental data and a non-linear fitting algorithm. The new method represents the net as Lagrangian points in a Eulerian fluid domain. This simplifies the overall numerical procedure in comparison to porous medium models. Further, the disturbances are extrapolated on surrounding fluid cells but their origins are kept at the net itself. This is in contrast to a porous medium representation where the net is non-physically thickened. The transition from a surface force to a volume force leads to the introduction of a new parameter which has to be determined to account for the correct velocity reduction behind the net. The issue of transferring existing force models to coupled numerical simulations is discussed for the first time. The coupling process influences the flow velocity at the net which has to be corrected to match the undisturbed velocity used for computing force coefficients. An intrinsic formula is derived to couple these velocities using Froude's momentum theory. The numerical model is extensively validated against existing experiments for fixed net panels, multiple panels and cages with varying

geometries and solidities in current and regular waves. For all cases, both a qualitative and quantitative analysis is performed. Overall, the proposed model performs reasonably for all presented cases because deviation bands of less than 10% can be achieved regularly and physical explanations can be given elsewhere. This is true for both force coefficients and the velocity reductions in the wake.

The validation process indicates a possible limitation of the screen force model for nets with small twine lengths due to its assumptions. In particular, the applicability of the strip theory on each twine and the derived formula for the characteristic cross-flow velocity at the twines (see [14]) might have a constraint which is not discussed so far. Further, the presented computations indicate a dependency of κ on the net solidity but a low influence from varying inflow velocities or angles of attack. This simplifies the future work of finding a generally applicable formula for this parameter. The neglect of turbulence throughout the validation process indicates that this effect is not important for the correct modelling of loads. However, it plays a crucial role for investigations of the flow within net cages including fish and, therefore, turbulence modelling should be considered in the future. Besides, more validation for complex wave and current-wave conditions and the inclusion of net deformation will be considered.

Acknowledgements

The authors are grateful for the grants provided by the Research Council of Norway under the HAVBRUK2 project (no. 267981). This research was supported in part with computational resources at NTNU provided by NOTUR (Norwegian Metacenter for Computational Sciences, http://www.notur.no) under project no. NN2620K.

References

[1] A. Aggarwal et al. “Estimation of breaking wave properties and their interaction with a jacket structure”. In: *Journal of Fluids and Structures* 91 (2019). DOI: 102722.

[2] A. Aggarwal et al. “Free Surface Reconstruction for Phase Accurate Irregular Wave Generation”. In: *Journal of Marine Science and Engineering* 6 (3), 105 (2018). DOI: 10.3390/jmse6030105.

[3] N. Aquelet and J. Wang. “Porous parachute modelling with an Euler-Lagrange coupling”. In: *European Journal of Computational Mechanics* 16.3-4 (2007), pp. 385–399.

[4] C.-W. Bi et al. “Drag on and flow through the hydroid-fouled nets in currents”. In: *Ocean Engineering* 161 (2018), pp. 195–204.

[5] C.-W. Bi et al. “Experimental investigation of the reduction in flow velocity downstream from a fishing net”. In: *Aquaculture Engineering* 57 (2013), pp. 71–81.

[6] C.-W. Bi et al. “Numerical simulation of the interaction between flow and flexible nets”. In: *J. Fluids Struct.* 45 (2014), 180–201.

[7] H. Bihs and A. Kamath. “A combined level set/ghost cell immersed boundary representation for floating body simulations”. In: *Int. J. Numer. Meth. Fluids* Volume 83 (2017), 905–916.

[8] H. Bihs et al. “A new level set numerical wave tank with improved density interpolation for complex wave hydrodynamics”. In: *Computers & Fluids* Volume 140 (2016), 191–208.

[9] J.U. Brackbill, D.B. Kothe, and C. Zemach. “A Continuum Method for Modeling Surface Tension”. In: *Journal of Computational Physics* Volume 100(2) (1992), 335–354.

[10] J.S. Carlton. *Marine Propellers and Propulsion*. Fourth. Butterworth-Heinemann, Oxford, UK, 2019.

[11] H. Chen and E.D. Christensen. “Development of a numerical model for fluid-structure interaction analysis of flow through and around an aquaculture net cage”. In: *Ocean Engineering* 142 (2017), 597–615.

[12] H. Chen and E.D. Christensen. “Investigations on the porous resistance coefficients for fishing net structures”. In: *J. Fluids Struct.* 65 (2016), 76–107.

[13] A. Chorin. “Numerical solution of the Navier-Stokes equations”. In: *Mathematics of Computation* Volume 22 (1968), 745–762.

[14] O.M. Faltinsen and A.N. Timokha. *Sloshing*. Cambridge University Press, 2009.

[15] A. Fredheim. *Current Forces on Net Structures*. Ph.D. thesis, NTNU Trondheim, Norway. 2005.

[16] G.S. Jiang and D. Peng. “Weighted ENO schemes for Hamilton Jacobi equations”. In: *SIAM Journal of Scientific Computing* Volume 21 (2000), 2126–2143.

[17] G.S. Jiang and C.W. Shu. “Efficient implementation of weighted ENO schemes”. In: *Journal of Computational Physics* Volume 126(1) (1996), 202–228.

[18] A. Kamath et al. “CFD Simulations of Wave Propagation and Shoaling over a Submerged Bar”. In: *Aquatic Procedia* 4 (2015), pp. 308–316.

[19] T. Kristiansen and O. M. Faltinsen. “Experimental and numerical study of an aquaculture net cage with floater in waves and current”. In: *Journal of Fluids and Structures* 54 (2015), pp. 1–26.

[20] T. Kristiansen and O. M. Faltinsen. “Modelling of current loads on aquaculture net cages”. In: *Journal of Fluids and Structures* 34 (2012), pp. 218–235.

[21] P.F. Lader and B. Enerhaug. “Experimental Investigation of Forces and Geometry of a Net Cage in Uniform Flow”. In: *IEEE Journal of Oceanic Engineering* 30.1 (2005), pp. 79–84.

[22] P.F. Lader and A. Fredheim. “Dynamic properties of a flexible net sheet in waves and current—A numerical approach”. In: *Aquacultural Engineering* 35 (3) (2006), pp. 228–238.

[23] P.F. Lader et al. “Experimental Investigation of the Interaction between Waves and Net Structures—Damping Mechanism”. In: *Aquacultural Engineering* 37.2 (2007), pp. 100–114.

[24] P.F. Lader et al. “Experimental Investigation of Wave Forces on Net Structures”. In: *Applied Ocean Research* 29.3 (2007), pp. 112–127.

[25] G. Løland. *Current forces on and flow through fish farms*. Ph.D. thesis, NTH Trondheim, Norway. 1991.

[26] T. Martin et al. “Efficient implementation of a numerical model for flexible net structures”. In: *Ocean Engineering* Volume 150 (2018), 272–279.

[27] J.A. Nelder and R. Mead. “A Simplex Method for Function Minimization”. In: *The Computer Journal* 7 (4) (1965), pp. 308–313.

[28] S. Osher and J.A. Sethian. “Fronts propagating with curvature-dependent speed: Algorithms based on Hamilton-Jacobi formulations”. In: *Journal of Computational Physics* Volume 79 (1988), 12–49.

[29] Ø. Patursson et al. “Development of a porous media model with application to flow through and around a net panel”. In: *Ocean Engineering* 37 (2010), 314–324.

[30] C. S. Peskin. “Numerical analysis of blood flow in the heart”. In: *Journal of Computational Physics* 25 (3) (1977), pp. 220–252.

[31] P.J. Roache. “Quantification of Uncertainty in Computational Fluid Dynamics”. In: *Annu.Rev. Fluid Mech.* No. 29 (1997), pp. 123–160.

[32] H. Rudi, G. Løland, and I. Furunes. *Experiments With Nets; Forces on and Flow Through Net Panels and Cage Systems*. Technical Report MT51 F88-0215, MARINTEK, Trondheim, Norway. 1988.

[33] H. Schlichting and K. Gersten. *Boundary-Layer Theory*. Ninth. Springer-Verlag Berlin Heidelberg, Germany, 2017.

[34] C.W. Shu and S. Osher. “Efficient implementation of essentially non-oscillatory shock-capturing schemes”. In: *Journal of Computational Physics* Volume 77(2) (1988), 439–471.

[35] M. Sussman, P. Smereka, and S. Osher. “A level set approach for computing solutions to incompressible two-phase flow”. In: *Journal of Computational Physics* Volume 114 (1994), 146–159.

[36] I. Tsukrov et al. “Finite element modeling of net panels using a consistent net element”. In: *Ocean Engineering* 30 (2003), pp. 251–270.

[37] H. van der Vorst. “BiCGStab: A fast and smoothly converging variant of Bi-CG for the solution of nonsymmetric linear systems”. In: *SIAM Journal of Scientific Computing* Volume 13 (1992), 631–644.

[38] Y. Yao et al. “Numerical modeling of current loads on a net cage considering fluid–structure interaction”. In: *Journal of Fluids and Structures* 62 (2016), pp. 350–366.

[39] J.M. Zhan et al. “Analytical and experimental investigation of drag on nets of fish cages”. In: *Aquacultural Engineering* 35 (1) (2006), pp. 91–101.

[40] Y.-P. Zhao et al. “Numerical Simulation of Interaction Between Waves and Net Panel Using Porous Media Model”. In: *Engineering Applications of Computational Fluid Mechanics* 8.1 (2014), pp. 116–126.

Paper 3

A non-linear implicit approach for modelling the dynamics of porous tensile structures interacting with fluids.

Martin, T. and Bihs, H. (2021).
Journal of Fluids and Structures, Vol. 100, doi: 10.1016/j.jfluidstructs.2020.103168.

A non-linear implicit approach for modelling the dynamics of porous tensile structures interacting with fluids

Tobias Martin* Hans Bihs

Department of Civil and Environmental Engineering, Norwegian University of Science and Technology (NTNU), 7491 Trondheim, Norway

Postprint
published in *Journal of Fluids and Structures*, 2021, Vol. **100**,
DOI: 10.1016/j.jfluidstructs.2020.103168.

Abstract

A new model for the simulation of large motions of porous tensile structures and their interaction with the surrounding fluid is developed in this paper. The discrete structure is represented by several non-linear elastic bars and knots connecting up to four bars. An implicit system of equations is derived from the fundamental relations of dynamics, kinematics and material and solved using an improved Newton's method. The Navier-Stokes equations are solved in a numerical domain to account for the interaction with the fluid. The presence of the porous structure is respected in these equations through an additional forcing term based on a modified Lagrangian-Eulerian coupling algorithm. Here, the forces on the structure are distributed on multiple Lagrangian points embedded in the fluid domain. Integration over a suitable Kernel function is applied to distribute these forces on the surrounding fluid. The derived numerical model is suitable for simulating the interaction of porous tensile structures of arbitrary geometry, non-linear material and under large motion with fluids including complex free surfaces. This is in contrast to existing models which either neglect important non-linearities, the physical interaction with the fluid or rely on explicit time integration. The validation process shows excellent agreement between the numerical simulations and existing experimental data and demonstrates the applicability of the new methodology for a wide range of applications.

Keywords: Hydroelasticity, Tensile structure, Porous medium, Fluid-structure interaction, CFD

*Corresponding author, tobias.martin@ntnu.no

1 Introduction

Offshore aquaculture has seen growing interest recently because of increasing size of the sites and greater concern over traditional aquaculture due to their environmental impact on coastal regions. The change of environment significantly increases the importance of the accurate prediction of the expected loads and the structural response due to an increased fluid-structure interaction (FSI). A major part of the structure is covered by flexible membranes. These are characterised as spatially intrinsically two-dimensional structures with tensile stress resistance but neglectable bending stiffness. In the case of aquaculture cages, the membranes have high porosity and two dominant stress directions. In the past, segregated approaches considered the motion of these nets without incorporating interaction with the fluid [22] or assuming the validity of potential theory [16]. These studies cannot be regarded as appropriate for offshore conditions due to the non-linearly increasing importance of the FSI for the accurate prediction of the structural and fluid dynamics. In contrast, numerical simulations using computational fluid dynamics (CFD) can be applied to understand the structural and environmental challenges by modelling the forces on and the fluid dynamics in and around the cage. Amongst others, Lewandowski and Pichot [21] simulated the flow around and inside a rigid net using the Reynolds-averaged Navier-Stokes equations without considering the net motion.

The significant length scale difference between the flow around the whole structure and the flow through each of its voids prevents the resolution of the complete porous structure within the discrete fluid domain. Therefore, a more elaborated approach separates the calculation of the structural and fluid dynamics while respecting their interaction by an appropriate coupling algorithm. The most dominant coupling algorithm is based on a porous medium representation of the porous sheet. For this purpose, a porous volume is defined around the membrane and the governing volume- and Reynolds-averaged Navier-Stokes equations are solved using a finite volume method [3, 28, 38]. Recently, Chen and Christensen [8, 9] improved the idea by utilising a less restricted model for the proper definition of the porous resistance coefficients. Martin et al. [24] analysed this approach and revealed several limitations which prevent the applicability of the porous volume analogy for arbitrary shapes and large deformations. They overcame this issue by proposing a new coupling model based on Lagrangian-Eulerian considerations which are generally efficient and broadly applicable. The main idea is built on the developments of Ryzhakov and Oñat [30] for closed membranes and Aquelet and Wang [1] for air-parachute interaction. Here, disturbances from the solid parts on the surrounding fluid are distributed using Lagrangian points. In comparison, the porosity of the structure led to several modifications of the original approach and the usage of the screen force model of Kristiansen and Faltinsen [17] to approximate the hydrodynamic forces from the fluid on the porous membrane. The coupling model of Martin et al. [24] is improved and extended for dynamic problems within the presented work.

Several approaches for modelling the dynamics of tensile structures were presented in the past. Tsukrov et al. [34] established a finite element modelling using perpendicular one-dimensional two-node elements with three degrees of freedom. Lader and Fredheim [19] introduced the lumped mass method which represents the discrete structure as massless bars connected by mass knots. The solution of the dynamics of the knots was found in terms of their acceleration from Newton's second law, and Runge-Kutta time integration was applied to calculate the knot velocities and positions from the accelerations. The constitutive equations are not automatically satisfied as no iterations are performed which can lead to stability

issues and very small time steps in comparison to the fluid solver. The time step restriction is also necessary due to the explicit time integration. A minor modified version of the original approach was successfully coupled to a porous medium model to simulate flexible porous sheets [3] and cylinders [2] in steady flow conditions. In order to overcome the issue of small time steps, implicit methods were proposed. The development of an implicit quasi-static net model was presented in [25]. The missing time step restriction increases the efficiency of the model, but the approach lacks justification for applications including large motions and snap loads. LeBris and Marichal [20] introduced an implicit dynamic net model based on the satisfaction of the kinematic relation between knot position and bar length. The original approach was based on inelastic material which leads to very high condition numbers due to missing elements on the main diagonal of the system matrix. Vincent [35] successfully overcame this drawback by including elastic material into the model. However, their derivation relied on a linear material assumption and linearised equations. This is a severe drawback considering the non-linearity of net material [19]. Thus, the need for an implicit non-linear dynamic net model arises to accurately model the motion of these distinct types of porous tensile structures. In this paper, such an approach is presented by taking Newton's second law as the basis. The external forces due to gravity, inertia and drag are calculated by extending the idea of the screen force model. A non-linear system of equations for the unknown tension forces is derived using high-order finite differences. The system is solved using an improved Newton's method leading to convergence within three to ten iterations for the considered validation cases.

The emerging numerical FSI algorithm is coupled to a numerical wave tank modelling the transport of the interface between two phases. Hence, the model is suitable for simulating the interaction of porous tensile structures of arbitrary geometry, non-linear material and under large motion with fluids including complex free surfaces. This is in contrast to existing models which either neglect important non-linearities, the physical interaction with the fluid or rely on explicit time integration.

The remaining paper is structured as follows. Section 2 presents the derivation of the new implicit non-linear structural model, whereas section 3 provides details about the numerical fluid solver and the coupling algorithm. In section 4, the model is verified, and sections 5 and 6 are devoted to several validation cases of porous rigid and flexible sheets and cages in varying wave and current conditions. A possible application of the proposed model is presented in section 7. Conclusions arising from the previous sections are given in section 8.

2 Non-linear dynamic numerical model for tensile structures

The considered tensile structure is assumed to consists of a large number of square or rhombic meshes forming a porous cylinder or sheet with two distinct stress directions. Thus, an appropriate discrete representation of the structure consists of multiple knots and connecting elastic bars in the principal directions of the meshes. The definition of so-called macro elements is needed for the coupling to the fluid dynamic solution. Each macro element contains four knots and four bars and, depending on the porosity of the structure, represents multiple physical meshes. Instead of the porosity, the solidity S is considered below. The solidity of a porous sheet is defined as the ratio of solid front area to the total area and therefore, equals one minus the porosity. Using the information about the physical twine diameter d_t and twine

length l_t, S is calculated from [12]

$$S = \frac{2d_t}{l_t} - \left(\frac{d_t}{l_t}\right)^2. \tag{1}$$

Each structural element is further split into four screens as shown in Fig. 1. Thus, each knot is related to up to four screens. As the screens are not explicitly resolved in the fluid grid, an approximation of the forces on the structure is introduced. Following the assumptions of Morison et al. [26] for hydrodynamic transparent structures, the mass of the S_i screens is lumped at knot $\mathbf{x}_i$ so that the total mass at that knot $\mathbf{m}_i$ can be approximated from

$$\mathbf{m}_i = \sum_{s=1}^{S_i} \begin{pmatrix} m_{\text{air}} + m_{\text{a}} n_x & 0 & 0 \\ 0 & m_{\text{air}} + m_{\text{a}} n_y & 0 \\ 0 & 0 & m_{\text{air}} + m_{\text{a}} n_z \end{pmatrix}_s, \tag{2}$$

with $m_{\text{air},s}$ the mass of the screen in air and $\mathbf{n}_s$ the unit normal vector of the screen pointing in relative velocity direction. The added mass $m_{a,s}$ is approximated as the mass of the water volume occupied by the screen under the assumption that the net is a mesh of multiple cylinders only. Here, the added mass is only applied in the normal direction of the structure.

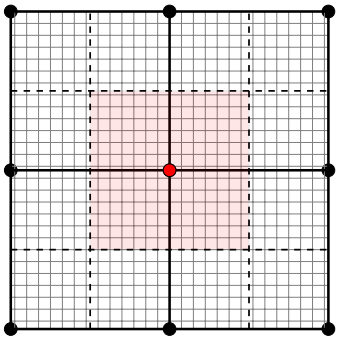

Figure 1: Discrete structure representation: the thin lines show the physical structure; the structural (macro) elements are represented by black dots connected with thick black lines; the dashed lines present the discretisation into several screens. The red area is related to the red dot for the force calculations.

The dynamic equilibrium equations are formulated for each $\mathbf{x}_i$ with N_i neighbouring knots under consideration of Fig. 2:

$$\mathbf{m}_i \; \mathbf{a}_i = \sum_{k=1}^{N_i} \mathbf{T}_{ik} + \mathbf{G}_i + \mathbf{H}_i. \tag{3}$$

Here, $\mathbf{G}_i$ represents the sum of the static gravity and buoyancy force and $\mathbf{H}_i$ the external hydrodynamic forces consisting of inertia forces $\mathbf{I}_i$ due to the fluid acceleration $\mathbf{a}_f$,

$$\mathbf{I}_i = \sum_{s=1}^{S_i} \begin{pmatrix} m_{\text{a}} + m_{\text{a}} n_x & 0 & 0 \\ 0 & m_{\text{a}} + m_{\text{a}} n_y & 0 \\ 0 & 0 & m_{\text{a}} + m_{\text{a}} n_z \end{pmatrix}_s \mathbf{a}_{f,s}, \tag{4}$$

and drag and lift forces $\mathbf{D}_i$ whose calculation are described below. The tension force vectors $\mathbf{T}_{ij}$ are defined as the unknown tension force magnitude T_{ij} times the unit vector $\mathbf{b}_{ij}$ of the corresponding bar

$$\mathbf{T}_{ij} = T_{ij}\ \mathbf{b}_{ij} = T_{ij} \cdot \left(\frac{\mathbf{x}_j - \mathbf{x}_i}{|\mathbf{x}_j - \mathbf{x}_i|} \right). \tag{5}$$

Assuming non-linear material, a constitutive equation is formulated as

$$T_{ij} = C_1 \varepsilon + C_2 \varepsilon^2 = C_1 \left(\frac{l_{ij}}{l_{0,ij}} - 1 \right) + C_2 \left(\frac{l_{ij}}{l_{0,ij}} - 1 \right)^2, \tag{6}$$

with l_{ij} the current length of the bar and $l_{0,ij}$ its original length. Lader and Fredheim [19] found this relation to be valid with $C_1 = 1160\ N$ and $C_2 = 37300\ N$ for nylon nets with squared meshes, which is used in the validation section below. Eq. (6) is reformulated for l_{ij} by eliminating the non-physical solution:

$$l_{ij} = \frac{l_0}{2C_2} \cdot \left(-C_1 + 2\ C_2 + \sqrt{C_1^2 + 4\ C_2\ T_{ij}} \right). \tag{7}$$

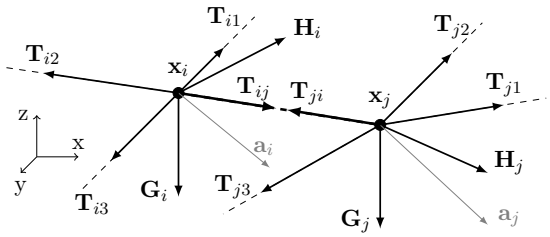

Figure 2: Illustration of the dynamic force equilibrium at the knots $\mathbf{x}_i$ and $\mathbf{x}_j$ showing only structural quantities.

At each new time step $(n+1)$, the unknown position of the knots is related to the unknown tension forces using the kinematic compatibility equation

$$\left(\mathbf{x_j}^{(n+1)} - \mathbf{x_i}^{(n+1)} \right)^2 = \left(l_{ij}^{(n+1)} \right)^2. \tag{8}$$

Inserting the constitutive relation (7) in (8) yields

$$\left(\mathbf{x_j}^{(n+1)} - \mathbf{x_i}^{(n+1)} \right)^2 = \frac{l_0^2}{4C_2^2} \cdot \left(-C_1 + 2C_2 + \sqrt{C_1^2 + 4C_2 T_{ij}^{(n+1)}} \right)^2. \tag{9}$$

The fulfilment of the dynamic equilibria (3) is ensured by replacing $\mathbf{x}^{(n+1)}$ in (9) with accelerations using high-order backward finite differences in time. The weight of each point included in the approximation is found iteratively using the algorithm of Fornberg [11] because

of variable time steps in the coupled simulations. In doing so, the first derivative of $\mathbf{x}^{(n+1)}$ is expressed as

$$\frac{d\mathbf{x}^{(n+1)}}{dt} = \mathbf{v}^{(n+1)} = \sum_{p=0}^{P} c_p \mathbf{x}^{(n+1-p)}, \tag{10}$$

and then reformulated for the position vector:

$$\mathbf{x}^{(n+1)} = \frac{1}{c_0}\mathbf{v}^{(n+1)} - \sum_{p=1}^{P} \frac{c_p}{c_0}\mathbf{x}^{(n+1-p)}. \tag{11}$$

The now arising unknown velocity vectors $\mathbf{v}^{(n+1)}$ are approximated using the same procedure, so that

$$\mathbf{v}^{(n+1)} = \frac{1}{c_0}\mathbf{a}^{(n+1)} - \sum_{p=1}^{P} \frac{c_p}{c_0}\mathbf{v}^{(n+1-p)}. \tag{12}$$

In the scope of the paper, third-order accurate polynomials are chosen by setting $P = 3$. By inserting (12) in (11), the left-hand side in (9) is approximated as

$$\begin{aligned}
&\left(\mathbf{x_j}^{(n+1)} - \mathbf{x_i}^{(n+1)}\right)^2 \\
=&\left[\frac{\left(\mathbf{a}_j^{(n+1)} - \mathbf{a}_i^{(n+1)}\right)}{c_0^2} - \sum_{p=1}^{P} \frac{c_p}{c_0^2}\left(\mathbf{v}_j^{(n+1-p)} - \mathbf{v}_i^{(n+1-p)}\right)\right. \\
&\left. - \sum_{p=1}^{P} \frac{c_p}{c_0}\left(\mathbf{x}_j^{(n+1-p)} - \mathbf{x}_i^{(n+1-p)}\right)\right]^2 \\
=&\frac{1}{c_0^4}\left[\left(\mathbf{a}_j^{(n+1)} - \mathbf{a}_i^{(n+1)}\right) + \mathbf{V}_{ij} + \mathbf{X}_{ij}\right]^2,
\end{aligned} \tag{13}$$

with the definitions

$$\mathbf{X}_{ij} = -c_0 \sum_{p=1}^{P} c_p \left(\mathbf{x}_j^{(n+1-p)} - \mathbf{x}_i^{(n+1-p)}\right), \tag{14}$$

$$\mathbf{V}_{ij} = -\sum_{p=1}^{P} c_p \left(\mathbf{v}_j^{(n+1-p)} - \mathbf{v}_i^{(n+1-p)}\right). \tag{15}$$

Under consideration of definition (3), the substitution of (13) in (9) yields a non-linear function F for each bar b_{ij}:

$$\begin{aligned}
F_{ij}\left(\mathcal{T}^{(n+1)}\right) = &\left(\sum_{k=1}^{N_j} \mathbf{m}_j^{-1}\mathbf{T}_{jk}^{(n+1)} - \sum_{k=1}^{N_i} \mathbf{m}_i^{-1}\mathbf{T}_{ik}^{(n+1)} + \mathbf{A}_{ij} + \mathbf{V}_{ij} + \mathbf{X}_{ij}\right)^2 \\
&- \frac{c_0^4\, l_0^2}{4\, C_2^2} \cdot \left(-C_1 + 2C_2 + \sqrt{C_1^2 + 4C_2 T_{ij}^{(n+1)}}\right)^2 = 0,
\end{aligned} \tag{16}$$

with $\mathcal{T}$ the global vector of tension force magnitudes and

$$\mathbf{A}_{ij} = \mathbf{m}_j^{-1}(\mathbf{G}_j^{(n)} + \mathbf{H}_j^{(n)}) - \mathbf{m}_i^{-1}(\mathbf{G}_i^{(n)} + \mathbf{H}_i^{(n)}). \tag{17}$$

The solution for $\mathcal{T}$ is found from (16) using a Newton's method. The improved iterative procedure

$$\begin{aligned} \mathcal{T}^{(*)} &= \mathcal{T}^{(n)} - \left[\mathcal{J}\left(\mathcal{T}^{(n)}\right)\right]^{-1} \mathcal{F}\left(\mathcal{T}^{(n)}\right), \\ \mathcal{T}^{(n+1)} &= \mathcal{T}^{(*)} - \left[\mathcal{J}\left(\mathcal{T}^{(n)}\right)\right]^{-1} \mathcal{F}\left(\mathcal{T}^{(*)}\right), \end{aligned} \tag{18}$$

is implemented for this purpose. Here, $\mathcal{F}$ represents the vector of the functions (16) and $\mathcal{J}$ is its Jacobian matrix. It is shown by Chun [10] that (18) converges with third-order. The derivatives of (16) are found separately for the joint bar b_{ij} and its adjoint bars (see A for the expressions). An approximation of the solution has to be given as initial condition. It is proposed to perform the first time step with the linearised version of this model. The solution of the arising linear system only depends on an approximation of the initial position of the structure. The derivation of this model follows the developments of Marichal [23] and can be found in B. The pre-processing consists of preparing connectivity matrices and follows thereby the concept described previously [25]. Once a converged result has been found for the tension forces, acceleration, velocity and position of the knots are found from (3), (11) and (12).

The description of the structural model is completed by providing details about the calculation of the velocity related forces $\mathbf{D}_i$ from the fluid using the screen force model [17]. Considering the inertia system of the fluid, this force can be split into a drag and a lift force component in normal ($\mathbf{n}_d$) and tangential ($\mathbf{n}_l$) direction of the local relative velocity vector $\mathbf{u}_{\mathrm{rel,s}} = \mathbf{u}_s - \mathbf{v}_s$:

$$\mathbf{D}_i = \sum_{s=1}^{S_i} \int_{\partial A_s} \frac{\rho}{2} u_{\mathrm{rel,s}}^2 (c_d \mathbf{n}_d + c_l \mathbf{n}_l)_s \, \mathrm{d}\mathbf{x}. \tag{19}$$

The surface integral is approximated by a second-order accurate quadrature rule using the geometrical centre as integration point. The drag and lift force directions are defined as

$$\mathbf{n}_{d,s} = \frac{\mathbf{u}_{rel,s}}{|\mathbf{u}_{rel,s}|}, \tag{20}$$

$$\mathbf{n}_{l,s} = \frac{(\mathbf{u}_{rel,s} \times \mathbf{n}_s) \times \mathbf{n}_s}{|(\mathbf{u}_{rel,s} \times \mathbf{n}_s) \times \mathbf{n}_s|}, \tag{21}$$

with $\mathbf{n}_s$ the unit normal vector of the screen pointing in the relative velocity direction. The coefficients c_d and c_l are calculated from a truncated Fourier series expanded for their dependency on the angle of attack α between fluid velocity vector and normal vector of the screen

$$c_d(\alpha) = c_{d,0} \sum_{k=1}^{\infty} a_{2k-1} \cos\left((2k-1)\alpha\right), \tag{22}$$

$$c_l(\alpha) = c_{l,\frac{\pi}{4}} \sum_{k=1}^{\infty} b_{2k} \cos\left(2k\alpha\right). \tag{23}$$

The definition of the constants $c_{d,0}$ and $c_{l,\frac{\pi}{4}}$ are given in [17]. The determination of the Fourier coefficients is based on non-linear fitting to experimental data as described by the authors in [24].

3 Direct coupling of the structural response to the fluid solution

3.1 Numerical model for solving the fluid dynamics

The conservation of mass and momentum for incompressible fluids arises in convective form as

$$\nabla \cdot \mathbf{u} = 0, \tag{24}$$

$$\frac{\partial \mathbf{u}}{\partial t} + \mathbf{u} \cdot \nabla \mathbf{u} = -\frac{1}{\rho}\nabla p + \nabla \cdot \left(\nu \left[\nabla \mathbf{u} + \nabla \mathbf{u}^T\right]\right) + \mathbf{g}, \tag{25}$$

with $\mathbf{u}$ the velocity vector, $\mathbf{g}$ the gravity acceleration vector, p the pressure and ν the kinematic viscosity. The system is solved numerically using finite differences on rectilinear grids. The convection term is discretised with the fifth-order accurate weighted essentially non-oscillatory (WENO) scheme of Jiang and Shu [15] adapted to non-uniform point distances, and the diffusion term is discretised using second-order accurate central differences. A staggered grid approach is chosen to ensure a tight connection of the pressure and velocity field. The solution process follows the incremental pressure-correction algorithm for incompressible flows as proposed by Timmermans et al. [33]. In the predictor step, continuity violating velocities $\mathbf{u}^{(*)}$ are calculated using pressure gradients from the previous time step:

$$\frac{\mathbf{u}^{(*)} - \mathbf{u}^{(n)}}{\Delta t} = -\mathbf{u}^{(n)} \cdot \nabla \mathbf{u}^{(n)} - \frac{1}{\rho}\nabla p^{(n)} + \nabla \cdot \left(\nu \left[\nabla \mathbf{u} + \nabla \mathbf{u}^T\right]\right)^{(*)} + \mathbf{g}. \tag{26}$$

The implicit handling of the diffusion term removes decisive restrictions from the CFL condition [5]. A third-order accurate total variation diminishing Runge-Kutta scheme [31] is applied to advance (26) in time. Here, the time step is determined from the CFL condition. At each sub-step, the projection step solves a Poisson equation for the pressure correction term p_{corr}

$$\nabla \cdot \left(\frac{1}{\rho}\nabla p_{\mathrm{corr}}\right) = \frac{1}{\Delta t}\nabla \cdot \mathbf{u}^{(*)}. \tag{27}$$

The total pressure is then found from the obtained pressure increment [6] using

$$p^{(n+1)} = p^{(n)} + p_{\mathrm{corr}} - \rho\nu \ \nabla \cdot u\_i^{(*)}. \tag{28}$$

Subsequently, the predicted velocities are projected onto the space of divergence-free fields so that

$$\mathbf{u}^{(n+1)} = \mathbf{u}^{(*)} - \frac{\Delta t}{\rho}\nabla p^{(n+1)}. \tag{29}$$

The algorithm is implemented in the open-source CFD solver REEF3D [4, 5]. Full parallelisation of the model is provided through an n-halo domain decomposition strategy and the message passing interface (MPI) for inter-processor communication. The solver utilises the fully parallelized BiCGStab algorithm with geometric multigrid preconditioning of the HYPRE library [36] for solving the Poisson equation.

If a free surface is present, defined as the interface between water and air phase, the same set of equations is solved. However, the material properties become space and time dependent which is implicitly described by the zero level set of a smooth signed distance function Φ [27]. The linear advection equation

$$\frac{\partial \Phi}{\partial t} + \mathbf{u} \cdot \nabla \Phi = 0, \tag{30}$$

is solved for propagating Φ in space and time. The fifth-order accurate HJ-WENO scheme of Jiang and Peng [14] is applied for the spatial discretisation and the temporal discretisation is performed by a Runge-Kutta method. The level set function has to be reinitialized regularly to keep its signed distance property. For this purpose, the reinitialisation equation [32]

$$\frac{\partial \Phi}{\partial \tau} + \mathrm{sign}(\Phi)\left(|\nabla \Phi| - 1\right) = 0, \tag{31}$$

is solved in pseudo time τ so that Φ converges to a valid solution of the Eikonal equation $|\nabla \phi| = 1$.

3.2 Lagrangian-Eulerian coupling algorithm

The development of a new coupling algorithm for the simulation of fluid dynamics around static porous structures was the subject of previous research [24]. Therefore, only the main concepts and modifications for dynamic calculations are provided in this section. The main idea is built on a Lagrangian-Eulerian approach where the hydrodynamic forces are calculated from interpolated fluid velocities, and the disturbances of the fluid through the solid parts of the structure are incorporated using forcing terms in the Navier-Stokes equations. A flowchart of the complete FSI algorithm is shown in Fig. 3.

An example of the distribution of the Lagrangian points on the discrete structure is shown in Fig. 4. They are defined so that the disturbances are nearly equally distributed over the area with distances similar to the surrounding cell sizes. This is achieved by splitting the macro elements into triangles and refine these according to the stationary grid size in their vicinity. The Lagrangian points are then defined in the geometrical centres of each triangle. A momentum loss vector $\mathbf{F}$ is defined at each fluid point $\mathbf{x}_e = (x_e, y_e, z_e)$ of the Eulerian grid and added to the predicted velocity before solving the Poisson equation. In comparison to [24], the vector is calculated using

$$\mathbf{F}(\mathbf{x}_e) = \sum_{L=1}^{L_e} \frac{\mathbf{f}(\mathbf{x}_L)}{\Delta x_L \Delta y_L \Delta z_L} \, \mathrm{D}\left(\frac{x_e - x_L}{\Delta x}\right) \, \mathrm{D}\left(\frac{y_e - y_L}{\Delta y}\right) \, \mathrm{D}\left(\frac{z_e - z_L}{\Delta z}\right), \tag{32}$$

with $\mathbf{f}(\mathbf{x}_L)$ the hydrodynamic force vector on the screen corresponding to the Lagrangian point $\mathbf{x}_L = (x_L, y_L, z_L)$, L_e the number of Lagrangian points within a defined Kernel around $\mathbf{x}_e$ chosen as the interpolation kernel of Peskin [29]

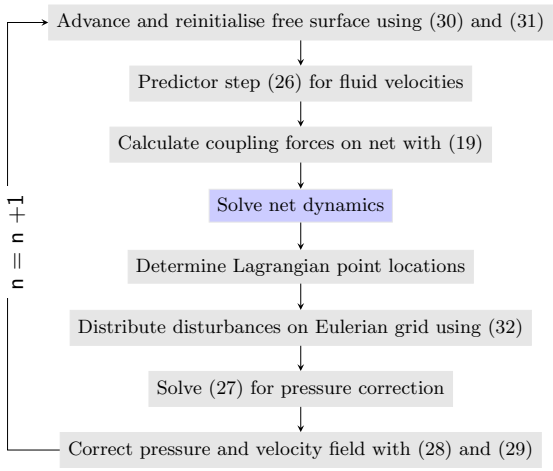

Figure 3: Flowchart of the proposed FSI solver for one time step n.

$$D(r) = \begin{cases} \frac{1}{4}\left(1 + \cos\left(\frac{\pi r}{2}\right)\right) & \text{if } |r| < 2.0 \\ 0.0 & \text{else.} \end{cases} \tag{33}$$

The forces $\mathbf{f}(\mathbf{x}_L)$ are represented by the integral of the external forces from (3) over the triangle area A_L

$$\mathbf{f}(\mathbf{x}_L) = \left[\frac{\rho}{2} u_{\text{rel}}^2 \cdot (c_d \mathbf{n}_d + c_l \mathbf{n}_l) + m_a \left(\mathbf{a_f} + \text{diag}(n_x, n_y, n_z) \cdot (\mathbf{a_f} - \mathbf{a})\right) + \mathbf{G}\right]_L \cdot A_L. \tag{34}$$

The chosen definition (32) removes effectively the free parameter which arose previously due to the usage of an inverse distance weighting.

A final remark applies to the necessity of correcting the fluid velocity around the structure within the determination of c_d and c_l in (19). Based on experimental data, these coefficients are determined as a function of the inflow velocity u_∞, whereas the given velocity information at the structure in the numerical domain is influenced by the pressure jump Δp caused by the porosity. To overcome this mismatch, a virtual inflow velocity is approximated using Froude's momentum theory [7], which is based on the momentum balance in front and behind an infinitesimally thin screen. This theory can be utilised to relate the velocity at the screen u_s to Δp:

$$u_s = u_\infty - \frac{\Delta p}{2\rho u_\infty}. \tag{35}$$

A detailed derivation can be found in [24]. The pressure jump arises from the disturbances in (34) normal to the screen and is defined as

$$\Delta p = \frac{\rho}{2} c_d(u_\infty) u_s^2. \tag{36}$$

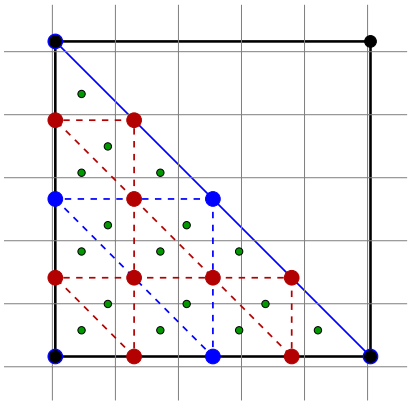

Figure 4: Illustration of the algorithm for calculating Lagrangian points (green dots) of one half of a structural element (thick black lines and points) in a Eulerian fluid domain (thin grey lines): the first triangulation loop results in the blue lines and dots, the second loop results in the red lines and dots.

In combination with (35), u_∞ can be approximated from u_s by solving the intrinsic equation

$$u_\infty = \frac{c_d(u_\infty)}{-1 + \sqrt{1 + c_d(u_\infty)}} \cdot \frac{u_s}{2}, \tag{37}$$

with a Newton-Raphson method and $u_\infty = u_s$ as initial value.

4 Verification of the FSI solver

First, the proper reproduction of the geometrical properties of the structural material is verified using the experimental setup proposed in [19]. A 68 meshes long and 4 meshes wide sheet with $d_t = 1.8$ mm and $l_t = 16$ mm is stretched in longitudinal direction using attached weights. The steady state elongation is measured over increasing forces, and the theoretical result is expected to follow (6). Fig. 5a exemplifies the convergence of the elongation of the numerical structural model presented in section 2. Under-relaxation techniques are used to accelerate the convergence and damp the initial shock of the applied force. As can be seen in Fig. 5b, the numerical model follows the theoretical results as expected. Further, the chosen material coefficients show a good approximation of the experimental results. Additionally, a linear material is tested and shown in the same figure. The results indicate proper representation of the elongation for $\varepsilon < 0.02$ but large deviations from physics for $\varepsilon > 0.08$.

In a second step, the convergence of the numerical simulation for the validation case of section 6.1 is shown in Fig. 6. Here, a porous sheet is fixed at the top and deformed from a steady inflow of $u_\infty = 0.226$ m/s. The global forces in x- and z- direction, the velocity at three different locations behind the sheet and the centre line of the deformed sheet are calculated. The convergence of the fluid solver is presented under usage of the finest possible sheet of $N = 15$ elements in both principal directions. As can be seen in the Figs. 6a, 6c and 6e, the

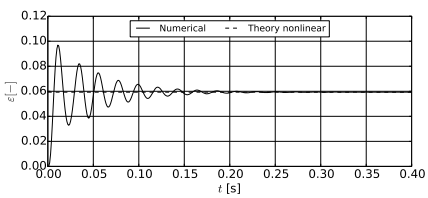

(a) Example for the convergence of the elongation ε over time t.

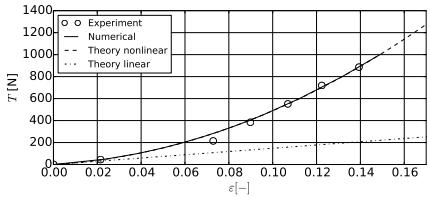

(b) Comparison of experimental, theoretical and numerical steady state elongations over applied forces T.

Figure 5: Verification test of the non-linear material properties using the elongation of a sheet for different weights.

numerical results converge fast after reaching cell sizes smaller than 0.05 m. The convergence of the structural solver is then shown using $\Delta x = 0.02$ m in the Figs. 6b, 6d and 6f. Both, forces and velocities are changing insignificantly for the different element sizes.

The deformed centre line reaches a steady state if at least 9×9 elements are used. The reason for the observed fast convergence is the coupling algorithm's mechanism to distribute the screen forces to the fluid domain by splitting the structural elements according to the cell size of the fluid grid. Hence, the chosen number of elements is mostly related to the accuracy of the structural deformation but less influential for load and momentum loss calculations.

Similar studies were conducted to find appropriate grid and structural element sizes for the following validation, showing only the converged results.

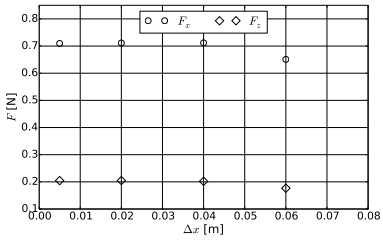

(a) Convergence of global forces over Δx.

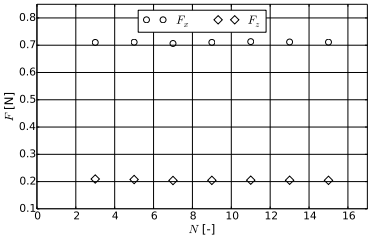

(b) Convergence of global forces over N.

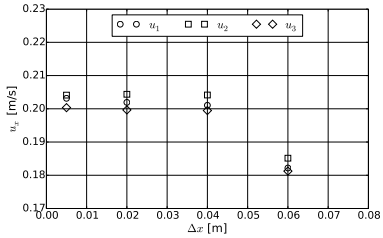

(c) Convergence of velocities at three different locations behind the porous sheet over Δx.

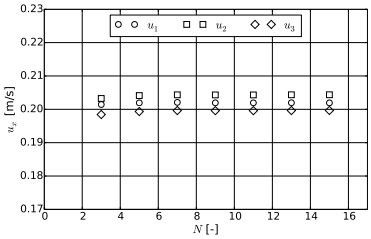

(d) Convergence of velocities at three different locations behind the porous sheet over N.

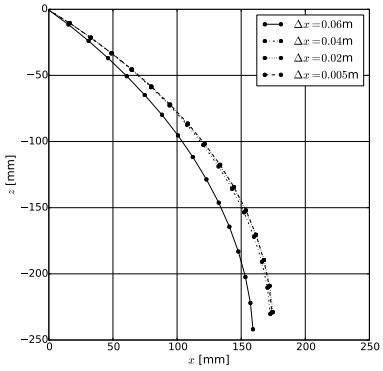

(e) Convergence of deformation over Δx.

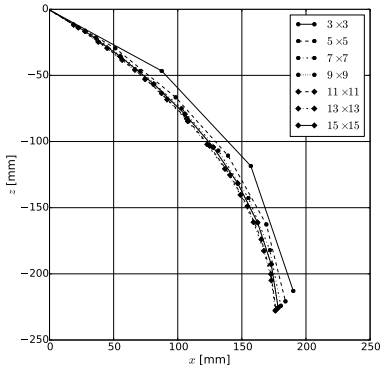

(f) Convergence of deformation over N.

Figure 6: Convergence test for a porous sheet in steady current. The left column shows the convergence for changing grid sizes using $N = 15 \times 15$ elements. The right column shows the convergence for changing number of structural elements $N \times N$ using $\Delta x = 0.02$ m.

5 Validation of the fluid-structure coupling algorithm

As the first step of the validation process, the coupling algorithm of section 3.2 is validated against measurements of rigid porous sheets in steady current and waves. Hence, the structural solver is not used. The deviation ε between the numerical result Φ_{num} and the experimental result Φ_{exp} is calculated using

$$\varepsilon = \frac{\Phi_{\text{exp}} - \Phi_{\text{num}}}{\Phi_{\text{exp}}} \cdot 100. \tag{38}$$

5.1 Rigid porous sheet in steady current flow

Following the experiments of Patursson et al. [28], a rigid sheet of 1.0 m × 1.0 m with $d_t = 0.0028$ m and $l_t = 0.029$ m is placed in a domain of 8.0 m × 3.66 m × 2.44 m. The domain is discretised using a uniform grid with $\Delta x = 0.06$ m. As shown in Fig. 7, the top bar of the sheet is kept at $(x, z) = (3, 0.81)$ m and different angles of attack α are investigated by rotating the structure counter-clockwise. Four different angles of attack, i.e. $\alpha = 0°, 30°, 45°, 60°$, and four different inflow velocities of 0.125 m/s, 0.25 m/s, 0.5 m/s and 0.75 m/s are taken into account. For each configuration, the global drag and lift forces are calculated using (19), and the velocity in the wake of the sheet is measured to validate the velocity reduction.

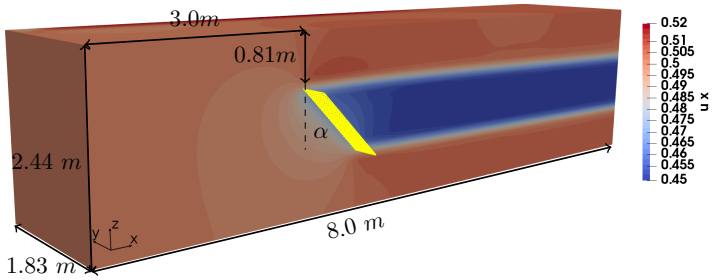

Figure 7: Half of the computational domain for the simulation of a rigid sheet in steady current. The complete domain is twice as wide. The flow direction is in positive x-direction. The colours show the velocity in x-direction for the case with $u_\infty = 0.5$ m/s and $\alpha = 45°$.

The results are shown in Fig. 8. The drag forces increase with increasing inflow velocity and decreasing angle of attack, whereas the lift forces increase with increasing inflow velocity and show a peak for $\alpha = 45°$. The velocity behind the sheet decreases due to the presence of the structure. This effect increases with higher inflow velocity but is not influenced by the angle of attack. The distributions of wake velocities in Fig. 8c show the correct behaviour for the numerical model. The deviations between the simulation and the measurements are presented in Tab. 1. Most errors are well below 10%, and the largest deviations are given for the predicted drag and lift forces at large inflow velocities and angles of attack.

Table 1: Deviations [%] between the numerical results and experimental data of Patursson et al. [28].

α [°]	u_∞ [m/s]											
	0.125			0.25			0.5			0.75		
	F_D	F_L	u_w	F_D	F_L	u_w	F_D	F_L	u_w	F_D	F_L	u_w
0	-6.83	-	4.59	8.91	-	-1.31	8.89	-	-1.82	7.52	-	-0.24
30	1.32	9.61	1.94	-0.98	-19.2	-1.75	8.29	-1.49	-2.18	1.92	-13.9	-0.41
45	-4.49	-7.04	-0.01	1.07	8.06	-3.39	2.61	5.25	-2.94	-1.61	-17.3	-0.49
60	14.6	-14.81	-2.07	3.44	9.54	-4.18	0.49	9.92	-4.71	-7.35	8.30	-3.21

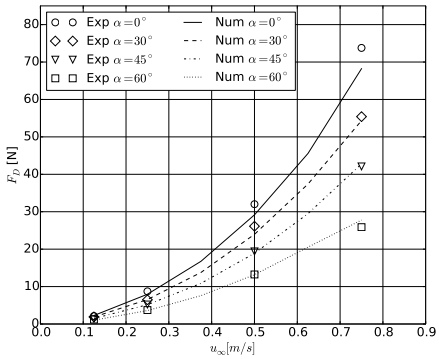

(a) Drag forces over inflow velocity.

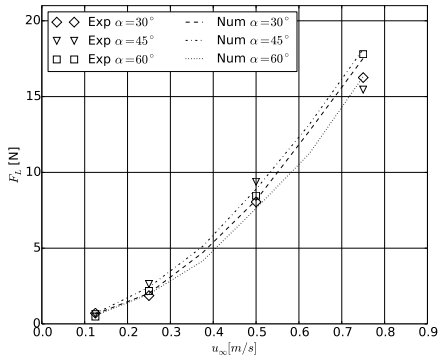

(b) Lift forces over inflow velocity.

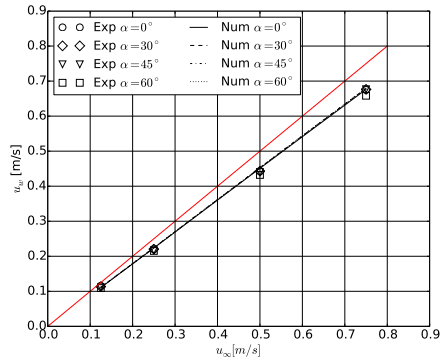

(c) Wake velocities 2.5 m behind the sheet over inflow velocity. The red line indicates the wake velocity without structure.

Figure 8: Comparison of the numerical and experimental results for a rigid porous sheet in steady current flow.

5.2 Rigid porous sheet in regular waves

A similar experiment was conducted in [37] to investigate the drag forces on a rigid sheet in regular waves. Here, two rigid sheets of 1.0 m × 0.5 m with $d_t = 0.002$ m and $l_t = 0.03$ m and $l_t = 0.06$ m are placed in a wave tank of 30.0 m × 2.0 m × 2.0 m with a water depth of 1 m. The centre of the sheet is at $(x, y, z) = (10, 1.0, 0.6)$ m. Five different waves with wave heights between $H = 0.1$ m and $H = 0.2$ m and a wave period of $T = 1.4$ s are investigated. They are modelled using Stokes' second-order theory. The computational domain is discretised using a uniform grid with $\Delta x = 0.05$ m.

The time series of the numerically calculated global drag forces on the two sheets are presented in Fig. 9. For comparison, the measured forces are indicated in red. Spectral analysis is conducted to quantify the period and amplitude of the forces, and the results are shown in Tab. 2 in comparison to the experimental data. Here, the positive and negative force amplitudes are considered separately due to the asymmetry of Stokes waves. In general, the forces increase with increasing wave height due to larger particle velocities below the wave and increasing solidity due to a larger surface passed by the fluid. A good agreement between simulation and experiment can be stated as the deviations are mostly well below 10%. As the measured forces are just provided over two wave periods, increased uncertainties for the experimental data have to be kept in mind.

Table 2: Numerical and experimental results and deviations ε [%] for the rigid porous sheet in waves [37].

H [m]	l_t [m]	T [s]	F^+ [N]	F^- [N]	T_{exp} [s]	F^+_{exp} [N]	F^-_{exp} [N]	ε_T	ε_{F^+}	ε_{F^-}
0.10	0.03	1.420	1.157	1.240	1.4	1.247	1.241	-1.43	0.18	0.16
0.12	0.03	1.420	1.590	1.750	1.4	1.522	1.786	-1.43	4.43	2.01
0.15	0.03	1.420	2.260	2.480	1.4	2.460	2.679	-1.43	0.15	7.44
0.18	0.03	1.419	3.450	3.780	1.4	3.382	3.814	-1.42	1.98	0.89
0.20	0.03	1.414	4.200	4.960	1.4	3.893	5.214	-1.00	7.88	4.87
0.10	0.06	1.421	0.330	0.390	1.4	0.477	0.398	-1.50	0.81	2.17
0.12	0.06	1.421	0.501	0.588	1.4	0.467	0.695	-1.51	7.07	15.42
0.15	0.06	1.428	0.698	0.860	1.4	0.791	1.044	-2.00	1.78	17.67
0.18	0.06	1.419	1.068	1.364	1.4	1.180	1.497	-1.41	0.52	8.90
0.20	0.06	1.419	1.36	1.780	1.4	1.417	1.878	-1.41	0.04	5.26

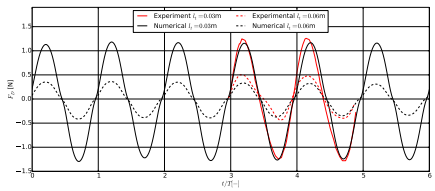

(a) $H = 0.1$ m, $T = 1.4$.

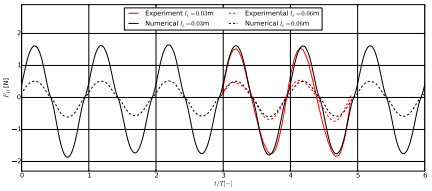

(b) $H = 0.12$ m, $T = 1.4$.

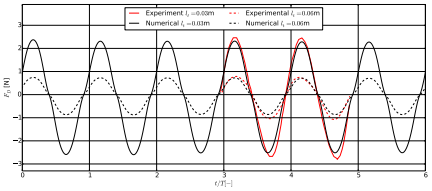

(c) $H = 0.15$ m, $T = 1.4$.

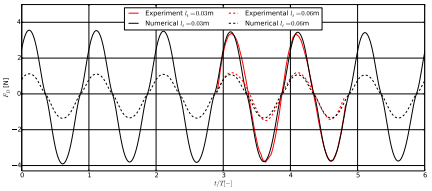

(d) $H = 0.18$ m, $T = 1.4$.

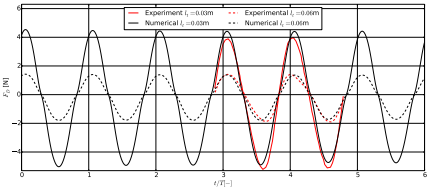

(e) $H = 0.2$ m, $T = 1.4$.

Figure 9: Comparison of the numerical and experimental time series of the drag forces on a rigid porous sheet in different regular waves with wave height H and wave period T.

6 Validation of the complete FSI model

The previous section indicates the proper working of the fluid solver and the coupling algorithm for both, constant inflow conditions and waves. In this section, the complexity of the fluid-structure problem is increased by adding the structural solver and hence, the deformation of the structure. First, a single sheet and a cylindrical structure are investigated in steady inflow conditions. Afterwards, the deformation of a porous sheet in waves is presented.

6.1 Deformation of a porous sheet in steady current flow

The deformation of a porous sheet in steady current flow is presented following the experimental setup by Bi et al. [3]. The sheet has a size of 0.3 m $\times$ 0.3 m with solidity $S = 0.243$. It is numerically represented by 9×9 elements. The top is fixed during the experiments and a steel bar with a mass of 73 g in air is attached to the bottom of the structure. In the numerical model, the mass and inertia effects of the bar is added to the lowest row of structural elements. The inertia effects are approximates as drag and added mass forces for a cylinder

using Morison's formula [26]. This procedure also holds for the validation cases below. A slice of the computational domain is shown in Fig. 10. Following the experiments, the domain is 3.8 m long, 0.4 m wide and 0.4 m high. It is numerically resolved using $\Delta x = 0.02$ m. The centre of the sheet is initially placed at $(x, y, z) = (1.0, 0.2, 0.25)$ m. The inflow velocities u_∞ are 0.056 m/s, 0.113 m/s, 0.17 m/s and 0.226 m/s. As the result, Fig. 11 shows the distribution of the centre line of the sheet, the global drag forces and velocity distribution through the structure for different inflow velocities.

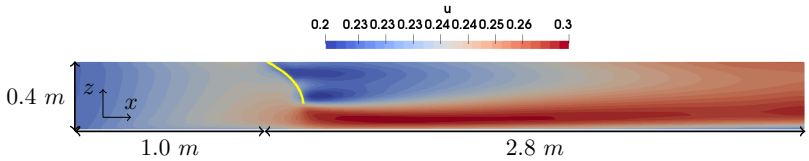

Figure 10: Slice through the centre of the computational domain for the simulation of a porous sheet in steady current incident from the left. The deformed sheet is shown in yellow. The contours show the velocity in x-direction for the case with $u_\infty = 0.226$ m/s.

The experimental results for the deformation are extracted from pictures of the whole structure presented in their paper and therefore, prone to larger uncertainties. Based on that, the qualitative comparison in Fig. 11c shows a satisfying performance of the numerical model. For larger velocities, the model tends to predict a larger curvature in the middle part of the sheet. This also affects the calculated global drag forces shown in Fig. 11a. Here, deviations below 10% are shown for the lower range of investigated inflow velocities, but a 20% under-prediction is given for largest velocity. This is probably linked to the slightly different deformation causing larger lift forces but smaller drag forces. Additionally, Fig. 11b shows the distribution of the velocity through and behind the sheet for two inflow velocities. As the flow passes the structure, a velocity drop is visible due to a loss of fluid momentum. The magnitude and position of the velocity reduction are well presented by the proposed model irrespective of the inflow velocity.

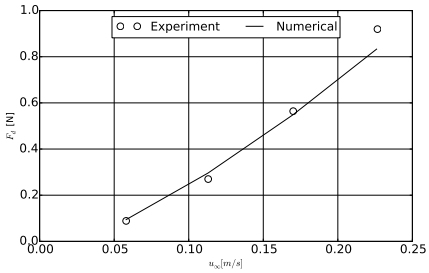

(a) Drag forces for different inflow velocities.

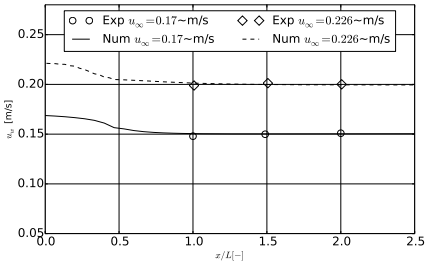

(b) Velocity profile along the x-axis through the centre of the sheet. $x/L = 0$ corresponds to the x-position of the fixed top of the sheet.

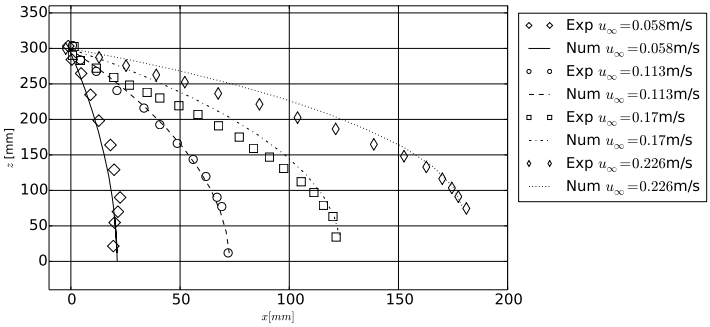

(c) Distribution of the deformed centre line for different inflow velocities.

Figure 11: Comparison of the numerical and experimental results for a porous sheet in steady current flow.

6.2 Deformation of a porous sheet in regular waves

In the previously considered experiment of Zhao et al. [37], additional measurements of the deformation of a porous sheet in regular waves were presented. The sheet is 0.78 m wide, 0.6 m high and consists of squared meshes with $d_t = 0.0018$ m and $l_t = 0.06$ m. The solidity ratio is approximated as 0.06. The numerical equivalent is modelled using 8×8 elements. The top is fixed during the experiments and an iron bar with a mass of 82 g in air is attached to the bottom of the structure. The same wave tank of 30.0 m $\times$ 2.0 m $\times$ 2.0 m with a water depth of 1 m is used (see Fig. 12). The centre of the sheet is at $(x, y, z) = (10, 1.0, 0.6)$ m. The same waves as given above are investigated. Additionally, results for waves with wave height $H = 0.15$ m and wave periods between 1.1 s and 1.5 s are reported. All waves are numerically modelled using second-order Stokes theory. The computational domain is discretised using a uniform grid with $\Delta x = 0.04$ m.

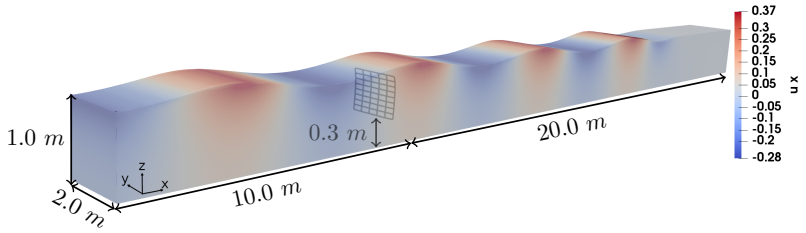

Figure 12: Computational domain of the water phase for the simulation of a porous sheet in regular waves. The waves propagate from the left to the right. The colours show the velocity in x-direction.

Fig. 13 presents three time instances showing typical flow situations encountered by the sheet. If the structure is under a wave crest, as shown in Fig. 13a, the flow pushes the structure in the positive x-direction. Here, the centre of the sheet deforms first because of the increased inertia of the lower part of the sheet due to the additional weight and higher velocities near the free surface. After the wave crest passes the structure, reduced velocities lead to a flattened profile rotated counter-clockwise. When the wave trough approaches as shown in Fig. 13c, the structure is pulled back and starts to rotate clockwise.

The amplitude and speed of this cycling motion depend on both, wave height and period, as it can also be seen in Fig. 14. It shows the maximum deformation of two probe points $P_1 = (10, 1, 0.3)$ m (bottom position) and $P_2 = (10, 1, 0.6)$ m (centre position) following the structural deformation. The deformation increases with the wave height. For both locations, doubling of the amplitudes is given for almost doubling the wave height. Similarly, the increase of the wave period increases the amplitude of the motion due to longer periods of almost unidirectional incident flow velocities. The centre point generally moves less than the bottom point in the numerical model, whereas the measurements indicate larger motion of the centre point for higher and longer waves. Tab. 3 provides the deviations between numerics and experiments for all considered cases. The motion of the lower part of the sheet is represented well as the error is below 10%. In contrast, the centre part deforms insufficient in the simulations for large waves showing under-predictions of up to 18%. These deviations can be linked to the wave representation or the calculated forces on the structure. Unfortunately, both are not reported in [37] so that further analysis of the errors cannot be given.

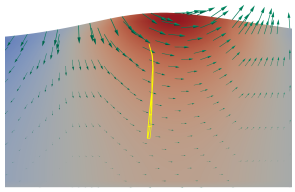

(a) Wave crest situation.

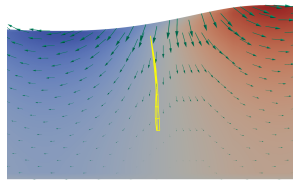

(b) Situation between crest and trough.

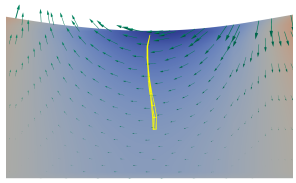

(c) Wave trough situation.

Figure 13: Deformation of the porous sheet (yellow) in different wave situations. The waves reach the sheet from the left. The green arrows indicate the directions of the streamlines.

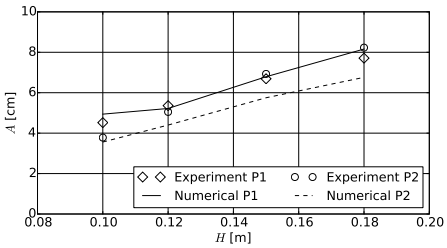

(a) Maximum deformation of the sheet for different wave heights and $T = 1.4$ s.

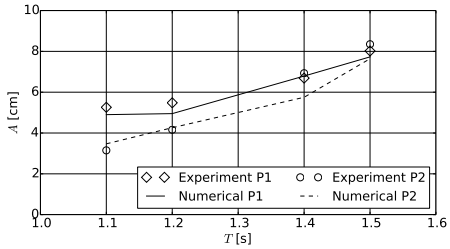

(b) Maximum deformation of the sheet for different wave periods and $H = 0.15$ m.

Figure 14: Comparison of the numerical and experimental results for a porous sheet in regular waves.

Table 3: Numerical and experimental results and deviations ε [%] for the maximum deformation of a porous sheet in regular waves [37].

H [m]	T [s]	$A_{1,exp}$ [cm]	$A_{2,exp}$ [cm]	A_1 [cm]	A_2 [cm]	ε_1	ε_2
0.10	1.4	4.52	3.78	4.94	3.56	9.25	-5.85
0.12	1.4	5.36	5.05	5.22	4.40	-2.61	-12.81
0.15	1.4	6.69	6.93	6.79	5.75	1.48	-16.98
0.18	1.4	7.71	8.23	8.16	6.76	5.81	-17.92
0.15	1.1	5.26	3.15	4.90	3.47	-6.79	10.16
0.15	1.2	5.48	4.16	4.95	4.26	-9.62	2.45
0.15	1.4	6.69	6.93	6.79	5.75	1.48	-16.98
0.15	1.5	8.02	8.35	7.73	7.64	-3.58	-8.50

6.3 Deformation of a porous cylindrical structure in steady current flow

As a final validation case, the deformation of a porous cylinder in steady current flow is considered. The setup and measurements are taken from [18]. The cylinder has a diameter of 1.435 m, a height of 1.44 m and consists of meshes with $d_t = 0.0018$ m and $l_t = 0.018$ m, which corresponds to a solidity of $S = 0.19$. It is numerically represented by 17×10 structural elements. The top is fixed during the experiments and 16 cylindrical weights of $0.4, 0.6$ and 0.8 kg each are attached to the bottom row of the cylinder. The computational domain together with the placement of the centre top position of the cylinder is shown in Fig. 15. The domain is discretised using $\Delta x = 0.08$ m. The inflow velocity u_∞ varies between 0.13 m/s and 0.56 m/s. As the results, Fig. 16 shows the global drag and lift forces and volume and area reduction coefficients for the different inflow velocities and attached weights. The reduction coefficients represent the ratio of the volume and area of the deformed structure to the initial structure and are calculated as proposed in [18] to be consistent with the experiments. Their accurate prediction demands a correct force calculation and proper velocity reduction through the front part of the cylinder since both influence the deformed shape.

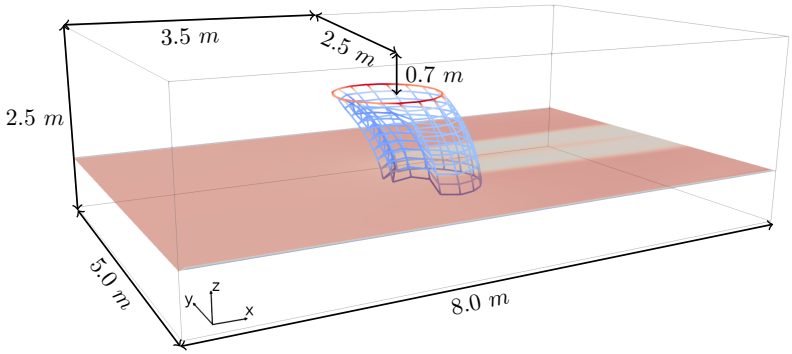

Figure 15: Computational domain for the simulation of a porous cylinder in steady current flow. The current propagates in positive x-direction.

The global forces on the structure, shown in Fig. 16a and Fig. 16b, increase with increasing inflow velocity, and the influence of the changing weights is only of importance for velocities larger than 0.33 m/s. For smaller velocities, the numerical model agrees well with the experiments due to consistent deviations below 10%. For the largest inflow velocity, the lift force is under-predicted. Here, the simulations show consistent results as the lift forces with the largest additional weight is generally the lowest due to the smallest deformation. In contrast, the experimental data shows the largest lift force for this configuration without providing a physical explanation for this phenomenon. The volume and area reduction (Figs. 16c and 16d) is negligible for inflow velocities smaller than 0.2 m/s. For larger velocities, the numerical model accords well with the experiments by predicting increasing volume and area reduction with increasing velocity. The largest deviation is observed for the predicted area reduction coefficient for velocities between 0.23 m/s and 0.27 m/s. A possible explanation is a slightly different deformation process of the numerical cage in comparison to the physical one. In the experiment, the deformation at this velocity seems to be related to a bend of the cylinder, whereas the cage also deforms through a reduced diameter numerically. However, a large uncertainty associated with accessing the area reduction by tracking only three points has to be considered. As expected, the largest deformation of the cylinder is predicted for the lowest additional weight.

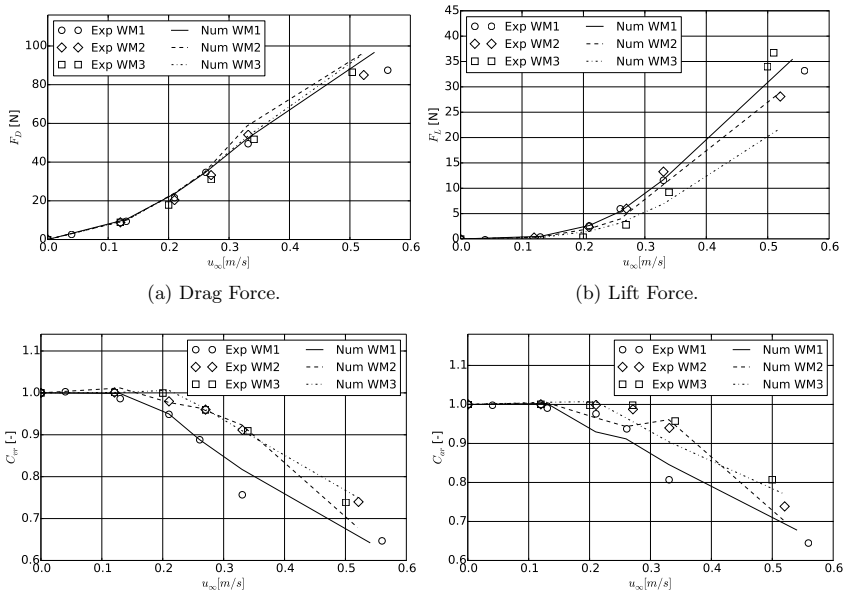

(a) Drag Force.

(b) Lift Force.

(c) Volume reduction coefficient.

(d) Area reduction coefficient.

Figure 16: Numerical and experimental results for the simulation of a porous cylinder in steady current flow. WM1 corresponds to 16×0.4 kg additional weight, WM2 corresponds to 16×0.6 kg additional weight and WM3 corresponds to 16×0.8 kg additional weight.

7 Application to the simulation of fish cage arrays in current flow

A possible application of the proposed model is the investigation of complex fish cage arrays consisting of multiple cylindrical nets defined as elastic porous sheets. In the following, the capabilities of the developed model are demonstrated by taking the previous case as the basis. As shown in Fig. 17, six cylinders of the same dimensions and material as above are placed in a 3×2 array. The distance between the top centre points is 2 m in longitudinal direction and d in lateral direction. The distance d is chosen as 3 m and 1.5 m to study the influence of the cages on each other. Each cage has an additional weight of 16×0.6 kg attached, and the considered inflow velocity is 0.33 m/s.

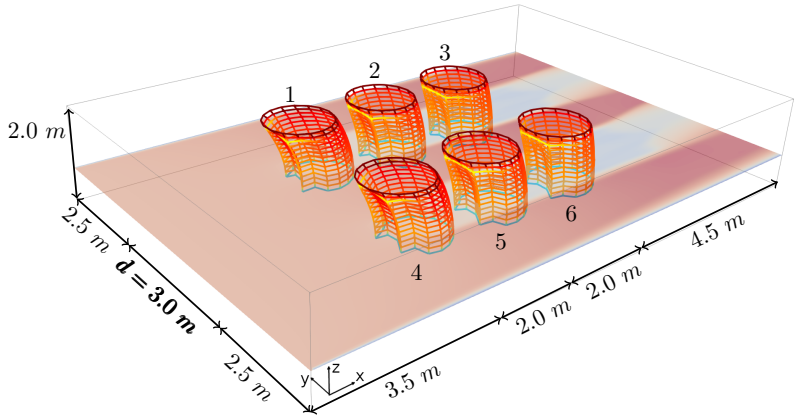

Figure 17: Computational domain for the simulation of fish cage arrays in current flow. The current propagates in positive x-direction.

The time series of the forces on the left array of nets are shown in Fig. 18. The global forces in x- and z-direction decrease for nets in the wake of another structure due to the momentum loss through the porous sheets in front. The simulations indicate a slight increase of these forces of the nets in the back if d is reduced. However, they are less influenced by d than the forces in the y-direction. For the bigger distance, no influence between the two arrays can be stated as the forces in the y-direction are close to zero. The decrease of the distance results in an increase of lateral forces due to the direct influence of the accelerated flow around the neighbouring structure.

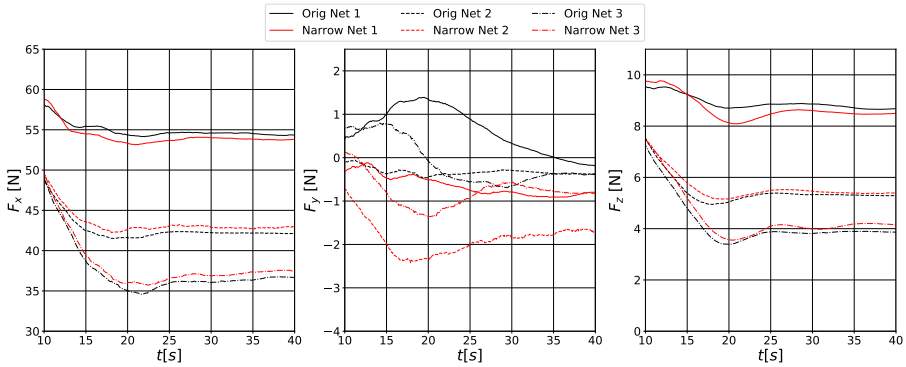

Figure 18: Time series of the numerically predicted forces in x-, y- and z-direction for the simulation of fish cage arrays in current flow. The numbering of the nets is indicated in Fig. 17. The results for $d = 3$ m (Orig) are shown in black, the results for $d = 1.5$ m (Narrow) in red.

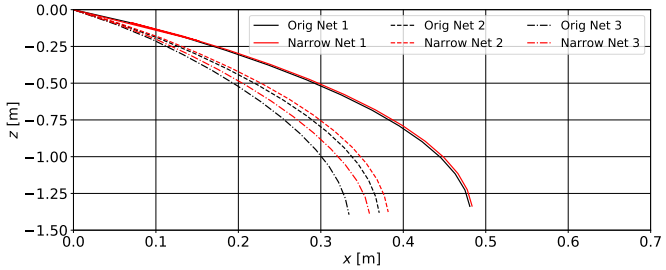

Figure 19: Deformation of the backside centre lines of the nets. The numbering of the nets is indicated in Fig. 17. The results for $d = 3$ m (Orig) are shown in black, the results for $d = 1.5$ m (Narrow) in red.

The changing loading conditions also influence the deformation of the structures as can be seen from Fig. 19. As expected, the reduction of velocity in the wake of the first structure results in less rotation of the nets behind. Further, the deformation increases with decreasing distance between the rows due to the increase of forces. In accordance with these observations, the distribution of the tension forces (Fig. 20) can be explained. The largest tension forces are to expected near the clamping on the top, and the strain reduces for the structures in the back of the array. Generally, the strain is larger on the frontside than on the backside due to the momentum loss of the fluid while passing the net.

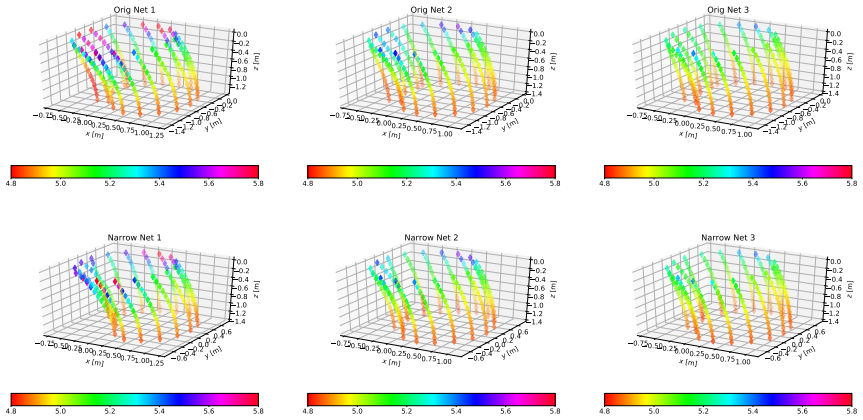

Figure 20: Tension force distribution [N] in the vertical twines of the different nets. The numbering of the nets is indicated in Fig. 17.

8 Conclusions

In this paper, a new methodology for modelling the non-linear dynamics of porous tensile structures and their interaction with the surrounding fluid was proposed.

An efficient structural model was derived for arbitrary deformations and non-linear material. It bases on solving Newton's second law for the unknown tension forces. A new approach for calculating the fluid loading on the structure was proposed as the structure is not directly resolved in the fluid. Here, fluid properties were interpolated on the structural domain using a Kernel function, and the hydrodynamic forces were approximated using a Morison-type approach. High-order backward finite differences were included to approximate the structural motion. Finally, a single matrix-vector problem arose which was solved using an accelerated Newton's method. In contrast to existing explicit algorithms, the implicit time and deformation handling increase stability and effectively remove strong time step restrictions from the fluid solver.

Two-way coupling was provided by including the loss of fluid momentum, due to passing a porous sheet, in the Navier-Stokes equations as a source term. It was determined from a Kernel integration of the hydrodynamic and body forces over multiple Lagrangian points which follow the structural deformation. This represents an innovative extension of the classical forcing approach for porous and hydrodynamic transparent structures. Hence, its application to couple the fluid with slender elastic structures, such as mooring lines and floating beams, and deforming porous media like vegetation is straightforward.

An extended verification and validation study was presented. The proposed model was validated against existing experiments for rigid and elastic porous sheets and cylinders with varying geometries and solidities in current and regular waves. Deviation bands of less than 10% were regularly achieved which indicate a proper calculation of the loads, the wake velocity field and the structural response. Hence, the chosen kernel for the distribution of the

momentum loss vector on the fluid domain is a valid alternative to the previous choice and removes effectively additional parameters from the model. The application to the simulation of the flow around multiple elastic net cages delivers insight into possible applications. Here, the proposed numerical model provides the possibility to study fluid dynamics around and inside the cages as well as the effects of waves and currents on the cage array deformations. The resulting fluid disturbances have not been numerically resolved yet but can now be modelled using the proposed approach. Within future work, the framework will also be extended to floating cage systems with mooring systems attached.

Acknowledgements

The authors are grateful for the grants provided by the Research Council of Norway under the HAVBRUK2 project (no. 267981). This research was supported in part with computational resources at NTNU provided by NOTUR (Norwegian Metacenter for Computational Sciences, http://www.notur.no) under project no. NN2620K.

A Analytical expressions for the derivatives of F_{ij}

The derivatives of (16) have to be calculated separately for the bar b_{ij} between knot $\mathbf{x}_i$ and $\mathbf{x}_j$ and the adjoint bars b_{ip} and b_{jp}:

- Derivative for the joint bar b_{ij}:

$$\begin{aligned}\frac{\partial\, F_{ij}\left(\mathcal{T}\right)}{\partial\, \mathcal{T}_{ij}} =& 2\left(\sum_{k=1}^{N_j}\frac{\mathbf{T}_{jk}}{m_j}-\sum_{k=1}^{N_i}\frac{\mathbf{T}_{ik}}{m_i}+\mathbf{A}_{ij}+\mathbf{V}_{ij}+\mathbf{X}_{ij}\right)\left(\frac{\mathbf{b}_{ji}}{m_j}-\frac{\mathbf{b}_{ij}}{m_i}\right)\\ &-c_1^4\,\frac{l_0^2}{C_2}\cdot\left(\frac{-C_1+2C_2+\sqrt{C_1^2+4C_2T_{ij}}}{\sqrt{C_1^2+4C_2T_{ij}}}\right)\end{aligned} \tag{39}$$

- Derivative for the bars b_{ip} with $i \neq j$:

$$\frac{\partial\, F_{ij}\left(\mathcal{T}\right)}{\partial\, \mathcal{T}_{ip}} = -\frac{2\,\mathbf{b}_{ip}}{m_i}\left(\sum_{k=1}^{N_j}\frac{\mathbf{T}_{jk}}{m_j}-\sum_{k=1}^{N_i}\frac{\mathbf{T}_{ik}}{m_i}+\mathbf{A}_{ij}+\mathbf{V}_{ij}+\mathbf{X}_{ij}\right) \tag{40}$$

- Derivative for the bars b_{jp} with $j \neq i$:

$$\frac{\partial\, F_{ij}\left(\mathcal{T}\right)}{\partial\, \mathcal{T}_{jp}} = \frac{2\,\mathbf{b}_{jp}}{m_j}\left(\sum_{k=1}^{N_j}\frac{\mathbf{T}_{jk}}{m_j}-\sum_{k=1}^{N_i}\frac{\mathbf{T}_{ik}}{m_i}+\mathbf{A}_{ij}+\mathbf{V}_{ij}+\mathbf{X}_{ij}\right) \tag{41}$$

The resulting Jacobian is inverted using the partially pivoted LU decomposition of the C++ library Eigen [13].

B Derivation of a linear system for solving the structural problem

The derivation of a linearised version of the proposed model is based on the kinematic relation

$$\left(\mathbf{x_j}^{(n+1)} - \mathbf{x_i}^{(n+1)}\right)^2 = \left(l_{ij}^{(n+1)}\right)^2. \tag{42}$$

Under the assumption of linear elastic material, the length of the bar between knot $\mathbf{x}_i$ and $\mathbf{x}_j$ is written as

$$l_{ij}^2 = l_{0,ij}^2 \cdot (1 + \kappa\ T_{ij})^2, \tag{43}$$

with $l_{0,ij}$ the original length and κ the elasticity constant. In each time step, the tension force is subject to an incremental increase so that $T^{(n+1)} = T^{(n)} + \Delta T$. Thus, the right-hand side of (42) can be linearised with the argument of small elasticity ($\kappa \ll 1$) and small tension fluctuations ($\Delta T \ll 1$):

$$\left(l_{ij}^{(n+1)}\right)^2 = l_{0,ij}^2 \cdot \left(1 + 2\kappa\ T_{ij}^{(n)}\right). \tag{44}$$

The location and velocity of each knot is approximated using first-order backward finite differences in time. Inserting them into (42) and linearising the left-hand side by neglecting terms of higher-order, yields under consideration of (44)

$$\begin{aligned}&\frac{l_{0,ij}^2}{2\Delta t} \cdot \left(1 + 2\kappa\ T_{ij}^{(n+1)}\right) - \frac{\left(\mathbf{x}_j^{(n)} - \mathbf{x}_i^{(n)}\right)^2}{2\Delta t} = \\ &\left(\mathbf{v_j}^{(n)} - \mathbf{v_i}^{(n)} + \Delta t\ \left(\mathbf{a}_j^{(n)} - \mathbf{a}_i^{(n)}\right)\right)\left(\mathbf{x}_j^{(n)} - \mathbf{x}_i^{(n)}\right).\end{aligned} \tag{45}$$

Thus, a linear system of equations arises for the tension forces at the new time step using (5) and proper rearrangement:

$$\begin{aligned}&\left(\sum_{k=1}^{N_j} \frac{\mathbf{b}_{jk}^{(n)} T_{jk}^{(n+1)}}{m_j} - \sum_{k=1}^{N_i} \frac{\mathbf{b}_{ik}^{(n)} T_{ik}^{(n+1)}}{m_i}\right)\left(\mathbf{x}_j^{(n)} - \mathbf{x}_i^{(n)}\right) - \frac{l_{0,ij}^2}{\Delta t^2}\kappa\ T_{ij}^{(n+1)} \\ =&\frac{l_{0,ij}^2}{2\Delta t^2} - \frac{\left(\mathbf{x}_j^{(n)} - \mathbf{x}_i^{(n)}\right)^2}{2\Delta t^2} - \frac{\left(\mathbf{v_j}^{(n)} - \mathbf{v_i}^{(n)}\right)\left(\mathbf{x}_j^{(n)} - \mathbf{x}_i^{(n)}\right)}{\Delta t} \\ &- \frac{\left(\mathbf{x}_j^{(n)} - \mathbf{x}_i^{(n)}\right)\mathbf{F}_j^{(n)}}{m_j} + \frac{\left(\mathbf{x}_j^{(n)} - \mathbf{x}_i^{(n)}\right)\mathbf{F}_i^{(n)}}{m_i}.\end{aligned} \tag{46}$$

The resulting system matrix is inverted using the partially pivoted LU decomposition of the C++ library Eigen [13].

References

[1] N. Aquelet and J. Wang. "Porous parachute modelling with an Euler-Lagrange coupling". In: *European Journal of Computational Mechanics* 16.3-4 (2007), pp. 385–399.

[2] C.-W. Bi et al. “A numerical analysis on the hydrodynamic characteristics of net cages using coupled fluid–structure interaction model”. In: *Aquaculture Engineering* 59 (2014), 1–12.

[3] C.-W. Bi et al. “Numerical simulation of the interaction between flow and flexible nets”. In: *J. Fluids Struct.* 45 (2014), 180–201.

[4] H. Bihs and A. Kamath. “A combined level set/ghost cell immersed boundary representation for floating body simulations”. In: *Int. J. Numer. Meth. Fluids* Volume 83 (2017), 905–916.

[5] H. Bihs et al. “A new level set numerical wave tank with improved density interpolation for complex wave hydrodynamics”. In: *Computers & Fluids* Volume 140 (2016), 191–208.

[6] D.L. Brown, R. Cortez, and M.L. Minion. “Accurate Projection Methods for the Incompressible Navier-Stokes Equations”. In: *Journal of Computational Physics* 168 (2001), 464–499.

[7] J.S. Carlton. *Marine Propellers and Propulsion*. Fourth. Butterworth-Heinemann, Oxford, UK, 2019.

[8] H. Chen and E.D. Christensen. “Development of a numerical model for fluid-structure interaction analysis of flow through and around an aquaculture net cage”. In: *Ocean Engineering* 142 (2017), 597–615.

[9] H. Chen and E.D. Christensen. “Investigations on the porous resistance coefficients for fishing net structures”. In: *J. Fluids Struct.* 65 (2016), 76–107.

[10] C. Chun. “Iterative Methods Improving Newton’s Method by the Decomposition Method”. In: *Computers and Mathematics with Applications* 50 (2005), pp. 1559–1568.

[11] B. Fornberg. “Calculation of Weights in Finite Difference Formulas”. In: *SIAM Rev.* 40 (3) (1998), pp. 685–691.

[12] A. Fredheim. *Current Forces on Net Structures*. Ph.D. thesis, NTNU Trondheim, Norway. 2005.

[13] G. Guennebaud, B. Jacob, et al. *Eigen v3*. http://eigen.tuxfamily.org. 2010.

[14] G.S. Jiang and D. Peng. “Weighted ENO schemes for Hamilton Jacobi equations”. In: *SIAM Journal of Scientific Computing* Volume 21 (2000), 2126–2143.

[15] G.S. Jiang and C.W. Shu. “Efficient implementation of weighted ENO schemes”. In: *Journal of Computational Physics* Volume 126(1) (1996), 202–228.

[16] T. Kristiansen and O. M. Faltinsen. “Experimental and numerical study of an aquaculture net cage with floater in waves and current”. In: *Journal of Fluids and Structures* 54 (2015), pp. 1–26.

[17] T. Kristiansen and O. M. Faltinsen. “Modelling of current loads on aquaculture net cages”. In: *Journal of Fluids and Structures* 34 (2012), pp. 218–235.

[18] P. F. Lader and B. Enerhaug. “Experimental Investigation of Forces and Geometry of a Net Cage in Uniform Flow”. In: *IEEE Journal of Oceanic Engineering* 30.1 (2005), pp. 79–84.

[19] P. F. Lader and A. Fredheim. "Dynamic properties of a flexible net sheet in waves and current—A numerical approach". In: *Aquacultural Engineering* 35 (3) (2006), pp. 228–238.

[20] F. LeBris and D. Marichal. "Numerical and experimental study of submerged supple nets applications to fish farms". In: *Journal of Marine Science Technology* 3 (1998), 161–170.

[21] R. Lewandowski and G. Pichot. "Numerical simulation of water flow around a rigid fishing net". In: *Comput. Methods Appl. Mech. Engrg.* 196 (2007), pp. 4737–4754.

[22] G. Løland. *Current forces on and flow through fish farms.* Ph.D. thesis, NTH Trondheim, Norway. 1991.

[23] D. Marichal. *Cod-end numerical study.* In: Proceedings of the 3rd International Conference on Hydroelasticity in Marine Technology, Oxford, UK., 2003.

[24] T. Martin, A. Kamath, and H. Bihs. "A Lagrangian approach for the coupled simulation of fixed net structures in a Eulerian fluid model". In: *Journal of Fluids and Structures* 94 (2020). DOI: https://doi.org/10.1016/j.jfluidstructs.2020.102962.

[25] T. Martin et al. "Efficient implementation of a numerical model for flexible net structures". In: *Ocean Engineering* Volume 150 (2018), 272–279.

[26] J. Morison et al. "The force exerted by surface waves on piles". In: *Pet. Trans. Amer. Inst. Min. Eng.* Volume 186 (1950), 149–154.

[27] S. Osher and J.A. Sethian. "Fronts propagating with curvature-dependent speed: Algorithms based on Hamilton-Jacobi formulations". In: *Journal of Computational Physics* Volume 79 (1988), 12–49.

[28] Ø. Patursson et al. "Development of a porous media model with application to flow through and around a net panel". In: *Ocean Engineering* 37 (2010), 314–324.

[29] C. S. Peskin. "Numerical analysis of blood flow in the heart". In: *Journal of Computational Physics* 25 (3) (1977), pp. 220–252.

[30] P.B. Ryzhakov and E. Oñat. "A finite element model for fluid–structure interaction problems involving closed membranes, internal and external fluids". In: *Comput. Methods Appl. Mech. Engrg.* 326 (2017), pp. 422–445.

[31] C.W. Shu and S. Osher. "Efficient implementation of essentially non-oscillatory shock-capturing schemes". In: *Journal of Computational Physics* Volume 77(2) (1988), 439–471.

[32] M. Sussman, P. Smereka, and S. Osher. "A level set approach for computing solutions to incompressible two-phase flow". In: *Journal of Computational Physics* Volume 114 (1994), 146–159.

[33] L.J.P. Timmermans, P.D.. Minev, and F.N. Van De Vosse. "An approximate projection scheme for incompressible flow using spectral elements". In: *International Journal for Numerical Methods in Fluid* 22 (1996), 673–688.

[34] I. Tsukrov et al. "Finite element modeling of net panels using a consistent net element". In: *Ocean Engineering* 30 (2003), pp. 251–270.

[35] B. Vincent. *A new generation of tools for trawls dynamic numerical simulation.* In: Proceedings of the 4th International Workshop on Methods for Development and Evaluation of Maritime Technologies, Rostock, Germany., 1999.

[36] H. van der Vorst. "BiCGStab: A fast and smoothly converging variant of Bi-CG for the solution of nonsymmetric linear systems". In: *SIAM Journal of Scientific Computing* Volume 13 (1992), 631–644.

[37] Y.-P. Zhao et al. "An experimental and numerical study of hydrodynamic characteristics of submerged flexible plane nets in waves". In: *Aquacultural Engineering* Volume 38 (2008), 16–25.

[38] Yun-Peng Zhao et al. "Numerical Simulation of Interaction Between Waves and Net Panel Using Porous Media Model". In: *Engineering Applications of Computational Fluid Mechanics* 8.1 (2014), pp. 116–126.

Paper 4

A numerical framework for modelling the dynamics of open ocean aquaculture structures in viscous fluids.

Martin, T., Tsarau, A. and Bihs, H. (2021).
Applied Ocean Research, Vol. 106, doi: 10.1016/j.apor.2020.102410.

A numerical framework for modelling the dynamics of open ocean aquaculture structures in viscous fluids

Tobias Martin*[a] Andrei Tsarau[b] Hans Bihs[a]

[a]Department of Civil and Environmental Engineering, Norwegian University of Science and Technology (NTNU), 7491 Trondheim, Norway
[b]SINTEF Ocean AS, Department for Seafood Technology, 7052 Trondheim, Norway

Postprint
published in *Applied Ocean Research*, 2021, Vol. **106**,
DOI: 10.1016/j.apor.2020.102410.

Abstract

This paper presents a complete numerical framework for modelling open ocean aquaculture structures in waves and current using Computational Fluid Dynamics (CFD). A structural dynamics model is incorporated to account for the motions and deformations of the net. It is based on the lumped mass method, a non-linear material law and implicit time step advancing. The presence of the porous net is considered in the momentum equations of the fluid using a forcing term based on Lagrangian-Eulerian coupling and the acting forces on the net. The proposed framework is suitable for simulating the interaction of nets of arbitrary geometry and under large motion with fluids including complex free surfaces. This is in contrast to existing models which either neglect important non-linearities, the physical interaction with the fluid or are limited to certain net geometries. In addition, the fluid-structure interaction of floating objects with mooring lines, nets and fluid is accounted for in the model. A new floating algorithm is presented for the interaction of the fluid and the rigid structure. It is based on a continuous direct forcing immersed boundary method and a level set representation of the object in the Eulerian fluid domain. This effectively avoids computationally expensive reconstruction processes of existing approaches and enables the application to large three-dimensional structures. The complete numerical framework is first validated against existing measurements for forces on rigid and flexible nets, net deformations and moored-floating structures with and without a net in waves. Then, a semi-submersible and a mobile floating open ocean aquaculture structure are investigated, and the possibilities of the numerical approach are highlighted.

Keywords: Hydroelasticity, Fluid-structure interaction, CFD, Open ocean aquaculture, Irregular waves

*Corresponding author, tobias.martin@ntnu.no

1 Introduction

The demand for aquatic food products is expected to increase by thirty million tonnes until 2050 [15], and aquaculture production has to play a significant role in satisfying the demand to avoid overfishing. In recent years, the traditional aquaculture industry has faced increasing criticism for the environmental impacts of their near-coast structures on the surrounding marine habitat [22]. This raises the need for alternative concepts in the aquaculture industry. One of the most promising and economically valuable ideas involves the increase of the dimensions of the structure in combination with the relocation of the structures offshore. However, this implies larger loads on the structure and higher risk of fish loss due to the influence of strong current and larger waves. Open ocean aquaculture (OOA) is concerned with the adaptation of fish cages and the risks during operations to an environment with significant exposure to wave action and severe sea conditions [15]. As a consequence, alternative design choices adapted from offshore related fields of engineering arose during recent years [12]. This includes semi-submerged and submerged fish cages [49] to reduce the loads as well as floating rigid structures with one or multiple nets attached. These new types of structures require more advanced tools in the design process to better understand the dominating factors for eventual structural failure and fish loss. Numerical modelling is a relatively inexpensive and flexible way of assessing these factors and reduce the risks if appropriate approaches are chosen during establishing the frameworks for OOA structures.

Historically, computational methods developed for investigating aquaculture systems relied on linear potential theory for load calculation and empirical formulae for estimating the velocity reduction through the net. The most comprehensive study applying these methods was performed by Kristiansen and Faltinsen [26]. They validated a lumped mass net model coupled to a dynamic beam equation for the floater, linear wave theory to approximate the excitation forces and the formula of Løland [31] to account for the shading effect of the net against experiments of a traditional aquaculture structure. A reasonable agreement could be achieved for small wave steepness and low current which is in accordance with linear theory. For the same type of structure, Shen et al. [42] validated their numerical model, which is based on the same assumptions, against measurements in both regular and irregular waves. They concluded that in severe sea states, the deformation of the net is of a more limiting factor in the design choices than the stresses in the floater. First numerical investigations of OOA structures were presented in [19, 20] using a finite element method for the net and linear potential theory for the excitation forces due to current and waves. The considered structure was a spar buoy with an octagonal rim held together by tensioned stays woven into the net. No shading effect was taken into account. The authors stressed the importance of non-linear effects of extreme waves and fluid-structure interaction for the correct prediction of the structural dynamics. Xu et al. [49] compared a numerical model based on potential theory and a rigid floater for submersible and moored floating net cages with physical model tests. The authors highlighted that the lowering of the structure resulted in smaller deformations of the net and reduced mooring line tension forces compared with the floating configuration. Also, varying wave steepness have minor effects on the structural loads in this condition. More recently, Li et al. [30] presented a numerical analysis of the concept of a vessel-shaped cage system using a panel method and linear wave theory as the basis. No validation against measurements was provided. However, it was concluded that a deformable net model is necessary and non-linear effects have to be taken into account if offshore environmental conditions are to

be investigated. These conditions are characterised by large loads on the structure and hence, strong non-linear fluid-structure interaction. Thus, the existing numerical tools cannot be regarded as appropriate for investigating OOA structures. In contrast, computational fluid dynamics (CFD) offers a two-way coupled numerical approach that can be applied to understand the environmental loading and structural response by modelling the hydrodynamic forces affecting the dynamics of the floating structure, the flexible net and mooring system, and their effect on the surrounding fluid. To the best of the authors' knowledge, the only numerical approach so far was the two-dimensional model presented by Chen and Christensen [10]. They solved the incompressible Navier-Stokes equations in a two-dimensional numerical wave tank and coupled it to a lumped mass net model using a porous medium approach. They validated their model against experiments for a net attached to a moored-floating cylinder in waves and current and showed promising results. However, the approach was not tested for three-dimensional structures such as OOA structures.

The complex problem of modelling the whole system can be split into the sub-problems of solving the interaction between the fluid and a rigid moored-floating structure and the flexible porous net, respectively. Several approaches exist to solve the fluid-structure interaction (FSI) involving rigid bodies only. Moving mesh methods fit a Eulerian grid to the body which is distorted by the changing position of the rigid body. Accurate results in the vicinity of the body can be achieved, but the method faces problems for large body motion and complicated structures. The grid distortion can be avoided effectively by applying the concept of dynamic overset grids. Here, the grid around the body moves with the structure, and the fluid information is transferred to a fixed background grid at a certain distance from the body. Amongst others, Carrica et al. [7] and Chen et al. [11] successfully developed numerical towing and wave tanks using dynamic overset grids. The drawback of this method is the increase of computational costs due to the interpolations necessary in the overlapping region of the grid, the parallelisation of the complete solver, and eventual instabilities due to incomplete interpolation stencils. Alternative methods based on an implicit representation of the structure in the Eulerian fluid grid have been developed to provide the computational efficiency necessary for simulating large three-dimensional structures. The most important implicit methods are based on the immersed boundary method by Peskin [41] for simulating elastic membranes in fluid. Later, Fadlun et al. [14] introduced this idea to rigid bodies as the direct forcing method. Here, the boundary conditions between fluid and solid are respected by incorporating an additional source term in the momentum equations. The term is calculated on fluid grid points near the surface using a reconstructed solution from the fluid domain and the known velocity at the nearby solid surface. It was pointed out by Uhlmann [47] that this reconstruction procedure can lead to spikes in the time series of the forces because the reconstruction stencil changes as the body moves. Yang and Stern [50] presented a solution to this problem by including an overset grid so that the reconstruction stencils remain constant in time. This, however, brings along the aforementioned challenges of these type of grids. Therefore, Uhlmann [47] proposed a continuous version of the direct forcing method by calculating the forcing term on Lagrangian markers which discretise the surface of the structure. The terms are then distributed on the Eulerian domain using the interpolation procedure of the original immersed boundary method [41]. The introduced smearing effectively removes force spikes but still keeps the nominal order of accuracy for the FSI problem. Additional computational costs arise from the back- and forth-transformations between the Eulerian grid and the Lagrangian markers. These costs can be avoided by using

a completely Eulerian calculation as developed by e.g. Yang [51]. Here, the Eulerian grid is split into a fluid and solid domain. The momentum equation is solved in the whole domain including a forcing term. This additional term is calculated from the rigid body velocities at each grid point and smeared over the fluid-solid interface using a smoothed Heaviside step function. The author validated the solver against two-dimensional benchmark cases and showed high stability and accuracy. Here, the author used markers moving with the body for reconstructing the Heaviside step function in each time step. In the present paper, the efficiency of this approach is further enhanced by utilising a ray-casting method and a level-set function to distinguish between fluid and solid.

The second FSI problem is concerned with the interaction of the fluid and the net. The net is an elastic structure with non-linear material properties [28] undergoing potentially large motions and deformations. The lumped mass method was established as the most common solution for solving net dynamics. Originally presented by Lader and Fredheim [28], the lumped mass method discretises the net into massless bars with mass knots in between. The dynamics of the knots are found by solving Newton's second law and a Runge-Kutta time integration. In [3, 4], the method was validated for flexible net sheets and cylinders in steady current flow. However, the explicit time integration and missing fulfilment of the constitutive equations within each time step lead to severe time step restrictions. Implicit methods are therefore more suitable for FSI problems involving a coupled fluid solution. In [36], an implicit quasi-static net model was proposed where the force equilibrium is solved for each knot with additional constraints on the connectivity of the bars. The missing time-stepping reduces the cost and simplifies the coupling to the fluid solver. However, the lack of dynamic effects prevents the application to large deformation problems including snap loads. A dynamic implicit net model based on the satisfaction of the kinematic relation between knot position and bar length was introduced in [29]. The original approach assumed inelastic material which can lead to ill-posed problems due to high condition numbers. Marichal [32] successfully overcame this drawback by including elastic material into the model. However, their derivation relied on a linear material assumption and linearised equations. This is a severe drawback considering the non-linearity of net material [28]. Therefore, the authors of this paper included non-linear material properties which led a non-linear system of equations for the unknown tension forces [33]. The method was successfully validated against model tests for top-fixed deforming net sheets and cages in waves and current. In the present paper, this model is extended to dynamic problems involving moving mounting points.

In contrast to conventional membranes, nets have high porosity and consist of multiple individual twines which are passed by the fluid. The length scale of the flow around each twine is significantly smaller than the length scale of the flow around the whole floating structure. This prevents the resolution of the net on the same numerical grid as the fluid domain, and an alternative representation of the FSI between net and fluid has to be introduced. One possible representation is the definition of a porous medium around the net. The fluid momentum equation is solved in the whole domain including an additional resistance coefficient in the porous zone (see [4, 8, 9, 40, 52] for various definitions of the coefficient). As shown in [34], this approach is not appropriate for complex shapes and deformations and lacks a physical basis. The authors of this paper proposed an alternative method based on the same principles as the immersed boundary methods by Peskin [41] and Uhlmann [47]. Here, a forcing term is calculated from the hydrodynamic loads on the net and distributed on the fluid domain using an interpolation kernel. This method was successfully validated for rigid [34] and deforming nets [33] and will be utilised in the present paper.

Based on the review of existing approaches, this paper presents itself as the first attempt to establish a numerical framework using CFD for OOA structures. All parts of the framework are chosen or newly developed aiming to simulate large, three-dimensional structures including fluid-structure, fluid-net and net-structure interaction in an efficient manner. The paper is structured as follows: section 2 presents the different modules of the complete numerical framework. Several validation cases are presented in section 3. The validated numerical model is then applied to two typical OOA structures in section 4. The paper concludes with final remarks in section 5.

2 Numerical framework

The different parts of the proposed numerical model are introduced in the following. The framework includes a two-phase numerical wave tank, a floating algorithm for modelling the interaction of rigid structures and fluid and an implicit solver for the net dynamics. Details regarding the coupling of the net solver to the fluid solver and the rigid body solver are also given. A flowchart at the end of the section (Fig. 4) provides an overview of the complete framework.

2.1 Fluid dynamics solver

The dynamics of any incompressible fluid obeys the conservation of mass and momentum. These conservation laws are described by the three-dimensional Navier-Stokes equations and continuity equation which are written in the convective form as

$$\nabla \cdot \mathbf{u} = 0, \tag{1}$$

$$\frac{\partial \mathbf{u}}{\partial t} + \mathbf{u} \cdot \nabla \mathbf{u} = -\frac{1}{\rho}\nabla p + \nabla \cdot \left(\nu \left[\nabla \mathbf{u} + \nabla \mathbf{u}^T\right]\right) + \mathbf{g}. \tag{2}$$

Here, $\mathbf{u}$ is the velocity vector, ρ is the density, p is the pressure, ν represents the kinematic and turbulent viscosity and $\mathbf{g}$ is the gravitational acceleration vector. The effect of turbulence is incorporated by adding turbulent viscosity to the diffusion term using the Boussinesq approximation and a modified k-ω turbulence model [5]. Following a one-fluid approach, the two phases, air and water, are covered by a single set of equations but space and time dependent material distributions. The transition between the phases is implicitly represented by the zero level set of the smooth signed distance function Φ [39]. The linear advection equation

$$\frac{\partial \Phi}{\partial t} + \mathbf{u} \cdot \nabla \Phi = 0, \tag{3}$$

is solved for propagating Φ in space and time. After each propagation, the reinitialisation equation of Sussman et al. [45] is solved to keep the signed distance properties of Φ. The density and viscosity is then calculated using

$$\rho = \rho_w H(\Phi) + \rho_a (1 - H(\Phi)), \tag{4}$$

$$\nu = \nu_w H(\Phi) + \nu_a (1 - H(\Phi)), \tag{5}$$

with w indicating water and a air properties. Further, the smoothed Heaviside step function H is given by

$$H(\Phi) = \begin{cases} 0 & \text{if } \Phi < -\epsilon \\ \frac{1}{2}\left(1 + \frac{\Phi}{\epsilon} + \frac{1}{\pi} sin(\frac{\pi\Phi}{\epsilon})\right) & \text{if } |\Phi| \leq \epsilon \\ 1 & \text{if } \Phi > \epsilon, \end{cases} \tag{6}$$

with $\epsilon = 2.1\Delta x$ and Δx the characteristic length of the discrete domain in the vicinity of each evaluation point.

The set of equations (1) - (3) is solved on a staggered rectilinear grid using finite differences. Fifth-order accurate weighted essentially non-oscillatory (WENO) schemes [23, 24] adapted to non-uniform point distances are applied for convection terms, and diffusion terms are discretised with second-order accurate central differences. Convection and source terms are treated explicitly with the third-order accurate TVD Runge-Kutta scheme of Shu and Osher [44], and an implicit Euler method is applied for the temporal discretisation of the viscous term. This effectively removes a quadratic reciprocal dependency on the cell size from the CFL condition [5]. An incremental pressure-correction algorithm [46] is used for solving system (1)-(2). In each k-th Runge-Kutta sub-step, a velocity field is predicted using the pressure gradients of the previous step:

$$\begin{aligned} \frac{\mathbf{u}^{(*)} - \alpha_k \mathbf{u}^{(n)}}{\alpha_k \Delta t} = \frac{\beta_k}{\alpha_k}\mathbf{u}^{(k-1)} - \mathbf{u}^{(k-1)} \cdot \nabla \mathbf{u}^{(k-1)} - \frac{\nabla p^{(k-1)}}{\rho} \\ + \nabla \cdot \left(\nu \left[\nabla \mathbf{u} + \nabla \mathbf{u}^T\right]\right)^{(*)} + \mathbf{g}, \end{aligned} \tag{7}$$

with $\alpha_k = 1.0, 1/4, 2/3$, $\beta_k = 0.0, 3/4, 1/3$ and $k = 1, 2, 3$. Afterwards, the Poisson equation

$$\nabla \cdot \left(\frac{1}{\rho} \nabla p_{\text{corr}}\right) = \frac{1}{\alpha_k \Delta t} \nabla \cdot \mathbf{u}^{(*)}, \tag{8}$$

is solved for the pressure correction term p_{corr} utilising a fully parallelized BiCGStab algorithm with geometric multigrid preconditioning from the HYPRE library [48]. An n-halo decomposition strategy and the message passing interface (MPI) handles inter-processor communication. The pressure and divergence free velocity fields are finally calculated from

$$p^{(k)} = p^{(k-1)} + p_{\text{corr}} - \rho\nu \ \nabla \cdot u^{(*)}, \tag{9}$$

$$\mathbf{u}^{(k)} = \mathbf{u}^{(*)} - \frac{\alpha_k \Delta t}{\rho} \nabla p^{(k)}. \tag{10}$$

2.2 Including rigid body motion in the fluid solver

A new continuous direct forcing approach is implemented to account for the presence of rigid floating objects in the fluid solver. The same level-set routines as for the free surface are utilised. Hence, high efficiency through parallelised routines is ensured and simulations of large three-dimensional structures are possible. This is in contrast to previous research on continuous methods which mostly concentrated on two-dimensional benchmark cases.

The floating object is transferred to the solver as an STL geometry consisting of multiple non-connected triangles. This information is sufficient to create a signed distance field Φ_s representing the geometry in the Eulerian fluid domain by applying a ray casting algorithm

[6] to receive inside-outside information near the body and the reinitialisation algorithm of Sussman et al. [45]. An example of a complex STL geometry and its level set representation is shown in Fig. 1. The generated level set function Φ_s is used for distinguishing between fluid and solid domain by extending (4) and (5):

$$\rho = \rho_s H(\Phi_s) + (1 - H(\Phi_s)) \cdot (\rho_w H(\Phi) + \rho_a (1 - H(\Phi))), \tag{11}$$

$$\nu = (1 - H(\Phi_s)) \cdot (\nu_w H(\Phi) + \nu_a (1 - H(\Phi))), \tag{12}$$

with s indicating solid.

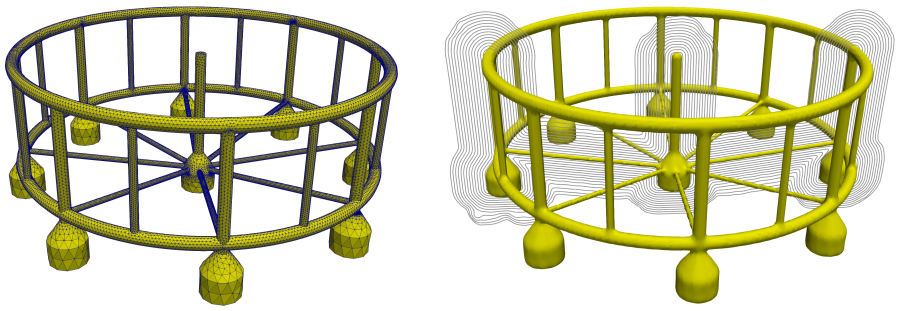

(a) Original STL representation.

(b) Level set representation indicated by grey contour lines in x-z plane. Yellow surface shows $\Phi_s = 0$.

Figure 1: Illustration of the representation of a complex object as a reconstructed signed distance function.

Following the derivation of Yang [51], the conservation laws

$$\begin{aligned} \nabla \cdot \mathbf{u} &= 0, \\ \frac{\partial \mathbf{u}}{\partial t} + \mathbf{u} \cdot \nabla \mathbf{u} &= -\frac{1}{\rho} \nabla p + \mathbf{g} + \mathbf{f}, \end{aligned} \tag{13}$$

with the forcing term

$$\mathbf{f} = \frac{\partial \mathbf{P}(\mathbf{u})}{\partial t} + \mathbf{P}(\mathbf{u}) \cdot \nabla \mathbf{P}(\mathbf{u}) + \frac{1}{\rho} \nabla p - \mathbf{g}, \tag{14}$$

hold in the solid domain. Here, $\mathbf{P}(\mathbf{u})$ represents the operator for projecting the velocity field into a divergence free rigid body velocity field. Comparing (13) with (1) and (2) reveals that the only difference between these two sets of equations is the term $\mathbf{f}$ and the diffusion term, respectively. Therefore, a single set of equations can be solved in the whole domain using $H(\Phi_s)$ for representing the transition of fluid to solid and the additional term $\mathbf{f}$ for incorporating the correct boundary conditions at the interface. At a discrete level, $\mathbf{f}$ reads at the new time step $n + 1$

$$\mathbf{f}^{(n+1)} = H(\Phi_s^{(n+1)}) \cdot \left(\frac{\mathbf{P}(\mathbf{u}^{(\mathbf{n+1})}) - \mathbf{P}(\mathbf{u}^{(\mathbf{n})})}{\Delta t} + \mathbf{P}(\mathbf{u}^{(\mathbf{n})}) \cdot \nabla \mathbf{P}(\mathbf{u}^{(\mathbf{n})}) + \frac{1}{\rho} \nabla p^{(n+1)} - \mathbf{g} \right). \tag{15}$$

The velocity at the new time step is unknown a priori. To overcome this issue and avoid expensive implicit calculations, the valid approximation $\mathbf{P}(\mathbf{u^{(n)}}) = \mathbf{u^{(n)}}$ is made and the pressure is taken from the previous time step as a good approximation. Then,

$$\mathbf{f}^{(n+1)} = H(\Phi_s^{(n+1)}) \cdot \left(\frac{\mathbf{P}(\mathbf{u^{(n+1)}}) - \mathbf{u^{(n)}}}{\Delta t} + \mathbf{u^{(n)}} \cdot \nabla \mathbf{u^{(n)}} + \frac{1}{\rho} \nabla p^{(n)} - \mathbf{g} \right), \tag{16}$$

and by comparing with (7), it can be identified that

$$\mathbf{f}^{(n+1)} = H(\Phi_s^{(n+1)}) \cdot \left(\frac{\mathbf{P}(\mathbf{u^{(n+1)}}) - \mathbf{u}^{(*)}}{\Delta t} \right). \tag{17}$$

A good approximation of the updated velocity field is $\mathbf{u}^{(*)}$ itself. Therefore, the predictor step (7) is first executed without the forcing term. Then, $\mathbf{f}^{(*)}$ is calculated from

$$\mathbf{f}^{(*)} = H(\Phi_s^{(*)}) \cdot \left(\frac{\mathbf{P}(\mathbf{u}^{(*)}) - \mathbf{u}^{(*)}}{\alpha_k \Delta t} \right), \tag{18}$$

and added to the predicted velocity field before solving the Poisson equation (8).

For the calculation of the rigid body velocity field, the translational motion of the rigid body is described by Newton's second law, and the rotational motion is described in a body-fixed coordinate system using the Euler parameter $\mathbf{e} = (e_0, e_1, e_2, e_3)^T$ with the property $\mathbf{e}^T\mathbf{e} = 1$. Their relation to Euler angles is provided in A. Following Shivarama and Fahrenthold [43], a first-order Hamiltonian system can be derived. The translational equations are converted into a system of first-order differential equations as well. Hence, the rigid body system can be integrated with the same explicit Runge-Kutta method as the fluid solver. The body forces and momenta are calculated on the triangulated surface using a trilinear interpolation of the fluid properties and an integration over all N triangles:

$$\begin{aligned} \mathbf{F_x} &= \int_\Omega (-\mathbf{n}p + \rho\nu\mathbf{n}\tau)\, d\Omega(\mathbf{x}) = \sum_{i=1}^{N} (-\mathbf{n}p + \rho\nu\mathbf{n}\tau)_i \cdot \Delta\Omega_i, \\ \mathbf{M_x} &= \int_\Omega \mathbf{r} \times (-\mathbf{n}p + \rho\nu\mathbf{n}\tau)\, d\Omega(\mathbf{x}) = \sum_{i=1}^{N} \mathbf{r}_i \times (-\mathbf{n}p + \rho\nu\mathbf{n}\tau)_i \cdot \Delta\Omega_i. \end{aligned} \tag{19}$$

Here, $\mathbf{n}$ is the surface normal vector, τ is the viscous stress tensor and $\mathbf{r}$ represents the distance vector to the centre of gravity. The calculated moments are transferred into the body-fixed coordinate system before solving the system. Once the body velocities are calculated, the projection can be calculated as

$$\mathbf{P}(\mathbf{u}^{(*)}) = \dot{\mathbf{x}}_\mathbf{s} + \omega_\mathbf{s} \times \mathbf{r}. \tag{20}$$

with $\dot{\mathbf{x}}_\mathbf{s}$ the translational and $\omega_\mathbf{s}$ the rotational rigid body velocity vector in the inertial reference frame.

2.3 Modelling the net dynamics

The main concept of the previously proposed net model [33] is presented in the following. The net is discretised in a finite number of mass points (knots) connected by non-linear elastic bars. Due to reasons to be mentioned in the next section, a structural element is defined as the combination of four points and their four connecting bars and covers multiple physical meshes of the net (see Fig. 2).

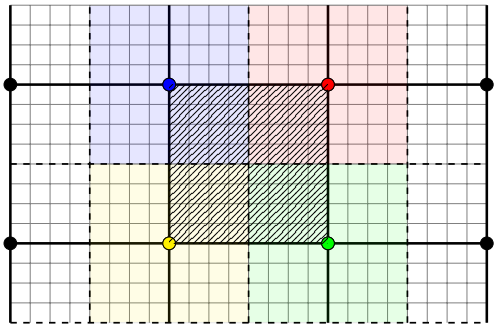

Figure 2: Illustration of the definitions for the net model: structural elements consist of four knots (thick dots) connected with bars (thick black lines). Each element (hatched area) covers multiple physical meshes (thin grey lines). The contribution of the structural elements to each knot is shown in matching colours.

A system of equations is formulated for the dynamics of the knots by distributing the external forces $\mathbf{F}_{ex}$ from each structural element to the attached knots. This leads to the dynamic equilibrium

$$\mathbf{m}_i \, \ddot{\mathbf{x}}_i = \sum_{k=1}^{N_i} \mathbf{T}_{ik} + \mathbf{F}_{ex,i}, \tag{21}$$

for each knot $\mathbf{x}_i$ and its N_i neighbouring knots. Here, dots indicate temporal derivatives and $\mathbf{T}_{ij}$ represents the tension force vector of each bar:

$$\mathbf{T}_{ij} = T_{ij} \; \mathbf{b}_{ij} = T_{ij} \cdot \left(\frac{\mathbf{x}_j - \mathbf{x}_i}{|\mathbf{x}_j - \mathbf{x}_i|} \right), \tag{22}$$

with T_{ij} the tension force magnitude and $\mathbf{b}_{ij}$ the unit vector of the bar. The mass matrix $\mathbf{m}_i$ is calculated considering the surrounding $N_{S,i}$ structural elements using

$$\mathbf{m}_i = \sum_{s=1}^{N_{S,i}} \begin{pmatrix} m_{\text{air}} + m_{\text{a}} n_x & 0 & 0 \\ 0 & m_{\text{air}} + m_{\text{a}} n_y & 0 \\ 0 & 0 & m_{\text{air}} + m_{\text{a}} n_z \end{pmatrix}_s, \tag{23}$$

with $m_{\text{air},s}$ the mass of the partial element, $\mathbf{n}_s$ the unit normal vector of the element pointing in relative velocity direction and $m_{a,s}$ the added mass contribution.

The external force vector consists of gravity and buoyancy forces as well as hydrodynamic forces. The latter consist of inertia forces $\mathbf{I}$ due to the fluid acceleration $\mathbf{a}_f$,

$$\mathbf{I}_i = \sum_{s=1}^{N_{S,i}} \begin{pmatrix} m_\mathrm{a} + m_\mathrm{a} n_x & 0 & 0 \\ 0 & m_\mathrm{a} + m_\mathrm{a} n_y & 0 \\ 0 & 0 & m_\mathrm{a} + m_\mathrm{a} n_z \end{pmatrix}_s \cdot \mathbf{a}_{f,s}, \tag{24}$$

and velocity related forces $\mathbf{D}$ which are calculated using the screen force model of Kristiansen and Faltinsen [27]. In the inertia system of the fluid, $\mathbf{D}$ can be split into drag and lift force components in normal ($\mathbf{n}_d$) and tangential ($\mathbf{n}_l$) direction of the local relative velocity vector $\mathbf{u}_\mathrm{rel,s} = \mathbf{u}_{f,s} - \dot{\mathbf{x}}_s$:

$$\mathbf{D}_i = \sum_{s=1}^{N_{S,i}} \frac{\rho}{2} A_s u_\mathrm{rel,s}^2 (c_d \mathbf{n}_d + c_l \mathbf{n}_l)_s. \tag{25}$$

The coefficients c_d and c_l are calculated from a truncated Fourier series expanded for their dependency on the angle of attack α between fluid velocity vector and structural element vector:

$$c_d(\alpha) = c_{d,0} \sum_{k=1}^{\infty} a_{2k-1} \cos\left((2k-1)\alpha\right), \tag{26}$$

$$c_l(\alpha) = c_{l,\frac{\pi}{4}} \sum_{k=1}^{\infty} b_{2k} \cos\left(2k\alpha\right). \tag{27}$$

The definition of the constants $c_{d,0}$ and $c_{l,\frac{\pi}{4}}$ can be taken from [27]. The determination of the Fourier coefficients is based on non-linear fitting to experimental data. This raises issues as most experimental data is normalised by the undisturbed inflow velocity. However, the velocity at the location where the forces are evaluated in the numerical simulation is disturbed by the presence of the structure. In [34], an equation is derived to approximate the inflow velocity without the structure. Based on momentum equilibria considerations, the undisturbed inflow velocity u_∞ is approximated by solving the intrinsic equation

$$u_\infty = \frac{c_d(u_\infty)}{-1 + \sqrt{1 + c_d(u_\infty)}} \cdot \frac{u_{rel,s}}{2}. \tag{28}$$

An implicit solution for the structural dynamics problem is found by starting from the trivial relation between the position of the knots $\mathbf{x_i}$ and $\mathbf{x_j}$ and the length of the bar l_{ij} between them:

$$\left(\mathbf{x_j}^{(n+1)} - \mathbf{x_i}^{(n+1)}\right)^2 = \left(l_{ij}^{(n+1)}\right)^2. \tag{29}$$

According to Lader and Fredheim [28], the material of nets follow the non-linear constitutive law

$$T_{ij} = C_1 \varepsilon + C_2 \varepsilon^2 = C_1 \left(\frac{l_{ij}}{l_{0,ij}} - 1\right) + C_2 \left(\frac{l_{ij}}{l_{0,ij}} - 1\right)^2, \tag{30}$$

with $l_{0,ij}$ the unstretched bar length and $(C_1, C_2) = (1160\ N, 37300\ N)$ for squared meshes. Inserting (30) in the right-hand side of (29) yields

$$\left(\mathbf{x_j}^{(n+1)} - \mathbf{x_i}^{(n+1)}\right)^2 = \frac{l_0^2}{4C_2^2} \cdot \left(-C_1 + 2C_2 + \sqrt{C_1^2 + 4C_2 T_{ij}^{(n+1)}}\right)^2. \tag{31}$$

The left-hand side of (29) is replaced by the dynamic equilibrium (21). This is done by expressing the position vectors by its accelerations using high-order backward finite differences and replacing them with forces (see B for the derivation). Thus, a non-linear expression f is found for each bar b_{ij}:

$$\begin{aligned} f_{ij}\left(\mathcal{T}^{(n+1)}\right) = &\left(\sum_{k=1}^{N_j} \mathbf{m}_j^{-1}\mathbf{T}_{jk}^{(n+1)} - \sum_{k=1}^{N_i} \mathbf{m}_i^{-1}\mathbf{T}_{ik}^{(n+1)} + \mathbf{m}_j^{-1}\mathbf{F}_{ex,j}^{(n)} - \mathbf{m}_i^{-1}\mathbf{F}_{ex,i}^{(n)} + \mathbf{V}_{ij} + \mathbf{X}_{ij}\right)^2 \\ &- \frac{c_0^4\ l_0^2}{4\ C_2^2} \cdot \left(-C_1 + 2C_2 + \sqrt{C_1^2 + 4C_2 T_{ij}^{(n+1)}}\right)^2 = 0, \end{aligned} \tag{32}$$

with $\mathcal{T}$ the unknown global vector of tension force magnitudes. A system of equations can be formulated and solved using the improved Newton's method [13]

$$\begin{aligned} \mathcal{T}^{(*)} &= \mathcal{T}^{(n)} - \left[\mathcal{J}\left(\mathcal{T}^{(n)}\right)\right]^{-1} \mathcal{F}\left(\mathcal{T}^{(n)}\right), \\ \mathcal{T}^{(n+1)} &= \mathcal{T}^{(*)} - \left[\mathcal{J}\left(\mathcal{T}^{(n)}\right)\right]^{-1} \mathcal{F}\left(\mathcal{T}^{(*)}\right), \end{aligned} \tag{33}$$

with $\mathcal{F}$ the vector of the expressions (32) and $\mathcal{J}$ its Jacobian matrix (see [33] for the expression). In practice, (33) converges well if the initial condition is chosen properly. More details can be found in [33]. The converged result of (33) can then be used for calculating the acceleration, velocity and position of the knots in a straightforward manner.

2.4 Coupling the net solver to the fluid solver

The solidity Sn of a net is defined as the ratio of solid front area to the total area and is calculated as [18]

$$Sn = \frac{2d_t}{l_t} - \left(\frac{d_t}{l_t}\right)^2, \tag{34}$$

with d_t the twine diameter and l_t the twine length. Sn typically varies between 0.1 and 0.3 for aquaculture nets. The resulting difference between the length scale of each mesh and the total structure prevents the resolution of the whole net in the discrete space. This raises the need for an alternative fulfilment of the boundary conditions at the fluid-structure interface because the physical fluid-structure interface is not present in the simulation. Following the Lagrangian approach developed in [34], these boundary conditions are replaced by a source term $\mathbf{S}$ which expresses the physical loss of fluid momentum due to the presence of the net, which leads to a pressure jump. The term is determined from the known external forces on the net and is added to the Navier-Stokes equations before the pressure correction step.
The momentum loss is assumed to be uniformly distributed over the net surface regardless of the difference between twines and voids. This implication requires uniformly distributed

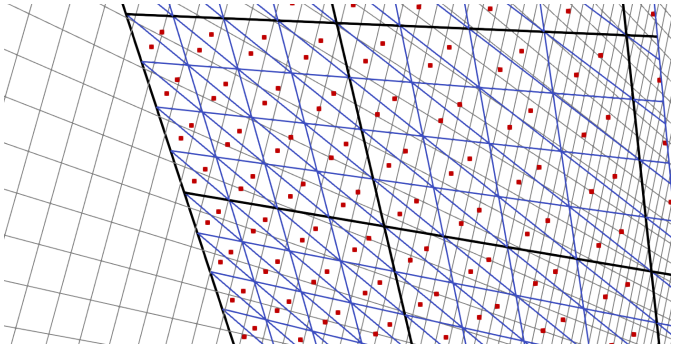

Figure 3: Illustration of the discrete net structure for the fluid-structure interaction. Black lines represent structural elements of the net, blue lines show the triangulated surface and the Lagrangian points are marked in red. the background shows the Eulerian fluid grid as thin grey lines.

markers holding $\mathbf{S}$ and that the area which is covered by each marker is nearly equal to the cell size of the encircling fluid domain. However, it is not practical to evaluate the structural dynamics on a scale where the knots fulfil these requirements. Therefore, additional Lagrangian markers are introduced to distribute $\mathbf{S}$. They are defined by splitting the structural elements in triangles according to the Eulerian grid size in their vicinity. The Lagrangian markers are then defined in the geometrical centres of each triangle. An example of the distribution of the markers on the discrete net structure is shown in Fig. 3.

The forces are distributed on the fluid grid points $\mathbf{x}_e$ using the interpolation

$$\mathbf{S}(\mathbf{x}_e) = \sum_{L=1}^{L_e} \frac{\mathbf{s}(\mathbf{x}_L)}{\Delta x \Delta y \Delta z} \, \mathrm{D}\left(\frac{x_e - x_L}{\Delta x}\right) \, \mathrm{D}\left(\frac{y_e - y_L}{\Delta y}\right) \, \mathrm{D}\left(\frac{z_e - z_L}{\Delta z}\right), \tag{35}$$

with L_e the number of markers within a defined kernel around $\mathbf{x}_e$ which is taken from [41]:

$$D(r) = \begin{cases} \frac{1}{4}\left(1 + \cos\left(\frac{\pi r}{2}\right)\right) & \text{if } |r| < 2.0 \\ 0.0 & \text{else.} \end{cases} \tag{36}$$

The forces vectors $\mathbf{s}(\mathbf{x}_L)$ at the marker with position $\mathbf{x}_L = (x_L, y_L, z_L)$ are calculated by integrating the external forces in (21) over the triangle area A_L:

$$\mathbf{s}(\mathbf{x}_L) = \left[\frac{\rho}{2} u_{\mathrm{rel}}^2 \cdot (c_d \mathbf{n}_d + c_l \mathbf{n}_l) + m_a \left(\mathbf{a_f} + \mathrm{diag}(n_x, n_y, n_z) \cdot (\mathbf{a_f} - \ddot{\mathbf{x}})\right) + \mathbf{G}\right]_L \cdot A_L. \tag{37}$$

2.5 Coupling net and rigid body dynamics

Additional remarks are given regarding the coupling of the fluid-net and fluid-rigid structure solver. At first, it is decided to explicitly couple the net dynamic solver to the remaining algorithm due to the different time advancement procedures. Therefore, the fluid velocity field of the previous time step is chosen for calculating the loading on the nets. The field

is interpolated to the points where the external forces are evaluated using the same kernel function as provided in section 2.4. After the external forces are evaluated, the new tension force distribution is calculated and used for updating the dynamic properties of the knots. Furthermore, the topmost knots are assigned to the rigid body motion to ensure a tight coupling. For this purpose, it is sufficient to replace the third or fourth term of the dynamic equilibria (32) with the known acceleration of the rigid body at these points. Two-way coupling is enabled by adding the tension forces acting on the top knots to the rigid body motion solver as external loading. It is also to be noticed that the later applied mooring system is incorporated in the same manner. It is referred to [35] for more details.

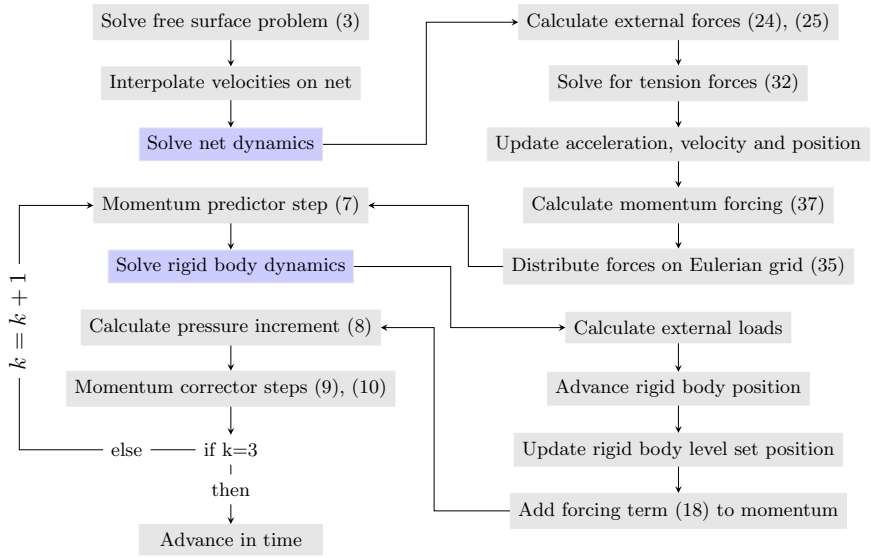

Figure 4: Flowchart of the numerical model.

3 Validation of the net model in current

The structural net model and its coupling to the fluid solver are validated for steady current flows in the following. A validation involving wave loads can be found in [33, 34]. At first, the forces on rigid net sheets, i.e. without considering net deformation, are investigated. Afterwards, the deformation of cylindrical cages and net sheets are compared to experiments in steady current flow. The main focus in these cases lies on the correct deformation and shading of and forces on nets with different geometrical properties.

3.1 Drag and lift forces on a rigid net sheet

Føre et al. [16] investigated rigid net sheets of different solidity in a steady current flow. The sheets are fixed in a frame of 1.215 × 0.985 m and towed in a tank of 175.0 × 10.5 × 5.6 m

with a distance of approximately 0.39 m between the upper part of the frame and free surface. As materials, knotless nets with the solidities $Sn = 0.15, 0.16, 0.23$ and 0.32 are considered. The twine thickness decreases from 2.5 mm for the lowest solidity to 1.3 mm for the highest. The length of the twines varies between 32.4 mm and 8.0 mm. The angle of attack between net and current α is $\alpha = 0°$ and $45°$, and additionally $22.5°$ and $67.5°$ for the second and third net. Different inflow velocities between 0.25 m/s and 2.0 m/s are considered. For most configurations, the global drag and lift forces are calculated using (25), and the velocity in the wake of the sheet is measured 0.715 m behind the sheet and 0.9 m below the free surface.

The numerical domain has the dimensions $12 \times 7 \times 5.6$ m and is shown in Fig. 5. The width and length of the tank are reduced due to efficiency reasons, but without affecting the results. The free surface is modelled as a symmetry plane. A uniform discretisation with $\Delta x = 0.07$ m is used. Convergence studies are not presented as the coupling is insignificantly dependent on the fluid grid size and the flow is mostly uniform.

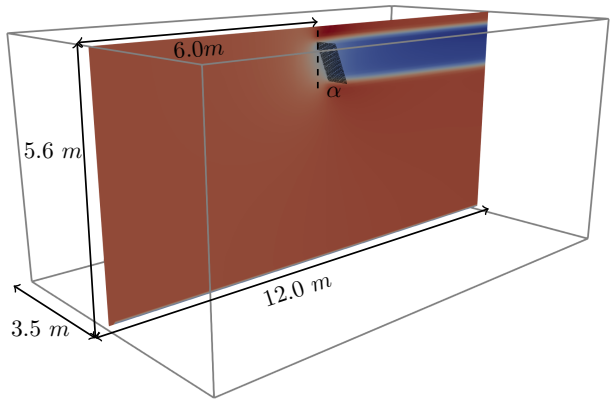

Figure 5: Computational domain for the simulation of a rigid net sheet in a steady current.

Fig. 6a presents the drag forces for perpendicular inflow, and Fig. 6b shows the drag force distribution for varying angles of attack for $u_\infty = 1.0$ m/s. The forces increase with the net solidity and decreasing α due to an increasing area of attack, and they increase quadratically with the inflow velocity as expected. The maximum deviations between numerics and experiment are 20% for the smallest velocities and solidities. A better agreement is seen for the lift forces at $\alpha = 45°$ (Fig. 6c) with deviations smaller than 10%. For $Sn = 0.16$, Føre et al. [16] report inaccurate measurements because the expected lift forces should be larger than for $Sn = 0.15$. Therefore, the numerical model seems to predict a more accurate result here. The distributions of the lift forces generally follow the drag forces due to the same reasons. However, the lift forces reach a peak value at around $45°$ and decrease again for larger angles because the net acts as a closed surface with flow detachment rather than as a porous sheet in these cases.

The flow decelerates through the net as indicated in Fig. 6d. The shading effect increases with the solidity of the net which is respected in the numerical model through the dependency on the drag forces. Further, the model predicts a lower influence of the inflow velocity on the

relative velocity reduction for all solidities. The same effect is reported in the experiments, except for in the case of the largest solidity. Additional measurements should be conducted to clarify the eventual existence of changing shading effects for high solidity nets. Generally, the numerical model over-predicts the momentum loss but the deviations stay within a 10% error bound.

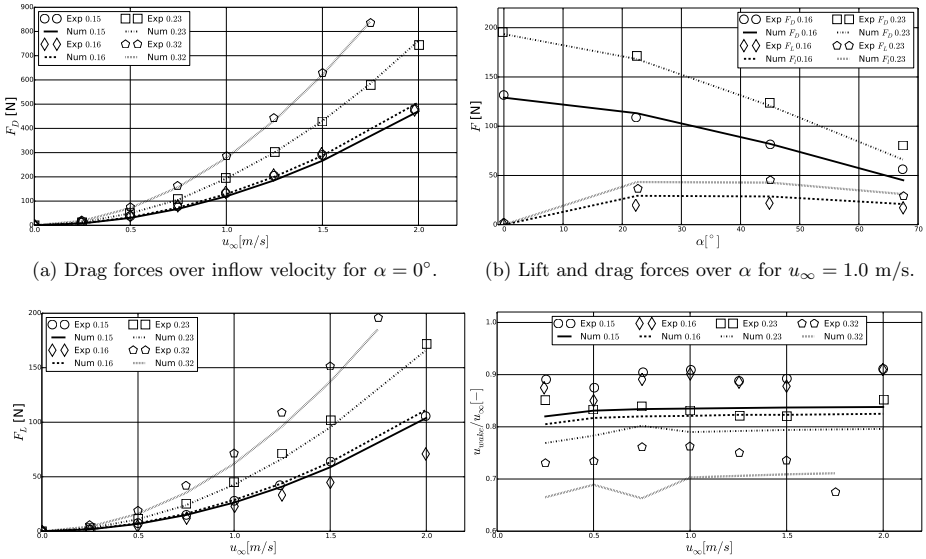

(a) Drag forces over inflow velocity for $\alpha = 0°$.

(b) Lift and drag forces over α for $u_\infty = 1.0$ m/s.

(c) Lift forces over inflow velocity for $\alpha = 45°$.

(d) Ratio of wake velocity to inflow velocity over inflow velocity for $\alpha = 0°$.

Figure 6: Comparison of the numerical and experimental results for a rigid net sheet in steady current. Numbers in legend refer to the solidity of the net.

3.2 Forces on and deformation of a cylindrical net cage

The complexity of the simulation is increased by considering the net deformation within the FSI solver. The physical model tests of Bi et al. [3] in which a top-fixed cylindrical net cage was investigated in steady current flow are considered for validation. The domain size is $5 \times 0.45 \times 0.4$ m which is adopted from the experimental setup. It is discretised using $\Delta x = 0.01$ m. The free surface is modelled as a symmetry plane for computational efficiency. Slices of the computational domain are shown in Fig. 7. The investigated cylinder has a diameter of 0.254 m, a height of 0.15 m and solidity of 0.12. The centre of the structure is placed at $(x, y, z) = (2.5, 0.225, 0.325)$ m. The large physical mesh size of the cylinder enables the usage of the original number of meshes in the simulation. As the net is knotted, additional drag and inertia forces are added to the dynamic equilibria to account for the presence of spherical knots. Similarly, the effect of a bottom sinker is added to the lowest row of structural elements using Morison's formula [37]. Four different inflow velocities, $u_\infty = 0.069$ m/s, 0.122 m/s, 0.178 m/s and 0.242 m/s are reported with a sinker weight of

8 g. Additionally, two heavier sinker weights are attached to the structure for $u_\infty = 0.242$ m/s to investigate their influence on the deformation of the net.

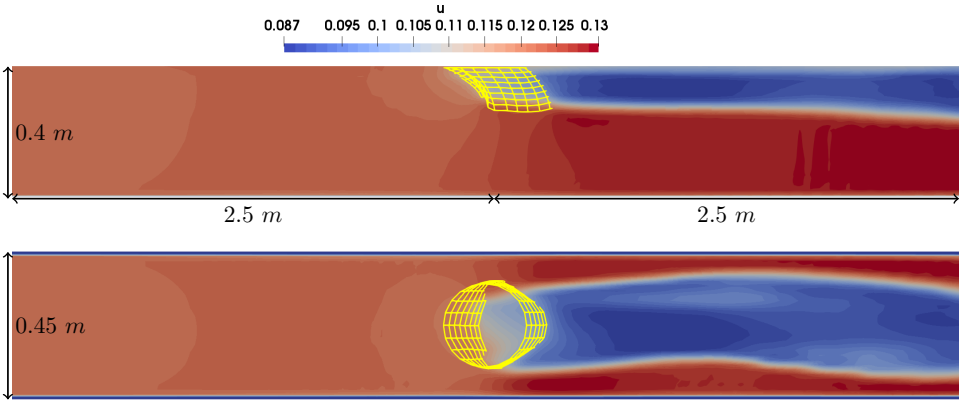

Figure 7: Slices through the computational domain for the simulation of a cylindrical net in steady current flow. Top: $x - z$ centre plane; bottom: $x - y$ plane at $z = 0.325$ m. The deformed structure is shown in yellow. The contours show the velocity in x-direction for the case with $u_\infty = 0.122$ m/s and an 8 g sinker.

The comparison of simulated and measured results for the sinker weight of 8 g is presented in Fig. 8. The drag forces qualitatively follow the theoretical distribution of forces on a cylinder for different inflow velocities. The velocity reduced by the presence of the net is well captured numerically as seen in Fig. 8b. Here, the model under-predicts the experimental data by up to 10%. Reported pictures from the experiments are used to compare the deformation of the cage though this implicates large uncertainties. The qualitative comparison of the rear vertical centreline is presented in Fig. 8c. As the velocity increases, larger hydrodynamic loads increase the deformation of the net structure. The numerical model presents a good approximation of the physical model test.

Similar effects can be observed if the sinker weight is increased (see Fig. 9a). The additional gravity forces counteract the hydrodynamic forces and, hence, decrease the deformation of the net in the flow direction. In principle, the numerical model agrees well with the experiment. It is however noticed that two different deformation pictures are shown for the same setup of $u_\infty = 0.242$ m/s and 8 g sinker weight in [3]. A possible explanation is the strong vortex shedding for this configuration, leading to oscillatory motion of the structure. The pictures might be taken from two different time instances. This explanation is confirmed numerically because it is possible to find matching distributions for both pictures within the converged solution. In addition, Fig. 9b presents the distribution of the x-velocity through the net. It clearly shows the momentum loss of the fluid through the front and back of the net. The simulation predicts similar velocity reduction for all weight configurations, whereas the experiments report an increasing reduction for more deformed nets with larger angles of attack between fluid and structure. This effect is a new observation presented by Bi et al. [3] but

stays in contrast to previous measurements of, e.g. [40] which showed a minor dependency of the angle of attack on the velocity reduction. The latter could also be confirmed numerically by the present approach [34].

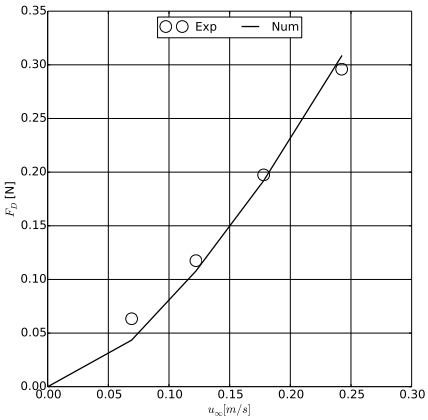

(a) Drag forces over inflow velocity.

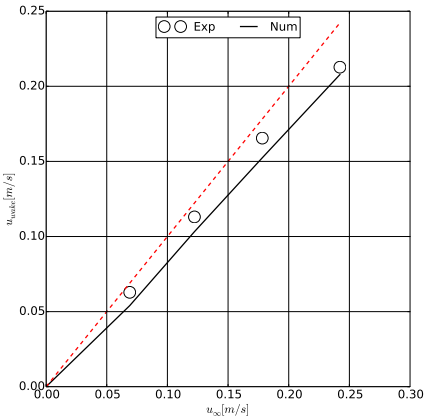

(b) Velocities inside the net cage over inflow velocity. Red line indicates velocities without considering the FSI.

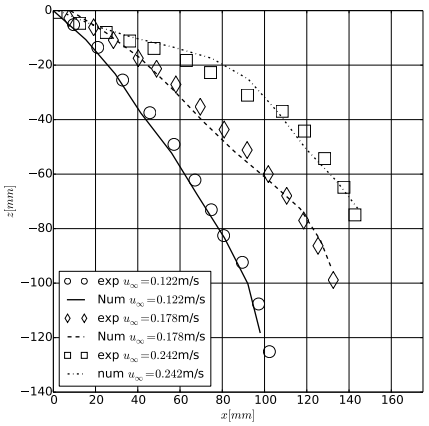

(c) Distribution of the deformed rear-centreline for different inflow velocities.

Figure 8: Comparison of the numerical and experimental results for a flexible net cylinder with a 8 g sinker weight in different steady current flow.

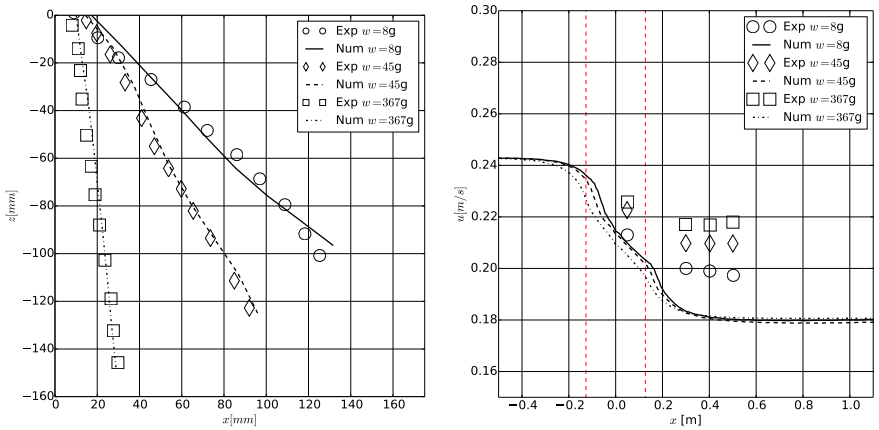

(a) Distribution of the deformed rear-centreline for different sinker weights.

(b) Distribution of the velocity along the centreline through the net.

Figure 9: Comparison of the numerical and experimental results for a flexible net cylinder with varying sinker weights in steady current flow of $u_\infty = 0.242$ m/s.

3.3 Tension forces in a deforming net sheet

Bardestani and Faltinsen [2] presented model test results for a deforming net sheet in steady current flow. In contrast to the previous case, tension forces acting at the top of the net were measured for different net geometries, sinker weights and inflow velocities. The proper determination of the structural forces is the result of accurate replication of the loads on and deformation of the structure itself. Hence, it is a reliable measure for validating numerical models for the interaction of net and floating structures. In the experiment, a wave tank at the Department of Marine Technology at the Norwegian University of Science and Technology was used. The tank has the dimensions $13.67 \times 0.6 \times 1.3$ m with 1 m water depth. The same tank size is used in the numerical simulations, and a cell size of 0.05 m is considered. All nets have the size 0.51×0.76 m and are placed in the middle of the tank with the top of the net fixed close to the free surface, which is replaced by a symmetry plane in the simulation to save computational costs. The considered nets consist of square meshes modelled by 10×10 elements and have a solidity of $0.16, 0.19$ and 0.23 with a twine diameter of $2.5, 2.5$ and 1.8 mm. The corresponding twine lengths are calculated from (34). A cylindrical sinker was attached to the bottom of the net. Its weight varies between $1.2, 1.4$ and 1.6 kg. The simulations are executed until a steady state is reached and then compared to the experimental data.

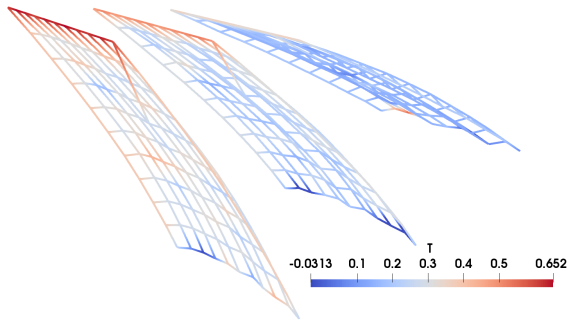

Figure 10: Deformation of the net sheet with $Sn = 0.16$ in a steady current flow of $u_\infty = 0.3$ m/s with different sinker weights attached. The weight decreases from the left to the right net in the picture. The colours indicate tension forces in the bars.

The resulting tension forces over changing inflow velocities in Fig. 11 reveal three characteristics for the investigated setup. At first, a non-linear increase of the tension force can be observed for increasing velocities irrespective of the solidity or sinker weight. This is caused by the increase of hydrodynamic forces as shown above. Further, the tension increases with increasing sinker weight even though the deformation of the net decreases as indicated in Fig. 10. This shows that the increase of gravity forces exceeds the decrease in hydrodynamic forces. Hence, the sinker weight significantly influences the behaviour of the system. This is confirmed by the last observation that the tension forces increase with the net solidity, due to the increase of net area, but the effect is negligible here. Qualitatively, the numerical framework agrees with the experiments on these phenomena, and most predicted results are within a 10% error bound. The largest deviations are seen for the highest velocity and solidity with errors of up to 20%. A reasonable explanation for the deviations is the fact that the flow around the sinker is not resolved in the simulation. Hence, the attachment between sinker and net is missing, and the important drag and inertia forces are approximated using Morison's formula.

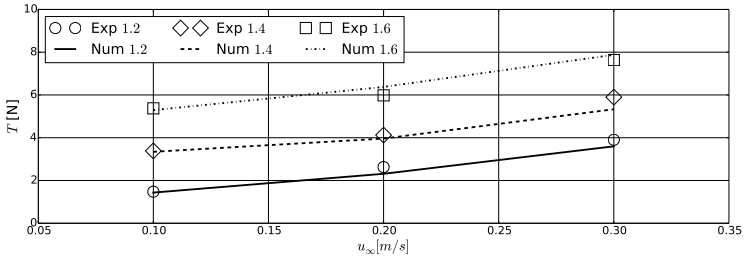

(a) $Sn = 0.16$.

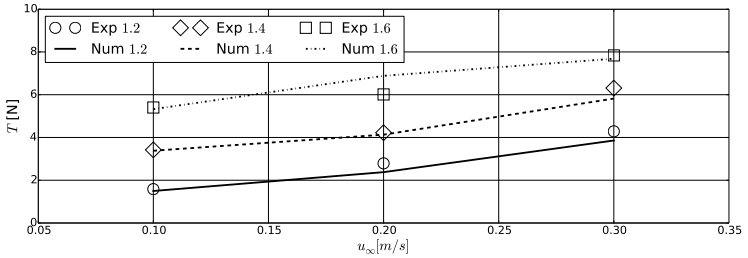

(b) $Sn = 0.19$.

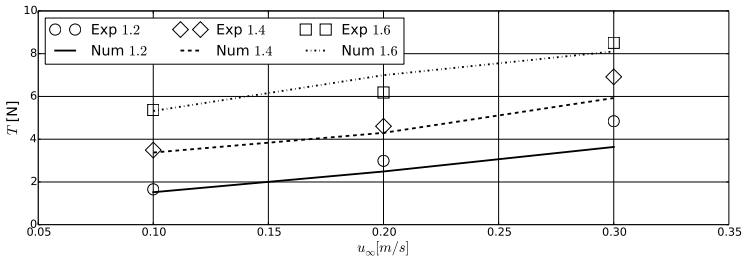

(c) $Sn = 0.23$.

Figure 11: Comparison of the numerical and experimental tension forces at the top of a net sheet in steady current flow. In [2], the results are normalised by the tension forces without inflow T_0. The shown data are obtained after multiplication with the numerically calculated T_0. The numbers in the legend refer to the sinker weight in kilogram.

3.4 Moored-floating cylinder in waves

The presented floating algorithm in section 2.2 is validated against measurements of a moored-floating cylinder in waves. The setup replicates the experiments of Kristiansen [25] which were performed in the same tank as described in section 3.3. A cylinder with diameter 0.1 m, the same length as the width of the tank and a mass of 3.94 kg/m is placed in the tank. A mooring system, consisting of ropes and springs with stiffness 151.2 N/m^2 and pre-tension 38.1 N/m, is attached to the cylinder. The other end of the lines is coupled to a pulley 2.43 m

away from the cylinder at a height of 0.136 m above the free surface. A two-dimensional setup of the experiments is investigated in the numerical wave tank shown in Fig. 12. The waves are generated in a wave generation zone of one wavelength, and a numerical beach damps the waves at the end of the tank. A description of these methods can be found in [5]. The mooring system is modelled as two springs mounted at the centre of the cylinder.

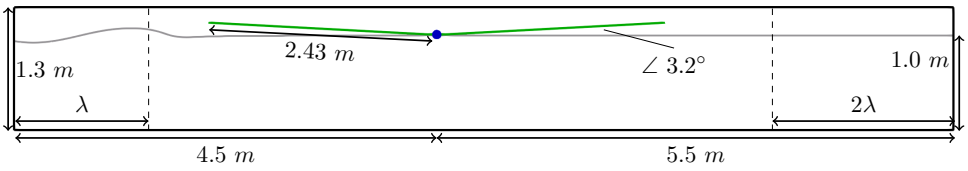

Figure 12: Two-dimensional domain for the simulation of a moored-floating cylinder in waves. The cylinder is shown in blue, the mooring lines in green and λ is the wavelength.

First, a convergence study is conducted using decays test of the moored-floating cylinder (see Fig. 13). In the experiments, only a surge decay of the moored-floating cylinder is reported. The comparison of the time series using numerical grids with $\Delta x = 0.01, 0.0075$ and 0.005 m is presented in the Figs. 13a and 13b. For all chosen cell sizes, the numerical model captures the first peak well. Numerical damping results in under-prediction of the subsequent amplitude for coarser grids. Similar observations are indicated for the free heave test (Fig. 13c). Although the medium grid seems to accurately predict the amplitudes, further refinement is needed for a convergence of the phase. As a consequence, the finest cell size is chosen for further testing.

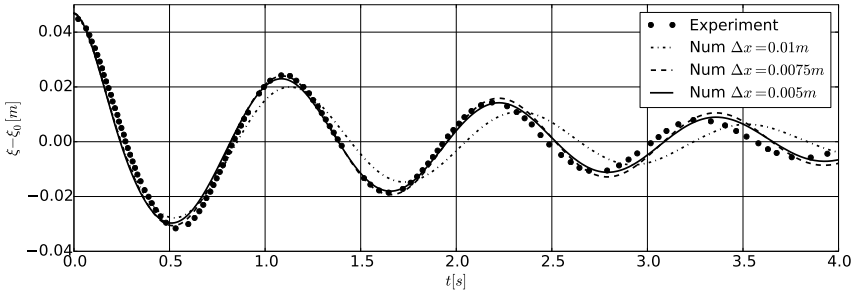

(a) Comparison of the time series of the surge decay test.

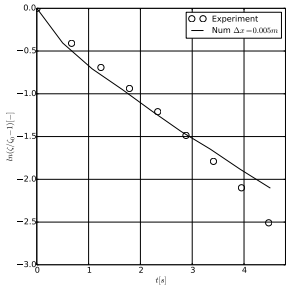

(b) Comparison of the decay rate for the surge decay test.

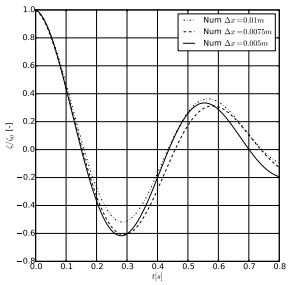

(c) Numerical heave decay test without mooring system.

Figure 13: Comparison of the numerical and experimental results for the decay tests of a moored-floating cylinder.

Next, the motion responses in surge and heave in regular waves with a constant steepness of 1/14 are compared. The waves have periods of $0.497, 0.544, 0.601, 0.761$ and 0.878 s and are modelled as 2nd-order Stokes waves in the numerical simulations. The comparison of the time series can be found in C and indicate a proper working of the framework. A more robust indication of the object's behaviour can be investigated through the amplitude responses over the wave periods as shown in Fig. 14. In general, the deviations are between 5% and 10%.

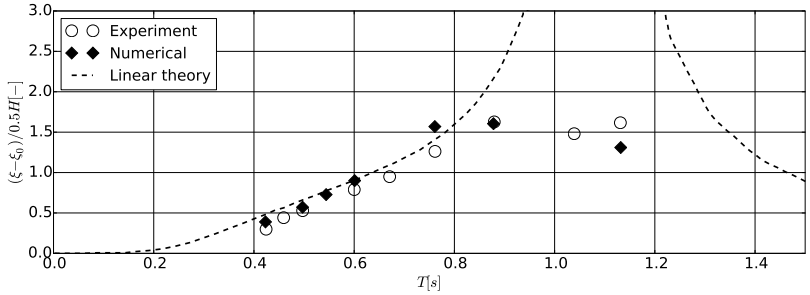

(a) Surge motion.

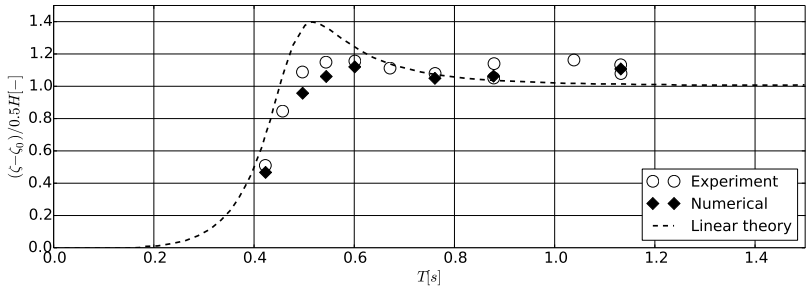

(b) Heave motion.

Figure 14: Comparison of the response amplitude operators (RAO) between the numerical model and the experiments for the moored-floating cylinder in regular waves. The linear solution is taken from [25].

In shorter waves, the surge motion oscillates with the encounter frequency plus a sub-harmonic component at half the frequency. This effect is captured well by the numerical model as seen in Fig. 15, which shows the power spectrum of the surge response for the shortest wave. Further, the model follows the linear relation between the wave period and surge amplitude response present for short waves. As shown in Fig. 16, the object thereby damps the waves almost completely as the wave height in the wake is significantly reduced. The heave motion gradually increases as the waves increase in height. Here, linear theory significantly over-predicts the heave response, whereas the numerical solution agrees well with the experiment. In longer wave periods, the heave response amplitude reaches a value slightly above 1 as the cylinder follows the surface of the long waves. As indicated in Fig. 16, highly non-linear fluid-structure interaction occurs in these conditions. Around the surge resonance frequency, the numerical model predicts amplitudes close to the experiments, whereas theoretical formulae typically overestimate the response.

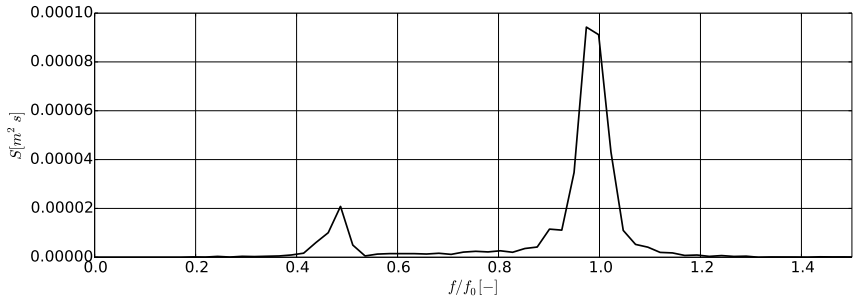

Figure 15: Numerically predicted power spectrum for the sub-harmonic surge motion in the wave with period $T = 0.497$ s.

Following the work of Kristiansen [25], further analysis of the wave excitation forces can be conducted by comparing the significant amplitude components of the acceleration signal. This is caused by the direct link of acceleration and hydrodynamic load through Newton's second law. The resulting linear, second and third harmonic components of the acceleration amplitudes are provided in Fig. 17 using discrete Fourier analyses. In surge direction, the excitation is mainly driven by the linear component. High-order components become more relevant for longer waves, in particular around the surge resonance. This increase might be caused by wave overtopping and viscous effects due to flow separation. For the vertical accelerations, second-order harmonics exceed the linear part for wave periods between 0.8 s and 1.0 s. It is noticed by Kristiansen [25] that this effect occurs because the second component occurs at a frequency close to the natural heave frequency of the system. As a consequence, the disregard of these high-order components can lead to a significant under-estimation of the loads on the structure.

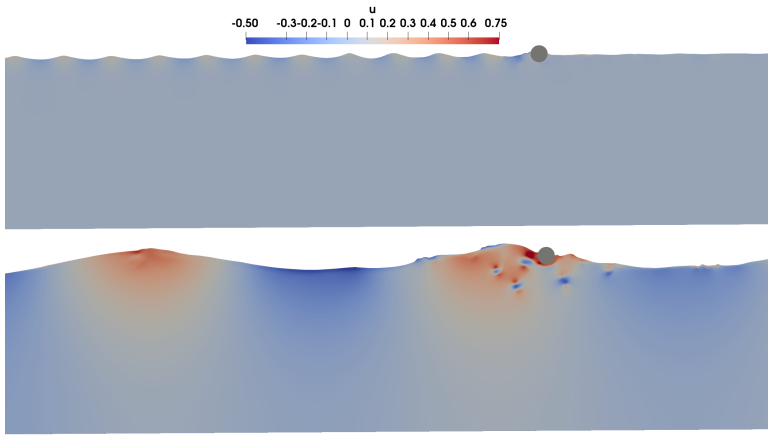

Figure 16: Time instances of the simulation of a moored-floating cylinder in regular waves. The figures show the x-velocity profiles in waves with period 0.491 s (top) and 1.131 s (bottom).

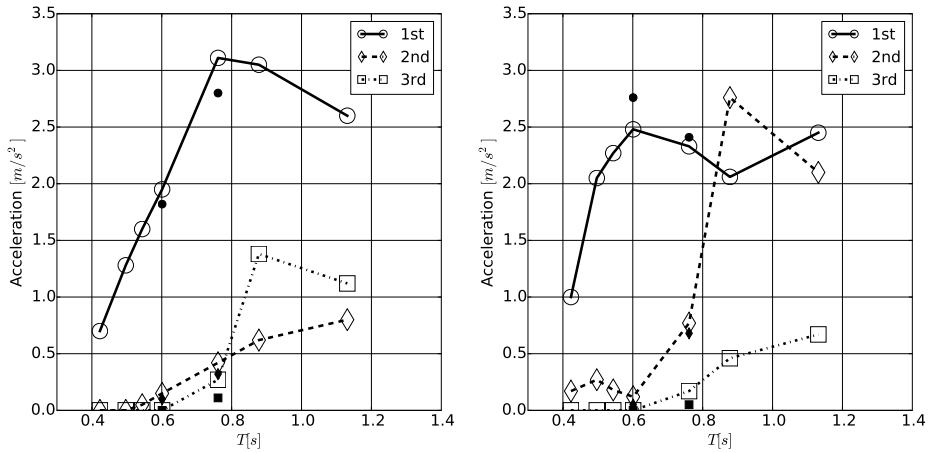

(a) Acceleration amplitudes in surge direction over wave period.

(b) Acceleration amplitudes in heave direction over wave period.

Figure 17: Fourier amplitudes of the first three harmonic components of the acceleration obtained from the numerical model for the moored-floating cylinder in regular waves. Experimental results are shown as black markers of corresponding shape.

3.5 Moored-floating cylinder with a net attached in waves

As a final step of the validation process, the complete numerical framework is tested against measurements of a moored-floating cylinder with an attached net in waves [2]. The considered experiment is a combination of previous cases. The moored floater is the same as in section 3.4, and the attached net with solidity 0.23 and sinker weight 1.64 kg is taken from section 3.3. Tension forces acting in the topmost twines are reported for regular waves with a wave steepness of 1/14 and wave periods between 0.4 s and 1.3 s. The dimensions of the numerical wave tank are adapted from the previous section, but a third dimension is added due to the presence of the net. A grid size of 0.005 m is defined for the x- and z-direction and a coarser resolution of 0.08 m is chosen in y-direction because no three-dimensional effects are expected. The complete setup is shown in Fig. 18.

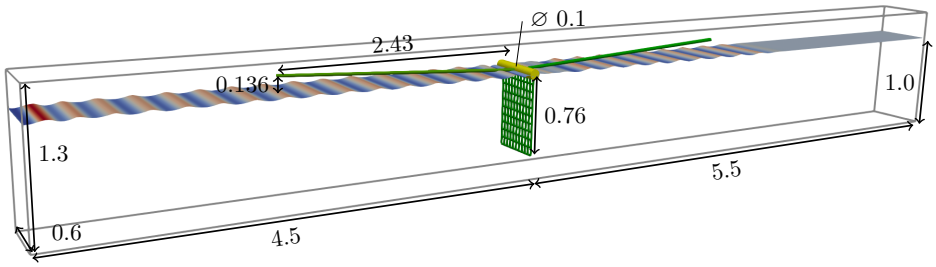

Figure 18: Computational domain for the simulation of a moored-floating cylinder with net in waves. Mooring system and net are shown in green, the floater in yellow.

Fig. 19 compares the predicted maximum tension forces with the experimental data. For small waves, the maximum tension forces are of similar magnitude as in a hydrostatic fluid due to the small motion of the cylinder in these waves. As the wave height increases and the wave period approaches the eigenperiod of the system, the maximum tension forces are approximately five times higher than in the hydrostatic condition and snap loads occur. These loads arise from the relative motion between the cylinder and sinker. Typically, when the cylinder is in a wave trough, the maximum elongation of the net reduces and the net becomes slack (see Fig. 20a). When the wave trough passes and the cylinder is accelerated upwards by the following wave crest, the net accelerates but its motion is restricted by the sinker mass. Thus, a large force is observed in the net which might lead to damage to the net in practice. The behaviour of the system changes for very long waves. Here, both the cylinder and the sinker follow the curvature of the waves, and the occurrence of snap loads becomes less likely. The numerical model quantitatively agrees very well with the experimental data in short and long waves. The snap loads tend to be over-predicted by up to 15%.

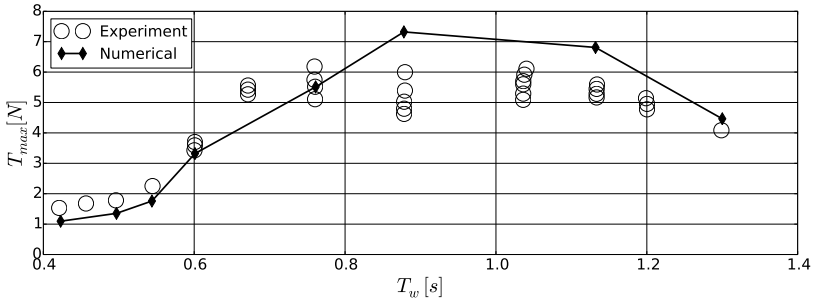

Figure 19: Comparison of the numerical and experimental maximum tension forces in the topmost twines over the wave period T_w for the moored-floating cylinder with net in regular waves.

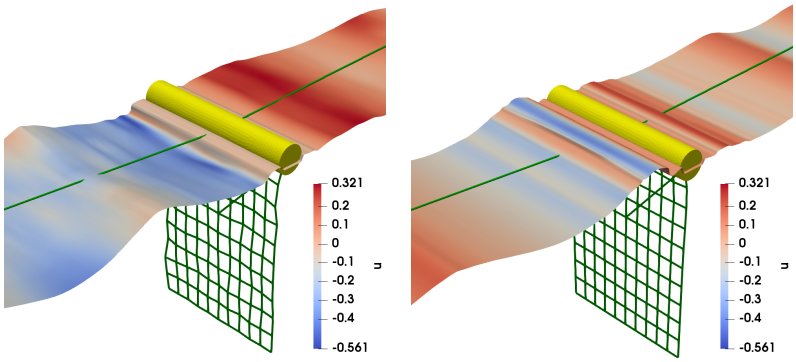

(a) Wave trough situation with slack net. (b) Wave crest situation with a taut net.

Figure 20: Two typical situations during the simulation of a moored-floating cylinder with net in a regular wave with $T = 0.761$ s. Colours show velocity on free surface in x-direction.

Additionally, the change of the motion of the moored cylinder due to the net with sinker is presented in Fig. 21. It shows that the amplitude responses in both, heave and surge, reduce. For the surge motion, the qualitative behaviour of the system is less influenced but smaller amplitudes can be expected. This might be caused by the inertia and drag of the net. In comparison, the characteristics of the system change significantly in the heave direction. The reason is the relatively heavy sinker weight which requires large excitation forces to accelerate in the fluid. Hence, it constrains the cylinder motion for small and medium wavelengths resulting in small amplitude responses.

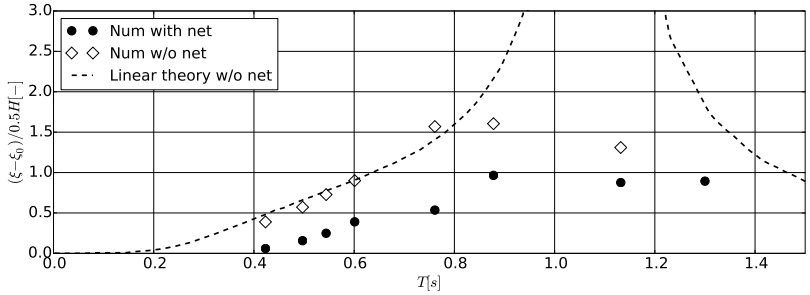

(a) Surge motion.

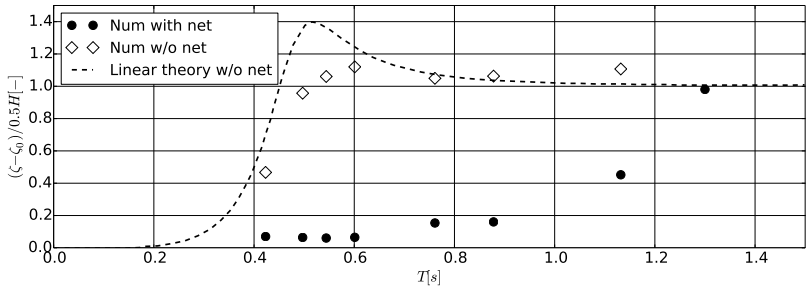

(b) Heave motion.

Figure 21: Numerically calculated RAO for the moored-floating cylinder with net in regular waves. The results from section 3.4 are shown for comparison.

4 Engineering applications

The functionality of the proposed numerical framework is elaborated for two types of OOA structures in regular and irregular waves as well as current.

4.1 Semi-submersible OOA structure

Semi-submersible offshore fish cages are characterised by being attached to a pre-tensioned mooring system which holds the structure in place but also influences the seakeeping properties of the system. Therefore, the accurate prediction of the dynamic responses to varies sea states is of importance and exemplarily investigated for a structure in the style of Ocean Farm 1. The structure was originally developed by SalMar, Norway and later replicated by Zhao et al. [53] for model tests in a wave-current flume at the State Key Laboratory of Coastal and Offshore Engineering, Dalian University of Technology, China. The experiments were performed in a 1:120 model scale and included three different draughts. Unfortunately, the documentation of the experiments lacks key information, amongst others, about the exact geometry, centre of gravity, mass and moments of the object and exact location of the mooring system. Also, the chosen scaling factor is far smaller than typical scale factors used in the marine technology

practice, where model tests are typically performed at 1:20-60 scale to minimize the scaling effects. Therefore, the experiments are not necessarily representative for the dynamics of Ocean Farm 1 and only taken as a rough reference for the setup of the simulations.

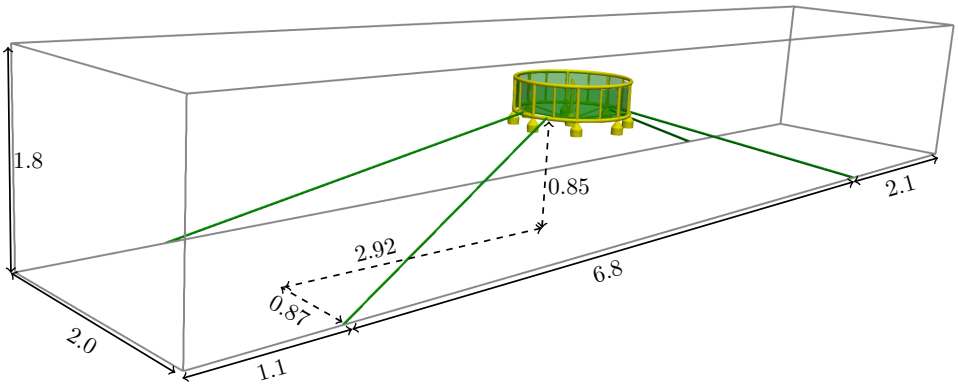

Figure 22: Numerical setup for the simulation of the semi-submersible OOA structure in waves. All measures are in metres.

The structure is assumed to be rigid and consists of 8 pontoons with straight columns attached. The columns are connected at three different heights via additional thinner columns so that a hexadecagon with a diameter of approximately 1 m is formed. An additional pontoon and column is placed in the middle of the structure slightly below the others and connected to the other columns with thin pipes. The complete structure is shown in Fig. 1. In comparison to the model of Zhao et al. [53], the thinnest pipes are not considered because of their negligible contribution for the loading and minor influence on the fluid. The draught of the model is 0.28 m in the simulations and reached by adjusting the overall mass of the structure and a free heave decay test. Uniform mass distribution is then assumed to calculate the moments of inertia for the rotational motions of the structure.

A characteristic of this semi-submersible OOA design is that the net is fastened more tightly to the structure than in traditional aquaculture cage systems [12]. As a consequence, the deformation of the net can be neglected. In the numerical model, this assumption is incorporated by making the net as part of the rigid structure instead of calculating its dynamics separately. The external forces on the net are added to the rigid body solver and used for determining the shading effect as before. The net covers the complete structure and is assembled using a cylinder for the side walls and a cone for the bottom. Each part of the net consists of twines with a length of 8 mm and thickness of 0.6 mm resulting in a solidity of 0.145. A mooring system is attached to the structure for the simulations in waves. The experimental setup includes four mooring lines, each consisting of a rope with a linear spring at the end. The stiffness of the lines is calculated as 195 N/m based on the reported relation between force and line elongation. Further, the pretension is set as 1.91 N. The exact position of mounting points on the structure remains unclear. It is therefore decided to place it on the lower connection columns such that the virtual line extensions intersect in the geometrical

centre of the structure. The moored-floating structure is placed in a numerical wave tank of the dimensions 10 $m \times 2\ m \times 1.8\ m$ which is a shortened version of the physical wave tank (Fig. 22). The water depth is set to 1 m. The waves are generated at the inlet using the wave relaxation method, and a numerical beach reduces wave reflections at the end of the tank. The simulations include regular waves with height $H = 0.06$ m, 0.1 m and period $T_w = 1.0\ s, 1.2\ s, 1.4\ s$, which are taken from the experiment. Additional simulations without the net are conducted to study the importance of the net for the motion of the structure. Further, the response of the structure in irregular waves is simulated to gain a deeper understanding of the structural response. Several JONSWAP spectra with a significant wave height of 0.1 m and peak periods between 0.5 s and 3.5 s are chosen for this purpose. The resulting power spectrum is shown in Fig. 25a. Each spectrum is generated by superposing multiple linear wave components as described in [1]. Power and cross power spectra are calculated using an FFT analysis, and the linear transfer functions (RAO), as well as the coherences γ, are subsequently determined using

$$\mathrm{RAO}_{\mathrm{motion}} = \sqrt{\frac{S_{\mathrm{motion}}}{S_{\mathrm{wave}}}}, \tag{38}$$

$$\gamma_{\mathrm{motion}} = \sqrt{\frac{|S_{\mathrm{wave,motion}}|^2}{S_{\mathrm{motion}} S_{\mathrm{wave}}}}, \tag{39}$$

with S_{motion} and S_{wave} the power spectra from auto-correlation analyses and $S_{\mathrm{wave,motion}}$ the cross-spectrum.

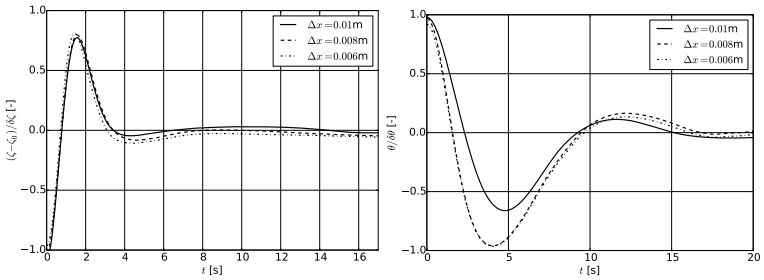

(a) Heave decay. (b) Pitch decay.

Figure 23: Free decay tests for the semi-submersible OOA structure. The net but no mooring system is included in these test.

At first, free heave and pitch decay tests are conducted to determine the mass of the structure and the necessary grid size. The net but no mooring lines are attached to the structure. Three different grids with a uniform cell size of 0.01 m, 0.008 m and 0.006 m in a box around the object are considered. The cells outside the inner box are stretched at a ratio of 1.02 towards the domain boundaries until the maximum cell size of 0.05 m is reached. The resulting grids have 9.5 M, 16 M and 33 M points. The time series of the decay tests are presented in Fig. 23. After the first peak, the motions are significantly damped due to the bottom net. The convergence of the results is observed. For the heave motion, the differences

are generally small, whereas at least a certain grid resolution is required to capture the pitch motion sufficiently. It is therefore decided to use $\Delta x = 0.008$ m for the simulations including waves. The results of these simulations are shown in Fig. 25 and Fig. 26 as the power spectra and response amplitude operators of the structure and maximum front and aft mooring line forces.

As shown in Fig. 26a, the heave amplitude increases with decreasing wave frequency and increasing wave amplitude. The maximum heave response is expected at $f = 0.4$ Hz. A second peak, which is indicated in the power spectrum in Fig. 25b, might occur at even lower frequencies. Further, the results indicate a highly damped system as the response to high-frequency excitations is small [19]. Similar observations can be stated for the surge motion in Fig. 26b. The surge motion increases non-linearly with decreasing wave frequency and approaches values closer to one in very long waves with $f < 0.6$ Hz as the structure increasingly follows the wave envelope. Also, the regular wave tests reveal larger surge motion for steeper waves due to increased wave energy. Here, the net plays a minor role as the motion without the net shows similar amplitudes. However, the horizontal forces on the net account for about 30% of the total horizontal forces on the system. This indicates that the horizontal forces are generally small, amongst others caused by the low solidity of the net, and that the surge response of the system is mainly dominated by the mooring system. This possible explanation is substantiated by observing the free surface travelling through the structure in Fig. 24. The fluid is accelerated along and wakes are developed behind each member of the structure. In contrast, the damping effect of the net is not visible.

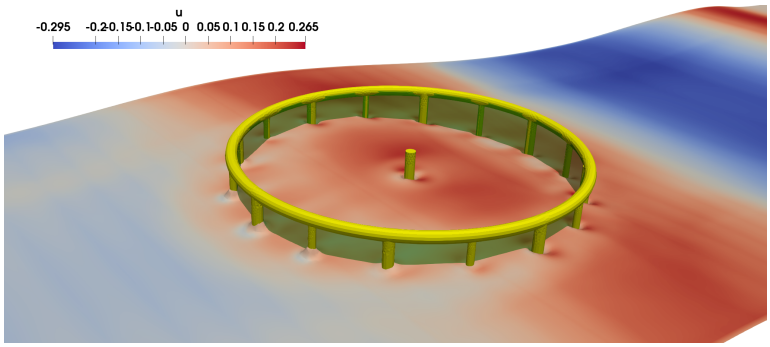

Figure 24: Free surface contour showing x-velocities in a wave crest situation for the simulation of the semi-submersible OOA structure in a regular wave with height 0.1 m and period 1.4 s.

For the rotational motion of the structure (Fig. 26c), a strong increase of the pitch amplitude indicates a possible resonance close to the lowest investigated wave frequencies. The response in pitch is relatively small for wave frequencies larger than 0.6 Hz compared to the translational motions. This might be caused by a rather horizontally than vertically acting mooring system. The maximum tension forces in the front and aft mooring lines increase naturally with increased structural motion and reach local maxima close to the maxima of the heave and surge responses. This strengthens the argument that mooring reaction forces are the driving excitation forces for the dynamics of the OOA structure. Generally, the front line forces are larger than the forces in the aft due to the undisturbed impact of the wave

loads. The difference between the front and aft forces tends to increase with larger encountered wave periods, whereas the wave steepness mostly affects the aft mooring line as steeper waves travel less disturbed through the upper part of the structure. Further, the simulations without the net reveal that the aft forces tend to decrease if the net is present, as already observed experimentally. This might be caused by the shielding and damping effect of the net. Generally, it is noticed that the results from the regular wave tests mostly coincide with the irregular test results, which indicates that both wave inputs are valid approaches to determine the response of OOA structures.

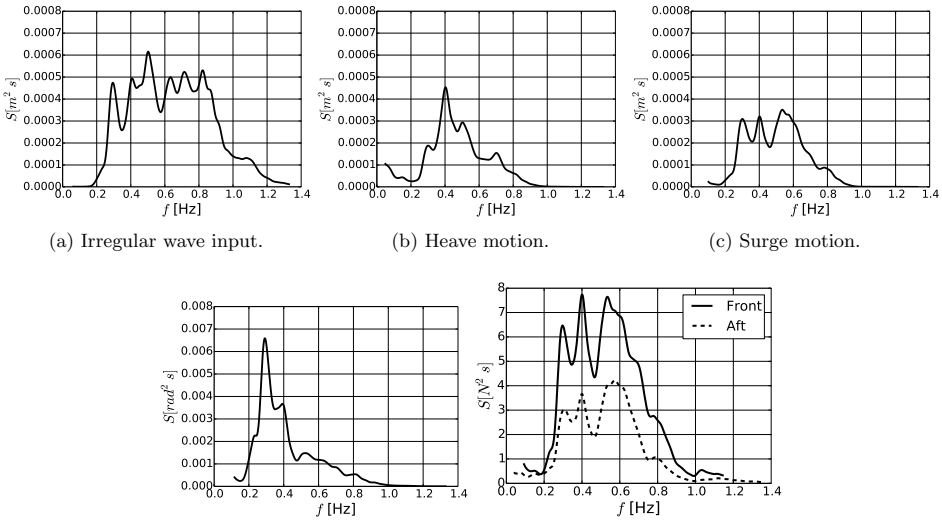

(a) Irregular wave input. (b) Heave motion. (c) Surge motion.

(d) Pitch motion. (e) Maximum tension forces.

Figure 25: Power spectra of the semi-submersible OOA structure using irregular wave input.

The obtained transfer functions are based on the assumption that the considered system is linear. The coherences for the motions and tension forces are presented in Fig. 27 to investigate the validity of this assumption. The shown distributions hint at a linear system for wave frequencies between 0.3 Hz and 0.8 Hz because γ is close to unity. The translational motions tend to become non-linear at smaller frequencies than the pitch motion which has a coherence close to one up to $f = 1.1$ Hz. The strongest non-linear effects are expected for the tension forces which is caused by the coupling to the wave loads and all degrees of freedom.

As a final remark, it is reported that the simulation of the fluid-structure interaction in irregular waves takes around 185 h for 300 s of simulation time on 64 cores (Intel Sandy Bridge) with 2.6 Ghz and 2 GB memory per core.

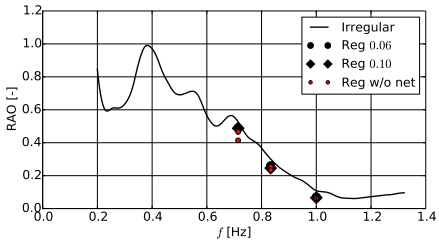

(a) Heave motion.

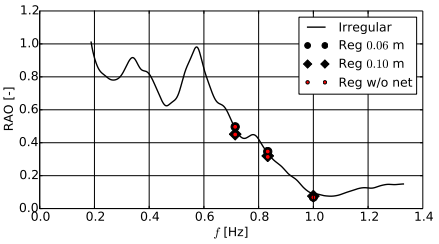

(b) Surge motion.

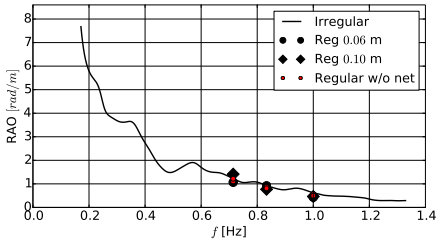

(c) Pitch motion.

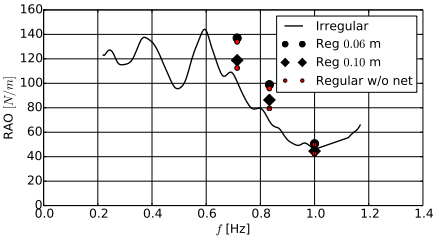

(d) Maximum front line tension forces.

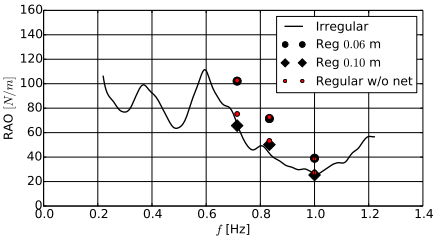

(e) Maximum aft line tension forces.

Figure 26: RAO of the semi-submersible OOA structure using regular and irregular wave input. For comparison, the motions without considering the net are shown in red.

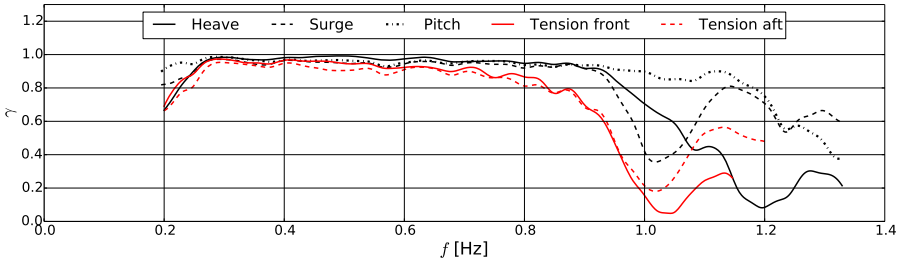

Figure 27: Coherence of the semi-submersible OOA structure using irregular wave input.

4.2 Mobile floating OOA structure

The offshore aquaculture facility Havfarm 2 (Fig. 28) is developed by Nordlaks and NSK Ship Design [38]. It can be considered as an example for a mobile floating OOA structure. The main structure is represented by a large, slender ship-shaped hull with several net cages attached. The design process faces challenges due to the complex interaction of multiple nets with the fluid and the resulting water quality change in the cages. The quality is expected to improve with increasing discharge through each net. For this purpose, Havfarm 2 is equipped with a dynamic positioning (DP) system which can change the heading angle between incident flow and structure. However, this increases the external loads which have to be withstood by all components involved. The DP system will be further applied to vary the location of the farm, dependent on the sea state and weather forecast. Hence, the manoeuvrability of the farm and thus, the prediction of global forces is important for the operation of Havfarm 2.

Model tests were performed in the ocean basin of SINTEF Ocean, Trondheim, Norway, in a $1:40$ model scale to investigate the fluid-structure interaction experimentally. Amongst others, towing tests with different heading angles between the structure and towing direction were conducted and are taken as a reference here.

The prototype of Havfarm 2 consists of multiple rectangular beams forming four equally sized box-shaped spaces. In each of these, a cylindrical net with solidity 0.22 is tightly fastened to the rigid structure. They are simulated as non-deforming nets moving with the rigid structure as explained above. Further, a flexible conical net with the same solidity is attached to the bottom of each cylinder, which requires dynamic modelling. A sinker weight of 2 kg is pre-tensioning this part of the net during the towing tests.

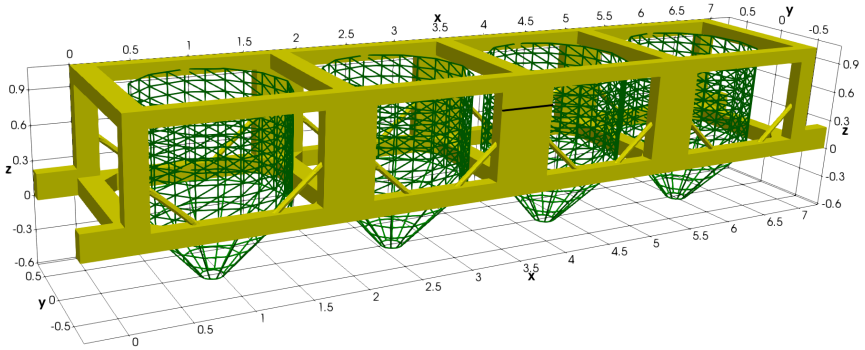

Figure 28: Geometry of the floating OOA structure. Rigid structure in model scale 1:40 is shown in yellow and nets in green. The design draft is indicated by the black line at the centre column. All measures are in metres.

Prior to this, free decay tests in heave and pitch are conducted to choose the grid size for the subsequent simulations. Three different grids with uniform cell sizes of 0.07 m, 0.05 m and 0.03 m are considered. Fig. 29 shows the predicted time series in comparison to the experimental results. For the heave motion, the coarser grids tend to over-damp whereas the finest grid predicts most peaks and the period sufficiently. Also, the refinement of the grid results in increased pitch amplitudes close to the experimental values. The period is

captured well for the first two peaks and over-predicted for the remaining peaks. A further grid refinement could be necessary to improve the pitch motion and obtain a grid independent solution. It is further noticed that small differences between the numerical and experimental geometry exist because of the neglect of very thin bracings. Their effect on the motion of the structure is, however, assumed to be of minor importance.

Based on the obtained results, a cell size of 0.03 m is chosen for a box around the structure. The box is placed in the middle of a tank of the dimensions $30 \times 20 \times 10$ m with a smooth growth of the cell size towards the boundaries. The water depth is chosen as 8.0 m to avoid interaction with the bottom of the domain. Constant inflows of 0.83 m/s and 1.0 m/s are predefined at the inlet and the flow freely leaves the tank at the outlet. The structure is rotated relative to the inlet with heading angles of $0°, 15°$ and $45°$. The structure can freely heave, roll and pitch during the simulations. However, the motions are not investigated further because the heave motion remains small and the rotational motions are below $1.0°$ for all cases.

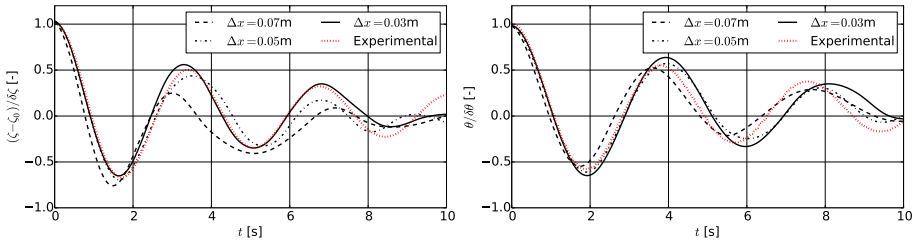

(a) Heave decay.

(b) Pitch decay.

Figure 29: Numerical and experimental results for the free decay tests of the floating OOA structure.

The mean velocities inside each net, 0.1 m below the free surface, are computed and compared to the experimental data in Fig. 30. The measurements showed large oscillations for which reason the variations are included in terms of one standard deviation. Additionally, slices of the x-y plane around the structure at this height are shown in Fig. 31 to reach a further understanding of the results. It is at first noticed that the computed x-velocities are mostly within the chosen interval of the experimental results. The values also coincide well with the theoretical formula for the velocity reduction through net panels by Løland [31]. This formula is however limited to the case of $\alpha = 0°$. For the front cage and small heading angles, the simulations predict an accelerated flow resulting in velocities higher than the inflow velocities. This is also visible in the Figs. 31a and 31b, where the two vertical beams in the front form a narrow channel passed by the flow. At these angles, the shading effects of the nets result in decreasing velocities in the cages behind. The flow separation at each beam becomes increasingly important for the flow field in each cage with increasing angles (see Fig. 31c). At large heading angles, the interaction between the cages becomes less significant. Thus, the differences between the predicted velocities in the different cages as well as the x-velocities itself become small as shown both experimentally and numerically. The mean y-velocities are generally smaller than the mean x-velocities, and the fluid oscillates more in this direction particularly for the front cage and large heading angles. A possible physical explanation is the development of an oscillating wake behind each beam. This causes the recirculation zones

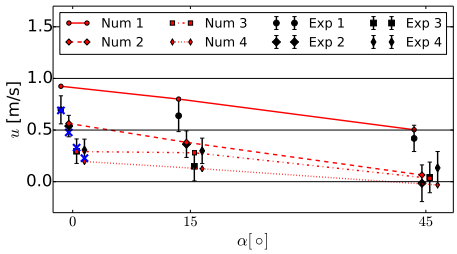

(a) Velocities in x-direction for $u_\infty = 0.83$ m/s.

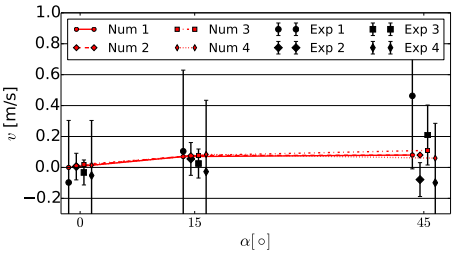

(b) Velocities in y-direction for $u_\infty = 0.83$ m/s.

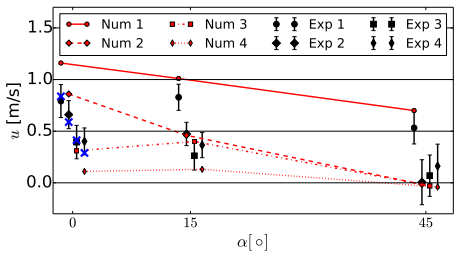

(c) Velocities in x-direction for $u_\infty = 1.0$ m/s.

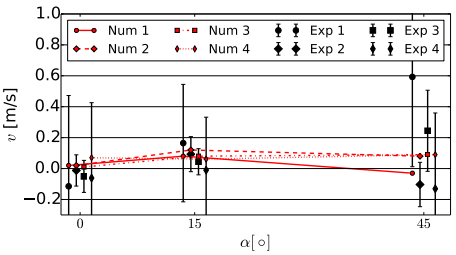

(d) Velocities in y-direction for $u_\infty = 1.0$ m/s.

Figure 30: Numerical and experimental results for the mean velocities inside the cages for different inflow velocities u_∞ and angles of attack $\alpha = 0°, 15°$ and $45°$. Cage 1 is in the front and cage 4 in the back. The bars indicate the variation of the measurements in terms of one standard deviation. Additionally, theoretical results for $\alpha = 0°$ using the formula of Løland [31] are indicated in blue

.

passing the probe points in the centre of each cage periodically.

The analysis of the velocity inside the upper part of the cages reveals that the intended improvement of water quality through increased discharge cannot be achieved by increasing the heading angle. However, this changes for the lower, flexible part of the cage. Fig. 32 shows the velocity distribution in the centre x-z plane along the longitudinal axis of the structure for different angles of attack α. As expected, the shading effect of the nets causes the increasing deceleration of the flow along the structure for $\alpha = 0°$ (see Fig. 32a). Thus, a lower discharge and less deformation are predicted for the cages in the back. By increasing the heading angle (Figs. 32b and 32c), the flow in front of each cage is less disturbed by the wake of cages placed in the front. As a result, similar deformation and discharge are predicted for all cages which consequentially indicates improved water quality in the back cages.

The water quality control through the rotation of the structure has the drawback of increased loads. In order to quantify this, Fig. 33 presents the loads on the net and the structure in x- and y-direction for the different cases. In general, the forces increase with increasing inflow velocity. Also, the loads on the nets are generally more crucial to consider in x- than in y-direction and are even dominant at small heading angles in x-direction. The increase of the loads on the nets is further less dependent on the heading angle than the

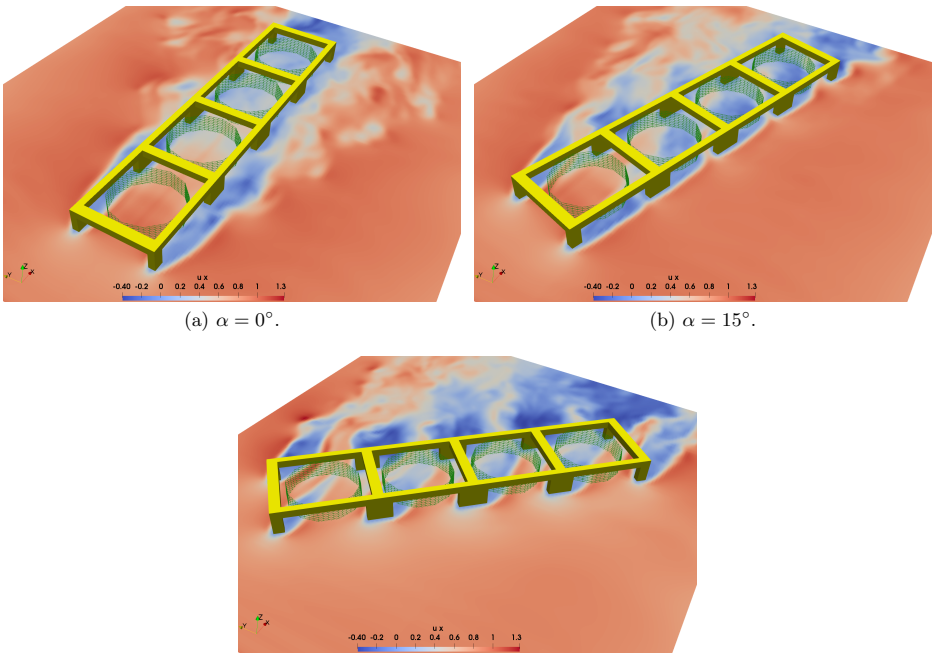

(a) $\alpha = 0°$.

(b) $\alpha = 15°$.

(c) $\alpha = 45°$.

Figure 31: Slices of the x-y plane at $z = 7.9$ m for the simulation of the floating OOA structure with different angles of attack α and $u_\infty = 0.83$ m/s. The contours show the velocity in x-direction.

rigid structure forces. This is caused by the symmetry of the cage geometry in comparison to the changing structural area exposed to the undisturbed inflow. Thus, the structural forces become the dominant factor for large heading angles. The same conclusion can be drawn in y-direction (Fig. 33b). The increase for larger heading angles is caused by the increased area but might also be influenced by intensified vortex shedding.

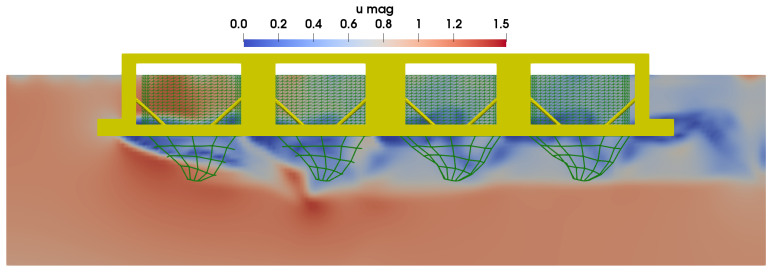

(a) $\alpha = 0°$.

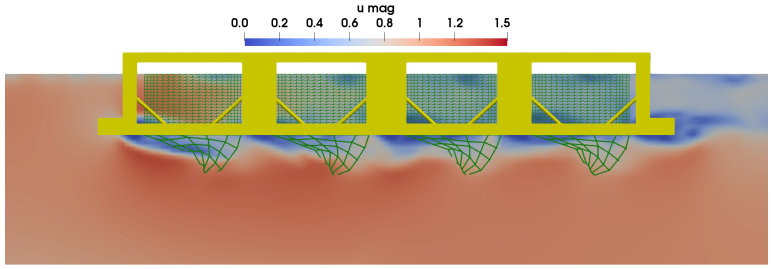

(b) $\alpha = 15°$.

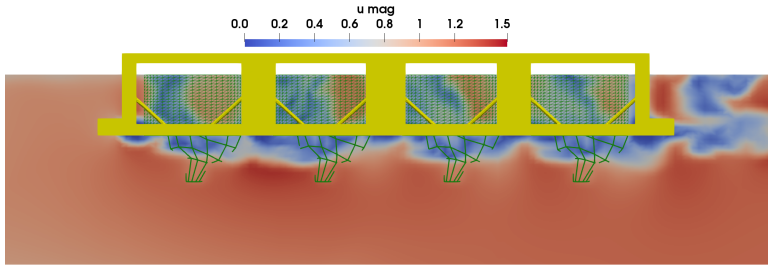

(c) $\alpha = 45°$.

Figure 32: Slices in the centre x-z plane along the longitudinal axis of the floating OOA structure for different angles of attack α and $u_\infty = 1.0$ m/s. The contours show the velocity magnitudes.

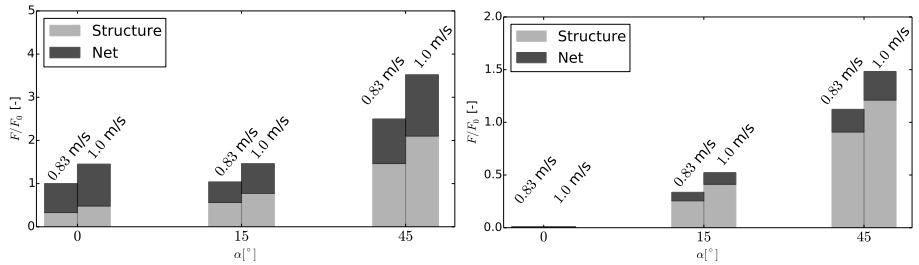

(a) Forces in x-direction.

(b) Forces in y-direction.

Figure 33: Numerically predicted mean forces for the floating OOA structure. Values are normalised using the total forces in x-direction for $u_\infty = 0.83$ m/s.

5 Conclusions

A new numerical framework for modelling the motion of OOA structures in waves and current was proposed and applied in this paper. It enables the study of the effects of waves and current on the motion of the system taking into account the fluid-structure interaction around and inside the cages, the motion of the rigid structure as well as the deformation of the net. The interactions of floating structures, mooring, nets and fluid are incorporated as two-way coupling problems. Efficient numerical approaches were chosen and newly developed to solve the governing equations of fluid and structural dynamics. In particular, the coupled solution of the rigid structural motion and the fluid flow was a necessary step to meet the requirements arising from the transition from traditional fish cages towards structures suitable for offshore environments. Several validation cases including rigid and deforming nets, moored-floating objects and a combination of these were presented. Reasonable agreements with available experimental data could be presented for all considered tests and deviations were justified on a physical level.

The response of a semi-submersible OOA structure in regular and irregular waves was investigated thoroughly. These structures typically contain rigid nets which implies no volume reduction of the net during operation. For the considered design concept, relatively small vertical motion and strong motion reduction for high-frequency excitation could be observed. This is a characteristic of offshore semi-submersible platforms due to their low centre of gravity, a relatively large mass and the mooring system. Further, the importance of incorporating the net into the investigation increases with the wave height and period due to the increased wave energy and the non-linear growth of the drag forces on the net. The shading effect of the net seems to play a minor role in wave-only cases.

Another application concentrated on the flow around a mobile floating OOA structure in steady current flow. This type of structure can freely rotate and move to different sight locations, which are advantages over semi-submersible structures. The numerical study reveals that the considered structural design results in complex flow patterns with separation and recirculation zones interacting with the upper part of the cages. This complicates the proper adjustment of the discharge through the cages by changing the heading angle. Further, the

lower flexible parts of the cages show partly large deformations whose influence on the biomass in the cage has to be taken into account.

It is finally noticed that the predicted small y-loads on the nets for the floating structure might be caused by neglecting the effect of them on the turbulence in the fluid. Both, the potential vortex shedding behind each twine and the change of the fluid vorticity while passing the net can eventually result in increased cross-flow and thus cross-flow forces. This might also change the importance of the net shading for the investigated wave only cases. The quantification of these effects and their inclusion in the numerical framework are left for further research. In future studies the presented framework will be applied to alternative OOA concepts with focus on structural responses under extreme loads.

Acknowledgements

The authors are grateful for the grants provided by the Research Council of Norway under the HAVBRUK2 project (no. 267981). This research was supported in part with computational resources at NTNU provided by NOTUR (Norwegian Metacenter for Computational Sciences, http://www.notur.no) under project no. NN2620K. Further, the authors want to thank Håkon Ådnanes from NSK Ship Design for providing the geometry and physical model test results for Havfarm 2 and Føre et al. [16] for providing the preprint version of their paper.

A Transformations between Euler angles and Euler parameters

The rigid body rotations are described by the quaternion $\mathbf{e} = (e_0\ e_1\ e_2\ e_3)^T$ in the numerical model. To compare with physical model test results, $\mathbf{e}$ has to be transformed to e.g. the Tait-Bryan angles for roll Φ, pitch Θ and yaw Ψ using [21]

$$e_0 = \cos\left(\frac{\Phi}{2}\right)\cdot\cos\left(\frac{\Theta}{2}\right)\cdot\cos\left(\frac{\Psi}{2}\right) + \sin\left(\frac{\Phi}{2}\right)\cdot\sin\left(\frac{\Theta}{2}\right)\cdot\sin\left(\frac{\Psi}{2}\right), \tag{40}$$

$$e_1 = \sin\left(\frac{\Phi}{2}\right)\cdot\cos\left(\frac{\Theta}{2}\right)\cdot\cos\left(\frac{\Psi}{2}\right) - \cos\left(\frac{\Phi}{2}\right)\cdot\sin\left(\frac{\Theta}{2}\right)\cdot\sin\left(\frac{\Psi}{2}\right), \tag{41}$$

$$e_2 = \cos\left(\frac{\Phi}{2}\right)\cdot\sin\left(\frac{\Theta}{2}\right)\cdot\cos\left(\frac{\Psi}{2}\right) + \sin\left(\frac{\Phi}{2}\right)\cdot\sin\left(\frac{\Theta}{2}\right)\cdot\sin\left(\frac{\Psi}{2}\right), \tag{42}$$

$$e_3 = \cos\left(\frac{\Phi}{2}\right)\cdot\cos\left(\frac{\Theta}{2}\right)\cdot\sin\left(\frac{\Psi}{2}\right) - \sin\left(\frac{\Phi}{2}\right)\cdot\sin\left(\frac{\Theta}{2}\right)\cdot\cos\left(\frac{\Psi}{2}\right). \tag{43}$$

The back transformation is necessary to initialise $\mathbf{e}$ for given Euler angles:

$$\Psi = \arctan 2\left(2\cdot(e_1\cdot e_2 + e_3\cdot e_0),\quad 1 - 2\cdot(e_2\cdot e_2 + e_3\cdot e_3)\right), \tag{44}$$

$$\Theta = \arcsin(2\cdot(e_0\cdot e_2 - e_1\cdot e_3)), \tag{45}$$

$$\Phi = \arctan 2(2\cdot(e_2\cdot e_3 + e_1\cdot e_0),\quad 1 - 2\cdot(e_1\cdot e_1 + e_2\cdot e_2)). \tag{46}$$

B Derivation of the left hand side in (31) to the implicit system (32)

The dynamic equilibria (21) have to be fulfilled at each knot $\mathbf{x}$ at any time. This can be ensured by replacing $\mathbf{x}^{(n+1)}$ in (31) with its accelerations using high-order backward finite differences. The weights of each time instance included in the difference are found from [17] because of variable time steps in the coupled simulations. Thus, the velocity of the knot is expressed as

$$\frac{d\mathbf{x}^{(n+1)}}{dt} = \dot{\mathbf{x}}^{(n+1)} = \sum_{p=0}^{P} c_p \mathbf{x}^{(n+1-p)}, \tag{47}$$

with c_p the weights of the P points of the interpolation. The unknown velocity vectors $\mathbf{v}^{(n+1)}$ are approximated by repeating the derivation:

$$\frac{d^2\mathbf{x}^{(n+1)}}{dt^2} = \ddot{\mathbf{x}}^{(n+1)} = \sum_{p=0}^{P} c_p \dot{\mathbf{x}}^{(n+1-p)}. \tag{48}$$

Inserting (48) in (47), the left hand side in (31) can be explicitly calculated as:

$$\begin{aligned}
&\left(\mathbf{x_j}^{(n+1)} - \mathbf{x_i}^{(n+1)}\right)^2 \\
=&\left[\frac{\left(\ddot{\mathbf{x}}_j^{(n+1)} - \ddot{\mathbf{x}}_i^{(n+1)}\right)}{c_0^2} - \sum_{p=1}^{P} \frac{c_p}{c_0^2}\left(\dot{\mathbf{x}}_j^{(n+1-p)} - \dot{\mathbf{x}}_i^{(n+1-p)}\right)\right. \\
&\left. - \sum_{p=1}^{P} \frac{c_p}{c_0}\left(\mathbf{x}_j^{(n+1-p)} - \mathbf{x}_i^{(n+1-p)}\right)\right]^2 \\
=&\frac{1}{c_0^4}\left[\left(\ddot{\mathbf{x}}_j^{(n+1)} - \ddot{\mathbf{x}}_i^{(n+1)}\right) + \dot{\mathbf{X}}_{ij} + \mathbf{X}_{ij}\right]^2,
\end{aligned} \tag{49}$$

with the definitions

$$\mathbf{X}_{ij} = -c_0 \sum_{p=1}^{P} c_p \left(\mathbf{x}_j^{(n+1-p)} - \mathbf{x}_i^{(n+1-p)}\right), \tag{50}$$

$$\dot{\mathbf{X}}_{ij} = -\sum_{p=1}^{P} c_p \left(\dot{\mathbf{x}}_j^{(n+1-p)} - \dot{\mathbf{x}}_i^{(n+1-p)}\right). \tag{51}$$

After rearranging this result, the implicit function (32) arises in a straightforward manner.

C Time series comparison of the motion of the moored-floating cylinder in regular waves

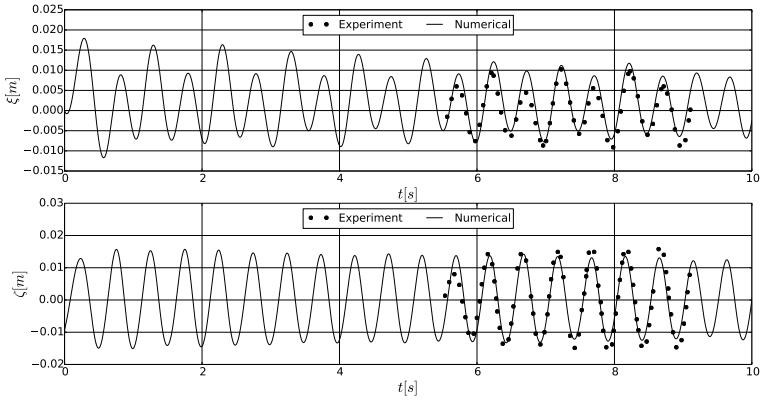

(a) Wave period $T = 0.497$ s.

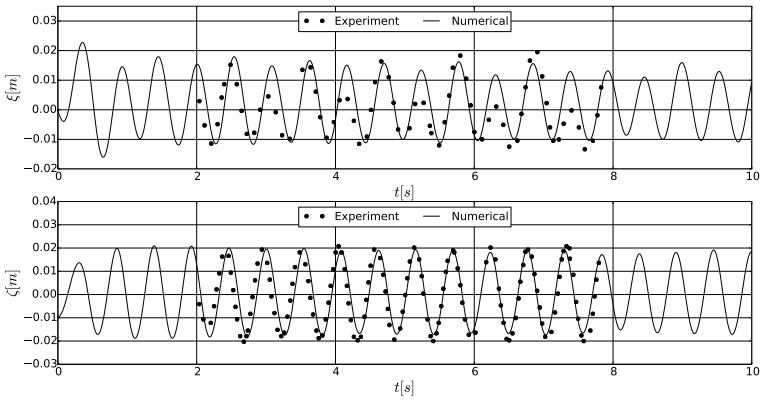

(b) Wave period $T = 0.544$ s.

Figure 34: Comparison of the numerical and experimental time series of the surge (ξ) and heave (ζ) motion for the moored-floating cylinder in a regular waves.

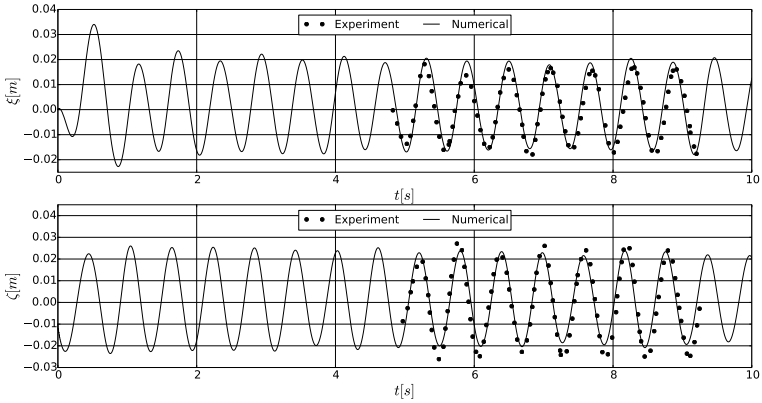

(a) Wave period $T = 0.601$ s.

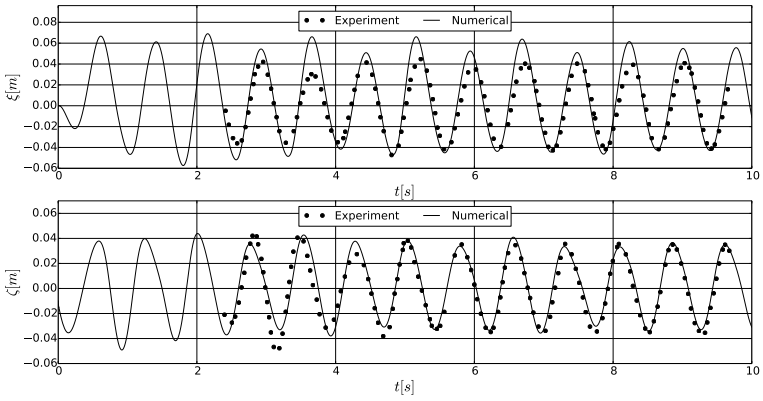

(b) Wave period $T = 0.761$ s.

Figure 35: Comparison of the numerical and experimental time series of the surge (ξ) and heave (ζ) motion for the moored-floating cylinder in a regular waves (continued).

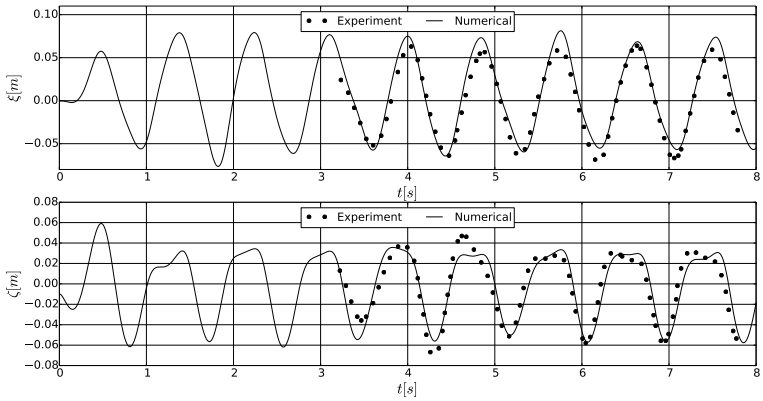

Figure 36: Comparison of the numerical and experimental time series of the surge (ξ) and heave (ζ) motion for the moored-floating cylinder in a regular wave of $T = 0.878$ s.

References

[1] A. Aggarwal et al. "Characteristics of breaking irregular wave forces on a monopile". In: *Applied Ocean Research* (2019). DOI: 10.1016/j.apor.2019.06.003.

[2] M. Bardestani and O.M. Faltinsen. "A two-dimensional approximation of a floating fish farm in waves and current with the effect of snap loads". In: *Proceedings of the ASME 2013 32nd International Conference on Ocean, Offshore and Arctic Engineering* (2013).

[3] C.-W. Bi et al. "A numerical analysis on the hydrodynamic characteristics of net cages using coupled fluid–structure interaction model". In: *Aquaculture Engineering* 59 (2014), 1–12.

[4] C.-W. Bi et al. "Numerical simulation of the interaction between flow and flexible nets". In: *Journal of Fluids and Structures* 45 (2014), 180–201.

[5] H. Bihs et al. "A new level set numerical wave tank with improved density interpolation for complex wave hydrodynamics". In: *Computers & Fluids* 140 (2016), 191–208.

[6] H. Bihs et al. "Complex geometry handling for a cartesian grid based solver". In: *MekIT, Ninth national conference on Computational Mechanics* (2017).

[7] P.M. Carrica, R.W. Noack, and F. Stern. "Ship motions using single-phase level set with dynamic overset grid". In: *Computers & Fluids* 36 (2007), 1415–1433.

[8] H. Chen and E.D. Christensen. "Development of a numerical model for fluid-structure interaction analysis of flow through and around an aquaculture net cage". In: *Ocean Engineering* 142 (2017), 597–615.

[9] H. Chen and E.D. Christensen. "Investigations on the porous resistance coefficients for fishing net structures". In: *Journal of Fluids and Structures* 65 (2016), 76–107.

[10] H. Chen and E.D. Christensen. "Simulating the hydrodynamic response of a floater net system in current and waves". In: *Journal of Fluids and Structures* 79 (2018), 50–75.

[11] H. Chen et al. "Application of an overset mesh based numerical wave tank for modelling realistic free-surface hydrodynamic problems". In: *Ocean Engineering* 176 (2019), 97–117.

[12] Y.I. Chu et al. "Review of cage and containment tank designs for offshore fish farming". In: *Aquaculture* (2020). DOI: 10.1016/j.aquaculture.2020.734928.

[13] C. Chun. "Iterative Methods Improving Newton's Method by the Decomposition Method". In: *Computers and Mathematics with Applications* 50 (2005), 1559–1568.

[14] E. A. Fadlun et al. "Combined Immersed-Boundary Finite-Difference Methods for Three-Dimensional Complex Flow Simulations". In: *Journal of Computational Physics* 161 (2000), 35–60.

[15] J.G. Ferreira et al. "Modelling of interactions between inshore and offshore aquaculture". In: *Aquaculture* (2014), 154–164.

[16] H.M Føre et al. "Loads on net panels with different solidities". In: *Proceedings of the ASME 2020 39th International Conference on Ocean, Offshore and Arctic Engineering* (2020).

[17] B. Fornberg. "Calculation of Weights in Finite Difference Formulas". In: *SIAM Rev.* 40 (3) (1998), 685–691.

[18] A. Fredheim. *Current Forces on Net Structures*. Ph.D. thesis, NTNU Trondheim, Norway. 2005.

[19] D.W. Fredriksson et al. "Fish cage and mooring system dynamics using physical and numerical models with field measurements". In: *Aquacultural Engineering* 27 (2003), 117–146.

[20] D.W. Fredriksson et al. "Moored fish cage dynamics in waves and currents". In: *IEEE Journal of Oceanic Engineering* 30(1) (2005), 28–36.

[21] H. Goldstein, C. P. Poole, and J. L. Safko. *Classical Mechanics*. Addison-Wesley, Boston, USA, 2001.

[22] K. Grigorakis and G. Rigos. "Aquaculture effects on environmental and public welfare – The case of Mediterranean mariculture". In: *Chemosphere* 855 (2011), 899–919.

[23] G.S. Jiang and D. Peng. "Weighted ENO schemes for Hamilton Jacobi equations". In: *SIAM Journal of Scientific Computing* 21 (2000), 2126–2143.

[24] G.S. Jiang and C.W. Shu. "Efficient implementation of weighted ENO schemes". In: *Journal of Computational Physics* 126(1) (1996), 202–228.

[25] D. Kristiansen. *Wave induced effects on floaters of aquaculture plants*. Ph.D. thesis, NTNU Trondheim, Norway. 2010.

[26] T. Kristiansen and O. M. Faltinsen. "Experimental and numerical study of an aquaculture net cage with floater in waves and current". In: *Journal of Fluids and Structures* 54 (2015), 1–26.

[27] T. Kristiansen and O. M. Faltinsen. "Modelling of current loads on aquaculture net cages". In: *Journal of Fluids and Structures* 34 (2012), 218–235.

[28] P.F. Lader and A. Fredheim. "Dynamic properties of a flexible net sheet in waves and current - A numerical approach". In: *Aquacultural Engineering* 35 (3) (2006), 228–238.

[29] F. LeBris and D. Marichal. "Numerical and experimental study of submerged supple nets applications to fish farms". In: *Journal of Marine Science Technology* 3 (1998), 161–170.

[30] L. Li et al. "Numerical Analysis of a Vessel-Shaped Offshore Fish Farm". In: *Journal of Offshore Mechanics and Arctic Engineering* 140 (2018). DOI: 10.1115/1.4039131.

[31] G. Løland. *Current forces on and flow through fish farms*. Ph.D. thesis, NTH Trondheim, Norway. 1991.

[32] D. Marichal. *Cod-end numerical study*. In: Proceedings of the 3rd International Conference on Hydroelasticity in Marine Technology, Oxford, UK., 2003.

[33] T. Martin and H. Bihs. "A non-linear implicit approach for modelling the dynamics of porous tensile structures interacting with fluids". In: *Journal of Fluids and Structures* (100) (2021). DOI: 10.1016/j.jfluidstructs.2020.103168.

[34] T. Martin, A. Kamath, and H. Bihs. "A Lagrangian approach for the coupled simulation of fixed net structures in a Eulerian fluid model". In: *Journal of Fluids and Structures* (94) (2020). DOI: 10.1016/j.jfluidstructs.2020.102962.

[35] T. Martin, A. Kamath, and H. Bihs. "Modelling and Simulation of Moored-floating Structures using the Tension-Element-Method". In: *Proceedings of the ASME 2018 37th International Conference on Ocean, Offshore and Arctic Engineering* 2 (2018).

[36] T. Martin et al. "Efficient implementation of a numerical model for flexible net structures". In: *Ocean Engineering* 150 (2018), 272–279.

[37] J. Morison et al. "The force exerted by surface waves on piles". In: *Pet. Trans. Amer. Inst. Min. Eng.* 186 (1950), 149–154.

[38] Nordlaks. https://www.nordlaks.no/havfarm/om-havfarm-prosjektet. accessed 08.06.2020.

[39] S. Osher and J.A. Sethian. "Fronts propagating with curvature-dependent speed: Algorithms based on Hamilton-Jacobi formulations". In: *Journal of Computational Physics* 79 (1988), 12–49.

[40] Ø. Patursson et al. "Development of a porous media model with application to flow through and around a net panel". In: *Ocean Engineering* 37 (2010), 314–324.

[41] C. S. Peskin. "Numerical analysis of blood flow in the heart". In: *Journal of Computational Physics* 25 (3) (1977), 220–252.

[42] Y. Shen et al. "Numerical and experimental investigations on mooring loads of a marine fish farm in waves and current". In: *Journal of Fluids and Structures* 79 (2018), 115–136.

[43] R. Shivarama and E.P. Fahrenthold. "Hamilton's Equations With Euler Parameters for Rigid Body Dynamics Modeling". In: *J. Dyn. Sys., Meas., Control* 126 (2004), 124–130.

[44] C.W. Shu and S. Osher. "Efficient implementation of essentially non-oscillatory shock-capturing schemes". In: *Journal of Computational Physics* 77(2) (1988), 439–471.

[45] M. Sussman, P. Smereka, and S. Osher. "A level set approach for computing solutions to incompressible two-phase flow". In: *Journal of Computational Physics* 114 (1994), 146–159.

[46] L.J.P. Timmermans, P.D. Minev, and F.N. Van De Vosse. “An approximate projection scheme for incompressible flow using spectral elements”. In: *International Journal for Numerical Methods in Fluid* 22 (1996), 673–688.

[47] M. Uhlmann. “An immersed boundary method with direct forcing for the simulation of particulate flows”. In: *Journal of Computational Physics* 209 (2005), 448–476.

[48] H. van der Vorst. “BiCGStab: A fast and smoothly converging variant of Bi-CG for the solution of nonsymmetric linear systems”. In: *SIAM Journal of Scientific Computing* 13 (1992), 631–644.

[49] T.-J. Xu et al. “Analysis of hydrodynamic behavior of a submersible net cage and mooring system in waves and current”. In: *Applied Ocean Research* 42 (2013), 155–167.

[50] J. Yang and F. Stern. “A non-iterative direct forcing immersed boundary method for strongly-coupled fluid-solid interactions”. In: *Journal of Computational Physics* 295 (2015), 779–804.

[51] L. Yang. “One-fluid formulation for fluid–structure interaction with free surface”. In: *Comput. Methods Appl. Mech. Engrg.* 332 (2018), 102–135.

[52] Y.-P. Zhao et al. “Numerical Simulation of Interaction Between Waves and Net Panel Using Porous Media Model”. In: *Engineering Applications of Computational Fluid Mechanics* 8.1 (2014), pp. 116–126.

[53] Y. Zhao et al. “Experimental Investigations on Hydrodynamic Responses of a Semi-Submersible Offshore Fish Farm in Waves”. In: *Journal of Marine Science and Engineering* 7 (2019). DOI: 10.3390/jmse7070238.

Paper 5

A CFD approach for modelling the fluid-structure interaction of offshore aquaculture cages and waves.

Martin, T. and Bihs, H. (2021).
ASME 40th International Conference on Ocean, Offshore and Artic Engineering, OMAE2021,
Accepted.

A CFD Approach for Modelling the Fluid-Structure Interaction of Offshore Aquaculture Cages and Waves

Tobias Martin* Hans Bihs

Department of Civil and Environmental Engineering, Norwegian University of Science and Technology (NTNU), 7491 Trondheim, Norway

Preprint
in *ASME 40th International Conference on Ocean, Offshore and Arctic Engineering*, 2021, Accepted.

Abstract

Open ocean aquaculture cages became recently a promising alternative to traditional fish cage designs. The offshore environment implies larger loads on the structures and higher risk of fish loss. Floating rigid aquaculture cages with stiff nets are considered as a possible solution to cope with these new challenges. Their design process requires more advanced tools to account for the non-linear fluid-structure interaction. This paper presents a suitable numerical approach for analysing the interaction of offshore aquaculture cages and waves using Computational Fluid Dynamics. Here, a numerical wave tank accounts for the accurate propagation of the waves, and structural dynamics solutions are utilised for the cage system. Two-way coupling is enabled by accounting for the influence of the net on the fluid. The numerical model is validated against measurements for the loads on and the responses of a mobile floating fish farm in waves and current.

1 Introduction

Traditional coastal aquaculture becomes less and less attractive due to its environmental impact on the surrounding marine environment. Open ocean aquaculture (OOA) is considered as a promising alternative today as it avoids near-coast restrictions and allows for the increase of the structural dimensions. Though, the relocation to offshore environments implies larger wave action and current velocities acting on the structures as well as a higher risk of fish loss due to structural failure [8]. Amongst others, floating rigid structures with relatively stiff nets are considered as a promising solution for this new environment. The dimensioning of these type of systems requires advanced knowledge about the non-linear fluid-structure interaction involving the complex structural dynamics of the floater, mooring and nets as well as a non-linearly propagating free surface including extreme waves and wave-current interaction.

*Corresponding author, tobias.martin@ntnu.no

In the design process, experimental studies are typically conducted only for the final prototype due to cost restrictions. In addition, historical data from measurements of fixed net panels in current [1, 9, 24], flexible net panels in current [2], net cages in current [15] or net panels and cages in waves [14, 16] are considered to design the nets. In contrast, numerical modelling represents a less expensive and more flexible way of determining the loads on different sub-modules and prototypes in the design phase. In the past, numerical methods for traditional aquaculture cages mostly relied on linear potential theory for the load calculation and empirical formulae for estimating the velocity reduction through the net [14, 26]. The existing numerical studies of OOA structures [10, 11, 17] used simplified methods to predict the structural deformations in linear waves. In order to accurately understand the impact of offshore conditions on the structural response, two-way coupled simulations are necessary. Here, the modelling of the hydrodynamic forces affecting the dynamics of the floating rigid structure, the net and the mooring system as well as their effect on the surrounding fluid are necessary. Advanced numerical methods, such as computational fluid dynamics (CFD) models, are considered to be appropriate for investigating this non-linear interaction of fluid and structure in complicated conditions.

Chen and Christensen [7] were the first to publish a CFD approach for the fluid-structure interaction of fish cages and waves. It was based on the solution of the RANS equations in a two-dimensional numerical wave tank, a dynamic mesh algorithm for the floater and a lumped mass method to account for the deformation of the net. The coupling between net and fluid was accomplished using the porous medium approximation as given in [2, 5, 6, 24, 33]. This kind of approximation is necessary due to the large length scale difference between the twines of a net and the size of the complete structure, which prevents the resolution of the net on the same numerical grid as the fluid domain. The numerical model was tested against physical measurements of a two-dimensional floater with a net sheet attached. Even though a good agreement could be achieved, the applicability of the chosen approach is limited to mostly two-dimensional studies due to the porous medium approach [19]. Recently [21], a new CFD model was proposed to overcome this issue following a Lagrangian approach for the coupling of rigid [19] and flexible [18] net sheets and cages. It is based on the idea of continuous immersed boundary methods for fluid-structure interaction [25, 30]. Here, an additional source term is included in the conservation law of momentum. The term accounts for the momentum loss of the fluid while passing the net and is calculated from the hydrodynamic loads on the net itself. The model was successfully validated for three-dimensional OOA structures in current.

The remaining work starts with an overview of the numerical framework in [21] with emphasise on the floating body algorithm and its new coupling to the motion of stiff nets. The model is then adopted to study the dynamic response of a floating rigid OOA structure in waves and current. Final remarks can be found at the end of the paper.

2 Numerical Model

2.1 Fluid Dynamics

The two-way coupled solution for the fluid and floating body dynamics is described by the conservation equations of mass and momentum. In convective and one-fluid form, they can

be expressed as

$$\nabla \cdot \mathbf{u} = 0, \tag{1}$$

$$\frac{\partial \mathbf{u}}{\partial t} + \mathbf{u} \cdot \nabla \mathbf{u} = -\frac{1}{\rho}\nabla p + \mathbf{g} + \mathbf{f} + \mathbf{S}, \tag{2}$$

with $\mathbf{u}$ the velocity vector, p the pressure, $\mathbf{g}$ the gravitational acceleration vector, $\mathbf{f}$ the floating source term and $\mathbf{S}$ the coupling term for the net. In the fluid, (1)–(2) are the three-dimensional Reynolds-averaged Navier-Stokes equations and continuity equation if the definition

$$\mathbf{f} = \nabla \cdot \left(\nu \left[\nabla \mathbf{u} + \nabla \mathbf{u}^T\right]\right), \tag{3}$$

is used. In the solid phase, the term is defined such that a divergence free rigid body velocity field is ensured (see below).

The material properties, i.e. the density ρ and the viscosity ν, of the three phases air, water and solid are implicitly described using the zero level sets of signed distance functions (see Fig. 1). In the fluid domain, the level set function ϕ_f is transported in space and time using [23]

$$\frac{\partial \phi_f}{\partial t} + \mathbf{u} \cdot \nabla \phi_f = 0, \tag{4}$$

and reinitialised after each time step as proposed in [28]. In addition, the level set function ϕ_s is utilised to distinguish the solid from the fluid phase. Thus, the density and viscosity are defined as

$$\rho = \rho_s H(\phi_s) + (1 - H(\phi_s)) \cdot (\rho_w H(\phi_f) + \rho_a (1 - H(\phi_f))), \tag{5}$$

$$\nu = (1 - H(\phi_s)) \cdot (\nu_w H(\phi_f) + \nu_a (1 - H(\phi_f))), \tag{6}$$

with the indices w for water, a for air and s for solid. The smoothed Heaviside step function

$$H(\phi) = \begin{cases} 0 & \text{if } \phi < -\epsilon \\ \frac{1}{2}\left(1 + \frac{\phi}{\epsilon} + \frac{1}{\pi} sin(\frac{\pi\phi}{\epsilon})\right) & \text{if } |\phi| \leq \epsilon \\ 1 & \text{if } \phi > \epsilon, \end{cases} \tag{7}$$

is utilised to ensure a smooth transition between the different phases. Here, $\epsilon = 2.1\Delta x$ and Δx is the characteristic cell length. Turbulence effects are included as additional turbulent viscosity using the Boussinesq approximation and a modified k-ω turbulence model [3].

The set of equations (1) - (4) is solved on a staggered rectilinear grid using the finite difference method. The diffusion term in the fluid domain is discretised with a second-order accurate central difference in space and treated with the first-order Euler implicit method in time. Convection terms are discretised with fifth-order accurate weighted essentially non-oscillatory (WENO) schemes [12, 13] adapted to rectilinear grids in space. All source terms are explicitly added to the equations. The pressure-velocity coupling is ensured by following an incremental pressure-correction algorithm [29] with the third-order accurate TVD Runge-Kutta scheme [27] for the time discretisation. In each k-th sub-step of the Runge-Kutta scheme, a

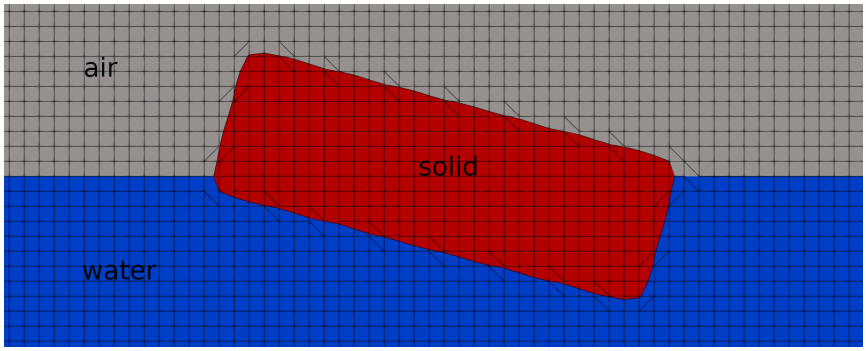

Figure 1: Illustration of the three phases in the computational domain. Water and air build together the fluid phase. The two interfaces between the phases are defined by the zero level sets of ϕ_f and ϕ_s.

predictor step is applied to approximate the velocity field using the pressure gradients of the previous step:

$$\frac{\mathbf{u}^{(*)} - \alpha_k \mathbf{u}^{(n)}}{\alpha_k \Delta t} = \frac{\beta_k}{\alpha_k}\mathbf{u}^{(k-1)} - \mathbf{u}^{(k-1)} \cdot \nabla \mathbf{u}^{(k-1)} - \frac{\nabla p^{(k-1)}}{\rho} + \mathbf{f}^{(*)} + \mathbf{g} + \mathbf{S}, \tag{8}$$

with $\alpha_k = 1.0, 1/4, 2/3$, $\beta_k = 0.0, 3/4, 1/3$ and $k = 1, 2, 3$. The pressure and final velocity fields are then found as

$$p^{(k)} = p^{(k-1)} + p_{\text{corr}} - \rho\nu \ \nabla \cdot u^{(*)}, \tag{9}$$

$$\mathbf{u}^{(k)} = \mathbf{u}^{(*)} - \frac{\alpha_k \Delta t}{\rho}\nabla p^{(k)}, \tag{10}$$

with the pressure correction term p_{corr} calculated from the Poisson equation

$$\nabla \cdot \left(\frac{1}{\rho}\nabla p_{\text{corr}}\right) = \frac{1}{\alpha_k \Delta t}\nabla \cdot \mathbf{u}^{(*)}. \tag{11}$$

The fully parallelized BiCGStab algorithm with geometric multigrid preconditioning from the HYPRE library [31] is utilised to solve (11) most efficiently.

2.2 Floating Body Dynamics

The floating body is described implicitly in the computational domain using the signed distance function ϕ_s. The function is generated from a STL geometry consisting of multiple non-connected triangles using a ray casting algorithm [4] to receive inside-outside information near the body and the same reinitialisation algorithm as for the free surface. Following the idea in [32], the coupling conditions between the floating body and the fluid is accomplished through the definition of the source term $\mathbf{f}$ in (2). In the solid phase, this term is defined as

$$\mathbf{f} = \frac{\partial \mathbf{P}(\mathbf{u})}{\partial t} + \mathbf{P}(\mathbf{u}) \cdot \nabla \mathbf{P}(\mathbf{u}) + \frac{1}{\rho}\nabla p - \mathbf{g}, \tag{12}$$

with $\mathbf{P}(\mathbf{u})$ the projection of the velocity field obeying the rigid body velocity constraint. Using $H(\phi_s)$ for representing the transition between the definition of $\mathbf{f}$ in the fluid and solid phase and the derivation in [21], the term can be written as

$$\mathbf{f}^{(n+1)} = H(\Phi_s^{(n+1)}) \cdot \left(\frac{\mathbf{P}(\mathbf{u}^{(\mathbf{n+1})}) - \mathbf{u}^{(*)}}{\Delta t} \right). \tag{13}$$

A good approximation of the updated velocity field is $\mathbf{u}^{(*)}$ itself. Thus, the forcing term is added to the predicted velocity field before solving the correction steps using the definition

$$\mathbf{f}^{(*)} = H(\phi_s^{(*)}) \cdot \left(\frac{\mathbf{P}(\mathbf{u}^{(*)}) - \mathbf{u}^{(*)}}{\alpha_k \Delta t} \right), \tag{14}$$

with the projection

$$\mathbf{P}(\mathbf{u}^{(*)}) = \dot{\mathbf{x}}_\mathbf{s} + \omega_\mathbf{s} \times \mathbf{r}. \tag{15}$$

Here, $\dot{\mathbf{x}}_\mathbf{s}$ are the three translational and $\omega_\mathbf{s}$ the three rotational rigid body velocities defined in the inertial system of the Eulerian computational domain and $\mathbf{r}$ equals the distance vector between a point in the domain and the centre of gravity of the floating body. The rigid body velocities are determined from the conservation laws of translational and rotational impulse. A first-order system was derived in [20] which can be solved with the same Runge-Kutta scheme as described above. The fluid forces and momenta acting on the floating structure are calculated using

$$\begin{aligned}
\mathbf{F}_\mathbf{x} &= \int_\Omega \left(-\mathbf{n}p + \rho\nu\mathbf{n}\tau\right) d\Omega(\mathbf{x}) = \sum_{i=1}^{N} \left(-\mathbf{n}p + \rho\nu\mathbf{n}\tau\right)_i \cdot \Delta\Omega_i, \\
\mathbf{M}_\mathbf{x} &= \int_\Omega \mathbf{r} \times \left(-\mathbf{n}p + \rho\nu\mathbf{n}\tau\right) d\Omega(\mathbf{x}) \\
&= \sum_{i=1}^{N} \mathbf{r}_i \times \left(-\mathbf{n}p + \rho\nu\mathbf{n}\tau\right)_i \cdot \Delta\Omega_i,
\end{aligned} \tag{16}$$

on the triangulated surface with trilinear interpolations of the fluid properties. Here, N is the number of STL triangles, $\mathbf{n}$ is the corresponding surface normal vector and τ is the viscous stress tensor. External forces from mooring lines are also added directly to the dynamic equations to enable two way coupled simulations.

2.3 Net Dynamics

The solidity ratio S_n of a net describes the ratio of solid front area to the total area including the voids between the twines. It is approximated using

$$S_n = \frac{2d}{l} - \left(\frac{d}{l}\right)^2, \tag{17}$$

with l the length and d the diameter of the twines. Aquaculture nets consist of a very large number of small twines compared to the complete structural dimension and the length scale

of the incoming waves. Thus, no conventional discretisation of the fluid domain around all details of the net structure is possible. In [19], a forcing method is proposed to approximate the correct boundary conditions at the fluid-structure interface. Here, a coupling term $\mathbf{S}$, which expresses the physical loss of fluid momentum due to the presence of the net leading to a pressure jump, is included in the momentum equations (see (2)). This term is calculated from the external forces acting on uniformly distributed Lagrangian points which follow the net. The uniformity is achieved by discretising the net surface into triangles with the same characteristic length as the surrounding fluid cells. The points are then defined in the geometrical centres of all triangles as illustrated in Fig. 2.

The external force vector $\mathbf{s}$ at the Lagrangian point with position $\mathbf{x}_L = (x_L, y_L, z_L)$ and corresponding area A_L is determined using an extended screen force model. Besides the gravity and buoyancy forces, this includes inertia as well as hydrodynamic drag and lift forces:

$$\mathbf{s}(\mathbf{x}_L) = (\mathbf{G}_L + \mathbf{I}_L + \mathbf{D}_L) \cdot A_L. \tag{18}$$

The gravitational force $\mathbf{G}$ is approximated from the weight of the occupied net surface A_L. Further, the inertia force $\mathbf{I}_L$ is calculated as

$$\mathbf{I}_L = m_{a,L} \left(\mathbf{a}_\mathbf{f} + \mathrm{diag}(n_x, n_y, n_z)\ \mathbf{a}_\mathrm{rel} \right)_L, \tag{19}$$

with $m_{a,L}$ the added mass, $\mathbf{n}_L$ the unit normal vector of A_L, $\mathbf{a}_{f,L}$ the fluid acceleration at $\mathbf{x}_L$ and $\mathbf{a}_{\mathrm{rel},L}$ the relative acceleration vector between fluid and structure. The added mass is thereby assumed to equal the mass of the water volume displaced by the solid cylindrical twines in A_L. As can be seen from (19), it is only applied in the direction of $\mathbf{n}_L$. The hydrodynamic drag and lift force $\mathbf{D}_L$ is given as

$$\mathbf{D}_L = \frac{\rho}{2} u_{\mathrm{rel},L}^2 \cdot (c_d \mathbf{n}_d + c_l \mathbf{n}_l)_L, \tag{20}$$

with $\mathbf{n}_d$ the normal and $\mathbf{n}_l$ the tangential direction of the relative vector $\mathbf{u}_{\mathrm{rel},L}$ between fluid and solid velocity. Further details about the calculation of (20) can be found in [19]. The forces are finally distributed on the fluid cell points $\mathbf{x}_e = (x_e, y_e, z_e)$ using

$$\mathbf{S}(\mathbf{x}_e) = \sum_{L=1}^{L_e} \frac{\mathbf{s}(\mathbf{x}_L)}{\Delta V}\ K\left(\frac{x_e - x_L}{\Delta x}\right)\ K\left(\frac{y_e - y_L}{\Delta y}\right)\ K\left(\frac{z_e - z_L}{\Delta z}\right), \tag{21}$$

with L_e the number of Lagrangian points within a defined kernel K around $\mathbf{x}_e$ and $\Delta V = \Delta x \Delta y \Delta z$.

In [18], an implicit method for solving the structural dynamics of nets was proposed. However, offshore aquaculture structures are typically equipped with relatively stiff nets with negligible deformations. It could be shown in [21] that it is appropriate to assume that the net moves with the rigid floating structure in this case. Thus, the Lagrangian points are updated in each time step using the translational and rotational velocities of the floating body. A two-way coupled approach is chosen by adding the forces acting on the net as external forces to the rigid body dynamics equations. The interaction of the net and fluid is accomplished through the described coupling term (21).

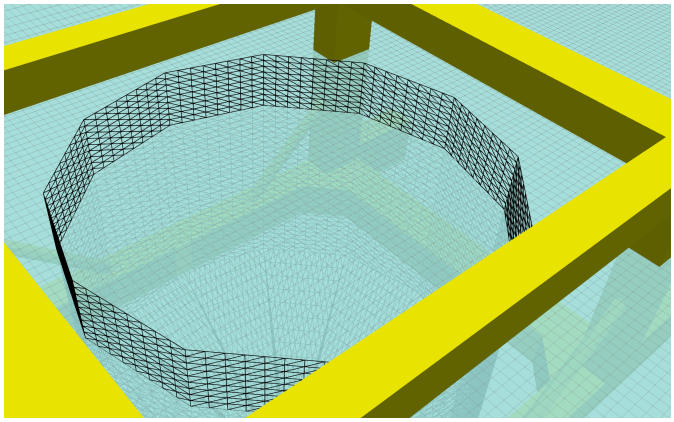

Figure 2: Illustration of the discretised net for the two-way coupling to the fluid solution. Each black triangle holds one Lagrangian point representing the portion of the net. The grey lines on the blue surface represent the fluid cells around the net. The solid floating body is shown in yellow.

3 Results

Extensive validation of the proposed numerical framework has been presented for floating body motion in waves, the fluid-net coupling in current and waves as well as the coupling of the floating body and the net in [18, 19, 21]. In the following, the rigid floating structure Havfarm 2 from Nordlaks and NSK Ship Design [22] is utilised to study the effects of wave and current on OOA structures. The $1 : 40$ model test results obtained from measurements in the ocean basin of SINTEF Ocean in Trondheim, Norway, are considered for validation purposes.

As can be seen from Fig. 3, multiple rectangular beams compose the main structure which is approximately 7.5 m long, 1.6 m wide and 1.1 m high. The design draft used in this study is 0.8 m. Between the longitudinal beams, four equally sized box-shaped spaces are formed. In each space, a net is embedded in the form of the frustum of a pyramid and tightly fastened to the frame. At the lower end of the nets, a pyramid-shaped net is attached to increase the enclosed volume. All nets have a solidity of 0.22. In contrast to previous research [21], the deformation of the nets is neglected due to its minor influence on the motion of these type of OOA structures. The validity of this assumption is confirmed below.

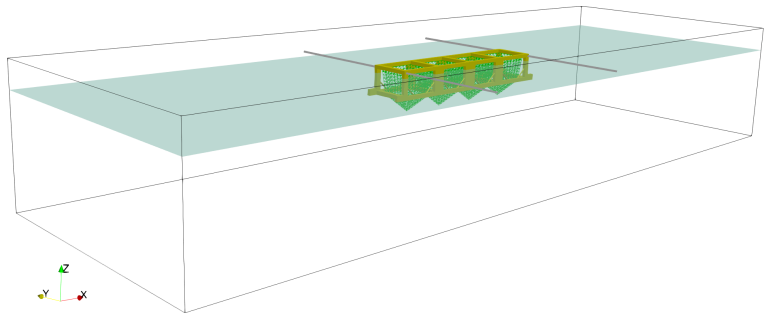

Figure 3: Rigid floating OOA structure in a numerical wave tank. The structure is shown in yellow, the nets in green and the mooring lines in grey. The free surface is indicated in blue.

3.1 Decay Tests

A grid convergence study is conducted using the decay tests in pitch and heave. A refinement box with a uniform cell size of $\Delta x = \Delta y = \Delta z = 0.045, 0.03$ and 0.015 m is placed in a rectangular domain of $15 \times 10 \times 10$ m. The chosen domain size is justified by placing numerical beaches at all domain boundaries to absorb the energy induced by the structural motion. The water height is 8 m. The cell size is gradually coarsened towards the domain boundaries with a ratio of 1.1. The OOA structure including the attached nets is placed in the centre of the refinement box with an initial displacement of $\Delta z = 0.09$ m for the heave decay test and $\Delta\Theta = 1.4°$ for the pitch decay test. Small displacements of the other degrees of freedom in the model tests are respected in the simulations as well.

The time series of the decay tests are compared to the measurements in Fig. 4. On the coarsest grid, a too-large heave frequency and a relatively large peak deviation are predicted (see Fig. 4a). A cell size of 0.03 m around the structure improves the results, especially for the first peaks. Further convergence of the solution towards the experimental data is seen for the finest grid size. In Fig. 4b, the decay rate is plotted as the damping ratio over time. The numerical solution can replicate the measured damping on all grids. Similarly, the time series and decay rate for the simulated pitch decay test is presented in the Figs. 4c-4d. The pitch frequency converges towards the reported value with decreasing cell size. The first three peaks are captured well with the two finer grids, whereas an under-prediction is present at the last peak. A further refinement might improve the results, but it should also be noticed that the angles itself are already very small in magnitude. Hence, small deviations in the setup can have significant effects on the results. As for the heave decay test, the decay rate is predicted well by the numerical model, and the convergence of the results with increasing grid size is visible. Based on these results, a cell size of 0.03 m is chosen around the structure for the analyses below.

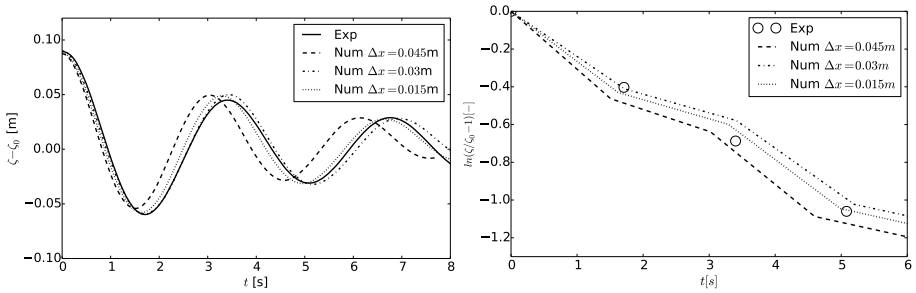

(a) Time series of the heave decay test.

(b) Decay rate for the heave decay test.

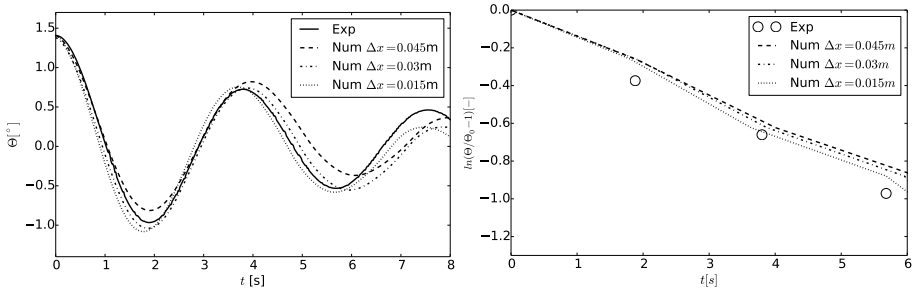

(c) Time series of the pitch decay test.

(d) Decay rate for the pitch decay test.

Figure 4: Comparison of the numerical and experimental results for the decay tests of the OOA structure.

3.2 Current

The current flow around the OOA structure is investigated next. The length of the numerical domain of the decay test is doubled in x- and y-direction for this purpose. At the inlet, a constant velocity of 0.83 m/s and 1.0 m/s is prescribed. The side boundaries are modelled as walls, and a free outflow boundary condition is placed at the outlet. The influence of the flow direction is investigated by rotating the structure gradually. Thus, angles of attack α of $0, 15, 45$ and $90°$ are considered. Physical model tests were performed for the first three angles of attack. The structure was fixed by a stiff mooring system during the experiments. In the simulations, all degrees of freedom are prevented to replicate this setup. The velocities in x and y direction are measured in the centre of each cage 0.1 m below the free surface over 30 s. The mean values are then computed and compared to the model test results in the Figs. 5-6. In x-direction, the velocities are presented as the velocity reduction factors $U_r = 1 - U/U_\infty$ which is a common quantity in aquaculture applications. The physically measured velocity time series showed large velocity oscillations for which reason the experimental values are plotted as bars indicating the variation of one standard deviation around the mean value.

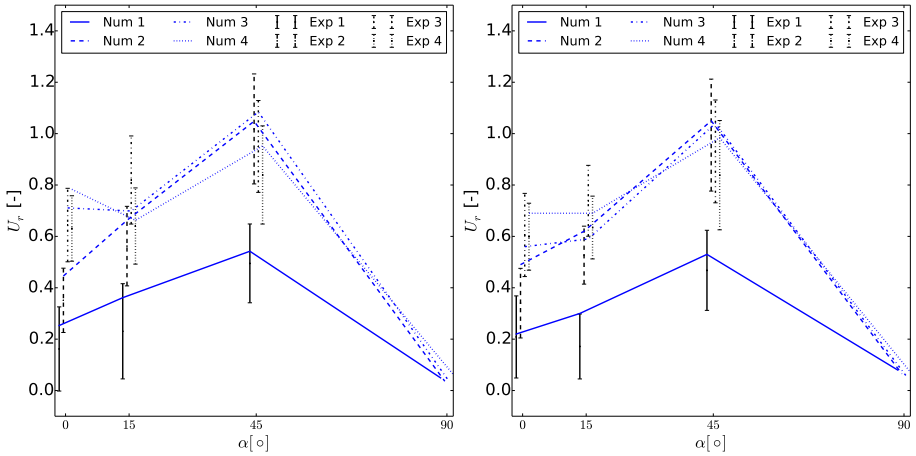

(a) Velocity reduction factors over α for U_∞ = 0.83 m/s.

(b) Velocity reduction factors over α for U_∞ = 1.0 m/s.

Figure 5: Mean velocity reduction factors inside the net cages for different inflow velocities U_∞ and angles of attack. The numbers in the legend indicate the cage number with 1 representing the cage in the fore. The vertical bars indicate the model test results in terms of one standard deviation around the mean value.

In Fig. 5, the velocity reduction factors are compared. It is first noticed that the factors are similar for the two inflow velocities. This is in accordance with the results in [19] for the flow through a rigid net panel. After the flow passes the front part of the net, the fluid velocity reduces by approximately 20% for $\alpha = 0°$. The velocity in the first net further decreases for angles of attack up to 45° because the recirculation zone behind the rigid parts of the structure is turned into the centric part of the net (see Fig. 7a). The reduction factors generally increase with each additionally past net if no heading angle is present. At the heading angles of 15 and 45°, this changes significantly as the factor in the aft net of the body is smaller than in the central nets 2 and 3. This is probably caused by a relatively undisturbed inflow at the last net compared to the more chaotic flow patterns in front of the central nets arising from the fluid-structure interaction at the front net. This effect is however rather small compared to the observation that the velocity reduction generally reduces again for heading angles larger than 45°. It is caused by the fact that with increasing angle, the flow is passing fewer net surfaces which would cause additional velocity reductions (compare Fig. 7b). At 90°, the velocity reduction factors are similar in all nets (about 0.08) due to the undisturbed inflow sidewards. All described phenomena are well captured by the numerical model because the predicted velocity reduction factors are within the chosen range of measured results.

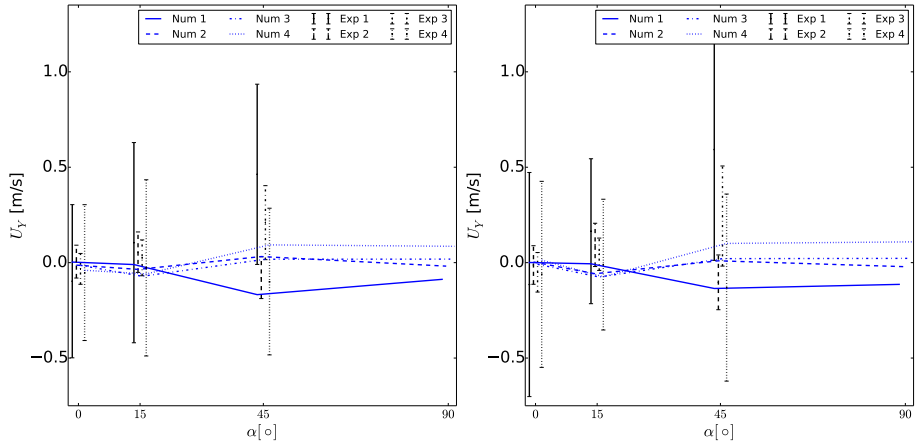

(a) Velocities in y-direction over α for U_∞ = 0.83 m/s.

(b) Velocities in y-direction over α for $U_\infty = 1.0$ m/s.

Figure 6: Mean velocities in y-direction inside the net cages for different inflow velocities U_∞ and angles of attack. See Fig. 5 for further explanations.

In contrast to the velocities in x-direction, the mean y-velocities in Fig. 6 are generally smaller and oscillate more. This is again caused by the recirculation zones behind each beam interacting the flow in the net cages. This effect is largest for the cages in the front and aft of the structure and $\alpha = 0$ and 45° because, at these locations, the inflow velocity is relatively large. This might cause stronger fluctuations of the turbulent recirculation zones. In contrast, the fluctuations in y-direction are small in the central cages due to the fluid being blocked by the structure and nets in front of them. It is finally noticed that for $\alpha = 90°$, both the y-velocities in the outer nets and the velocities in the central nets are symmetrical. Here, the velocities in the outer nets tend to be larger because of the asymmetrical frame enclosing these nets compared to the symmetrical configuration around the inner nets.

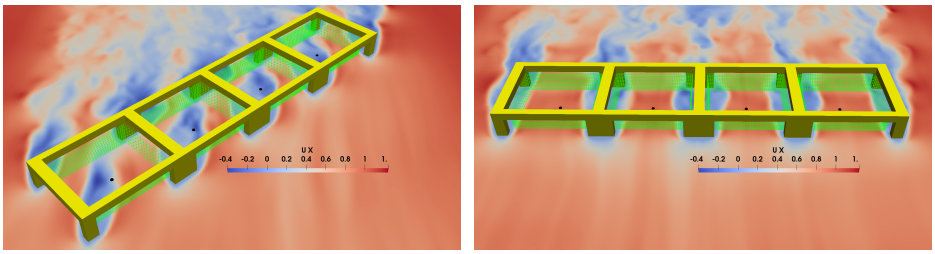

(a) $\alpha = 45°$.

(b) $\alpha = 90°$.

Figure 7: X-velocity profiles in the plane through $z = 7.8$ m for two different heading angles and $U_\infty = 1.0$ m/s. Incident flow from the bottom. The black dots indicate the probe points.

3.3 Waves

Next, the dynamic response of the OOA structure in waves is investigated. Two regular waves with a height of $H = 0.1125$ m and the frequencies of $f = 0.421$ Hz (wave 1) and $f = 0.294$ Hz (wave 2) were considered in the experiment. A numerical wave tank is established to reproduce the physical setup (see Fig. 3). At the inlet, a relaxation zone [3] is defined to generate the waves as second-order Stokes waves. A numerical beach at the end of the tank damps the waves such that reflections can be avoided. The structure is placed in the middle of the tank with heading angles between 0 and 90°. Four mooring lines are horizontally attached to the sides of the structure to keep the structure in the centre of the tank. The lines are modelled as springs with predefined pre-tension in accordance with the experimental setup.

Table 1: Measured meain frequencies for the motion of the OOA structure in waves. G1 and G3 are the two wave gauges. All measures in Hz.

$H[m]$	f	α	$G1$	$G3$	$Surge$	$Heave$	$Roll$	$Pitch$	Yaw
0.1125	0.421	0	0.424	0.424	–	0.424	–	0.425	–
0.1125	0.421	15	0.424	0.424	–	0.425	0.425	0.424	0.425
0.1125	0.421	45	0.424	0.424	0.425	0.425	0.425	0.425	0.424
0.1125	0.294	0	0.291	0.291	0.291	0.291	–	0.291	–
0.1125	0.294	15	0.291	0.292	0.294	0.291	0.293	0.291	0.291
0.1125	0.294	45	0.292	0.291	0.293	0.291	0.294	0.293	0.294

Table 2: Numerically calculated main frequencies for the motion of the OOA structure in waves. G1 and G3 are the two wave gauges. All measures in Hz.

$H[m]$	f	α	$G1$	$G3$	$Surge$	$Heave$	$Roll$	$Pitch$	Yaw
0.1125	0.421	0	0.422	0.422	–	0.419	–	0.421	–
0.1125	0.421	15	0.422	0.422	–	0.424	0.421	0.422	0.422
0.1125	0.421	45	0.421	0.422	0.421	0.420	0.421	0.420	0.422
0.1125	0.294	0	0.293	0.294	0.293	0.294	–	0.294	–
0.1125	0.294	15	0.293	0.294	0.295	0.294	0.292	0.293	0.295
0.1125	0.294	45	0.293	0.294	0.293	0.294	0.293	0.294	0.294

At first, the waves are validated at two different wave gauges. G1 is located 1.5 m in front of the structure and G3 is located 1.5 besides the centre of the structure. The measured frequencies are summarised in the Tabs. 1 and 2, and the amplitudes can be found in Fig. 8a. The model tests measure a minor increase of the frequency for the short wave and a minor decrease in the frequency for the long wave. In contrast, the simulation predicts wave frequencies very close to the input signal. The maximum deviation is less than 1%. Similar accuracy is achieved for the amplitudes except for the short wave at G3 were an under-prediction of about 7% is present.

The translational motions surge and heave, as well as the rotational motions around all three axes, are considered next. The frequencies can be found in Tabs. 1 and 2, whereas the Figs. 8b and 8c compare the amplitudes obtained from a FFT analysis of the time series signal. The simulated results show motion frequencies close to the wave frequency and the

experimental results. Further, the heave and surge amplitudes are larger for the longer wave which has a wavelength of twice the structural length. Generally, a good agreement between experimental and numerical results can be stated for the translational motions with deviations of less than 15% for all cases.

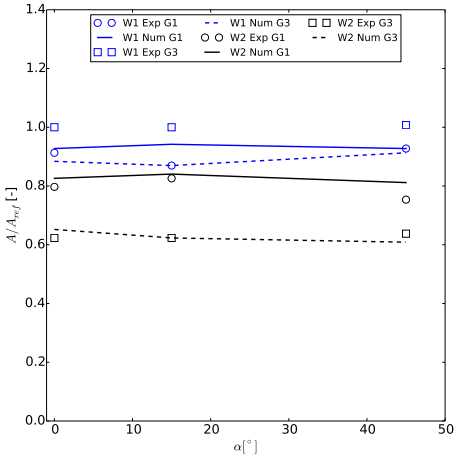

(a) Wave amplitude at the two wave gauges.

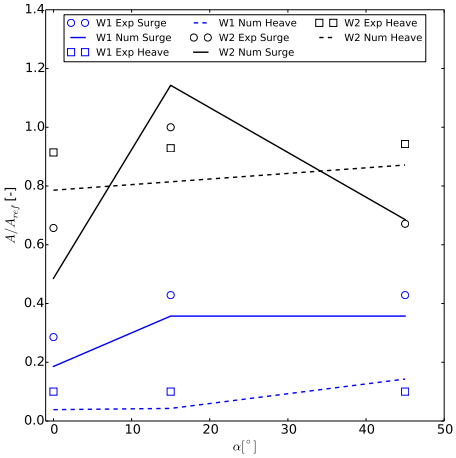

(b) Amplitudes of the translational motions.

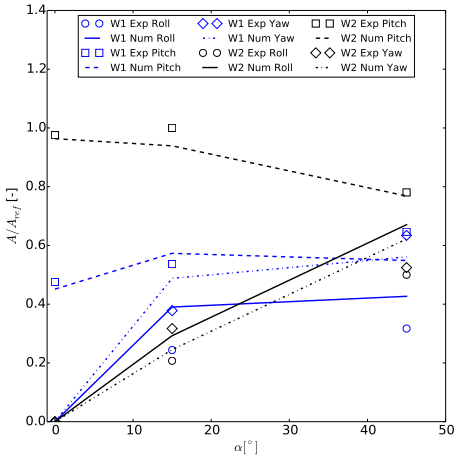

(c) Amplitudes of the rotational motions.

Figure 8: Numerical and experimental results for the mean wave amplitudes and mean response amplitudes for different heading angles α. The amplitudes are calculated using a FFT and normalised with the largest measured amplitude. The two wave inputs are indicated in blue (wave 1) and black (wave 2).

The amplitudes of the rotational motions are presented in Fig. 8c. The largest rotations are observed around the y-axis (pitch) with up to 0.8°. Pitch is also larger in the long wave because the wave crest reaches the front of the structure while at the same time a wave trough is present at the aft. In comparison, two wave crests are at both ends of the structure in the shorter wave with a wavelength similar to the structure (compare Fig. 9). The pitch motion tends to decrease with increasing heading angle due to the shortening of the structural dimensions in wave direction. In contrast, the rotations around the body fixed x- and z-axis increase with α due to the same reason. In general, the numerical model agrees well with the experiments at small heading angles as the deviations are below 5%. Larger differences are observed for the roll motion at $\alpha = 45\%$ (about 15%) which might be caused by a slightly different attachment position of the mooring lines in the experiments.

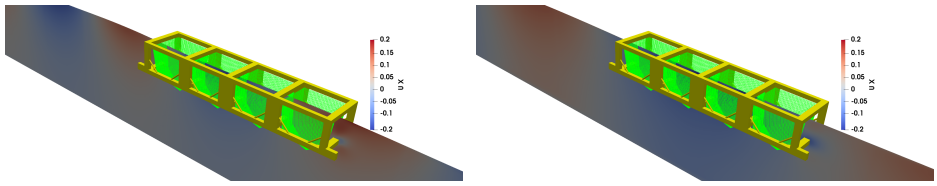

(a) Short wave (wave 1). (b) Long wave (wave 2).

Figure 9: X-velocity profiles under the free surface in the plane through the centre of the structure for $\alpha = 15°$ and the two different wave inputs. The waves propagate from the left to the right.

Finally, the mean force amplitudes of the four different nets are analysed in Fig. 10. No experimental data are given for this property. If no heading angle is present, the forces are largest in x-direction whereas the forces in y-direction are close to zero. Despite the circular motion of the fluid particles in the given waves, the forces in z-direction are smaller due to the small bottom surface of the net compared to the vertical surfaces. Also, the forces are larger in the short wave than in the long wave. This might be due to the smaller structural motions in wave 1 leading to a more direct inflow into the cages. The force magnitudes tend to decrease with increasing heading angles due to a stronger blockage effect through the rigid structure. It is further noticed that no clear pattern of the force direction and magnitude can be found for the different net cage positions. This indicates that the structural motion, including its blockage effects at different heading angles, has an important effect on the expected net forces, whereas the shielding effect of the nets plays an insignificant role for the nets in the aft of the OOA structure.

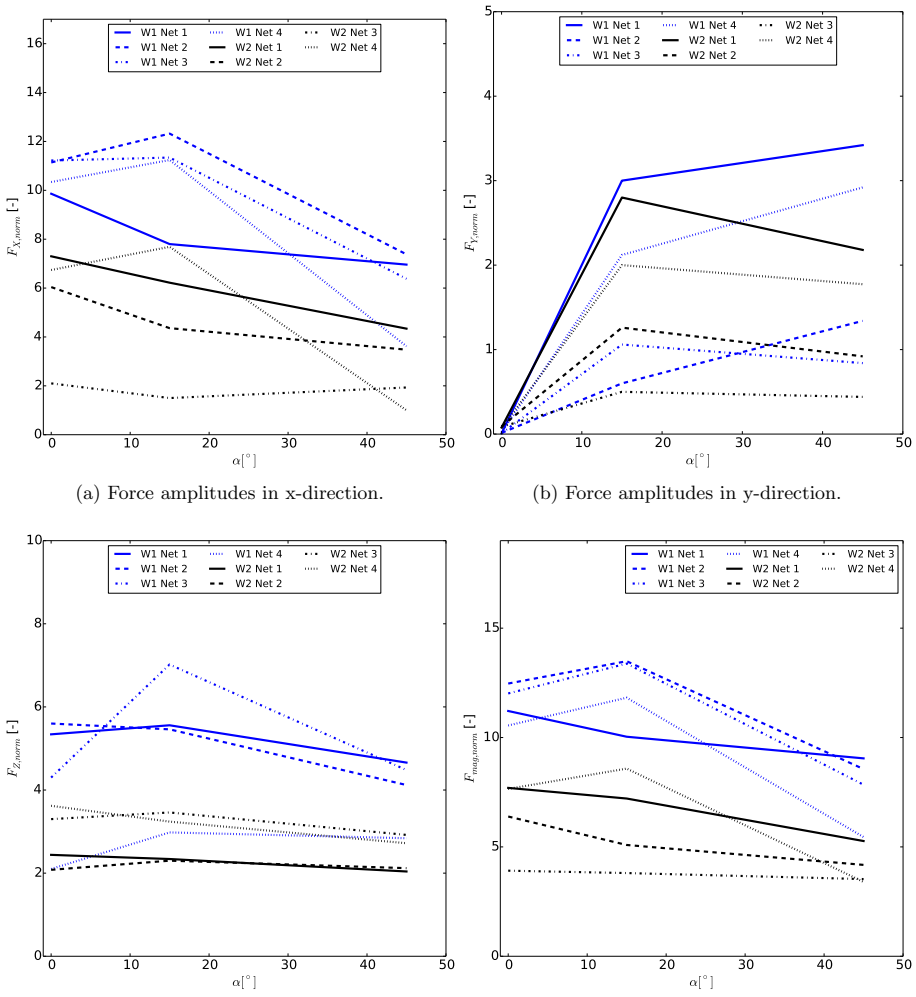

(a) Force amplitudes in x-direction.

(b) Force amplitudes in y-direction.

(c) Force amplitudes in z-direction.

(d) Force magnitude amplitudes.

Figure 10: Numerical results for the mean net force amplitudes for different heading angles α. The results are normalised with the smallest force in x-direction at net 4.

4 Conclusion

In this paper, a CFD approach for the simulation of OOA structures in waves is presented. The model solves the Navier-Stokes equations for an incompressible two-phase fluid with additional source terms to account for the floating rigid structure and the shielding effects of the net. Hence, two-way coupled simulations of all involved parts are enabled. It is proposed that the

net in OOA structures can be modelled as a rigid surface moving with the frame structure due to its high stiffness. The presented study indicates the validity of this assumption. Thus, it would be straightforward to apply this approach to deforming nets as shown in [18]. The numerical model was applied to the rigid floating aquaculture facility Havfarm 2 in current and waves. The correct representation of the structural motion in the fluid was successfully validated using decay tests in heave and pitch. In current, the velocities inside the cages are mainly influenced by the heading angle of the structure. For angles between 0 and 90°, complex flow patterns are observed. Angles of 90° result in smooth flow patterns and the highest velocities inside all cages. In practice, this would be the ideal flow condition as it ensures the optimal circulation of oxygen and removal of pollution. The investigation of the motion in waves reveals relatively large translational motions in long waves and relatively large rotational motions in waves with lengths equal to the length of the structure. Besides, it could be shown that the forces on the net cages are rather influenced by the motion and location of the structure than by the shielding effect of the cages. This is in contrast to the observations in current.

Acknowledgement

The authors are grateful for the grants provided by the Research Council of Norway under the HAVBRUK2 project (no. 267981). The computations were performed on resources provided by UNINETT Sigma2 - the National Infrastructure for High Performance Computing and Data Storage in Norway (`http://www.sigma2.no`) under project No. NN2620K. Further, the authors want to thank Håkon Ådnanes from NSK Ship Design for providing the geometry and physical model test results for Havfarm 2.

References

[1] C.-W. Bi et al. “Experimental investigation of the reduction in flow velocity downstream from a fishing net”. In: *Aquaculture Engineering* 57 (2013), pp. 71–81.

[2] C.-W. Bi et al. “Numerical simulation of the interaction between flow and flexible nets”. In: *J. Fluids Struct.* 45 (2014), 180–201.

[3] H. Bihs et al. “A new level set numerical wave tank with improved density interpolation for complex wave hydrodynamics”. In: *Computers & Fluids* 140 (2016), 191–208.

[4] H. Bihs et al. “Complex geometry handling for a cartesian grid based solver”. In: *MekIT, 17-Ninth national conference on Computational Mechanics* (2017).

[5] H. Chen and E.D. Christensen. “Development of a numerical model for fluid-structure interaction analysis of flow through and around an aquaculture net cage”. In: *Ocean Engineering* 142 (2017), 597–615.

[6] H. Chen and E.D. Christensen. “Investigations on the porous resistance coefficients for fishing net structures”. In: *J. Fluids Struct.* 65 (2016), 76–107.

[7] H. Chen and E.D. Christensen. “Simulating the hydrodynamic response of a floater net system in current and waves”. In: *J. Fluids Struct.* 79 (2018), 50–75.

[8] J.G. Ferreira et al. “Modelling of interactions between inshore and offshore aquaculture”. In: *Aquaculture* (2014), pp. 154–164.

[9] H.M Føre et al. “Loads on net panels with different solidities”. In: *ASME 2020 39th International Conference on Ocean, Offshore and Arctic Engineering* (2020).

[10] D.W. Fredriksson et al. “Fish cage and mooring system dynamics using physical and numerical models with field measurements”. In: *Aquacultural Engineering* 27 (2003), 117–146.

[11] D.W. Fredriksson et al. “Moored fish cage dynamics in waves and currents”. In: *IEEE Journal of Oceanic Engineering* 30(1) (2005), 28–36.

[12] G.S. Jiang and D. Peng. “Weighted ENO schemes for Hamilton Jacobi equations”. In: *SIAM Journal of Scientific Computing* 21 (2000), 2126–2143.

[13] G.S. Jiang and C.W. Shu. “Efficient implementation of weighted ENO schemes”. In: *Journal of Computational Physics* 126(1) (1996), 202–228.

[14] T. Kristiansen and O. M. Faltinsen. “Experimental and numerical study of an aquaculture net cage with floater in waves and current”. In: *Journal of Fluids and Structures* 54 (2015), pp. 1–26.

[15] P. F. Lader and B. Enerhaug. “Experimental Investigation of Forces and Geometry of a Net Cage in Uniform Flow”. In: *IEEE Journal of Oceanic Engineering* 30.1 (2005), pp. 79–84.

[16] Pål Lader et al. “Experimental Investigation of Wave Forces on Net Structures”. In: *Applied Ocean Research* 29.3 (2007), pp. 112–127.

[17] L. Li et al. “Numerical Analysis of a Vessel- Shaped Offshore Fish Farm”. In: *Journal of Offshore Mechanics and Arctic Engineering* 140 (2018). doi: 10.1115/1.4039131.

[18] T. Martin and H. Bihs. “A non-linear implicit approach for modelling the dynamics of porous tensile structures interacting with fluids”. In: *Journal of Fluids and Structures* Volume 100 (2021). doi: 10.1016/j.jfluidstructs.2020.103168.

[19] T. Martin, A. Kamath, and H. Bihs. “A Lagrangian approach for the coupled simulation of fixed net structures in a Eulerian fluid model”. In: *Journal of Fluids and Structures* (94) (2020). doi: 10.1016/j.jfluidstructs.2020.102962.

[20] T. Martin, A. Kamath, and H. Bihs. “Accurate modeling of the interaction of constrained floating structures and complex free surfaces using a new quasistatic mooring model”. In: *International Journal for Numerical Methods in Fluids* (2020). doi: 10.1002/fld.4894.

[21] T. Martin, A. Tsarau, and H. Bihs. “A numerical framework for modelling the dynamics of open ocean aquaculture structures in viscous fluids”. In: *Applied Ocean Research* In Press (2020). doi: 10.1016/j.apor.2020.102410.

[22] Nordlaks. `https://www.nordlaks.no/havfarm/om-havfarm-prosjektet`. accessed 21.12.2020.

[23] S. Osher and J.A. Sethian. “Fronts propagating with curvature-dependent speed: Algorithms based on Hamilton-Jacobi formulations”. In: *Journal of Computational Physics* 79 (1988), 12–49.

[24] Ø. Patursson et al. “Development of a porous media model with application to flow through and around a net panel”. In: *Ocean Engineering* 37 (2010), 314–324.

[25] C. S. Peskin. “Numerical analysis of blood flow in the heart”. In: *Journal of Computational Physics* 25 (3) (1977), pp. 220–252.

[26] Y. Shen et al. “Numerical and experimental investigations on mooring loads of a marine fish farm in waves and current”. In: *Journal of Fluids and Structures* 79 (2018), pp. 115–136.

[27] C.W. Shu and S. Osher. “Efficient implementation of essentially non-oscillatory shock-capturing schemes”. In: *Journal of Computational Physics* 77(2) (1988), 439–471.

[28] M. Sussman, P. Smereka, and S. Osher. “A level set approach for computing solutions to incompressible two-phase flow”. In: *Journal of Computational Physics* 114 (1994), 146–159.

[29] L.J.P. Timmermans, P.D.. Minev, and F.N. Van De Vosse. “An approximate projection scheme for incompressible flow using spectral elements”. In: *International Journal for Numerical Methods in Fluid* 22 (1996), 673–688.

[30] M. Uhlmann. “An immersed boundary method with direct forcing for the simulation of particulate flows”. In: *Journal of Computational Physics* 209 (2005), 448–476.

[31] H. van der Vorst. “BiCGStab: A fast and smoothly converging variant of Bi-CG for the solution of nonsymmetric linear systems”. In: *SIAM Journal of Scientific Computing* 13 (1992), 631–644.

[32] L. Yang. “One-fluid formulation for fluid–structure interaction with free surface”. In: *Comput. Methods Appl. Mech. Engrg.* 332 (2018), 102–135.

[33] Y.-P. Zhao et al. “Numerical Simulation of Interaction Between Waves and Net Panel Using Porous Media Model”. In: *Engineering Applications of Computational Fluid Mechanics* 8.1 (2014), pp. 116–126.

ISBN 978-82-326-6630-0 (printed ver.)
ISBN 978-82-326-6197-8 (electronic ver.)
ISSN 1503-8181 (printed ver.)
ISSN 2703-8084 (online ver.)

NTNU
Norwegian University of
Science and Technology